# Modeling and Simulation of Electrical Breakdown in DC for Dielectric-Loaded Systems with Non-Orthogonal Boundaries Including the Effects of Space-Charge and Gaseous Collisions

by

Manuel Thomas Pangelinan Aldan III

A dissertation submitted in partial satisfaction of the
requirements for the degree of
Doctor of Philosophy

in

Engineering - Nuclear Engineering

in the

GRADUATE DIVISION
of the
UNIVERSITY OF CALIFORNIA, BERKELEY

Committee in charge:
Professor John P. Verboncoeur, Co-Chair
Professor Ka-Ngo Leung, Co-Chair
Professor Eric B. Norman
Professor Michael A. Lieberman

Fall 2015

**Modeling and Simulation of Electrical Breakdown in DC for Dielectric-Loaded Systems with Non-Orthogonal Boundaries Including the Effects of Space-Charge and Gaseous Collisions**

## Abstract

Modeling and Simulation of Electrical Breakdown in DC for Dielectric-Loaded Systems with Non-Orthogonal Boundaries Including the Effects of Space-Charge and Gaseous Collisions

by

Manuel Thomas Pangelinan Aldan III
Doctor of Philosophy in Engineering - Nuclear Engineering

University of California, Berkeley

Professor John P. Verboncoeur, Co-Chair
Professor Ka-Ngo Leung, Co-Chair

Improved modeling of angled-dielectric insulation in high-voltage systems is described for use in particle-in-cell (PIC) simulations. Treatment of non-orthogonal boundaries is a significant challenge in modeling angled-dielectric flashover, and conditions on boundaries are developed to maintain uniform truncation error in discretized space across the dielectric angles studied. Extensive effort was expended in isolating particular operating regimes to illustrate fundamental phenomenological surface effects that drive the discharges studied herein; consequently, this document focuses on the phenomenology of two specific dielectric angles at 6.12° for multiplicative breakdown (the so-called single-surface multipactor) and 22.9° for a non-multiplicative discharge that evolves into a dark current at steady state.

Phenomenological results for simulations in vacuum through "ultra-low pressures" on the order of a few hundred mTorr are presented. A multipactor front forms via net emission of electrons from impact on the dielectric surface, where emission leads to saturated field conditions in the wake of the front, producing a well-defined forward-peaked wave. A treatment of the gain and saturation characteristics is presented, isolating the surface electric fields as the driving contributor to both metrics. Physical models include often-neglected effects such as space-charge, dielectric-surface charging, and particle distributions in energy and space. For the discharges treated in this study, breakdown voltages of the typical Paschen form are not applicable, since multiplicative conditions are driven primarily by surface effects.

Phenomenological results are also presented for simulations at low pressure ($\sim 1$ Torr), which is shown to be a transitional limit where volume effects become appreciable compared to surface effects. A coupling between space charge and surface charge is shown to lead to oscillatory effects in otherwise DC discharges. Surface multipactor leads to increased ionization and space charge, and the ensuing space-charge momentum alters what would have been a steady-state saturation as in the case of vacuum-like discharges. Models for diffusive outgassed species are developed and implemented, extending the capabilities of the PIC suite.

The overarching theme of this study is to communicate the dependence of multiplicative discharges dominated by surface effects on near-surface electric field conditions. It

is shown through various examples from vacuum through low pressures, and in diffusive gases, that single-surface multipactor conditions can be expressed solely in terms of the dielectric surface field angles. This treatment lays the foundation for a novel extension of RF breakdown susceptibility theory [1] to the DC regime, grounding breakdown susceptibility to the well-established fundamentals on secondary emission [2, 3]. This theory shows that breakdown characteristics can be modeled in an *a-priori* framework, hence the lack of a Paschen-type curve.

Finally, the effect of the seed source on discharge characteristics is also studied. A comparison between a constant-waveform source, a Fowler-Nordheim source, and an application of a modified source based on theoretical treatment from [4] are presented, showing that the seed is a necessary but insufficient condition for surface flashover, where the dominant contributor is the configuration of the surface fields downstream of the seed source. While the seed can influence upstream conditions to alter the injected current, the gain characteristics of the downstream region are still well described by the framework developed in the remainder of this document.

To my nieces, Chantelle and Charlynn.

# Contents

**List of Figures** v

**List of Tables** x

**1 Introduction** 1
- 1.1 Purpose and Scope . . . 1
- 1.2 Initial Motivation . . . 3
- 1.3 Vacuum to Gas Discharges and their Applications . . . 4
  - 1.3.1 Electrical Breakdown . . . 5
  - 1.3.2 Single-Surface Multipactor . . . 7
  - 1.3.3 Gaseous Electron Avalanche . . . 9
- 1.4 Overview of Particle In Cell . . . 10

**2 Models and Methods** 14
- 2.1 Space Charge . . . 15
- 2.2 Taverniers' Model . . . 15
  - 2.2.1 The Numerical Grid . . . 16
  - 2.2.2 Analysis of Rotated-Grid Geometry . . . 19
- 2.3 Secondary Emission . . . 24
  - 2.3.1 Metal Model . . . 24
  - 2.3.2 Dielectric Extension . . . 25
- 2.4 Outgassing and Diffusion Models . . . 29
- 2.5 Seed-Current Models . . . 31
  - 2.5.1 Constant-Waveform Source . . . 31
  - 2.5.2 Fowler-Nordheim Source . . . 32
  - 2.5.3 Schächter Source . . . 32
- 2.6 Notable Corrections and Additions . . . 35
- 2.7 Standard Parameters and Reduced Parameters . . . 37
- 2.A Schächter Formulation . . . 37
  - 2.A.1 The Triple Point . . . 37
  - 2.A.2 The Triple-Point Potential . . . 39
  - 2.A.3 The Triple-Point Fields and Charge . . . 41
  - 2.A.4 Electrostatic Energy Around the Triple Point . . . 42
  - 2.A.5 Capacitance of the Triple-Point Region . . . 43
  - 2.A.6 The Effective Voltage of the Triple-Point Region . . . 44
  - 2.A.7 Integrated Current with Constant Charge . . . 45

2.A.8 Integrated Current with Constant Effective Voltage . . . 47
2.B Diffusion Model . . . 49
2.B.1 Derivation of a 1-D Diffusion Relation . . . 50
2.B.2 Crank-Nicolson in 1-D . . . 52
2.B.3 Extending to 2-D with ADI . . . 53
2.B.4 Extending to Spatially-Varying Diffusivity . . . 54

**3 Vacuum and Ultra-low Pressure Breakdown 56**
3.1 Ideal Multipactor Breakdown . . . 56
3.1.1 VULP Theoretical Gain . . . 56
3.1.2 Single-Particle Test . . . 63
3.2 Pressure Limits of VULP Breakdown . . . 67
3.3 VULP General Parameters . . . 68
3.3.1 Grid Resolution in Vacuum . . . 69
3.3.2 Quasistatic Considerations . . . 70
3.4 VULP General Phenomenology . . . 71
3.4.1 Multipactor-Dominated Breakdown . . . 71
3.4.2 Dark-Current Steady-State . . . 79
3.5 The Influence of Scattered and Reflected Particles . . . 84
3.6 The Influence of Ionization on VULP Breakdown . . . 85
3.6.1 Multiplicative Transient . . . 86
3.6.2 Non-Multiplicative Transient . . . 87
3.6.3 The Effect of Ion Collisions . . . 92
3.7 Comments on Methods for VULP Suppression . . . 92
3.8 Chapter 3 Conclusions . . . 94
3.A Source-Sink Simplification . . . 95
3.B Thomson-Model Ionization and VULP Pressure Limit . . . 98
3.C 1-D Fractional Change in $E$ . . . 101
3.D Definition of the Immediate-Downstream Region . . . 103

**4 Gaseous Breakdown and Diffusion in Multipactor 105**
4.1 Theoretical Gain in Gaseous Discharges . . . 105
4.1.1 Extension from VULP . . . 106
4.2 Grid Resolution in Gaseous Discharges . . . 109
4.3 Gaseous Breakdown General Parameters . . . 109
4.4 Low-Pressure Breakdown . . . 110
4.4.1 Multiplicative Breakdown in Low Pressure Gas . . . 110
4.4.2 Dark-Current Multipactor in Low Pressure Gas . . . 116
4.5 Outgassing and Diffusion . . . 124
4.5.1 The Malthus Diffusion Equation . . . 125
4.5.2 Diffusive Outgassing in PIC . . . 130
4.5.2.1 Constant-Flux, 1-D Diffusive Outgassing . . . 130
4.5.2.2 Impact-Dependent, 1-D Diffusive Outgassing . . . 131
4.5.2.3 2-D Diffusive Outgassing . . . 132
4.5.2.4 Continuing Work in Diffusive Outgassing . . . 132
4.6 Future Work . . . 132

4.7 Chapter 4 Conclusions . . . 133

**5 DC Breakdown Susceptibility** **135**
5.1 RF Susceptibility . . . 135
5.2 DC Susceptibility . . . 137
5.2.1 Vacuum Susceptibility . . . 139
5.2.2 Low-Pressure Susceptibility . . . 142
5.2.3 Comments on High-Pressure Susceptibility . . . 149
5.3 VULP Susceptibility Diagrams . . . 149
5.3.1 VULP in Multiplicative Breakdown . . . 149
5.3.2 VULP in Dark-Current Steady-State . . . 151
5.4 Low-Pressure DC Susceptibility Diagrams . . . 155
5.4.1 Low Pressure in Multiplicative Breakdown . . . 155
5.4.2 Low-Pressure Dark-Current Steady-State . . . 157
5.5 Chapter 5 Conclusions . . . 157
5.A Excursion, Lifetime, and Energy Equations . . . 159
5.B Surface Field Correction . . . 163
5.B.1 Correction of Charge-Biased Surface Fields . . . 163
5.B.2 Formulation of Charge-Bias Correction . . . 166
5.B.3 Application of Surface Field Correction . . . 170

**6 Source Studies** **173**
6.1 Standard Emitter Configuration . . . 174
6.2 Summary of Constant Waveform Current Effects . . . 177
6.3 Extended Constant Waveform Emitter . . . 179
6.4 Fowler-Nordheim Effects . . . 179
6.5 Schächter Source Effects . . . 182
6.6 Chapter 6 Conclusions . . . 186

**7 Conclusions and Future Work** **188**
References . . . 197

# List of Figures


1.1 Ideal and discrete representations of the target system. . . . . 2
1.2 Examples of various forms of breakdown. . . . . 7
1.3 Single-surface multipactor schematic. . . . . 8
1.4 Paschen curves for various gases of interest. . . . . 10
1.5 Schematic of the main PIC loop. . . . . 11
1.6 Schematic of bi-linear weighting of standard PIC techniques. . . . . 13

2.1 Schematic examples of typical grid errors when discretizing problems in continuous space. . . . . 16
2.2 General schematic for rotating the target two-electrode system. . . . . 17
2.3 Grid errors in $(m_5, m_6)$. . . . . 20
2.4 Reference electric-field values above and below the dielectric. . . . . 20
2.5 Reference electric-field angles above and below the dielectric. . . . . 22
2.6 Convergence plots for (a) electric fields and (b) electric-field angles as a function of the half-gap multiple, $n$. . . . . 22
2.7 Convergence of permittivity with grid size in discrete system. . . . . 24
2.8 Secondary-emission coefficient, $\delta$, from base XOOPIC model, for various impact angles, $\theta_{\text{imp}}$. . . . . 25
2.9 Updated secondary-emission coefficient model. . . . . 28
2.10 Comparison of Schächter, Fowler-Nordheim with parameters from Table 2.5, and Child-Langmuir, for $\alpha = 6.12°$. . . . . 34
2.11 Comparison of Schächter integrated current from [4] to the development in this work. . . . . 35
2.12 Maxwellian flux model error and correction. . . . . 36
2.13 Schematic of original boundary normal and modified boundary normals in code. . . . . 36
2.14 Geometry for deriving triple-point potentials. . . . . 37
2.15 $\nu$ as a function of $\varepsilon_r$. . . . . 40
2.16 Equipotentials near the triple-point for $\alpha = 6.12°$. . . . . 41
2.17 Diffusivity vs. pressure, normalized to diffusivity at atmospheric pressure. 51

3.1 Generalized single-surface multipactor schematic for VULP breakdown, with reproduction of Figure 1.3 for convenience. . . . . 57
3.2 Impact energy, $W_{\text{imp}}$, vs. electric-field angle, $\chi_E$, for VULP breakdown. . 59
3.3 Low-current multipactor test for a multiplicative discharge at 6.12°. . . . 65

3.4 Maximum excursions of electrons in Cartesian coordinates, normalized to standard grid size. . . . 70
3.5 Configuration-space example of VULP breakdown at 6.12°. . . . 72
3.6 Characteristic dielectric-surface charging for a multipactoring discharge at 6.12°. . . . 73
3.7 Primary-electron and secondary-electron energy distributions functions (EDFs) on the dielectric surface for 6.12°. . . . 74
3.8 Reconstructed secondary-emission curve from simulation for 6.12°. . . . 75
3.9 Plots of the weighted-average density,$n_w$, for secondary electrons over the dielectric surface at $\alpha = 6.12°$. . . . 77
3.10 Electric-field angle, $\chi_E$ at the center of the dielectric surface vs. time for 6.12 deg. . . . 78
3.11 Particle number plots and average secondary-emission coefficient, $\delta_{\text{avg}}$, and anode current, $I_{\text{anode}}$, for the case of $\alpha = 6.12°$ in VULP breakdown. . . . 78
3.12 Configuration-space example of VULP breakdown at 22.9°. . . . 79
3.13 Characteristic dielectric-surface charging for a non-multipactoring discharge at 22.9°. . . . 80
3.14 Primary-electron and secondary-electron energy distributions functions (EDFs) on the dielectric surface for 22.9°. . . . 81
3.15 Reconstructed secondary-emission curve from simulation for 22.9°. . . . 81
3.16 Plots of the weighted average density, $n_w$, for secondary electrons over the dielectric surface at $\alpha = 22.9°$. . . . 82
3.17 Electric-field angle, $\chi_E$ at the center of the dielectric surface vs. time for 22.9 deg. . . . 83
3.18 Particle number plots and average secondary-emission coefficient, $\delta_{\text{avg}}$, and anode current, $I_{\text{anode}}$, for the case of $\alpha = 22.9°$ in VULP breakdown. . . . 84
3.19 Average secondary-emission coefficient, $\delta_{\text{avg}}$, and anode current, $I_{\text{anode}}$, for the case of $\alpha = 6.12°$ in VULP breakdown with SRP. . . . 85
3.20 Electric-field angle, $\chi_E$ at the center of the dielectric surface vs. time for 6.12 deg with SRP. . . . 85
3.21 Reconstructed secondary-emission curve from simulation for 6.12° with background pressure of 500 mTorr. . . . 87
3.22 Electric-field angle, $\chi_E$ at the center of the dielectric surface vs. time for 6.12 deg, 500 mTorr. No ion collisions. . . . 88
3.23 Average secondary-emission coefficient, $\delta_{\text{avg}}$, and anode current, $I_{\text{anode}}$, for the case of $\alpha = 6.12°$ in VULP breakdown, 500 mTorr. No ion collisions. . . . 88
3.24 Particle number plots for computational particles from simulation for 6.12° with background pressure of 500 mTorr. No ion collisions. . . . 89
3.25 Fourier transform of $Ar^+$ number history compared to electron and ion plasma frequencies. . . . 89
3.26 Reconstructed secondary-emission curve from simulation for 22.9° with background pressure of 500 mTorr. . . . 90
3.27 Electric-field angle, $\chi_E$ at the center of the dielectric surface vs. time for 22.9 deg, 500 mTorr. No ion collisions. . . . 91

3.28 Average secondary-emission coefficient, $\delta_{\text{avg}}$, and anode current, $I_{\text{anode}}$, for the case of $\alpha = 22.9°$ in VULP breakdown, 500 mTorr. No ion collisions. . 91
3.29 Particle number plots for computational particles from simulation for 22.9° with background pressure of 500 mTorr. No ion collisions. . . . . 92
3.30 Particle number plots from simulation for 6.12° with background pressure of 500 mTorr, including ion collisions. . . . . 93
3.31 Particle number plots from simulation for 22.9° with background pressure of 500 mTorr, including ion collisions. . . . . 93
3.32 Comparison of Thomson, first-order Thomson, and Rapp/Golden ionization cross sections for Ar. . . . . 100
3.33 Cross sections at low energies with reaction-rate constant integrands from Equation (3.40) for Ar. . . . . 101

4.1 Ionization cross section and electron distribution for use in reaction rate calculations. . . . . 107
4.2 Ideal gaseous gain vs time. . . . . 108
4.3 Debye length at various pressures. . . . . 109
4.4 Configuration-space example of VULP breakdown at 6.12° in 1 Torr background argon gas. . . . . 111
4.5 Characteristic dielectric-surface charging for a multipactoring discharge at 6.12° in 1 Torr background argon gas. . . . . 112
4.6 Primary-electron and secondary-electron energy distributions functions (EDFs) on the dielectric surface for 6.12°. . . . . 113
4.7 Reconstructed secondary-emission curve from simulation for 6.12° at 1 Torr. 114
4.8 Plots of the weighted-average density, $n_w$, for secondary electrons over the dielectric surface at $\alpha = 6.12°$ in 1 Torr background argon gas. . . . . 115
4.9 Plot of the species average kinetic energy for $\alpha = 6.12°$ in 1 Torr background argon gas. . . . . 116
4.10 Electric-field angle, $\chi_E$ at the center of the dielectric surface vs. time for 6.12 deg in 1 Torr of background argon gas. . . . . 117
4.11 Particle number plots and average secondary-emission coefficient, $\delta_{\text{avg}}$, and anode current, $I_{\text{anode}}$, for the case of $\alpha = 6.12°$ in 1 Torr background argon gas. . . . . 117
4.12 Configuration-space example of VULP breakdown at 22.9° in 1 Torr background argon gas. . . . . 118
4.13 Characteristic dielectric-surface charging for a multipactoring discharge at 22.9° in 1 Torr background argon gas. . . . . 119
4.14 Primary-electron and secondary-electron energy distributions functions (EDFs) on the dielectric surface for 22.9°. . . . . 120
4.15 Reconstructed secondary-emission curve from simulation for 22.9°. . . . . 121
4.16 Plots of the weighted-average density,$n_w$, for secondary electrons over the dielectric surface at $\alpha = 22.9°$ in 1 Torr background argon gas. . . . . 122
4.17 Plot of the species average kinetic energy for $\alpha = 22.9°$ in 1 Torr background argon gas. . . . . 123
4.18 Electric-field angle, $\chi_E$ at the center of the dielectric surface vs. time for 22.9 deg in 1 Torr of background argon gas. . . . . 124

4.19 Particle number plots and average secondary-emission coefficient, $\delta_{\text{avg}}$, and anode current, $I_{\text{anode}}$, for the case of $\alpha = 22.9°$ in 1 Torr background argon gas. . . . 125
4.20 Simple 1-D test configuration for outgassing. . . . 127
4.21 Crank-Nicolson solution to the 1-D Malthus diffusion equation, Equation (4.7), with no losses. . . . 128
4.22 Solution to the Malthus diffusion equation with moderate loss over 100 ns. 129
4.23 Solution to the Malthus diffusion equation with significant loss over 100 ns. 129
4.24 Number density and anode current for constant flux of outgassed neutral density in 1-D diffusion. . . . 130
4.25 Number density and anode current for impact-dependent flux of outgassed neutral density in 1-D diffusion. . . . 131
4.26 Number density and anode current for impact-dependent flux of outgassed neutral density in 2-D diffusion. . . . 132

5.1 RF susceptibility diagram example. . . . 136
5.2 RF susceptibility example with field trace in breakdown. . . . 137
5.3 General form of a susceptibility diagram under vacuum conditions for grazing incidence. . . . 141
5.4 Field ratios, $E_\perp/E_\parallel$, vs. impact angle, $\theta_{\text{imp}}$, in vacuum. . . . 142
5.5 Low-pressure particle lifetimes from iterative solution of Equation (5.15), $p_{\text{bg}} = 1$ Torr. . . . 144
5.6 Errors for the first-order expansion of the exponential term in Equation (5.15). . . . 145
5.7 Low-pressure particle lifetimes from iterative solution of Equation (5.15), $p_{\text{bg}} = 1$ Torr. . . . 146
5.8 Lifetime errors and weighted lifetime error at 1 Torr. . . . 147
5.9 Lifetime errors and weighted lifetime error at 760 Torr. . . . 147
5.10 $E_\perp/E_\parallel$ vs. $\theta_{\text{imp}}$ for the low pressure case. . . . 148
5.11 $E_\perp/E_\parallel$ plotted at the dielectric surface with $\alpha = 6.12°$ in vacuum. . . . 150
5.12 Snapshots of $E_\perp/E_\parallel$ plotted at the dielectric surface with $\alpha = 6.12°$ in vacuum. . . . 152
5.13 $E_\perp/E_\parallel$ plotted at the dielectric surface with $\alpha = 22.9°$ in vacuum. . . . 153
5.14 Snapshots of $E_\perp/E_\parallel$ plotted at the dielectric surface with $\alpha = 22.9°$ in vacuum. . . . 154
5.15 $E_\perp/E_\parallel$ plotted at the dielectric surface with $\alpha = 6.12°$ in $p_{bg} = 1$ Torr of neutral Ar. . . . 155
5.16 Snapshots of $E_\perp/E_\parallel$ plotted at the dielectric surface with $\alpha = 6.12°$ in $p_{bg} = 1$ Torr of neutral Ar. . . . 158
5.17 $E_\perp/E_\parallel$ plotted at the dielectric surface with $\alpha = 22.9°$ in $p_{bg} = 1$ Torr of neutral Ar. . . . 159
5.18 Snapshots of $E_\perp/E_\parallel$ plotted at the dielectric surface with $\alpha = 22.9°$ in $p_{bg} = 1$ Torr of neutral Ar. . . . 160
5.19 2-D Gaussian pillbox schematic for $E_y$ correction. . . . 164
5.20 2-D Gaussian pillbox schematic for $E_x$ correction. . . . 165

5.21 DC susceptibility diagram in breakdown with surface field correction, through 400 ps. . . . 171
5.22 DC susceptibility diagram in breakdown with surface field correction. . . . 172

6.1 Integrated current as a function of emitter length. $R$, and applied field, $E_0$. 176
6.2 Schächter current as a function of distance, $R$, integrated from the triple point along the emitter. . . . 176
6.3 DC Susceptibility diagrams for CW sources over different emitter lengths. 178
6.4 Broadened CW source electron energy distribution functions (EEDFs) on the dielectric surface for 6.12°. . . . 180
6.5 Broadened CW source characteristic dielectric-surface charging for a multipactoring discharge at 6.12°. . . . 180
6.6 Full DC Susceptibility diagram for CW source over $\sim 28.4\,\mathrm{nm}$. . . . 181
6.7 FN source electron energy distribution functions (EEDFs) on the dielectric surface for 6.12°. . . . 183
6.8 FN source characteristic dielectric-surface charging for a multipactoring discharge at 6.12°. . . . 183
6.9 Full DC Susceptibility diagram for FN source over $\sim 28.4\,\mathrm{nm}$. . . . 184
6.10 Schächter source electron energy distribution functions (EEDFs) on the dielectric surface for 6.12°. . . . 185
6.11 Schächter source characteristic dielectric-surface charging for a multipactoring discharge at 6.12°. . . . 185
6.12 Full DC Susceptibility diagram for Schächter source over $\sim 28.4\,\mathrm{nm}$. . . . 186

# List of Tables

2.1 Discrete parameters for meeting minimum-error conditions. . . . . 21
2.2 Comparison of boundary conditions for modeling a two-electrode system. 23
2.3 Typical values for Equation (2.21). . . . . 27
2.4 Parameters for the BSL diffusivity of Equation (2.27). . . . . 30
2.5 Factors for Fowler-Nordheim emitter, Equation (2.30), used in this study. 32
2.6 Factors for Schächter FN emitter model, Equation (2.31) . . . . . 33
2.7 General parameters for standard simulation system. . . . . 38
2.8 Reduced parameter set used to limit surface gain. . . . . 39

3.1 General parameters for single-particle verification test in vacuum through ultra low pressure (VULP) conditions. . . . . 64
3.2 Comparison of reaction-rate constants, $K_{iz}$ using Equation (3.40) with Thomson, first-order Thomson, and Rapp/Golden. . . . . 101

4.1 Parameters for outgassing test problem. . . . . 128

5.1 Typical parameters used in constructing the baseline susceptibility curve. 141

6.1 List of standard physical and simulation parameters for Chapter 6 configurations. . . . . 175
6.2 List of pertinent figures from Chapter 3 for discussion in this chapter. . . 178

# Acknowledgments

Firstly, I thank my research advisor and dissertation-committee co-chair, Professor John P. Verboncoeur, formerly of UC Berkeley and now at Michigan State University (MSU), for all his guidance and suggestions, and continually extending support through the difficult dealings across universities. I thank my committee for their time and expertise, and I would like to thank Professor Eric B. Norman for providing a forum to discuss my research in the absence of my research advisor as he relocated to MSU in my final years at Berkeley. Special thanks go to Ms. Lisa Zemelman, as she has been instrumental in navigating through one bureaucratic crisis after another. I would also like to thank the Graduate Division of UC Berkeley for providing financial support through the Chancellor's Fellowship, and the Air Force Office of Scientific Research (AFOSR) for research funding via a grant on the Basic Physics of Distributed Plasmas.

My most humble gratitude goes to Professor Yaron Danon of Rensselaer Polytechnic Institute (RPI), and Professor Bryndol Sones of Westpoint Military Academy, as well as the staff at the RPI LINAC, for guiding me in my formative undergraduate years and providing an invaluable experience in the lab, in which I had practically free reign to indulge in random curiosities. I also thank my research advisor, Dr. Michael Schaeffer, during my time at General Atomics for his guidance, support, and indulging my interest in plasma physics and numerics.

On a personal note, I extend special gratitude to the few people that have helped me in ways that shaped who I am, including Sherrie Hardy, Dr. Selby Cull, Kristen Weaver, Kristina Richter, and the indomitable Kamron Fazel. In no small part, I would not have made this journey if not for their contributions to my life.

Most importanly, I thank my domestic partner, Dr. Barbara Sue Wang, for sharing this adventure with me, and for all her support and patience, which will take me a lifetime to repay. I look forward to such a challenge, and most especially to our time beyond this horizon.

At the risk of sounding mentally unstable, I also thank my 1997 Chevrolet S10, who has been my constant companion through many adventures off the beaten path, near brushes with death through multiple states, months of four-day sleepless nights just to make ends meet, and months of (partially voluntary and apparently illegal) homelessness on the streets of California. I have kept him alive with duct tape and elbow grease all these years, and I look forward to the day I can provide him with new boots for a much-deserved semi-retirement.

Lastly, I thank my parents for what they were able to provide me, and despite our stark differences, they cannot be extricated from all the things that have seen me down this path.

# Chapter 1

# Introduction

## 1.1 Purpose and Scope

The purpose of this study is to develop a baseline physical understanding of electrical breakdown using new and existing analytical and numerical tools to properly order and further characterize various contributions to electrical breakdown. This study will focus on phenomenology of fundamental processes in breakdown, limited to dielectric-surface phenomena, volume gas effects, and the influence of seed electrons, all operating under DC conditions. The overarching goal of this research is to develop the predictive capability that will allow control or elimination of breakdown over a range of parameters and system characteristics using the understanding developed here as a physics basis; however, this particular study will not directly address methods for breakdown suppression, and will instead concentrate on phenomenological characterization and analysis of systems *in breakdown*. Furthermore, this study will target discharges dominated by surface effects, addressing volume phenomena in the context of limits between breakdown dominated by surface effects against breakdown dominated by volume effects (e.g. ionization and diffusion). The well-known technique of particle-in-cell (PIC) simulation with Monte-Carlo collisions (MCC) [5, 6] is used to model idealized systems in this study, where an existing 2D PIC suite called XOOPIC (X-windows object-oriented particle-in-cell) is enhanced and employed [7]. Figure 1.1 details the target geometry: a simple, azimuthally-symmetric diode loaded with an angled dielectric in vacuum through atmospheric pressure of select gases in an asymptotically semi-infinite formulation, generically representing common configurations for a wide array of systems discussed in Section 1.3. The idealized geometry is shown in Figure 1.1a, and a discretized representation of this configuration is shown in Figure 1.1b, taken directly from the diagnostics in XOOPIC.

The remainder of this chapter will discuss motivation and general characteristics of electrical breakdown via gas discharges, starting with a brief overview of initial motivating studies in Section 1.2. A review of target systems of interest and their applications is provided in Section 1.3. Section 1.3.1 discusses the phenomenon of electrical breakdown, its effects, and its role in modern research and engineering, highlighting key conditions and parameters of concern in this study. Section 1.3.2 provides phenomenological details on single-surface multipactor, an avalanche process requiring secondary-emission from surfaces that is largely considered the most fundamental effect responsible for catastrophic

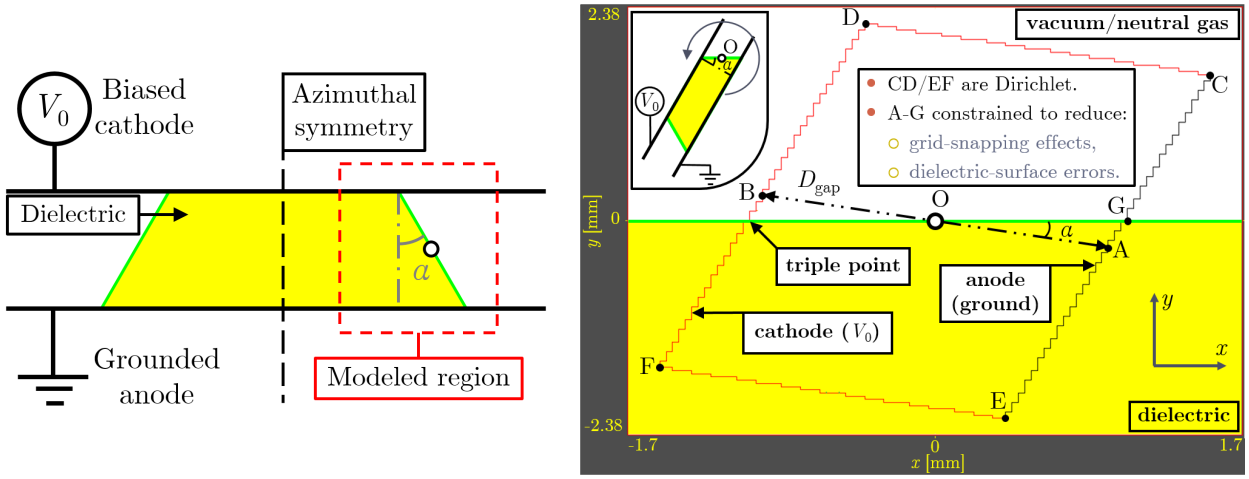


(a) Ideal model. (b) Discrete model.

Figure 1.1: Ideal and discrete representations of the target system. (a) Idealized two-electrode model with an angled dielectric, a biased cathode, and grounded anode; and (b) a representation of the discretized form of (a) taken from XOOPIC. The constraints on the discrete model and the reasons for rotating the geometry are detailed in Section 2.2. Standard $x$-$y$ Cartesian coordinates used.

breakdown through exponential growth [2, 3, 8, 9]. Section 1.3.3 contains a brief discussion of gaseous volume avalanches, which is treated here as a higher mode of growth, but discharge characteristics can effectively evolve via competing effects between volume growth and surface growth. Finally, an overview of PIC is given in Section 1.4, covering the basics of the method and mathematical techniques.

Chapter 2 provides a brief description of XOOPIC and major considerations and additions. Vacuum and low-collisionality electrical breakdown are discussed in Chapter 3, outlining general phenomenology and basic scaling of ideal characteristics, such as multipactor gain. Gaseous breakdown up to low pressure is outlined in Chapter 4, discussing the influence of bulk ionization and volume charging in the system while exploring additional oscillatory effects as a result of coupling between volume space-charge and surface charge. An extension of gaseous breakdown including diffusive outgassed species from the dielectric surface is also delineated in Chapter 4, illustrating the influence of additional neutral species that can move through a vacuum system over timescales on the order of the discharge time. Chapter 5 details a novel breakdown susceptibility theory in DC mapping surface-field conditions to secondary-emission models, leveraging work from the University of Michigan [1, 10, 11] and key fundamental phenomena from the literature [2, 3] to provide baseline characteristics of breakdown susceptibility. Chapter 6 looks at the influence of the electron-current source, comparing a constant-waveform source, a field-emission model, and a generic wedge model based on the work of Schächter [4]. Finally, Chapter 7 outlines the major results and conclusions of this study. Chapter-specific supporting material are provided in corresponding appendices.

## 1.2 Initial Motivation

This work started as an extension of previous developments from the University of Michigan, in which N.M. Jordan, under the supervision of Dr. Y.Y. Lau, detailed limits on field parameters for the occurrence of a single-surface multipactor avalanche [12], a process further described in Section 1.3.2. In Jordan's work, the first-orbit of a seed electron emitted from the so-called triple-point (the junction between metal, dielectric, and vacuum, noted in Figure 1.1b) was analyzed to give a range of dielectric angles that were likely to produce avalanche, i.e. breakdown, conditions. These breakdown conditions were limited to the first-impact characteristics of the primary seed-electron in which the impact energy and angle would have to be sufficient to fall between the first- and second-crossover energies of the impacted dielectric according to the applied theory on secondary-emission, where the particular model used in this study is described in [2, 3] and further delineated in Section 2.3. Such a condition on the first-impact would produce a net emission of electrons from the impacted dielectric surface and it was presumed this would be indicative of a successfully-seeded multipactor avalanche. Jordan's results were analyzed for DC discharges and argued to be extensible through RF via quasistatic arguments, which is a similar approach to that taken in this study. To first order, the work presented here simply extends Jordan's theories to more general conditions, which is a hallmark of using simulation techniques to study physical phenomena.

Additional works have guided the development goals of this study where significant holes and nuances in the theory of electrical breakdown are under active investigation. A number of academic institutions and national labs have substantial theoretical and empirical programs studying breakdown, including Texas Tech University (Texas Tech), the University of California at Berkeley, the University of Michigan (as mentioned above), Lawrence Berkeley National Laboratories (LBNL), and Sandia National Laboratories, among others. One of the major areas of interest at Texas Tech's Center for Pulsed Power and Power Electronic is dielectric-window breakdown in high-power microwave (HPM) systems, covering extensive empirical measurements and imaging [13–15] as well as considerable computational work using Monte-Carlo and general finite-difference time-domain (FDTD) methods with scaling laws to characterize various breakdown parameters [16, 17]. Their work mostly focuses on late-discharge characteristics excluding volume space-charge with methods well-suited to longer time scales, while the work presented here can model the early transient with space-charge effects while also modeling fundamental processes as a general characteristic of PIC methods rather than relying on scaling laws for particle interactions. Michigan has published a number of theoretical developments over the years, characterizing breakdown phenomena for various systems, including the limits for triple-point seeded multipactor breakdown mentioned earlier [12] and susceptibility characteristics of dielectric-loaded RF systems [1], largely excluding the effects of space charge and (in the former) particle distributions in energy and space, which the PIC methods used in this study are well-suited to include. Finally, at the microscopic level, extensive work has been done at Sandia characterizing and imaging breakdown damage to microswitches with small actuation distances capable of high-voltage standoff [18, 19]. Experiments at high pressure show that breakdown follows a modified Paschen curve in submicron gaps due to favoring of vacuum-arc processes over gaseous-avalanche processes. This work can characterize these effects in simulation by directly modeling par-

ticle interactions and fundamental processes, including the transition from field-emission vacuum-arc processes to Townsend avalanches.

Much of the theory to understand various contributions neglects important phenomena such as space charge, surface-charge, particle distributions in energy and space, scattered and reflected primaries, and the influence of the background gas in an effort to develop tractable relations and a practicable understanding of complex phenomena. As noted earlier, while individual contributions have been studied extensively, there remains no consensus on the ordering of various phenomena, making breakdown notoriously difficult to predict or control under general conditions and parameters. From the examples above, it is clear that the problem of electrical breakdown affects a considerable number of disciplines that would benefit greatly from deeper understanding of such a fundamental problem, and the focus of this work has ultimately evolved into a study on extending the existing knowledge-base of the physics of electrical breakdown and developing the analytical tools capable of handling a wide array of parameters while including neglected effects; furthermore, the tools developed in this study will be of critical importance for engineering methods to control/eliminate breakdown under general conditions.

Processes such as secondary emission depend critically on impact energy and angle; however, modeling angled-dielectric systems with discrete methods is difficult due to the distortion of non-orthogonal boundaries, particularly those boundaries undergoing particle impact. The first task is therefore to improve the modeling scheme for angled dielectric insulators in PIC simulations and quantify baseline behavior of systems in DC vacuum breakdown. The geometry of Figure 1.1b is typically attributed to Bergeron [20], having studied similar configurations in the late 1970's. This study employs and extends the model developed by S. Taverniers, et al. [21], at Berkeley in which XOOPIC was applied to a preliminary study of dielectric-loaded systems with non-orthogonal boundaries. Taverniers' model was developed to reduce numerical grid errors at the dielectric so that the physics of fundamental surface effects could be modeled with minimal error. The next task is to verify and enhance the existing models in XOOPIC to appropriately model the regimes and parameters of interest. There exists a concerted effort to develop the understanding between gaseous-volume effects and surface effects, as experiments and simulations show substantial coupling between volume and surface growth [22, 23], so the capacity to model target volume effects will be developed, adding new capabilities as needed. Experiments are often affected by undesirable outgassing [13, 24], so development of diffusive outgassing from surfaces will follow as a natural extension to developing volume gaseous effects, allowing a surface-emitted flux of embedded species to diffuse into the existing model of stationary gas. The influence of the seed electron and the characteristics of the seed source have not been studied extensively, so the final task in this study is to provide a fundamental base to build the understanding of triple-point seeded discharges.

## 1.3 Vacuum to Gas Discharges and their Applications

The target application for this study was originally high-power microwave (HPM) components and physics. The interest in HPM has grown considerably in recent years, with typical applications in communication, large-scale research ventures, and military

defensive weaponry, with a number of institutions researching various aspects, including theoretical considerations at the University of Michigan [1, 12, 25], experimental developments and imaging at Texas Tech [15, 22, 24, 26], experiments in alternative configurations and techniques for breakdown control at Rafael Laboratories [27–29], and numerical simulation techniques at the University of California at Berkeley [7, 30, 31] and Sandia National Laboratories [32]. The tools developed in this work will aid in determination of characteristic operating conditions such as HPM component failure modes, sources of key limiting problems in HPM such as pulse shortening and the processes that contribute to such limitations, while also providing the extensibility to determine key parameters such as power and energy efficiency. While the primary target application is HPM, basic results are rooted in first principles, with the configuration of Figure 1.1 generally representing a high-standoff, biased system with parametrically variable dielectric properties. Results herein can therefore be extended to numerous applications across multiple scales and operating conditions with appropriate assumptions, including microelectromechanical systems (MEMS) at the micro-scale [18, 19], detectors and amplifiers at the research laboratory scale [33], lithography on the high-capacity commercial scale [34], high-current and high-field applications at deployable military scales [9, 35–37], accelerator and plasma heating technologies at the large research scale [38–40], pylons and space applications at the large commercial scale [8, 41], and dissipation and rerouting of lightning at very-large scales for protection of weapons and national interests [42, 43].

The last century has seen substantial research in vacuum discharges, gaseous discharges, and the fundamental processes that induce discharges, both desirable and deleterious. The wide range of practical uses for high-standoff, dielectric-loaded systems are all invariably plagued by similar problems rooted in operational fundamentals, where one of the most pervasive and practical problems for all applications is the phenomenon of electrical breakdown.

### 1.3.1 Electrical Breakdown

The role of breakdown in electrical systems has been studied concurrently with applications research in the areas described above, but the ordering of various phenomena contributing to electrical breakdown remains largely undetermined [8, 9]. Much of the existing understanding of breakdown and motivation for studying the phenomenon is summarized in seminal review texts such as [8, 9], and this section will highlight some key points that contributed to the motivation for this work.

As noted above, the problem of electrical breakdown pervades many disciplines and applications over a wide range of parameters. Some examples of electrical breakdown are shown in Figure 1.2. Figure 1.2a is the simplest example of a static discharge that is typically characterized as breakdown in atmospheric air seeded in a number of ways, e.g. physical contact between disparately-charged objects or collisions of particles with surrounding gases that causes avalanche breakdown between such objects. Static discharges are known to cause damage to consumer electronic components on the small scale, but is more commonly observed as lightning at the much larger, natural scales. PIC is readily capable of modeling particle-seeded avalanche breakdown with appropriate cross sections and collision models, but the original XOOPIC code base at the start of this study lacked appropriate gas models to simulate atmospheric air, and so the interest here is to include

such models. A corollary concern is how the discharges are seeded, and interest lies in adding fundamental models for seeding discharges to get closer to first principles while providing the capability to cover a range of possible scenarios.

Figure 1.2b is an example of an arc discharge formed by gaseous breakdown between two graphite electrodes, where a plasma has formed between the electrodes, providing a continuous path for current to flow. Arc discharges are an example of useful breakdown behavior, having been employed in early light and projection technologies and widely used in modern arc-welding methods [44], but the effect can also be deleterious by consuming and damaging materials where arcs are undesirable, sometimes readily observed in large-scale transmission lines in atmosphere and poorly-designed circuitry in consumer electronics where sudden current cutoff leads to arc formation. Again, PIC methods are well suited to modeling early-transient characteristics of arc discharges, and can be extended to longer times as necessary (which are often characteristically steady-state and may be less interesting as a result), but the XOOPIC code base lacked appropriate models for target atmospheric gases.

Figure 1.2c is a reproduction of a work from Texas Tech University [22] investigating HPM-window breakdown in which J.T. Krile imaged the surface flashover of a Lexan dielectric surface between two electrodes in atmosphere, which usually occurs through various avalanche effects over the surface and in the bulk gas. Typical contributions to electrical breakdown in this regime include multipactor, Townsend avalanche, ionization-enhanced effects with volume-bulk gas and/or near-surface outgassing, among other effects. The evolution of the discharge depends on the gas, where electron arcs in nitrogen are known to detach from the surface while arcs in electronegative oxygen gases surprisingly leads a surface-conforming discharge. In principle, the simulation methods used in this study have the capacity to simulate such effects, but again, require additional gas models and diffusive emission models from the surface.

Finally, Figure 1.2d shows an imaging example of micron-scale breakdown reproduced from work by Strong at Sandia [18, 19]. Strong's work effectively showed that there is a modified Paschen curve when dealing with very small scales, where high-fields across small gaps can lead to vacuum-like arcs even at high pressures due to competing scale lengths where the mean free path of gaseous collisions can be much larger than the system length. Again, since the mean free path is a function of the cross sections, PIC methods are well-suited to reproduce such behavior, so interest is in providing tools to further understand how such discharges progress. Another interest for micron-scale structures is in the geometric variation, which can be complex structures designed over a single substrate, possibly adding costly design constraints to limit component failure by breakdown and reduce the need to remanufacture. Advancing the tools to simulate complex, non-orthogonal boundaries is a particular area of interest to enable study of more variable geometries that could potentially reduce engineering costs for many applications.

The leading-order concerns for electrical breakdown are largely in the deleterious effects caused by a breakdown condition, including decreased power output by saturated system potential, increased local pressure due to desorption from particle interactions with surfaces (and subsequent effects), damage to windows and components in accelerators and microwave sources which could lead to catastrophic failure in the worst case, among other concerns largely motivating the need to eliminate breakdown in certain sys-

(a) Static discharge.

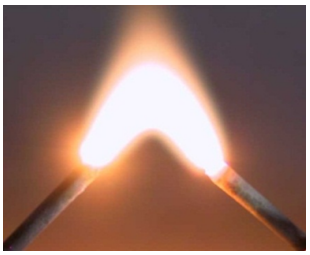

(b) Arc discharge.

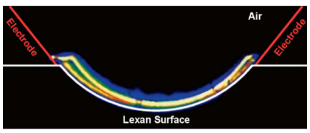


(c) Dielectric-window breakdown [22], ©2005 IEEE.

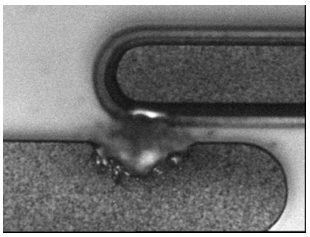

(d) Micron-scale breakdown [18], ©2005 IEEE.

Figure 1.2: Examples of various forms of breakdown. (c) is reproduced from [22], with permission, ©2005 IEEE. (c) is reproduced from [18], with permission, ©2006 IEEE.

tems. However, there is also interest in being able to induce breakdown for the purpose of creating particle sources or protecting radiation sources for communications and other applications, motivating the interest in developing both the capacity to eliminate breakdown as well as to control it when desired. The tools developed and general understanding obtained in this study should be able to address many key, fundamental concerns in all applications mentioned; however, not all of the problems and parameters addressed above will be directly studied in this work due to the considerable range of the parameter space.

### 1.3.2 Single-Surface Multipactor

In attempting to focus efforts in understanding contributions to electrical breakdown and the ordering of such contributions, this work assumes the most fundamental effect is the single-surface multipactor avalanche, herein referred to as simply "multipactor". The possibility of breakdown via multipactor is present at all pressures with no limitations on mean free path as exists for Townsend-like avalanches, even though the required energies to sustain growth can be higher than ionization energies that might trigger Townsend breakdown. Most importantly, multipactor is the most likely candidate for an initial avalanche in all scenarios with configurations similar to that in Figure 1.1 owing to the existence of the triple point. Developments such as [4] show that the composition and geometry of the triple point result in local fields that can diverge sufficiently to provide seed electrons via field emission without enhancement factors. Consequently, multipactor is described in this section as a phenomenological baseline by considering the fundamental processes of secondary emission, which is highly sensitive to impact energy and angle. A general schematic of the single-surface multipactor process is shown in Figure 1.3, while a

plot of the secondary-emission coefficient as a function of impact energy for various angles is shown in Figure 2.9 of Section 2.3.

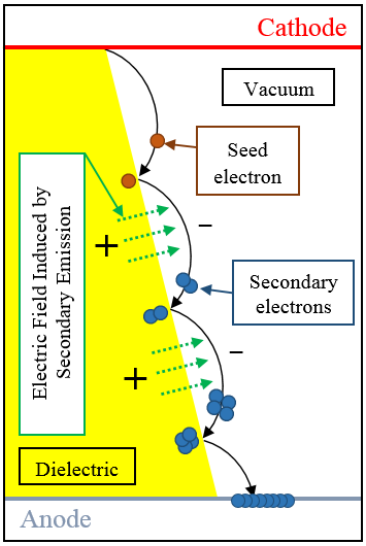


Figure 1.3: Single-surface multipactor schematic. A rotated Bergeron geometry is employed, consisting of an angled-dielectric between two electrodes in vacuum. In principle, multipactor can be initiated by a single seed electron from the triple point. A secondary cascade can form until current is developed at the anode comprising an $n$th generation of secondary electrons.

With sufficient energy for a given impact angle, electrons incident on system boundaries may initiate secondary-electron emission, which was well characterized through semi-empirical formulations by Vaughan [2, 3], further elaborated in Section 2.3. If a net number of electrons are emitted from the dielectric surface, a corresponding electric field is generated between the net positive charge left on the dielectric and the negatively-charged secondary-electron cloud just over the surface. The field induced by secondary emission pulls secondaries back to the surface, and if the secondaries gain sufficient energy in their trajectory, another net generation of secondaries (i.e. tertiaries) can be produced that induces similar phenomena downstream, pulling new secondaries back to the surface to lead to a surface-driven cascade. Secondaries are generally low-energy, and therefore remain relatively close to the dielectric surface with a short flight time. The impact characteristics are consequently driven by the near-surface, quasistatic fields, implying that another way to think of the cascade is to consider that if near-surface fields are of sufficient magnitude and phase to give newly-generated secondaries the necessary energy to produce net secondaries through a significant fraction of the surface, the electron population will be able to exponentially cascade from cathode to anode on a short timescale (typically fractions of nanoseconds for the systems studied here), hence flashover. Of course, with the inclusion of gases, another kind of avalanche can develop that may be driven by the same initiating factor as multipactor, i.e. a triple-point seed, but obviously requires the existence of gaseous species to be able to proceed. In principle, Townsend-like avalanches can compete for growth, and interesting characteristics start to develop as a function of this competition, to be explored in Chapters 3 and 4.

### 1.3.3 Gaseous Electron Avalanche

Gaseous avalanches are a form of cascading multiplication seeded by initial ionization of bulk gases in a number of ways, e.g. ionizing radiation, where charged product species gain energy through acceleration in background fields, proceeding to further ionize neutral species if impacting energies are above the ionization energy. A common form of gaseous avalanche dominated by electron interactions with neutrals is the so-called Townsend avalanche, and is considered second-order with respect to multipactor in this study. In general, self-sustaining avalanche breakdown between electrodes in gas can be described by the empirically-derived Paschen curve, which describes the breakdown voltage as a function of pressure, $p$, and gap length, $D_{\text{gap}}$:

$$V_b = \frac{A_{\text{gas}} \cdot pD_{\text{gap}}}{\log\left(\frac{B_{\text{gas}} \cdot pD_{\text{gap}}}{\log(1 + 1/\gamma_{\text{ion}})}\right)}, \tag{1.1}$$

where $A_{\text{gas}}$ and $B_{\text{gas}}$ are gas-dependent constants, and $\gamma_{\text{ion}}$ is the secondary-emission yield for the cathode material resulting from ion bombardment (as opposed to the typical secondary-emission yield resulting from electron bombardment with which this study is particularly concerned). Paschen's original work revealed that breakdown strength (the highest voltage at which a circuit can withstand electrical breakdown) was a function of the product of pressure and gap distance, $pD_{\text{gap}}$. Qualitatively, at the higher pressures studied by Paschen, reduction of the gap distance at fixed pressure and voltage led to reduced breakdown strength (breakdown is initiated at lower voltages) since average electron energy, $\bar{W}_e = qV/D_{\text{gap}}$, increases at fixed voltage, allowing electrons to ionize neutrals (with sufficient energy, $\bar{W}_e > \mathcal{E}_{iz}$). Alternatively, reduction of the system pressure at constant gap distance and voltage would also lead to reduced breakdown strength since the average collision frequency is reduced with reduced pressure, increasing average electron energy and allowing electrons to further ionize neutrals with sufficient energy as above. Subsequent works would reveal a minimum after which further reduction in gap distance led to increased breakdown strength (breakdown is initiated at higher voltages) [18, 19]. Further reduction of the pressure or the gap width past the minimum leads to an inversion of the mean free path length to the gap width. The interaction frequency is reduced in the region prior to the breakdown-voltage minimum because either neutral species are rarefied or the gap length is on the order of the mean free path or smaller, and the likelihood of breakdown is reduced, i.e. breakdown strength increases. Physically, this means that there is a minimum breakdown voltage required to have a sustained Townsend avalanche for any case, which can be found by differentiating Equation (1.1):

$$\frac{dV_b}{d(pD_{\text{gap}})} = 0 \Rightarrow (pD_{\text{gap}})_{\text{min}} = \frac{e \log(1 + 1/\gamma_{\text{ion}})}{B_{\text{gas}}}. \tag{1.2}$$

Figure 1.4 plots Equation (1.1) for various gases of interest, showing the minima described by Equation (1.2). It should be noted that Pashens's law, particularly in the form of Equation (1.1), describes the start of a self-sustaining discharge balancing secondary emission from the cathode and ionization in the volume, limiting the applicability of Paschen's law to such discharges. An initial source of ionization is assumed such that ions can produce

the necessary secondary electrons for self-sustainment, where $\gamma_{\text{ion}}$ plays a significant but relatively weak functional role in the breakdown-voltage characteristic. Paschen's law does not generally consider the formation of classically-defined regions in DC discharges such as the sheath, dark spaces, or the positive column [34, 44], and other effects can influence breakdown conditions such as external sources of free-electrons, e.g. thermionic emission or field emission. Such sources are important at very small gaps, where Pashen's law would predict a breakdown voltage approaching infinity, while field-enhanced seeding would lead to vacuum-like arcing even at very high pressures [18, 19].

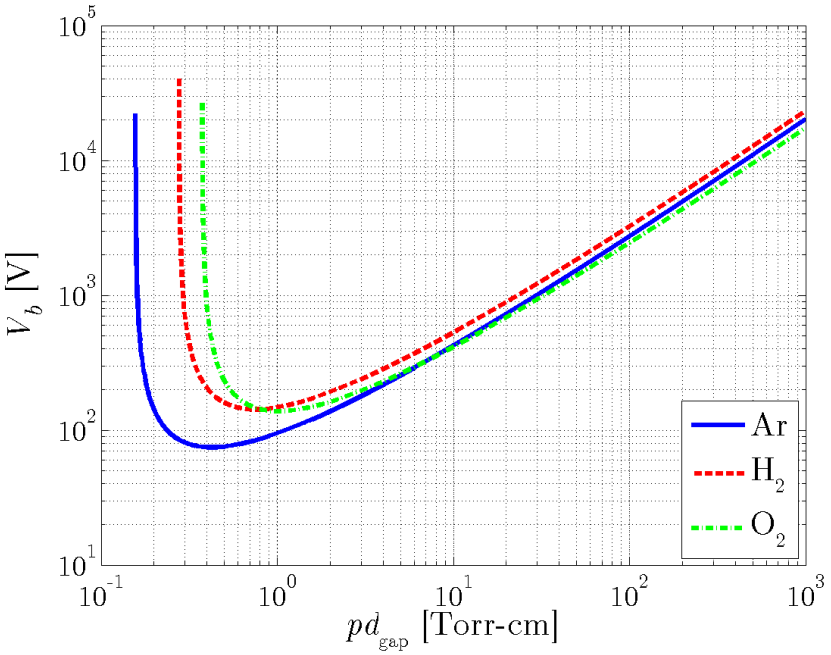


Figure 1.4: Paschen curves for various gases of interest. Plotting Equation (1.1) using values for $A_{\text{gas}}$ and $B_{\text{gas}}$ from [34], with $\gamma_i = 0.20$. Minima correspond to Equation (1.2).

## 1.4 Overview of Particle In Cell

Seminal texts and review articles exist covering the basic principles of PIC techniques, such as [5, 6, 45], with the primary reference to XOOPIC in [7]. PIC models plasmas as a collection of discrete macro-particles (i.e. particles representing many elementary particles; macro-particles will typically be referred to as simply "particles") subject to electromagnetic forces in a discrete-space formulation [7], with linear-weighting of particles to the nearest grid points [5] and an MCC scheme for particle collisions [6, 46]. The basic flow-chart of the PIC model is shown in Figure 1.5, starting from (1) weighting of particles to the numerical grid, (2) integration of Poisson and fields, (3) weighting of fields back to particle positions, (4) application of forces on charged particles via fields, (5) collisions via MCC, (6) emission/collection at boundaries and surfaces, and finally iterating back to (1).

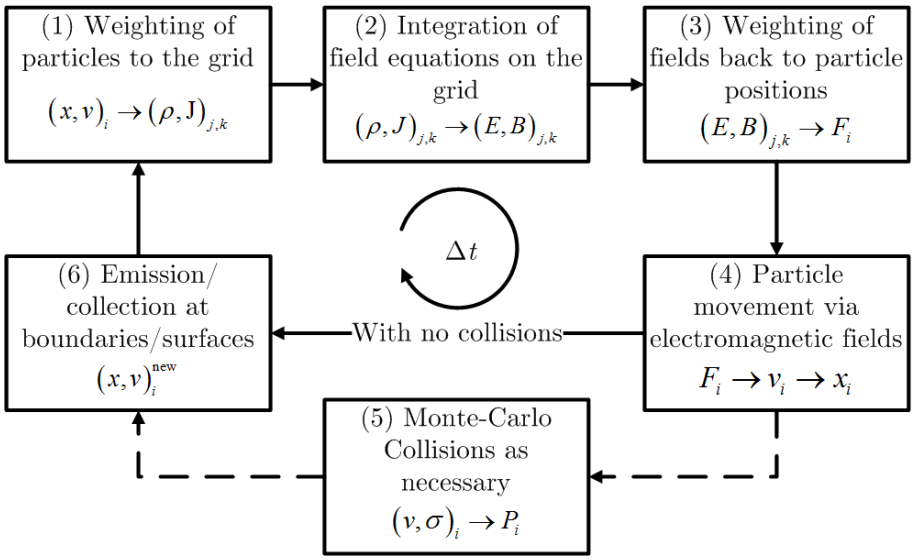


Figure 1.5: Schematic of the main PIC loop. Particle indices are denoted by index $i$, while grid indices are denoted by $(j,k)$.

As noted earlier, weighting of particles to the grid is done through bi-linear weighting to the nearest grid point in this work, as in Figure 1.6, where the relative weighting of the particle to each of the neighboring grid points is shown schematically, and can be thought of as the ratio of the corresponding areas (i.e. a $\rightarrow$ A) to the total area in the cell for the case of Cartesian coordinates employed in this study (n.b. this does necessarily hold true for all coordinate systems and frames, particularly in a curvilinear system with cell sides defined parametrically, e.g. $s = f(r,\theta)$, where $s$ is a line element in cylindrical coordinates in the $(r,\theta)$ plane). This study will be limited to the electrostatic approximation, which essentially means there are no time-varying contributions to the electric field, which is generally a good approximation in DC and for slowly-developing discharges at higher pressures. In other words, considering Maxwell's equations, the partial differentials in time are assumed slow enough to neglect:

$$\begin{aligned}
&\nabla \cdot \vec{E} = \frac{\vec{\rho}}{\varepsilon}, \\
&\nabla \cdot \vec{B} = 0, \\
&\nabla \times \vec{E} = -\frac{\partial \vec{B}}{\partial t} \Rightarrow \nabla \times \vec{E} = 0, \\
&\nabla \times \vec{B} = \frac{4\pi k}{c^2}\vec{J} + \frac{1}{c^2}\frac{\partial \vec{E}}{\partial t} \Rightarrow \nabla \times \vec{B} = \frac{4\pi k}{c^2}\vec{J}.
\end{aligned} \tag{1.3}$$

However, magnetic fields will generally be ignored for this study, and Ampere's law will therefore not be treated in any case. Integration of the potential is typically done through high-order schemes, such as the unconditionally-stable dynamic alternating-directions implicit (DADI) method [47, 48]. The primary numerical method used in this study for integrating the field equations is DADI, which attempts to solve the elliptic PDE with linear operator $L$ operating on some function $u$:

$$L(u) \equiv (A+B)u = f \rightarrow \nabla \cdot (\epsilon \nabla)\phi = \rho, \tag{1.4}$$

by converting to the parabolic PDE:

$$u_t = (A+B)u - f \rightarrow \phi_t = \nabla \cdot (\epsilon \nabla)\phi - \rho, \tag{1.5}$$

and solving Equation (1.5) to a steady-state value within specified error limits. Typically, ADI is obtained by writing Equation (1.5) in a Crank-Nicolson form, expanding the linear operator, and ignoring higher-order terms in $\mathcal{O}(\Delta t^2)$ (which also happens to contain cross terms in space) to be able to write a spatially-separable form, hence alternating directions. The general premise of DADI is to vary the (pseudo-)timesteps to quickly converge to a solution, using small timesteps to damp high-order components and large timesteps to damp low-order components until a steady-state solution is achieved, varying the timesteps according to a test parameter that effectively estimates the truncation error, maintaining suitably small error throughout the operation [49].

Electric fields are calculated in a finite-difference manner in the well-known Yee mesh configuration, and interpolated back to particle positions for the particle move. In the electrostatic approximation, the potential difference across grid notes is calculated first, and then normalized to the grid as needed in a forward difference with respect to the nodes, but centered with respect to the Yee mesh where fields are calculated between nodes:

$$\int_a^b \vec{E} \cdot d\vec{\ell} = V(a) - V(b) \Rightarrow \begin{cases} E_{x,j+1/2,k} = \dfrac{V_{j,k} - V_{j+1,k}}{\Delta x} \\ E_{y,j,k+1/2} = \dfrac{V_{j,k} - V_{j,k+1}}{\Delta y} \end{cases}. \tag{1.6}$$

A leap-frog scheme is typically employed to move particles, where position in space and velocity are advanced at interleaved time points, i.e. position is advanced at integer time steps while velocity is advanced at a half time step off of the position-advance time step. A general formulation for a leap-frog scheme is:

$$\begin{aligned} \frac{dv}{dt} &\Rightarrow \frac{v_{t+\Delta t/2} - v_{t-\Delta t/2}}{\Delta t} = F(t), \\ \frac{dx}{dt} &\Rightarrow \frac{x_t - x_{t-\Delta t}}{\Delta t} = v_{t+\Delta t/2}, \end{aligned} \tag{1.7}$$

where $F(t)$ is the force at time, $t$. Typically, Equation (1.7) requires the velocity be pulled back in time by a half time step before advancement begins to correctly model the initial conditions while maintaining second-order accuracy for the leap-frog scheme. It should be noted that any temporal pull-back is done only once, and methods such as those in [50] may be employed to maintain the accuracy of the scheme. The primary benefits of using leap-frog are that the method is time-reversible, symplectic (i.e. energy-conserving), stable at constant time step as long as the fastest time-varying component is resolved, explicit, and second-order accurate. The specific method used in the XOOPIC implementation is the Boris Push [5].

Collisions are implemented by the well-known Monte-Carlo collision method, calculating the probability for collisions based on cell densities of neutrals, using a random-number generator to determine if collisions occurred. Collection is monitored at all boundaries, with options to retain charge at dielectric surfaces. Finally, emission of particles

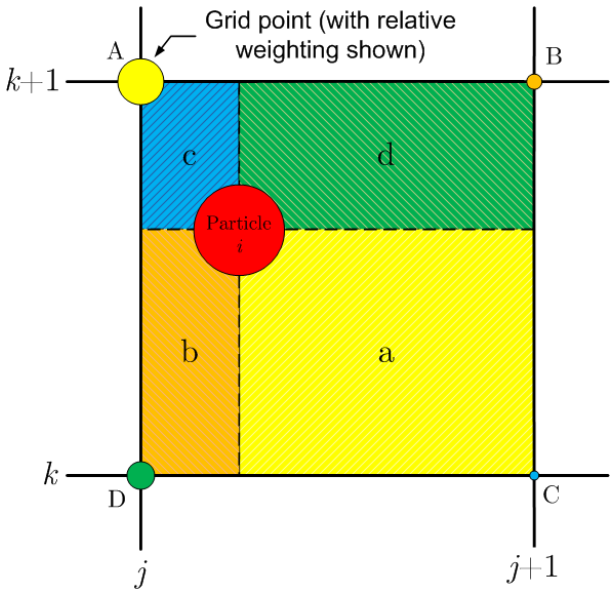


Figure 1.6: Schematic of bi-linear weighting of standard PIC techniques. Weighting is done for particle $i$ to the neighboring grid points indexed with $(j, k)$, fields are integrated via densities and currents calculated on the grid, and fields are interpolated back to particle positions to move particles via fields. Weights at each labeled point, e.g. A, are effectively the ratios of each area, e.g. area a, to the total area of the cell.

is done through various algorithms as necessary, with models for monoenergetic beams, distributed-energy injection, isotropic emission, etc.

Again, the this work enhances and employs XOOPIC, a PIC-MCC code suite designed with the modularity of the object-oriented coding paradigm. XOOPIC was originally designed and developed at the University of California at Berkeley via the Plasma Theory and Simulation Group (PTSG) in the mid-1990's to provide the physics-simulation development community a modular environment to add new physics on the fly [7], using a platform-independent front-end [51], making XOOPIC the ideal base code for this study. Chapter 2 covers specific implementation details of XOOPIC and the particular models used in this study.

# Chapter 2

# Models and Methods

This chapter details the physical and numerical models used in this work, key additions and modifications, and considerations for future modeling. As mentioned previously, the simulation package used in this study is XOOPIC [7], which was written to be a modular code where new models could be added with relative ease. This work leverages the modularity of XOOPIC to add models for secondary emission from dielectrics, the triple-point source, various gas models for collisional effects, and outgassing from the dielectric surface. Additionally, careful consideration was taken when reviewing existing models, where key changes and enhancements will be noted in the following sections.

Section 2.1 discusses space charge, which is the most important aspect of using PIC methods in studying potentially fast-growing discharges since space charge is notoriously difficult to model generally and theoretically over the temporal ranges and physical domain (charge densities, size, pressure, etc.) studied here. Section 2.2 details steps taken in minimizing modeling errors for non-orthogonal boundaries, discussing the numerical grid in Section 2.2.1 with an error analysis in Section 2.2.2. Secondary emission models are discussed in Section 2.3. Section 2.3.1 notes the model implemented in the base XOOPIC package [3], herein called the "metal model" as it is more readily able to model secondary emission from metallic surfaces, while Section 2.3.2 delineates the changes made to allow better fits to dielectric data, herein referred to as the "dielectric extension". The implementation of seed-current models are discussed in Section 2.5, where the constant-waveform source noted in Section 2.5.1 and the Fowler-Nordheim source noted in Section 2.5.2 were previously implemented as part of the base XOOPIC package, while the triple-point source delineated in Section 2.5.3 was added to approach a first-principles implementation. Seed models are used in Chapter 6 to assess the influence of seed characteristics on discharges dominated by surface effects. Outgassing and diffusion models are outlined in Section 2.4 for use in Chapter 4. Notable modifications to the XOOPIC suite, otherwise not requiring a separate section herein, are delineated in Section 2.6. Finally, a summary of standard parameters and reduced parameters used in this study is provided in Section 2.7, where reduced parameters are used in cases where control of surface gain is required to mitigate limitations in computational resources, relegating to vacuum or near-vacuum conditions where concerns for collisional effects are negligible.

## 2.1 Space Charge

Space charge is an often neglected effect in theoretical treatments of breakdown, but it influences the probability for breakdown by affecting local fields and hence the forces on charged particles that ultimately determine whether impacts lead to secondary emission, ionization, and other effects. Space-charge effects are included in the standard PIC scheme via coupling of charged-species densities to the field solve [6, 7]. Using the electrostatic approximation:

$$\vec{\nabla} \cdot (\varepsilon[x,y]\vec{\nabla}V[x,y,t]) = -\left(\rho[x,y,t] + \frac{\sigma[x,y,t]}{\Delta y}\right). \tag{2.1}$$

Equation (2.1) is written for the 2D Cartesian case, where the effect of surface charge on the dielectric is made explicit via the surface-charge density, $\sigma$ (as opposed to volume charge and its associated density, $\rho$), written for the surface charge in a cell associated with geometry in Figure 1.1b. Permittivity, $\varepsilon(x,y)$, is spatially dependent, The charge density is conformal to the $x$ axis in this case, c.f. Figure 1.1b. In the implemented PIC model, charge impacts are collected on the dielectric surface and linearly weighted to the numerical grid as noted in Section 1.4. In the context of multipactor, space-charge affects impact energy and particle flux on flight to the dielectric, since seed electrons and subsequent secondaries may not see the full applied potential, or may see a modified local potential that drastically alters particle characteristics and subsequent discharge evolution. The timescale of surface charging is much shorter than the dielectric relaxation time for non-conducting materials, so the charging transient is very important to the calculation of the local field, with implications for global fields as well. Local variations in potential are further exacerbated by the presence of ambient gas and desorbed species in the system, where volume ionization could lead to local shielding in quasineutral regions such that collective behavior becomes prominent in the so-called Debye sphere. The Debye sphere is simply a region where the influence of local charges dominates, and charges beyond the length-scale called the Debye length are effectively screened out in a Yukawa-like potential, a common treatment found in classic texts such as [52, 53]. In a cold plasma with relatively immobile ions and Boltzmann electrons, the Debye length is:

$$\lambda_D = \sqrt{\frac{\varepsilon_0 k_B T_e}{n_e q_e^2}}. \tag{2.2}$$

Finally, it should be noted that space charge limits the current which can be propagated through a voltage drop V over a distance $d$ as per the Child-Langmuir law [34]:

$$J_{\mathrm{CL}} = \frac{4\varepsilon_0}{9}\sqrt{\frac{2e}{m}}\frac{V^{3/2}}{d^2} \tag{2.3}$$

## 2.2 Taverniers' Model

Taverniers' model for implementing PIC in non-orthogonal boundaries is discussed in this section, providing further details than that provided in [21].

### 2.2.1 The Numerical Grid

As noted earlier, the representation of the ideal system requires careful treatment of the discretization scheme. Moving from a continuous-space model to a discrete-space model introduces numerical grid effects that generally affect the physics of boundary-coupled phenomena, including emission, desorption, charge accumulation, fields and field angles, etc. Other effects include numerical heating and particle diffusion [5, 45, 54, 55], which will not be covered in this work since the interest here is in general modeling of non-orthogonal boundaries. Spatial discretization inherent in any numerical boundary can lead to "snapping" to the nearest grid node and "stair-stepping" of boundaries, illustrated in Figures 2.1a and 2.1b, respectively. Snapping affects the representation of real-boundary characteristics, e.g. length and angle with respect to fixed axes. More subtly, snapping also perturbs derived quantities such as electric fields that rely on boundary characteristics relative to other boundaries. Stair-stepping further adds perturbations to derived quantities like the solution of the fields, affecting physics by propagating errors in boundary characteristics and phenomena (e.g. applied voltage, accumulated charge, etc.) through the whole grid. Of course, snapping and stair-stepping may occur in tandem, introducing higher-order errors by coupling the above effects.

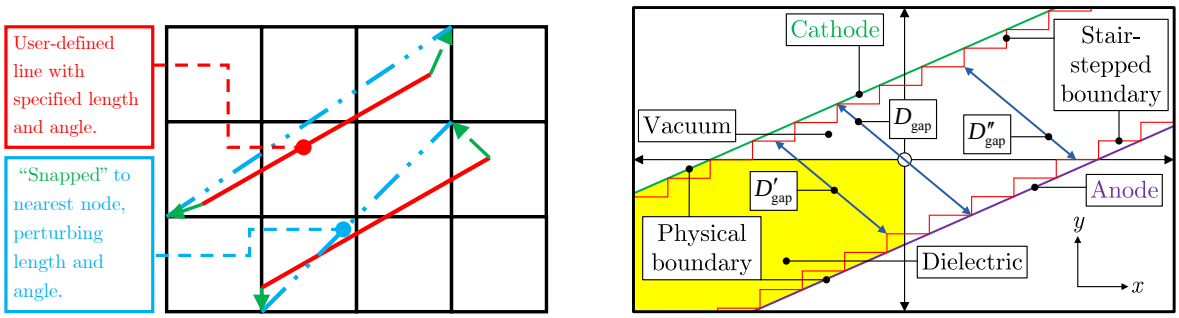


(a) Grid-snapping.

(b) Stair-stepping.

Figure 2.1: Schematic examples of typical grid errors when discretizing problems in continuous space. (a) illustrates the perturbation of physical lines as they are "snapped" to the grid, creating errors in characteristics and relative positions of boundaries. (b) illustrates the effect of stair-stepping on non-orthogonal boundaries that leads to varying gap widths, i.e. $D_{\text{gap}} \neq D'_{\text{gap}} \neq D''_{\text{gap}}$. Note that any apparent regularity is not general, and snapping will produce further variations in the stair-stepped boundaries of (b).

The representation of impact surfaces is of particular importance when minimizing errors in the physics of secondary emission, which is, again, herein assumed the most fundamental effect for growth. The grid introduces key errors in electron-impact characteristics, particularly impact energy, denoted in this work as $W_{\text{imp}}$, and impact angle, denoted as $\theta_{\text{imp}}$, with respect to the impacted-surface normal. The solution developed in this work builds upon work done by Taverniers, et al. [21], where the geometry is rotated so that the dielectric surface is conformal to the numerical grid. While this solves the issue of calculating the correct impact trajectory and energy, there are now perturbations introduced in the calculation of the electric field on the grid. To minimize errors, limits are set on the allowable values for the angle of the dielectric and the grid dimensions. A

general schematic for the rotated system is shown in Figure 2.2, on which the discretized representation in Figure 1.1b is based.

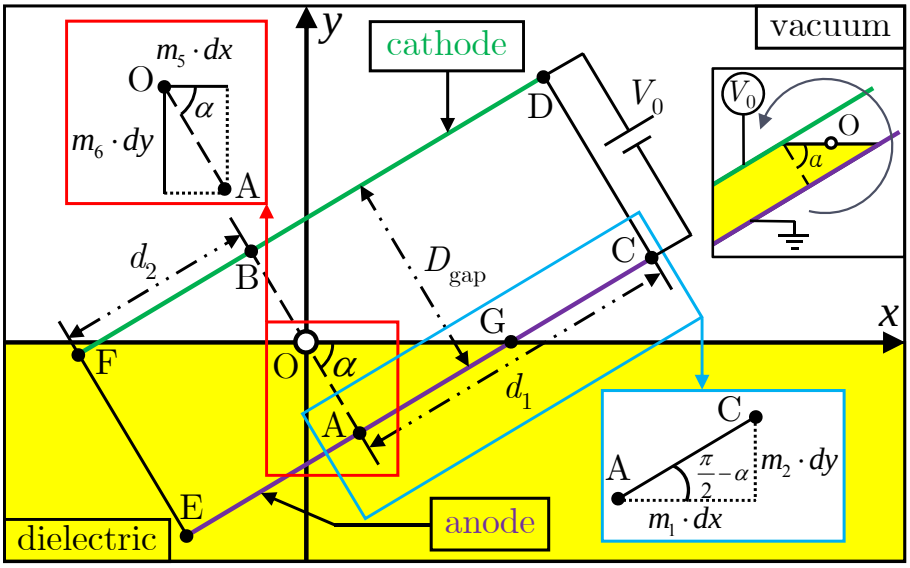


Figure 2.2: General schematic for rotating the target two-electrode system. The cathode is at $\overline{\text{FD}}$, and the anode at $\overline{\text{EC}}$. A voltage of $V_0$ is applied across the gap width, which is denoted by $D_{\text{gap}}$. The origin at O is located symmetrically between $\overline{\text{FD}}$ and $\overline{\text{EC}}$, but may be offset from boundaries $\overline{\text{EF}}$ and $\overline{\text{CD}}$.

All subscripted $m$'s in Figure 2.2 indicate a number of independent, user-defined, integer values used in calculating the allowable set of angles and end-points for a given discrete mesh. The task here is to limit the domain space of each parameter under consideration for restricting errors in field calculations. $d_1$ and $d_2$ are the distances of finite boundaries $\overline{\text{CD}}$ and $\overline{\text{EF}}$ from the origin. These boundaries are required to define the finite computational domain. The system is rotated with an angle $\alpha$, and the center of the gap width, $D_{\text{gap}}$, is placed at point O.

To ensure a gap width of $D_{\text{gap}}$ through the origin, O, point A is limited to a distance $D_{\text{gap}}/2$ from the origin and restricted to $m_5$ node points in the $x$ direction and $m_6$ node points in the $y$ direction, expressed as:

$$\begin{aligned} x_A &= \frac{D_{\text{gap}}}{2}\cos(\alpha) = m_5 dx, \\ y_A &= -\frac{D_{\text{gap}}}{2}\sin(\alpha) = -m_6 dy. \end{aligned} \tag{2.4}$$

Similar, symmetric relations can be written for point B. In general, this treatment can be made more arbitrary by choosing different values of $dx$ and $dy$, but this work constrains $dx = dy$ for this initial analysis. Following from Equation (2.4), the dielectric angle, $\alpha$ is then:

$$\alpha = \arctan\left(\frac{m_6}{m_5}\right), \tag{2.5}$$

which precludes the use of arbitrary $\alpha$ since both $m_5$ and $m_6$ are integers with limited practical domain, since computational resources do not allow arbitrarily large $(m_5, m_6)$.

Setting $m_5$ and $m_6$ sets $dx$ (and by extension $dy$):

$$dx = \frac{D_{\text{gap}}}{2}\frac{\cos(\alpha)}{m_5} = dy. \tag{2.6}$$

The interest here is to ensure that measurements of the electric field magnitude and angle are done to the same accuracy across all implemented dielectric angles. Recalling $\vec{E}$ is calculated by finite difference methods across grid nodes, ensuring uniform accuracy of the electric field requires $dx$ (and, again, by extension $dy$) be invariant with rotation of the system. The metric for limiting the $(m_5, m_6)$ parameter space can be expressed as limiting the error in $dx$ as the system is rotated. Consider the error in $dx$ with respect to an arbitrary reference at 45°; additionally, consider an arbitrary reference for $m_5$ and $m_6$ to be 20 for baseline comparison. The working error condition is therefore:

$$e_{dx}(m_5, m_6) = \frac{dx(m_5, m_6) - dx(20, 20)}{dx(20, 20)} < 0.01 = 1\,\%. \tag{2.7}$$

The diode is closed on both "sides" with the boundaries $\overline{\text{CD}}$ and $\overline{\text{EF}}$ as per Figure 2.2, where points C, D, E, and F lie on mesh nodes. For the purposes of this study, $d$ is restricted by looking for integers $m_1$ and $m_2$ such that point C follows:

$$\begin{aligned} x_C &= d\sin(\alpha) = m_1 dx, \\ y_C &= d\cos(\alpha) = m_2 dy. \end{aligned} \tag{2.8}$$

Letting $d$ be some integer multiple, $n$, of $D/2$ as a baseline reference:

$$\begin{aligned} x_C = m_1 dx &= n\frac{D_{\text{gap}}}{2}\sin(\alpha) = n m_6 dx, \\ y_C = m_2 dy &= n\frac{D_{\text{gap}}}{2}\cos(\alpha) = n m_5 dy. \end{aligned} \tag{2.9}$$

where the last equality is from Equations (2.8). A suitable $n$ is required to match:

$$\begin{aligned} m_1 &= n m_6, \\ m_2 &= n m_5. \end{aligned} \tag{2.10}$$

The dielectric region in this model fills the diode gap from cathode to anode and the half-space below $y = 0$, so point C should be above the dielectric surface and point F should be below. This condition requires $\overline{\text{AC}}$ to be a minimum length of:

$$|\overline{\text{AC}}|_{\text{min}} = \frac{D_{\text{gap}}}{2}\tan(\alpha). \tag{2.11}$$

Testing this condition for $\alpha = 45°$ means $|\overline{\text{AG}}| = D/2$, and since $|\overline{\text{AC}}| = |\overline{\text{AG}}| + |\overline{\text{GC}}|$, values for $n$ require:

$$|\overline{\text{AC}}| = n\frac{D_{\text{gap}}}{2} = |\overline{\text{AC}}| + |\overline{\text{GC}}| = \frac{D_{\text{gap}}}{2}\tan(45°) + |\overline{\text{GC}}|. \tag{2.12}$$

Varying $d$ in $n$ integer multiples of $D_{\text{gap}}/2$, the magnitude of $E$ and its angle with respect to the dielectric surface can be measured and convergence of the metrics described

above (electric field and angle above and below the dielectric surface) can be tested to find a suitable lower limit for $n$. It should be noted that electric field can be measured via existing diagnostics for $E_x$ and $E_y$, so the metrics to compare are simply:

$$\begin{aligned} E &= \sqrt{E_x^2 + E_y^2}, \\ \chi_E &= \arctan\left(\frac{E_y}{|E_x|}\right). \end{aligned} \tag{2.13}$$

where $\chi_E$ is measured with respect to the $-x$ axis in the configuration of Figure 2.2. A final convergence test can be formed recalling the dielectric interface boundary conditions, which must be satisfied at all interfaces for finite fields:

$$\begin{aligned} E_{\text{dielectric},t} &= E_{\text{vacuum},t}, \\ \varepsilon_r \varepsilon_0 E_{\text{dielectric},n} &= \varepsilon_0 E_{\text{vacuum},n}, \end{aligned} \tag{2.14}$$

where $\varepsilon_r$ is the relative permittivity of the dielectric, and subscripted $n$ and $t$ refer to "normal" and "tangential" components, respectively. Reducing $dx$ and $dy$ in simulation means the diagnostics in XOOPIC for the component-fields are measuring progressively closer to the dielectric-surface and should therefore converge to the limits of the dielectric boundary conditions:

$$\frac{\varepsilon_r \varepsilon_0 E_{y,\text{dielectric}}}{E_{x,\text{dielectric}}} = \frac{\varepsilon_0 E_{y,\text{vacuum}}}{E_{x,\text{vacuum}}} \Rightarrow \lim_{dx \Rightarrow 0} \frac{\tan(\chi_{\text{vacuum}})}{\tan(\chi_{\text{dielectric}})} = \varepsilon_r, \tag{2.15}$$

In the context of classical treatments for the dielectric boundary conditions, $E_x$ is the tangential field, $E_t$, and $E_y$ is the normal field, $E_n$. Again, note explicitly that tangential fields in the context of this development are with respect to the $-x$ direction and normal fields are with respect to the $+y$ direction.

### 2.2.2 Analysis of Rotated-Grid Geometry

Continuing with Equation (2.7), limiting the grid error at the dielectric center, $e_{dx}$, to less than 1 %, where the shape of the relative errors as a function of $m_5$ and parameterized with a subset of $m_6$ is shown in Figure 2.3a. Sampling the $(m_5, m_6)$ domain from $[1, 30]$ for each parameter, provides a good sampling of the angles from 0° to 90° that meet the condition of Equation (2.7). The space of $(m_5, m_6)$ with acceptably low error is shown in Figure 2.3b. The values that are used in this study are summarized in Table 2.1 with the associated dielectric angles, $\alpha$, in degrees.

As noted in Section 2.2.1, the electric field components are measured one cell above and one cell below the origin, O (cf. Figure 2.2), for various values of $\varepsilon_r$ (relative permittivity) with an applied voltage of $-2400\,\text{V}$ on the cathode, ground on the anode, and a gap width of 2 mm. From Figure 2.4a and Figure 2.4b for the vacuum dielectric case (i.e. the dielectric region has dielectric properties equivalent to vacuum with $\varepsilon_r = 1$) the nominal fields are $1.2\,\frac{\text{MV}}{\text{m}}$, as expected. Increasing the dielectric constant, the electric field in vacuum is expected to be larger than the field in the dielectric from the boundary conditions of Equation (2.14). Physically, this is due to bound charges setting up fields that oppose the applied field; consequently, the electric fields in the dielectric region are

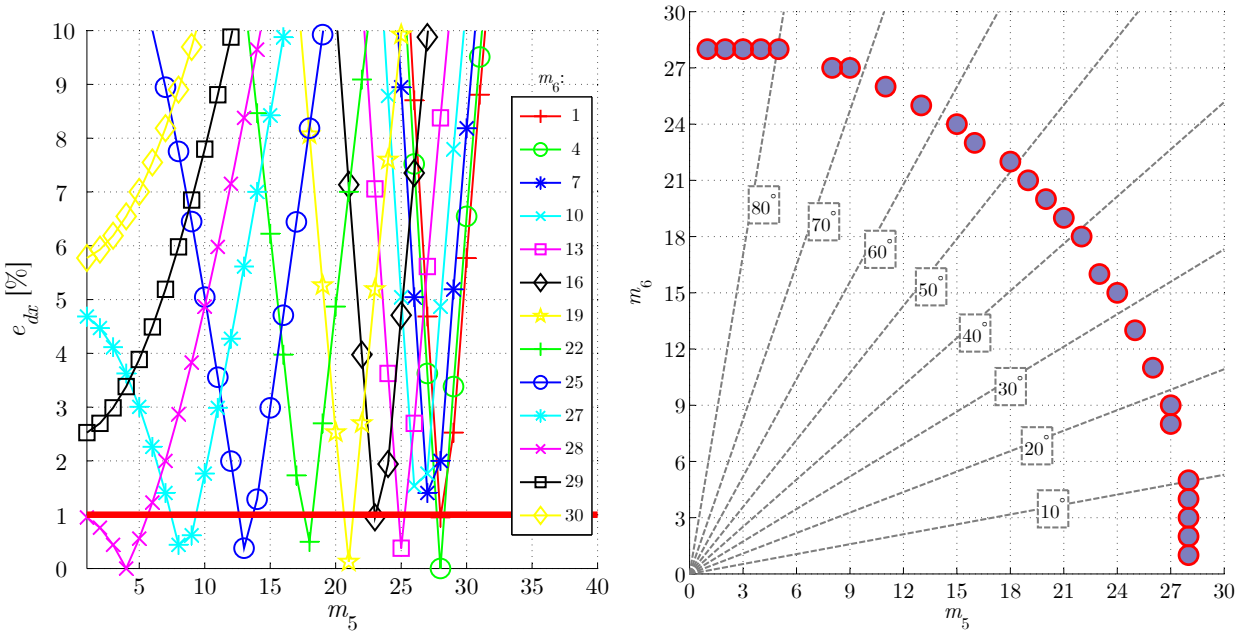


(a) Relative error in $dx$.

(b) $(m_5, m_6)$-space for errors below 1 %.

Figure 2.3: Grid errors in $(m_5, m_6)$. Curves in (a) are parameterized for various values of $m_6$. A relative error of 1 % is marked for reference in (a), where all points below the 1 % line meet the condition in Equation (2.7). All points satisfying 1 % relative error are replotted in the $(m_5, m_6)$-space in (b), showing the associated dielectric angle, $\alpha$, and the effective coverage of the domain for $\alpha$.

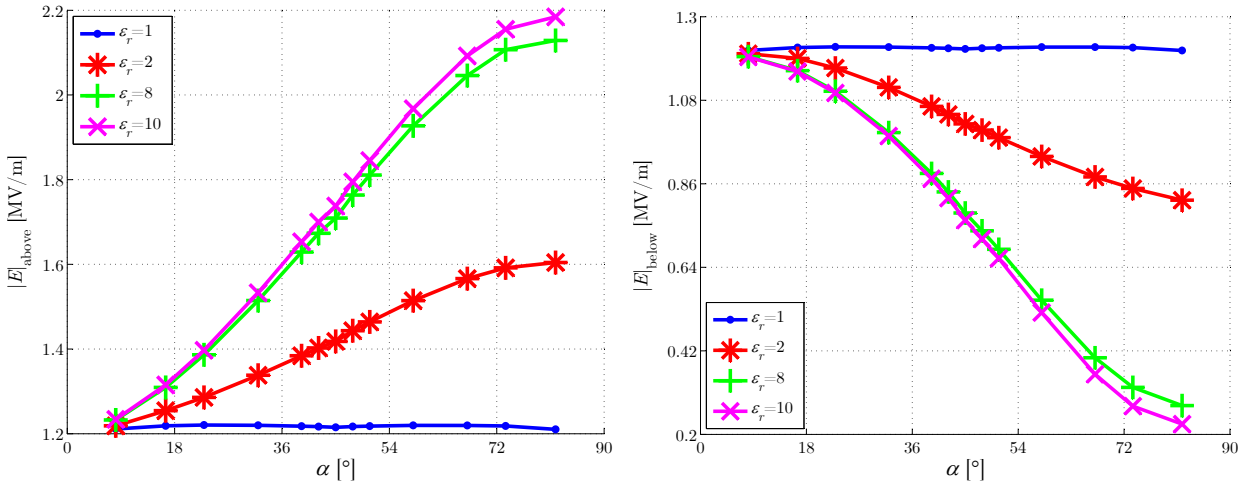


(a) $E$ fields above the dielectric.

(b) $E$ fields below the dielectric.

Figure 2.4: Reference electric-field values above and below the dielectric. Fields are measured in vacuum, one cell above (or below) the dielectric surface at the origin, O, of Figure 2.2.

Table 2.1: Discrete parameters for meeting minimum-error conditions. Values of $m_5$ and $m_6$, the associated dielectric angle, $\alpha$, and the error in $dx$ such that $e(m_5, m_6)$ is less than unity are shown.

| $m_5, m_6$ | $\alpha$[deg] | $e(m_5, m_6)$ | $m_5, m_6$ | $\alpha$[deg] | $e(m_5, m_6)$ |
|---|---|---|---|---|---|
| 1,28 | 87.95 | 9.5e-01 | 21,19 | 42.14 | 1.2e-01 |
| 2,28 | 85.91 | 7.6e-01 | 22,18 | 39.29 | 5e-01 |
| 3,28 | 83.88 | 4.4e-01 | 23,16 | 34.82 | 9.5e-01 |
| 4,28 | 81.87 | 5.8e-14 | 24,15 | 32.01 | 6.2e-02 |
| 5,28 | 79.88 | 5.6e-01 | 25,13 | 27.47 | 3.8e-01 |
| 8,27 | 73.50 | 4.4e-01 | 26,11 | 22.93 | 1.9e-01 |
| 9,27 | 71.57 | 6.2e-01 | 27,9 | 18.43 | 6.2e-01 |
| 11,26 | 67.07 | 1.9e-01 | 27,8 | 16.50 | 4.4e-01 |
| 13,25 | 62.53 | 3.8e-01 | 28,5 | 10.12 | 5.6e-01 |
| 15,24 | 57.99 | 6.2e-02 | 28,4 | 8.13 | 1.9e-14 |
| 16,23 | 55.18 | 9.5e-01 | 28,3 | 6.12 | 4.4e-01 |
| 18,22 | 50.71 | 5.0e-01 | 28,2 | 4.09 | 7.6e-01 |
| 19,21 | 47.86 | 1.3e-01 | 28,1 | 2.05 | 9.5e-01 |
| 20,20 | 45.00 | 0.0e+00 | | | |

driven down compared to the base $\varepsilon_r = 1$ case while fields in the vacuum region must grow accordingly to ensure Equation (2.14) is satisfied.

Figure 2.5a and Figure 2.5b are the analogous plots of Figure 2.4a and Figure 2.4b for the electric-field angle. For the vacuum dielectric case, $\chi_E = \alpha$, as expected since the boundary incurs no discontinuity in the matched permittivity case. In the case of $\varepsilon_r > 1$, the dielectric boundary conditions of Equation (2.14) require $\chi_E$ approaching the dielectric surface from the vacuum side should be larger than the $\chi_E$ from the dielectric side; from Figure 2.5a and Figure 2.5b, it is shown that this is indeed the case.

Having verified accurate behavior of the electric-field magnitude and angle, the placement of the boundaries $\overline{\text{CD}}$ and $\overline{\text{EF}}$ of Figure 2.2 must now be determined to correctly model the asymptotically semi-infinite system. A reference case at 45° with $\varepsilon_r = 1$ is plotted for $E$ and $\chi_E$ as a function of $n$ in Figure 2.6a and Figure 2.6b, respectively. Plots are shown measuring their respective metrics one cell above the dielectric surface and one cell below.

Figure 2.6a and Figure 2.6b shows convergence for the calculation of the electric-field magnitude and angle for $n = 2$, or $d/D = 1$. For the formulation in Equation (2.12), this condition is met with:

$$|\overline{\text{GC}}| > \frac{D}{2}, \tag{2.16}$$

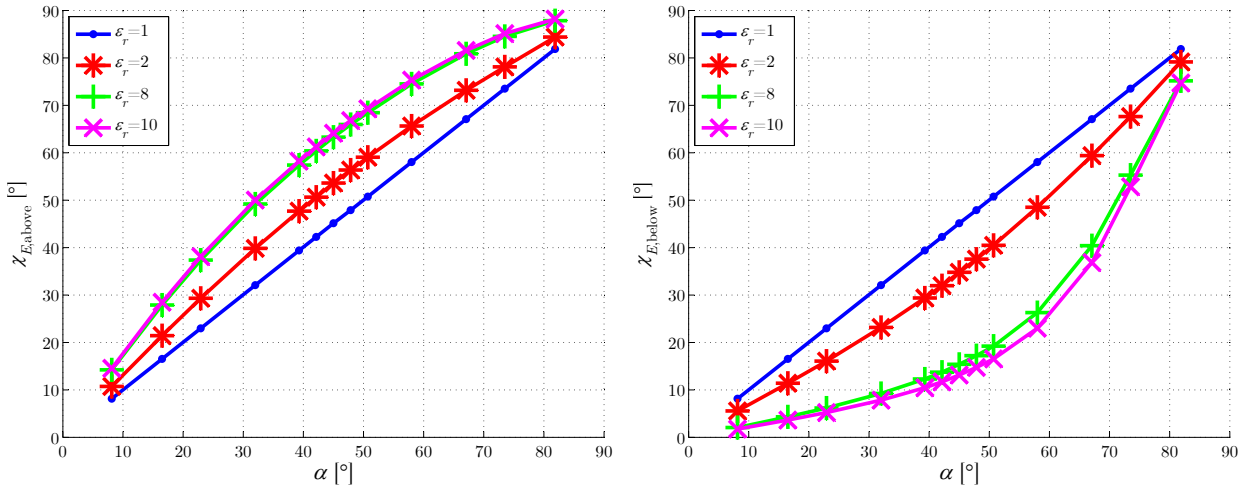


(a) $E$-field angles above the dielectric.

(b) $E$-field angles below the dielectric.

Figure 2.5: Reference electric-field angles above and below the dielectric. Field angles are measured in vacuum, one cell above (or below) the dielectric surface at the origin, O, of Figure 2.2.

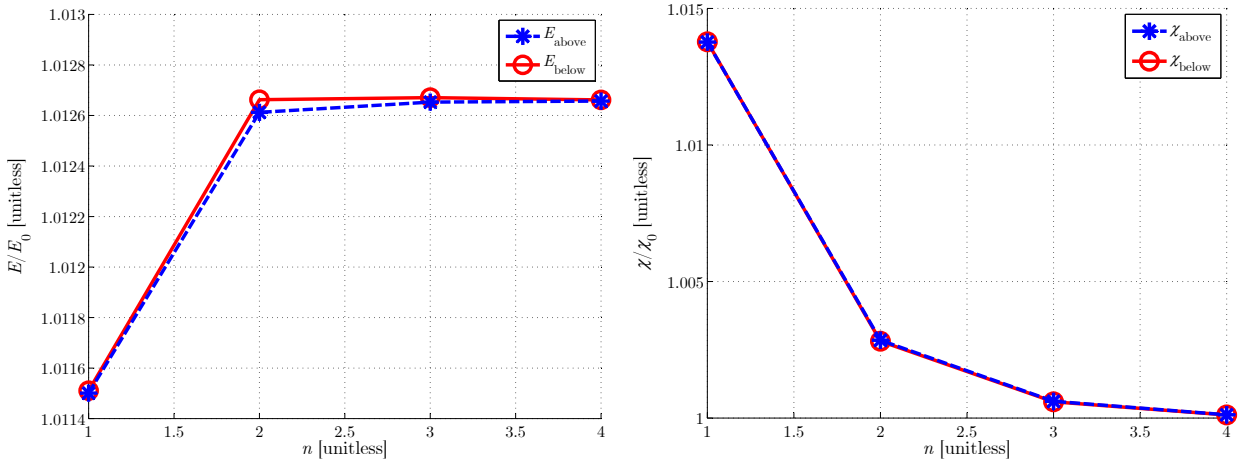


(a) Convergence of $E$ fields.

(b) Convergence of $E$-field angles.

Figure 2.6: Convergence plots for (a) electric fields and (b) electric-field angles as a function of the half-gap multiple, $n$. $\alpha = 45°$ in a vacuum dielectric, $\varepsilon_r = 1$, with $E_0 = 1.2\,\frac{\text{MV}}{\text{m}}$, and $\chi_0 = 45°$. Looking for convergence with $n$ from Equation (2.12).

or, more generally, by inspection: ,

$$n\frac{D}{2} = |\overline{\mathrm{AG}}| + |\overline{\mathrm{GC}}| \geq \frac{D}{2}\tan(45°) + \frac{D}{2} \\ \Rightarrow n \geq \tan(45°) + 1. \tag{2.17}$$

Taking this to be the condition for arbitrary $\alpha$, the general requirement for $n$ is to be the smallest integer such that:

$$n \geq 1 + \tan(\alpha). \tag{2.18}$$

It should be noted that the fields both saturate to slightly greater than 1 % in Figure 2.6a of the expected value, which can be understood as the propagation of all boundary errors since the fields in Figure 2.6a are effectively a solution to the Laplace equation, which averages all nearby cells for a given cell to find a global minimum; any boundary errors are consequently propagated through the field-solve averaging. Similar characteristics can be said for Figure 2.6b, which has a smaller saturation error, and incidentally will be an important characteristic as field angles at the dielectric surface will be shown to play a significant role in the systems of interest for this study.

Another numerical concern in correctly modeling the semi-infinite problem is to identify an appropriate boundary condition for $\overline{\mathrm{CD}}$ and $\overline{\mathrm{EF}}$ of Figure 2.2 to allow invariant and accurate vacuum fields at reference points above and below the dielectric boundary. Two standard types of boundary conditions are considered: Neumann ($E_\perp = 0$ and Dirichlet (linearly varying potential). Table 2.2 shows the measurements for the electric field above and below the origin, O, in Figure 2.2, as well as the relative error from the exact solution of 1.2 $\frac{\mathrm{MV}}{\mathrm{m}}$ in the vacuum-dielectric case of $\varepsilon_r = 1$.

Table 2.2: Comparison of boundary conditions for modeling a two-electrode system. Magnitude of the electric field measured one cell above ($E_a$) and one cell below ($E_b$) the origin, O, of Figure 2.2 for Neumann and Dirichlet conditions on $\overline{\mathrm{CD}}$ and $\overline{\mathrm{EF}}$. $E_0 = 1.2\mathrm{MV/m}$, $e_{\mathrm{rel}} = \Delta E/E_0 = |E_a - E_b|/E_0$. Vacuum dielectric ($\varepsilon_r = 1$) is used. Dielectric angle, $\alpha = 45°$.

| Boundary Type | $E_a$[MV/m] | $E_b$[MV/m] | $e_{\mathrm{rel}}$ |
|---|---|---|---|
| Neumann | 1.213757 | 1.205849 | $6.59 \times 10^{-3}$ |
| Dirichlet | 1.215135 | 1.215195 | $5.00 \times 10^{-5}$ |

The relative error ($e_{\mathrm{rel}}$) in Table 2.2 illustrates the invariance of the field. Again, the field should be precisely 1.2 $\frac{\mathrm{MV}}{\mathrm{m}}$ in the vacuum case and any error in the magnitude here is introduced from the finite difference scheme in the Poisson solve using stair-stepped boundaries and the designated boundary type. From Table 2, the Dirichlet condition is more suitable for maintaining a constant potential across the gap, with $e_{\mathrm{rel}}$ two orders of magnitude smaller than Neumann. Moreover, forcing the linear potential at the boundary maintains the linear relation at points far from the origin, as it should for the semi-infinite system modeled in this study. Inspection of Table 2.2 suggests that Neumann could be better for reproducing the target magnitude of 1.2 $\frac{\mathrm{MV}}{\mathrm{m}}$ at the reference points, but the deviation from the exact case is around an acceptable 1 % for both Neumann and

Dirichlet. Dirichlet is chosen for this study due to better characteristics in maintaining field invariance, allowing for more uniform errors in simulation.

The final numerical consideration is in the convergence of the dielectric boundary condition as $dx$ is reduced, verifying accuracy of the numerical model near the dielectric surface. In the limit $dx \to 0$, the ratio of the electric-field angle above and below the dielectric should approach $\varepsilon_r$ as designated by Equation (2.15). Figure 2.7 illustrates the deviation in Equation (2.15) from $\varepsilon_r$ with decreasing grid size for the case of a dielectric with $\varepsilon_r = 4.1$. At the largest $dx = 35.5\,\mu\text{m}$, the error is on the order of 6 %, and by the smallest $dx = 3.55\,\mu\text{m}$, the error is below 1 %. Correlation of the error in Equation (2.15) is equivalent to a truncation error on the field, and Figure 2.7 shows the error to be first-order with grid size as expected for the linear interpolation schemes used in PIC.

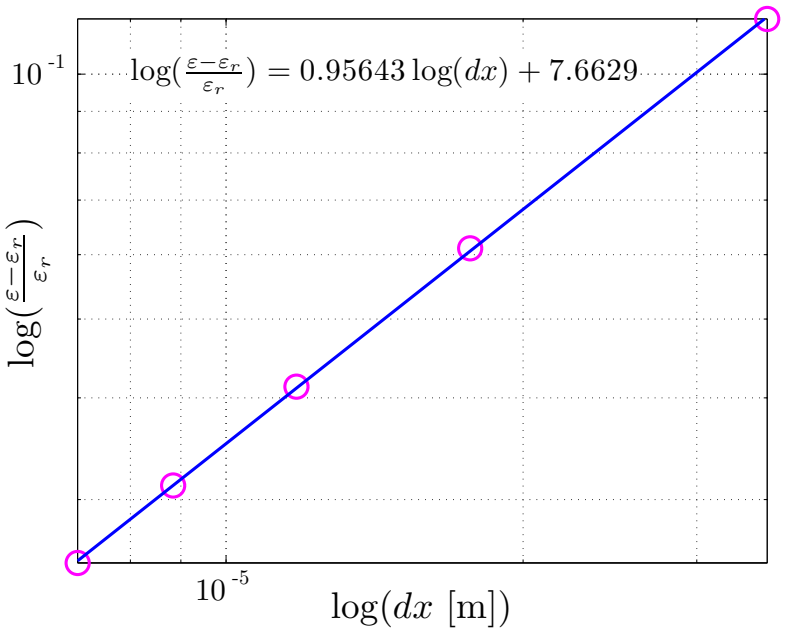


Figure 2.7: Convergence of permittivity with grid size in discrete system. Deviation in $\varepsilon_r$ from $\varepsilon_r = 4.1$ calculated with Equation (2.15). The fit noted in the plot shows a first-order dependence of the error with grid size.

## 2.3 Secondary Emission

### 2.3.1 Metal Model

The process of secondary emission in XOOPIC is modeled by semi-empirical relations developed by Vaughan [2, 3], defining the so-called secondary-emission coefficient, $\delta(W_{\text{imp}}, \theta_{\text{imp}})$, which is the ratio of the average number of secondary electrons emitted from an impacted surface to the number of primary electrons impacting the surface, per unit energy and unit angle. $\delta$ is dependent on impact energy, $W_{\text{imp}}$ and impact angle, $\theta_{\text{imp}}$, with respect to the surface normal; the shape of $\delta(W_{\text{imp}}, \theta_{\text{imp}})$ is dependent on the material and is fitted against empirical data via a number of fitting parameters. Data for Teflon

is used in this study for practical reasons, particularly for considerations of planned experiments. The working model in XOOPIC for secondary-emission from metallic surfaces is:

$$\delta(W_{\text{imp}}, \theta_{\text{imp}}) = \delta_{\text{max},0} \left(1 + k_{sd} \frac{\theta_{\text{imp}}^2}{2\pi}\right) W(w) \tag{2.19}$$

where

$$\begin{aligned} W(w) &= \begin{cases} (w \exp(1-w))^k & w < 3.6 \\ 1.125 w^{-0.35} & w > 3.6 \end{cases} \\ w &= \frac{W_{\text{imp}} - E_0}{E_{\text{max},0}(1 + k_{sw}\theta_{\text{imp}}^2/2\pi) - E_0} \\ k &= \begin{cases} 0.56 & w < 1 \\ 0.25 & 1 \le w \le 3.6 \end{cases} \end{aligned} \tag{2.20}$$

$E_0$ is the secondary-emission threshold energy (12.5 eV for this study), $E_{\text{max},0}$ is the energy at the peak of secondary-emission, $\delta_{\text{max},0}$ is the peak secondary-emission coefficient, and $0 < k_{sd} < 2$, $0 < k_{sw} < 2$ are empirical surface-roughness coefficients where the highest value indicates a highly polished surface. This model emits true secondaries with an isotropic Maxwell-Boltzmann distribution, and also allows a user-defined fraction of reflected and scattered electrons. The shape of the secondary-emission curve is assumed universal across materials. A typical plot is provided in Figure 2.8

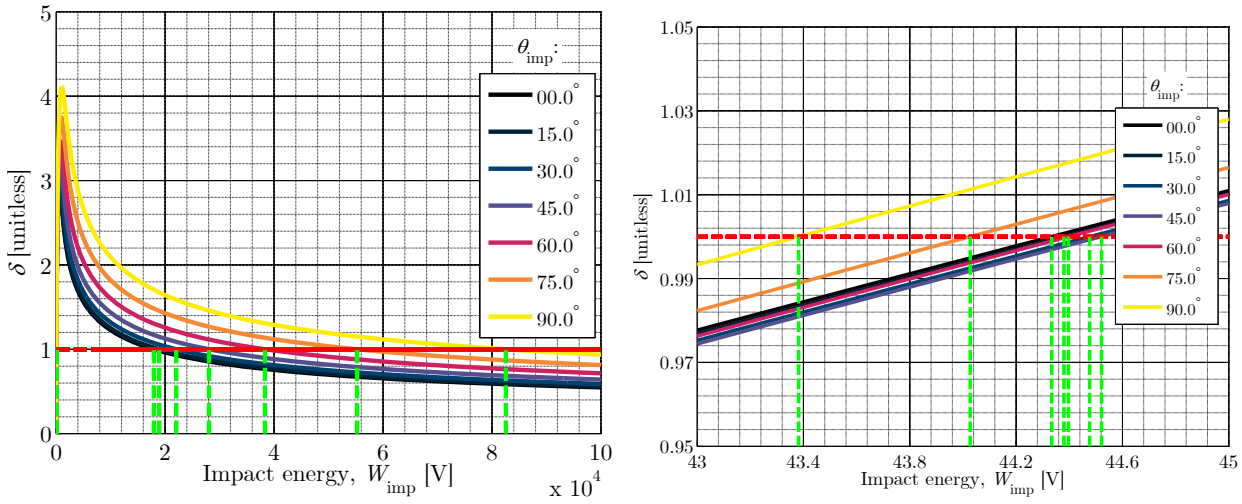


(a) Full scale showing $W_1$ and $W_2$.

(b) $W_1$ region.

Figure 2.8: Secondary-emission coefficient, $\delta$, from base XOOPIC model, for various impact angles, $\theta_{\text{imp}}$. $\delta$ is shown as a function of impact energy plotted for various impact angles. Specifically plotting Equation (2.19) with data for copper.

### 2.3.2 Dielectric Extension

The most pertinent characteristics of the secondary-emission process are the locations of the first and second crossover energies, denoted by $W_1$ and $W_2$, respectively. Between

the crossover energies, secondary-electron emission per primary-electron impact is greater than unity (i.e. $\delta > 1$), so multiplication is expected. Values for $W_1$ are relatively material-independent, with typical magnitudes of a few tens of eV; however, $W_2$ spans a large, material-dependent range, with magnitudes below a few thousands of eV for dielectrics and up to tens of thousands of eV for metals. As observed in Figure 2.8, the original implementation in XOOPIC was not well-suited to match dielectric data, so a version of the Vaughan model [2] was implemented with a non-linear fitting routine to fit the smaller window of net secondary-emission for dielectrics. The working form of Vaughan's equations are:

$$\begin{aligned}
\delta_{\max} &= \delta_{m0}\left(1 + k_s\frac{\theta^2}{2\pi}\right), \\
V_{\max} &= V_{m0}\left(1 + k_s\frac{\theta^2}{2\pi}\right), \\
z_{\max} &= (n+1)\exp\left(-z^{n+1}\right) - n\left(z^{(-n-1)}\right)\left(1 - \exp\left(-z^{n+1}\right)\right), \\
v_i &= \frac{V_i - V_0}{V_{\max} - V_0}, \\
k &= \begin{cases} k_1 & v_i < 1 \\ k_2 & v_i > 1 \end{cases}, \\
\delta_{\text{low}} &= \delta_{\max}\left(v_i \exp\left(1 - v_i\right)\right)^k, \\
g\left(z, n\right) &= \frac{1 - \exp\left(-z^{n+1}\right)}{z^n}, \\
\delta_{\text{high}} &= \delta_{\max}\frac{1}{g\left(z_{\max}, n\right)} g\left(z_{\max}\frac{V_i}{V_{\max}}, n\right),
\end{aligned} \tag{2.21}$$

where $k_s$, $k_1$, $k_2$, $n$, and $w$ are free parameters. The usual material-dependent parameters still apply, with $\delta_{m0}$ representing the maximum secondary-emission coefficient at normal incidence and $V_{m0}$ representing the impact voltage at which $\delta_{m0}$ occurs. $k_s$ also remains the smoothness parameter as before. The parameterization for $\delta$ is done over two regions: a low-impact-energy region, denoted by $\delta_{\text{low}}$, where $k_1$ and $k_2$ apply; and a high-impact-energy region, denoted by $\delta_{\text{high}}$, where $n$ applies. Vaughan provides a continuous form for determining the $k$ parameter:

$$k = \frac{k_1 + k_2}{2} - \frac{k_1 - k_2}{\pi}\tan^{-1}\left(\pi \log\left(v_i\right)\right). \tag{2.22}$$

In any case, the sensitivity of the fit to $k_1$ occurs prior to the peak $\delta$ while sensitive to $k_2$ occurs past the peak. The demarcation between the low and high region, $w$ is somewhat arbitrary, and can, in principle, be extended to the non-linear regression applied here; however, the increase in parameter space makes finding a global minimum increasingly difficult, so the fit parameters are limited to $k_1$ and $k_2$ for minimizing the low-impact-energy residuals, while $n$ is used to minimize the high-impact-energy residuals. Typical values are shown in Table 2.3.

Table 2.3: Typical values for Equation (2.21). See the text on a note about setting static $k_1$.

| Parameter | Variable | Typical Range | Notes |
|---|---|---|---|
| Smoothness parameter | $k_s$ | 1 to 2 | Typically set to 1. |
| First $\delta_{\text{low}}$ factor | $k_1$ | 0 to 2 | Typically static at 0.5. |
| Second $\delta_{\text{low}}$ factor | $k_2$ | 0 to 2 | Floating to fit. |
| $\delta_{\text{high}}$ factor | $n$ | 0 to 2 | Floating to fit. |
| $\delta_{\text{low}} \rightarrow \delta_{\text{high}}$ cutoff | $w$ | 1 to 4 | Typically set to 2. |

Two predictor functions are used of the following form:

$$A_{\text{low}} = \begin{bmatrix} \left.\frac{\partial \delta_{\text{low}}}{\partial k_1}\right|_{x_1,\lambda} & \left.\frac{\partial \delta_{\text{low}}}{\partial k_2}\right|_{x_1,\lambda} \\ \left.\frac{\partial \delta_{\text{low}}}{\partial k_1}\right|_{x_2,\lambda} & \left.\frac{\partial \delta_{\text{low}}}{\partial k_2}\right|_{x_2,\lambda} \\ \vdots & \vdots \\ \left.\frac{\partial \delta_{\text{low}}}{\partial k_1}\right|_{x_m,\lambda} & \left.\frac{\partial \delta_{\text{low}}}{\partial k_2}\right|_{x_m,\lambda} \end{bmatrix} \quad A_{\text{high}} = \begin{bmatrix} \left.\frac{\partial \delta_{\text{high}}}{\partial n}\right|_{x_1\lambda} \\ \left.\frac{\partial \delta_{\text{high}}}{\partial n}\right|_{x_2\lambda} \\ \vdots \\ \left.\frac{\partial \delta_{\text{high}}}{\partial n}\right|_{x_m\lambda} \end{bmatrix} \tag{2.23}$$

evaluated for all points $x_1, x_2, \ldots, x_m$ for $m$ points, and for the set of parameters $\lambda = (k_1, k_2), (n)$. After considerable algebra, the final form of the partials used in minimizing the fit residuals is:

$$\begin{aligned} \frac{\partial f}{\partial k_1} &= \delta_{\max} \left(v \exp\left(1-v\right)\right)^k \log\left(v \exp\left(1-v\right)\right) \left(\frac{1}{2} - \frac{1}{\pi} \tan^{-1}\left[\pi \log\left(v\right)\right]\right), \\ \frac{\partial f}{\partial k_2} &= \delta_{\max} \left(v \exp\left(1-v\right)\right)^k \log\left(v \exp\left(1-v\right)\right) \left(\frac{1}{2} + \frac{1}{\pi} \tan^{-1}\left[\pi \log\left(v\right)\right]\right), \\ \frac{\partial f}{\partial n} &= \delta_{\max} \left( \begin{array}{l} \frac{-1}{\left[g\left(z_{\max}, n\right)\right]^2} \left[\frac{\partial}{\partial n} g\left(z_{\max}, n\right)\right] g\left[z_{\max}\frac{V_i}{V_{\max}}, n\right] + \\ \frac{1}{g\left[z_{\max}, n\right]} \left[\frac{\partial}{\partial n} g\left(z_{\max}\frac{V_i}{V_{\max}}, n\right)\right] \end{array} \right), \\ \frac{\partial g}{\partial n} &= \frac{z^{2n+1} \log\left(z\right) \exp\left(-z^{n+1}\right) - z^n \log\left(z\right)\left[1 - \exp\left(-z^{n+1}\right)\right]}{z^{2n}}. \end{aligned} \tag{2.24}$$

The residuals to minimize for a given set of data to fit, $\vec{y}$, and the calculated set of secondary-emission coefficients from Vaughan, $\delta$, are then just:

$$d\vec{\rho} = \vec{y} - \vec{\delta} \tag{2.25}$$

As with the metal model, the shape of the secondary-emission curve is assumed universal across materials. A typical plot based on polytetrafluoroethylene (PTFE) data is illustrated in Figure 2.9.

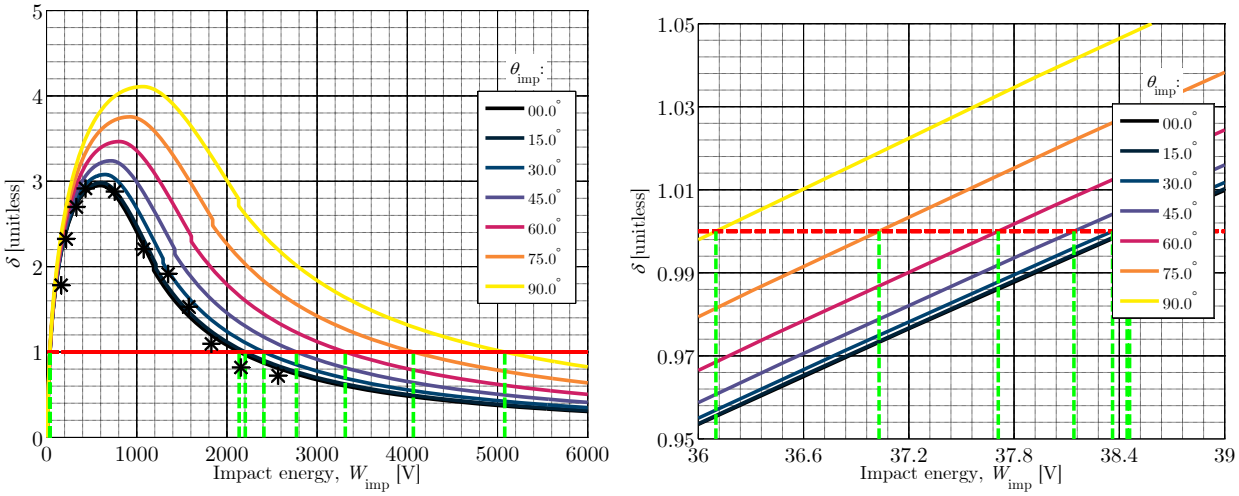


(a) Full scale showing $W_1$ and $W_2$.

(b) $W_1$ region.

Figure 2.9: Updated secondary-emission coefficient model. $\delta$ is shown as a function of impact energy plotted for various impact angles. Specifically plotting Equation (2.19), where the baseline orthogonal-impact curve is fitted against data from seminal studies on PTFE [56, 57], and all other curves are produced via the theory described in Section 2.3.

It is obvious from comparison of Figure 2.8a and Figure 2.9a that the growth window in the dielectric extension is dramatically reduced. This has obvious implications in modeling growth transients and saturation characteristics, where the metal model would lead to excessive growth with increased applied voltage, or growth with applied voltages that would otherwise not be present with the dielectric extension. At higher applied voltages (i.e. higher impact energies on average), the characteristics of the secondary-emission curve for the metal model imply that saturation would occur earlier in the discharge as well. At lower applied voltages (i.e. lower impact energies on average), characteristics can be similar since the shape of the curves in the metal model and dielectric extension appear similar; however, saturation sensitivity is important in this region since it will be shown, particularly in Chapters 3 to 5, that the $W_1$ region is of particular importance to the discharge evolution as surface-field characteristics tend to move the discharge towards an average impact energy of $W_1$.

It should be noted that the Vaughan model could have some difficulty in modeling the $W_1$ region, which is apparent in Figure 2.8b where it is qualitatively expected that impacts approaching *grazing* incidence (i.e. $\theta_{\text{imp}} \to 90°$) should produce more secondaries as a result of increased tangential velocity that reduces impinging distance into the surface, consequently leading to smaller escape distance for secondaries or scattered and reflected particles. In terms of first crossover, $W_1$ will occur at a *lower* energy since the required energy to gain unit growth is smaller with reduced escape path. This characteristic tends to be neglected since the range of first-crossover energies is evidently very small compared to the range of second-crossover energies, c.f. Figures 2.8a and 2.9a where the $W_1$ region is obscured at the lower energies due to dominance of the $W_2$ region at this scale. For this study, it should be noted that the parameter $k_1$ was observed to be most sensitive parameter to this characteristic, where a value of $k_1 > 0.5$ produces

aberrant behavior. Limiting to $k_1 = 0.5$ as in Table 2.3 generally solves the issue, and is taken as standard for this study, producing the ordering in Figure 2.9b. The conditional form of setting $k$ via Equation (2.21) is favored over the use of Equation (2.22) for this implementation; however, it must be stressed that the $W_1$ region should be monitored in general use, with static parameters chosen accordingly if the fit does not generate acceptable crossover behavior. Lastly, it should be noted that there are two discontinuities in this model, one occurring within the low-energy region when switching between $k_1$ and $k_2$, but as noted in [2], the form of $v_i$ in Equation (2.21) makes $\delta_{\text{low}}$ insensitive to $k$ when $v_i \to 1$, i.e. $\delta_{\text{low}} \to \delta_{\text{max}}$. The discontinuity between the low-energy and high-energy regions in the form of $w$ can pose a problem when modeling at higher energies by underestimating growth, and Figure 2.9a shows that the discontinuity gets exacerbated towards grazing angles; however, this will generally not be a problem for near-surface phenomena that tends to the $W_1$ limit, which will be shown to be the case for much of the phenomena of interest herein. That said, careful consideration of the high-energy region for configurations favoring $W_2$ should be admonished.

One final note to consider is that recent advances have been made in alternative models that consider the low-energy region in more detail, namely the Furman model [58], and active research is being done in comparing and implementing new models for multipactor research [59]. Furman's model provides a probabilistic approach to the low-energy region that leads to non-zero emission at energies where Vaughan's model would predict zero emission via a cutoff energy. As per the issues seen above with the Vaughan model, such a change in modeling the low-energy region would have implications for further growth around $W_1$, shown herein to be a sensitive regime in which to operate. This work does not consider the Furman model further, but it must be stressed that current work is investigating effects of such alternative models, and, in principle, the insights herein should provide guidance concerning expected behavior on the shift to new models.

## 2.4 Outgassing and Diffusion Models

Outgassing is implemented as a zero-velocity flux for this study, where the neutral-gas density (NGD) is treated as a fluid following the existing NGD model. This treatment is best considered as an infinite-source, adsorbed layer just over the dielectric surface, where the only mechanism for excursion is diffusion, isolating diffusive effects. Theoretical and implementational considerations follow insights from [13, 24, 60], using tabulated data from [60] for specific materials. The outgassing rate is treated as either a fixed flux or as dependent on electron impact. The outgassing rate is chosen as a constant flux due to the lack of general models for a-priori emission. Models for emission as a function of the surface temperature or the energy deposited on the surface from, e.g. primary impact, are employed, informed by empirical observations [24, 60–62]; however, the aforementioned zero-velocity characteristic will be maintained in all cases to isolate the diffusion phenomenon.

A diffusion model is implemented that operates independently of all other effects, just prior to the particle-species move and associated collision models. The basic assumption in this kind of treatment is that all associated effects can be decoupled within a sufficiently fine spatial grid over a given time step; this assumption typically applies to excursions

that are well resolved, and this study will be careful to ensure such criteria is met. The diffusion model follows classical treatment for variable diffusivity [63–65], using a form of alternating directions implicit (ADI) for variable coefficients that averages the functional coefficients (in this case, diffusivity) in both space and time at each step (looking in the backward direction in each dimension) [66]. This section summarizes the analytical details provided in Appendix 2.B for the diffusion model. The physics of interest to this study are encapsulated in the so-called Malthus reaction-diffusion equation:

$$\frac{\partial n_{\text{diff}}}{\partial t} = \nabla \cdot \left( \mathscr{D}_{\text{diff}} \left( \vec{r}, t \right) \nabla n_{\text{diff}} \right) - L \left( \vec{r}, t \right) + G \left( \vec{r}, t \right), \tag{2.26}$$

where $\mathscr{D}_{\text{diff}}$ is the diffusion coefficient, i.e. diffusivity, written here as spatially and temporally dependent, although $\mathscr{D}_{\text{diff}}$ is treated in this study as state-dependent and therefore only implicitly dependent on space and time; $L(\vec{r}, t)$ is a loss (sink) term, limited in this study to losses through ionization; and $G(\vec{r}, t)$ is a gain term, neglected in this study, but may include reintroduction of neutrals by recombination, e.g. oxygen.

The diffusivity is evaluated in the form from [64], which will be referred to herein as the "BSL diffusivity", good for low pressures and acceptable up to one atmosphere with $\sim 8\,\%$ error:

$$\mathscr{D}_{\text{diff}} \left[ \frac{\text{cm}^2}{\text{s}} \right] = C_1 \left( \frac{T\,[\text{K}]}{\sqrt{T_{c,\text{A}} T_{c,\text{B}}}} \right)^{C_2} \left( T_{c,\text{A}} T_{c,\text{B}} \right)^{5/12} \left( \frac{1}{M_{\text{A}}} + \frac{1}{M_{\text{B}}} \right)^{1/2} \frac{\sqrt{p_{c,\text{A}} p_{c,\text{B}}}}{p\,[\text{atm}]}. \tag{2.27}$$

$C_1$ and $C_2$ are gas-dependent constants, but are typically set to values in Table 2.4 for non-polar gas pairs. $p_{cs}$ is the critical pressure for species $s$ in atm, $T_{cs}$ is the critical temperature for species $s$ in K, and $M_s$ is the molecular mass for species $s$ in u (i.e., amu). Common values for all parameters used in this study are summarized in Table 2.4.

Table 2.4: Parameters for the BSL diffusivity of Equation (2.27).

| Variable | Value | Units | Notes |
|---|---|---|---|
| $C_1$ | $2.745 \times 10^{-4}$ | $\text{u}^{1/2}(1/\text{K})^{5/12}\text{cm}^2/\text{s}$ | Diffusivity pre-factor |
| $C_2$ | 1.823 | (unitless) | Temperature exponent |
| | | Argon, Ar | |
| $p_{c,\text{Ar}}$ | 48.0 | atm | Critical pressure |
| $T_{c,\text{Ar}}$ | 151.0 | K | Critical temperature |
| $M_{\text{Ar}}$ | 39.948 | u | Molecular mass |
| | | Hydrogen, $H_2$ | |
| $p_{c,\text{H}_2}$ | 12.80 | atm | Critical pressure |
| $T_{c,\text{H}_2}$ | 33.3 | K | Critical temperature |
| $M_{\text{H}_2}$ | 2.016 | u | Molecular mass |

It will generally be assumed that the spatial variation in $\mathscr{D}_{\text{diff}}$ is negligible for theoretical considerations, and can therefore be pulled out of the divergence term; however,

this assumption does not hold well under outgassing in very low pressures, i.e. in the presence of large density gradients where diffusivity varies greatly with variations in low pressure (c.f. Figure 2.17), and numerical treatment will address variations as needed. The so-called "Crank-Nicolson" (CN) scheme [47] is a common approach to solving PDE's of the type in Equation (2.26), written in matrix and vector form:

$$\begin{pmatrix} \mathbf{I} + \frac{kn_e\sigma_{iz}v_e}{2} + \\ -\mathscr{D}_{\text{diff}}\frac{k}{2}\sum_{\beta} D_{+\beta}D_{-\beta} \end{pmatrix} \mathbf{n}_{\text{diff}}^{i+1} = \begin{pmatrix} \mathbf{I} - \frac{kn_e\sigma_{iz}v_e}{2} + \\ \mathscr{D}_{\text{diff}}\frac{k}{2}\sum_{\beta} D_{+\beta}D_{-\beta} \end{pmatrix} \mathbf{n}_{\text{diff}}^{i}. \tag{2.28}$$

where superscripted $i$'s are time indices, $k$ is the time-step, $D_{+\beta}$ is the forward finite-difference scheme in the direction $\beta$, and $D_{-\beta}$ is the backward finite-difference scheme in the direction $\beta$, the summation is over orthogonal directions, and $\mathbf{I}$ is the identity matrix, with further details are provided in Appendix 2.B.2. This study assumes $v_{\text{rel}} = v_e$ in common practice for cases where electron velocities are much larger than ion or neutral background-gas velocities, i.e. $v_e >> v_i > v_{\text{bg}}$.

The terms in parentheses in Equation (2.28) are just matrix operators, with the term operating on the forward time typically denoted as the implicit operator, while the term operating on the current time is the explicit operator. In the one-dimensional case, rewriting to solve for the solution $\mathbf{n}^{i+1}$, Equation (2.28) becomes:

$$\mathbf{n}_{\text{diff}}^{i+1} = \left(\mathbf{A}_{\text{impl}}^{y}\right)^{-1} \mathbf{B}_{\text{expl}}^{y} \mathbf{n}_{\text{diff}}^{i} \tag{2.29}$$

where the direction chosen here is the $y$ direction with respect to the typical configuration of Figure 2.2. $\mathbf{A}_{\text{impl}}$ and $\mathbf{B}_{\text{expl}}$ are the implicit and explicit matrix operators, respectively, written for the 1-D case in Equation (2.100) and Equation (2.101) in Appendix 2.B.2.

## 2.5 Seed-Current Models

### 2.5.1 Constant-Waveform Source

XOOPIC's original models for the source current did not have a direct, self-consistent model for the triple-point primary seed current, so early studies were seeded with electrons from existing emission models, particularly a constant-waveform (CW) seed source which is not influenced by the local potential. This poses some interesting physical phenomena since the source is neither enhanced nor quenched (as long as the system remains below space-charge limited current) by changes in the local electric field as would normally be expected for sources akin to field emission. The constant-amplitude model can be interpreted as representing strong thermionic sources that are not affected by local changes in the fields, although thermal effects are not modeled for this study. Charges are emitted uniformly in time as a Maxwellian flux, where particles are emitted from an infinite reservoir and integration of the flux in any direction produces the characteristics of the well-known Maxwellian distribution. Injection of particles is achieved by inversion of a cumulative distribution function [5, 67].

### 2.5.2 Fowler-Nordheim Source

Field emission is a well-known electron-emission phenomenon characterized by quantum tunneling of electrons from a solid surface; the treatment of field-emission sources were characterized in the 1920's by Fowler and Nordheim [68] discussed in classical texts, such as [8], and valid for low-temperature emission where a relatively small number of states above the Fermi level are occupied. Field-emission sources will be referred to in this work as Fowler-Nordheim (FN) sources. A field-enhanced FN emitter that is part of the base XOOPIC package is employed for this study. The working relation for the current density in XOOPIC is:

$$J_{\mathrm{FN}} = A_{\mathrm{FN}} \frac{\left(|\beta_{\mathrm{FN}} E|\right)^2}{\phi_w} \exp\left(-\frac{B_{\mathrm{FN}} v\,[y]\,\phi_w^{1.5}}{|\beta_{\mathrm{FN}} E|}\right), \tag{2.30}$$

where $E$ is the electric field and definitions of all other factors with typical values are listed in Table 2.5. The field-enhancement factor, $\beta_{\mathrm{FN}}$, is the most crucial parameter for this study, as it tends to be highly empirical and is part of both the exponential term and a growing pre-exponential factor, i.e. $\beta_{\mathrm{FN}}$ contributes significantly to the non-linearity of FN sources. The most significant difference in moving to the FN emitter compared from the CW source is that local field variations influence the magnitude of the emitted current in the FN model.

Table 2.5: Factors for Fowler-Nordheim emitter, Equation (2.30), used in this study.

| Variable | Value | Units | Notes |
|---|---|---|---|
| $A_{\mathrm{FN}}$ | $1.5414 \times 10^{-6}$ | $\mathrm{A \cdot eV/V^2}$ | |
| $\beta_{\mathrm{FN}}$ | 10 | [unitless] | Field-enhancement factor |
| $\phi_w$ | 4.4 | eV | Work-function (in this case, copper) |
| $B_{\mathrm{FN}}$ | $6.8308 \times 10^9$ | $\mathrm{V/(m \cdot V^{1.5})}$ | |
| $y(E)$ | $C_{y,\mathrm{FN}} \frac{\sqrt{\lvert\beta_{\mathrm{FN}} E\rvert}}{\phi_w}$ | [unitless] | |
| $v(y)$ | $1 - C_{v,\mathrm{FN}} y^2$ | [unitless] | Valid for $2 \times 10^9 \leq E \leq 5 \times 10^9$ V/m |
| $C_{v,\mathrm{FN}}$ | 1.062 | [unitless] | |
| $C_{y,\mathrm{FN}}$ | $3.79 \times 10^{-5}$ | $\mathrm{V/\sqrt{V/m}}$ | |

### 2.5.3 Schächter Source

The implementation of the Schächter seed-current model is an attempt to approach first principles, effectively using the configuration geometry to approach first-principles treatment of seed-current sources in the triple-point region. The Schächter model is technically a field-emission variant following the FN model, but it requires fewer semi-empirical parameters than the FN model in the base XOOPIC package, and happens to provide an intermediate model between FN models and current limited models as illustrated in Figure 2.10. The Schächter current source is treated with a Fowler-Nordheim

form and presumed to be the most fundamental emitter used in this study. The form of the Schächter current in this study applies an analysis of the triple-point fields, the associated charge on the conductors as a result of the polarization in the dielectric medium, and integration of the current density over a finite region near the triple point. It should be noted that there is no automatic space-charge limit. Full details for this development are provided in Appendix 2.A, with the most pertinent details outlined here.

The Schächter current density is written in a simplified FN form:

$$J \simeq k_1 E^2 \exp\left(-\frac{k_2}{E}\right) \tag{2.31}$$

where parameters are listed in Table 2.6, and the differences between this form and the FN form of Equation (2.30) with $\beta = 1$ are shown in Figure 2.10, using the relations of Section 2.A.3 for the fields and charge.

Table 2.6: Factors for Schächter FN emitter model, Equation (2.31)

| Variable | Value | Units | Notes |
|---|---|---|---|
| $k_1$ | $\dfrac{1.5414 \times 10^{-6}}{\phi_w}$ | A/V$^2$ | |
| $k_2$ | $6.8308 \times 10^9 \phi_w^{1.5}$ | V/m | The pre-factor in [4] was two orders of magnitude smaller, so there will be differences in shape and magnitude in this treatment. |
| $\phi_w$ | 4.4 | eV | Work-function (in this case, copper) |

This study is largely concerned with configurations where voltage biases are held constant; therefore, a framework with constant effective voltage is employed, but the framework for constant electrode charge is outlined in Appendix 2.A.7. The metric for effective voltage is taken directly from the electrostatic energy in the fields per unit charge in the integrated region, delineated in Appendix 2.A.6:

$$V_{\text{eff}} = \frac{W_E}{Q_{\text{total}}} = \frac{\nu^2 A_1 R^\nu}{\chi(\nu)}. \tag{2.32}$$

where:

$$\chi(\nu) = \frac{2\nu \sin\left(\nu\left[\frac{\pi}{2}+\alpha\right]\right)\left(\sin\left[\nu\left(\frac{\pi}{2}+\alpha\right)\right] + \varepsilon_r \sin\left[\nu\left(\frac{\pi}{2}-\alpha\right)\right]\right)}{\left(\frac{\pi}{2}-\alpha\right)\sin^2\left(\nu\left[\frac{\pi}{2}+\alpha\right]\right) + \left(\frac{\pi}{2}+\alpha\right)\varepsilon_r \sin^2\left(\nu\left[\frac{\pi}{2}-\alpha\right]\right)}. \tag{2.33}$$

This interpretation of effective voltage is in keeping with the equivalent metric of simple circuit analysis for effective voltage of a time-varying source, written as the average power multiplied by the inverse of the effective current in the circuit, ultimately reducing to the familiar RMS voltage in the latter case. For Equation (2.32), the electrostatic energy in the fields, $W_E$, is the effective equivalent to integrated power, and the total charge on the electrode is simply the effective current multiplied by the integration time. The charge in this case is induced by the applied fields interacting with the dielectric.

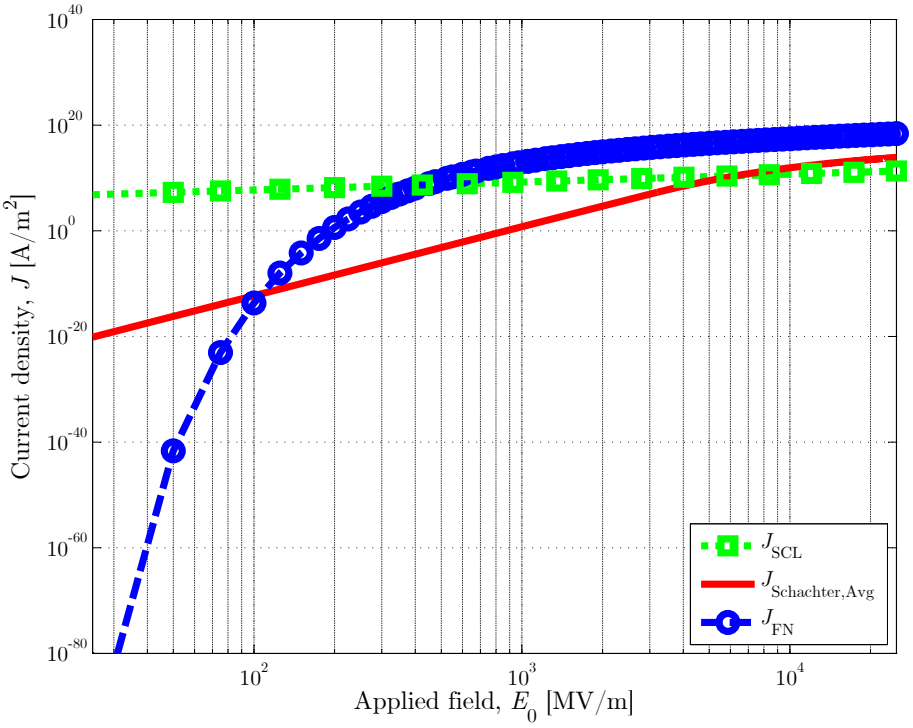


Figure 2.10: Comparison of Schächter, Fowler-Nordheim with parameters from Table 2.5, and Child-Langmuir, for $\alpha = 6.12°$. Specifically plotting Schächter as implemented in this work via Equation (2.34), FN in the form of Equation (2.30), and Child-Langmuir from Equation (2.3).

Integrating the current density, worked out in Appendix 2.A.8, the final result is copied from Equation (2.87) here for the purposes of exposition:

$$I_{\mathrm{top}}^{V_{\mathrm{eff}}} = I_1 \frac{\chi^2(\nu)}{\nu^2(2\nu-1)} \left[ \exp\left(-\frac{b_0\nu}{\chi(\nu)}\right) + \frac{b_0\nu}{\chi(\nu)} \int_0^1 y^{-\frac{2\nu-1}{\nu-1}} \exp\left(-\frac{b_0\nu}{\chi(\nu)} y\right) dy \right]. \tag{2.34}$$

The form presented in [4] is as follows:

$$I_{\mathrm{top}}^{V_{\mathrm{eff}},[4]} = I_1 \frac{\chi^2(\nu)}{2\nu-1} \left[ \exp\left(-\frac{b_0}{\chi(\nu)}\right) + \frac{b_0}{\chi(\nu)} \int_0^1 y^{-\frac{2\nu-1}{\nu-1}} \exp\left(-\frac{b_0}{\chi(\nu)} y\right) dy \right] \tag{2.35}$$

Equation (2.35) differs from Equation (2.34) with an additional $1/\nu^2$, and an additional $\nu$ accompanying all $b_0/\chi(\nu)$ terms. Equation (2.34) is inverted in the code rather than the published form of Equation (2.35) to maintain consistency of analysis herein. A comparison of Equations (2.34) and (2.35) is provided in Figure 2.11, showing the difference is within a factor of two for the particular configuration shown, but does increase nonlinearly at higher fields. The model implemented for this work, Equation (2.34), provides a slightly larger current overall, but remains close to The published for in the applied voltages of interest, typically less than a few hundred V/m.

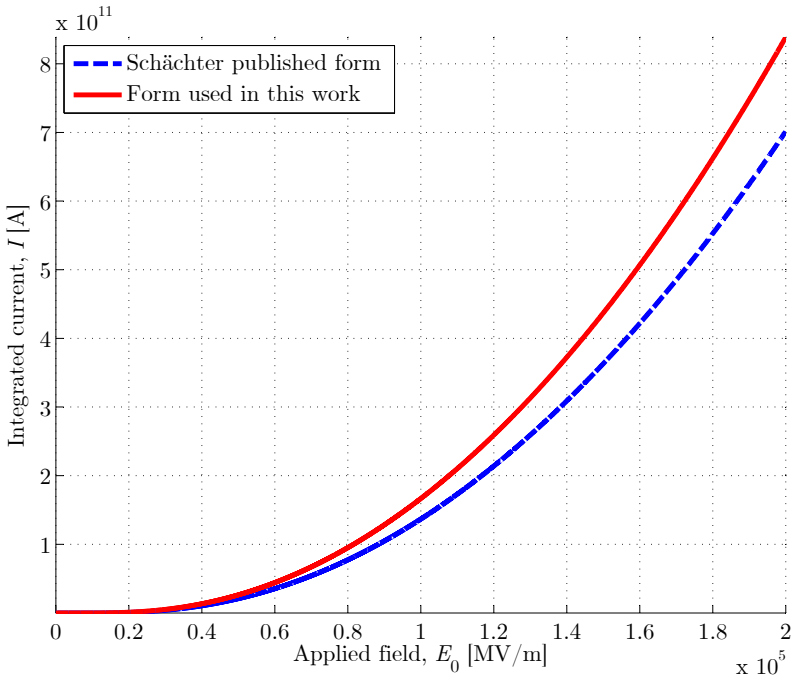


Figure 2.11: Comparison of Schächter integrated current from [4] to the development in this work. Specifically comparing Equations (2.34) and (2.35). The solid, red curve is the form implemented in this work.

## 2.6 Notable Corrections and Additions

The earliest notable error found in XOOPIC through the course of this study was a bug in the MaxwellianFlux class causing significant errors in preliminary results due to an incorrect modeling of emission from a given surface. Prior to correction of the model, emission for a Maxwellian flux was typically set with a null velocity in the direction normal to the emitting surface, i.e. $\vec{v} \cdot \hat{n} = 0$. Careful inspection revealed that this was the result of a poor initialization for the MaxwellianFlux class in the code, and the corrected model does indeed produce a Maxwellian distribution with sufficient statistics, as shown in Figure 2.12.

Additionally, as the development of XOOPIC is continually "in-progress", several modules were completed only as need dictates, e.g. the original coders of the boundary class assumed that orthogonal boundaries would be the only definitions needed for simulation of a typical system, so the original definition of the boundary normal was coded for the whole boundary. While the original definition for the normals was consistent inasmuch as a positive normal is up/right and negative normal is left/down as illustrated in Figure 2.13a, the concept of boundary "sides" is not consistent, and actually requires negated normals for adjacent segments, as illustrated in Figure 2.13b. The need to create non-orthogonal boundaries required defining normals on a piece-wise basis to maintain the usual definitions of "sides" for a boundary, since the original definition for the normals lead to emission errors at various boundaries as emission modules typically rely on the normal definition to decide in which direction to emit. Recasting the normal in terms of boundary segments was necessary to allow "one-sided" emission from non-orthogonal

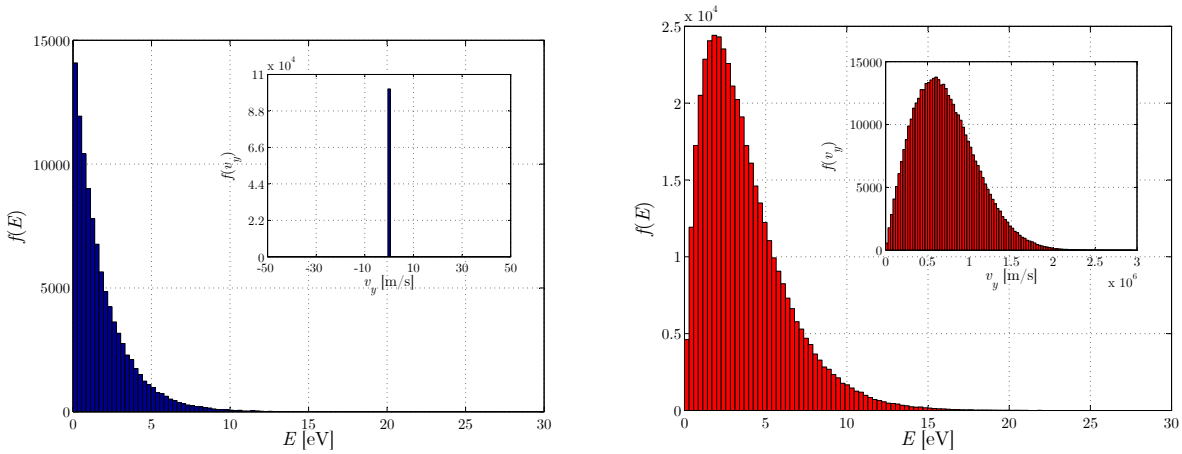


(a) Uncorrected Maxwellian

(b) Corrected Maxwellian

Figure 2.12: Maxwellian flux model error and correction. Original code effectively had an implementation error that led to an incorrect velocity in the direction normal to the emission surface.

boundaries.

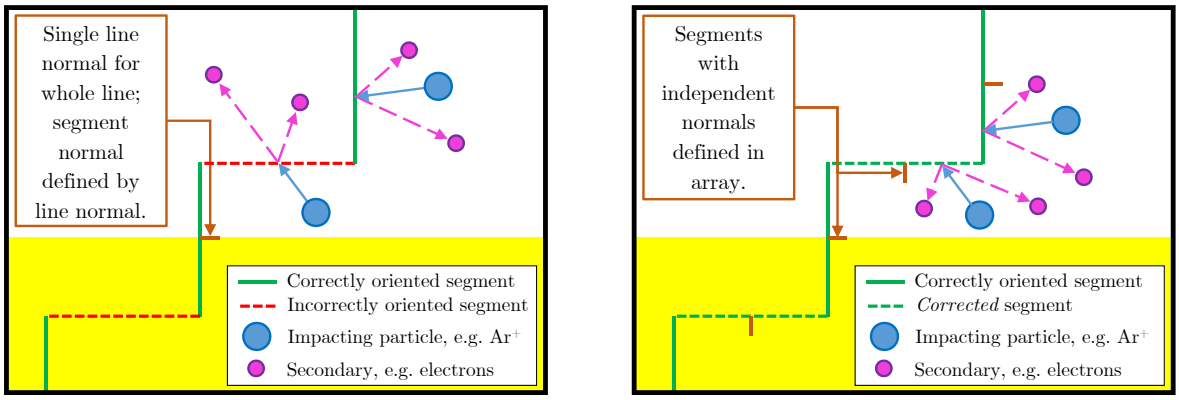


(a) Original boundary normal.

(b) Modified boundary normal.

Figure 2.13: Schematic of original boundary normal and modified boundary normals in code. Original coding of boundary normals did not account for non-orthogonal boundaries, which lead to incorrect emission modeling in some cases.

Other minor but notable additions include the completion of some missing dump-file routines that lead to infinite-loop errors in code and the addition of a text export function in XGRAFIX to allow faster post-processing in external visualization and analysis programs, particularly with the current popularity of interpreted languages such as Python and Matlab as a front-end for both on-the-fly post-processing (mostly in the case of Python) and creation of highly customizable, publication-caliber figures.

## 2.7 Standard Parameters and Reduced Parameters

Two main parameter sets for gap width and applied voltage were used in the course of this study to accommodate difficulties in modeling gain conditions. The standard parameter set used for much of this study is summarized in Table 2.7, showing basic metrics for numerical consideration.

Table 2.8 shows the reduced parameter set that was used in cases where the gain was deliberately limited to reduce particle population. The reduced parameter set posed a few physical caveats, most notably the ratio of mean free path to gap length could approach unity and therefore present a different operating regime (vis-à-vis breakdown) than those that would otherwise be encountered at high pressures in the standard parameter set. Due to the smaller time steps, a reduced mass ratio is also used to allow observation of ion momentum over a shorter time period.

# 2.A Schächter Formulation

### 2.A.1 The Triple Point

The triple point is defined as the junction between metal, dielectric, and vacuum, and can be shown to have divergent fields under certain boundary conditions. The following sub-sections will detail treatment of the triple-point potential and fields, considering the geometry in Figure 2.14. The cathode and $\alpha$ are shown conformal with Figure 1.1b; the "bottom" electrode is taken to be the half of the cathode below the dielectric-vacuum boundary, and the "top" electrode is the half above the boundary. This treatment is background primarily for developments in Section 2.5.3, largely following developments in [4, 12, 69] and completing details otherwise not available in such references.

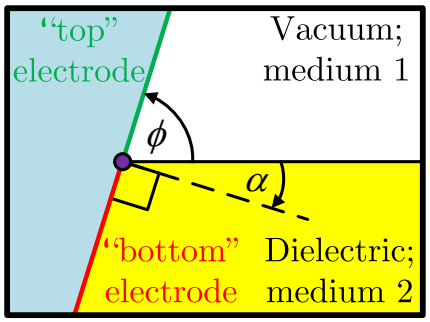


Figure 2.14: Geometry for deriving triple-point potentials.

As noted in Section 3.8, it must be cautioned that the results of Chapter 3 suggest that the characteristics of the seed source is irrelevant since the evolution of the discharges were highly dependent on the characteristics of the surface-field conditions, relegating the beam-like source to a necessary (in terms of being a seed source, not a triple-point source) but insufficient condition for breakdown to occur. The seed in Chapter 3 is a highly idealized source, which is not influenced by local field conditions and has a highly formed, beam-like distribution that influences surface-field characteristics in different ways than a more distributed source would.

Table 2.7: General parameters for standard simulation system. These are uniform values for parameters, where variations are listed as needed. SE="Secondary Emission". SE parameters quoted for PTFE [57]. Symbols are mapped to the schematic of Figure 2.2. The ratio of the number of physical to computational particles is denoted as "np2c", otherwise understood as the macroparticle weighting.

| Physical Parameter | Symbol | Value |
|---|---|---|
| Dielectric angle | $\alpha$ | 6.12° or 22.9° |
| Dielectric permittivity | $\epsilon_r$ | 2.1 |
| Max (normal) SE coefficient | $\delta_{\max}$ | 2.95 |
| Energy at $\delta_{\max}$ | $W_{\max}$ | 600 eV |
| SE threshold energy | $V_{\text{th}}$ | 12.5 eV |
| SE emission-energy mode | $W_{\text{emit}^{\text{mode}}}$ | 1.85 eV |
| SE average emission energy | $W_{\text{avg}}$ | 2.36 eV |
| Gap width | $D_{\text{gap}}$ | 2 mm |
| Source current | $I_0$ | 1 A |
| Source-current temperature | $T_0$ | 0.025 eV |
| Seed drift velocity in $x$ | $v_{d,x}$ | $(W_{\text{imp}}^{\max} - q_e E \delta y)\cos(\pi/2 - \theta_{\text{imp}})$ eV |
| Seed drift velocity in $y$ | $v_{d,y}$ | $(W_{\text{imp}}^{\max} - q_e E \delta y)\sin(\pi/2 - \theta_{\text{imp}})$ eV |
| Fraction scattered | $f_{\text{Scattered}}$ | 0 or 0.07 |
| Fraction reflected | $f_{\text{Reflected}}$ | 0 or 0.03 |
| Mass ratio | $\xi_{\text{mass}}$ | 1 (unitless) |
| Subcycle | $N_{\text{subcycle}}$ | 1 (ion cycles)/(electron cycles) |
| Averaged cross section | $\langle \sigma_{iz} \rangle$ | $2.74 \times 10^{-20}$ m$^2$ |
| Pressure | $p_{\text{bg}}$ | 0 mTorr |
| Applied voltage | $V_0$ | 3500 V |
| Pressure | $p_{\text{bg}}$ | 1 Torr |
| Applied voltage | $V_0$ | 8500 V |
| Mean free path | $r_{\text{mfp}}$ | 1.095 mm |
| Collision ratio | $r_{\text{mfp}}/D_{\text{gap}}$ | 0.548 (unitless) |

| Numerical Parameter | Symbol | Value |
|---|---|---|
| Integer discretization in $x$ | $m_5$ | 28 (6.12°) or 25 (22.9°) |
| Integer discretization in $y$ | $m_6$ | 3 (6.12°) or 11 (22.9°) |
| Macro-particle weighting | np2c | $6 \times 10^5$ |
| Time-step | $\Delta t$ | 1 ps |
| Grid-size | $dx$ and $dy$ | 35.5 µm |

Table 2.8: Reduced parameter set used to limit surface gain. Showing only parameters that have changed from Table 2.7. Although not explicitly delineated herein, numbers are included for test systems at 1 Torr, facilitating discussion of reduced systems at pressures greater than VULP.

| Parameter | Symbol | Value |
|---|---|---|
| Gap width | $D_{\text{gap}}$ | 0.2 µm |
| Pressure | $p$ | 1 Torr |
| Applied voltage | $V_0$ | 8500 V |
| Mean free path | $r_{\text{mfp}}$ | 1.095 mm |
| Mass ratio | $\xi_{\text{mass}}$ | 40 (unitless) |
| Subcycle | $N_{\text{subcycle}}$ | 1 (ion cycles)/(electron cycles) |
| Collision ratio | $r_{\text{mfp}}/D_{\text{gap}}$ | 5.48e3 (unitless) |

### 2.A.2 The Triple-Point Potential

The potential for the configuration of Figure 2.14, written in cylindrical coordinates with $z$ conformal to the usual Cartesian $z$ used in this study, is given by:

$$\Phi = \begin{cases} A_1 \sin\left(\nu\left[\phi - \frac{\pi}{2} + \alpha\right]\right) r^\nu + V_0 & 0 < \phi < \frac{\pi}{2} - \alpha \\ A_2 \sin\left(\nu\left[\phi + \frac{\pi}{2} + \alpha\right]\right) r^\nu + V_0 & -\frac{\pi}{2} - \alpha < \phi < 0. \end{cases} \tag{2.36}$$

The curvature parameter, $\nu$, is found by applying the dielectric-vacuum boundary conditions. For the component tangential to the dielectric surface (equivalent to $r$ when along the surface):

$$\begin{gathered} E_{1t}(r,0) = E_{2t}(r,0) \;\Rightarrow\; E_{1r}(r,0) = E_{2r}(r,0), \\ -A_1\nu \sin\left(\nu\left[\tfrac{\pi}{2} - \alpha\right]\right) r^{\nu-1} = +A_2\nu \sin\left(\nu\left[\tfrac{\pi}{2} + \alpha\right]\right) r^{\nu-1}. \end{gathered} \tag{2.37}$$

For the component normal to the dielectric surface (equivalent to $\phi$ when along the surface):

$$\begin{gathered} \varepsilon_0 E_{1n}(r,0) = \varepsilon_0 \varepsilon_r E_{2n}(r,0) \;\Rightarrow\; E_{1\phi}(r,0) = \varepsilon_r E_{2\phi}(r,0), \\ A_1\nu \cos\left(\nu\left[\tfrac{\pi}{2} - \alpha\right]\right) r^{\nu-1} = \varepsilon_r A_2\nu \cos\left(\nu\left[\tfrac{\pi}{2} + \alpha\right]\right) r^{\nu-1}. \end{gathered} \tag{2.38}$$

Eliminating constants gives:

$$\varepsilon_r \tan\left(\nu\left[\frac{\pi}{2} - \alpha\right]\right) = -\tan\left(\nu\left[\frac{\pi}{2} + \alpha\right]\right). \tag{2.39}$$

The range for $\nu$ as a function of $\varepsilon_r$ can be derived by looking at the limits for $\varepsilon$. In the case of $\varepsilon_r = 1$, pulling the negative into the transcendental and applying a periodic offset of $m\pi$ (letting $m = 1$ for this treatment) to preclude the trivial solution of $\nu = 0$:

$$\begin{gathered} \varepsilon_r = 1 \Rightarrow \tan\left(\nu\left[\frac{\pi}{2} - \alpha\right]\right) = \tan\left(-\nu\left[\frac{\pi}{2} + \alpha\right]\right), \\ \left.\begin{gathered} \nu\left[\frac{\pi}{2} - \alpha\right] = -\nu\left[\frac{\pi}{2} + \alpha\right] + m\pi = -\nu\left[\frac{\pi}{2} + \alpha\right] + (1)\pi \\ \left(\nu\left[\frac{\pi}{2} - \alpha + \frac{\pi}{2} + \alpha\right] = \nu\left[\frac{\pi}{2} + \frac{\pi}{2}\right] = \nu\pi\right) = \pi \end{gathered}\right\} \Rightarrow \nu = \frac{\pi}{\pi} = 1. \end{gathered} \tag{2.40}$$

Similarly for $\varepsilon_r \to \infty$, applying the same periodic offset, $m\pi$, with $m = 1$:

$$\begin{aligned} &\varepsilon_r \to \infty \Rightarrow -\tan\left(\nu\left[\frac{\pi}{2}+\alpha\right]\right) \to \infty, \\ &\left.\begin{aligned} &\nu\left[\frac{\pi}{2}+\alpha\right] = -\frac{\pi}{2} + m\pi = -\frac{\pi}{2} + (1)\pi \\ &\nu = +\frac{\pi}{2}\frac{1}{\left[\frac{\pi}{2}+\alpha\right]} = \frac{\pi}{2\frac{\pi}{2}+2\alpha} = \frac{\pi}{\pi+2\alpha} = \frac{1}{1+2\alpha/\pi} \end{aligned}\right\} \Rightarrow \nu = \frac{1}{1+2\alpha/\pi}. \end{aligned} \tag{2.41}$$

The full relation can be plotted for $\nu(\varepsilon_r, \alpha)$ as in Figure 2.15 using $\alpha = 6.12°$ and $\alpha = 22.9°$, where the limit for $\varepsilon_r \to \infty$ varies per dielectric angle.

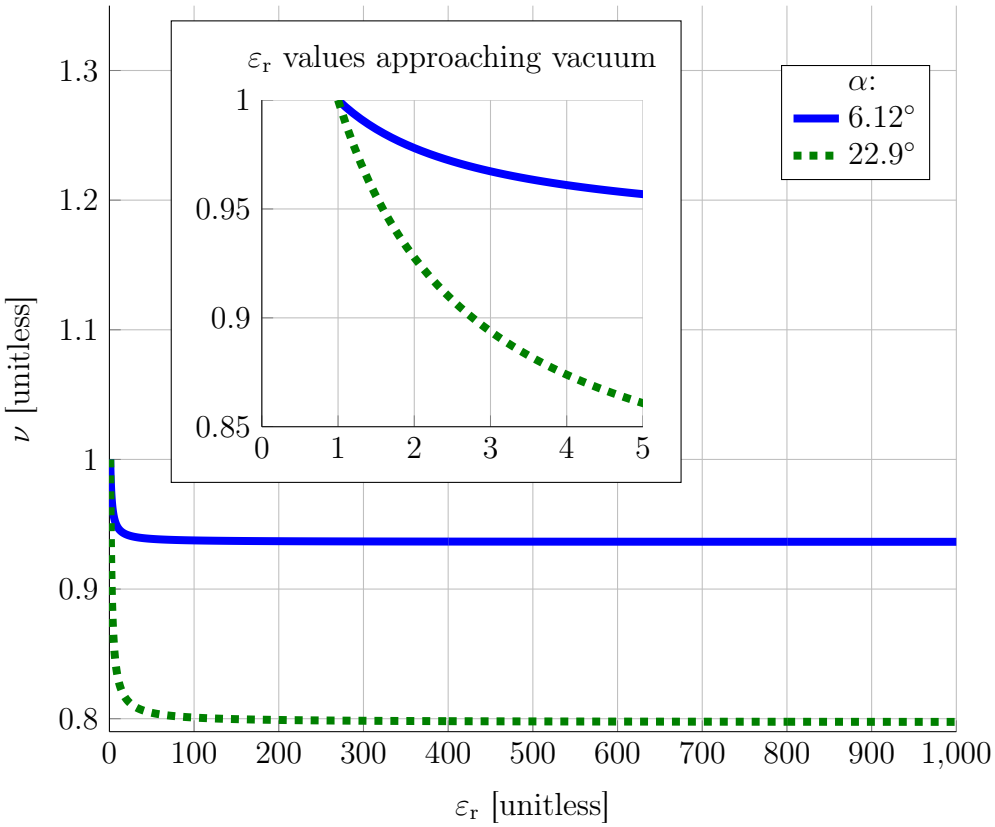


Figure 2.15: $\nu$ as a function of $\varepsilon_r$. When $\nu$ is less than unity, as is the case for all values of $\varepsilon_r$ for the angles shown above, the electric-field values can diverge on the approach to the triple point.

The equipotentials of $\alpha = 6.12°$ configuration is shown in Figure 2.16.

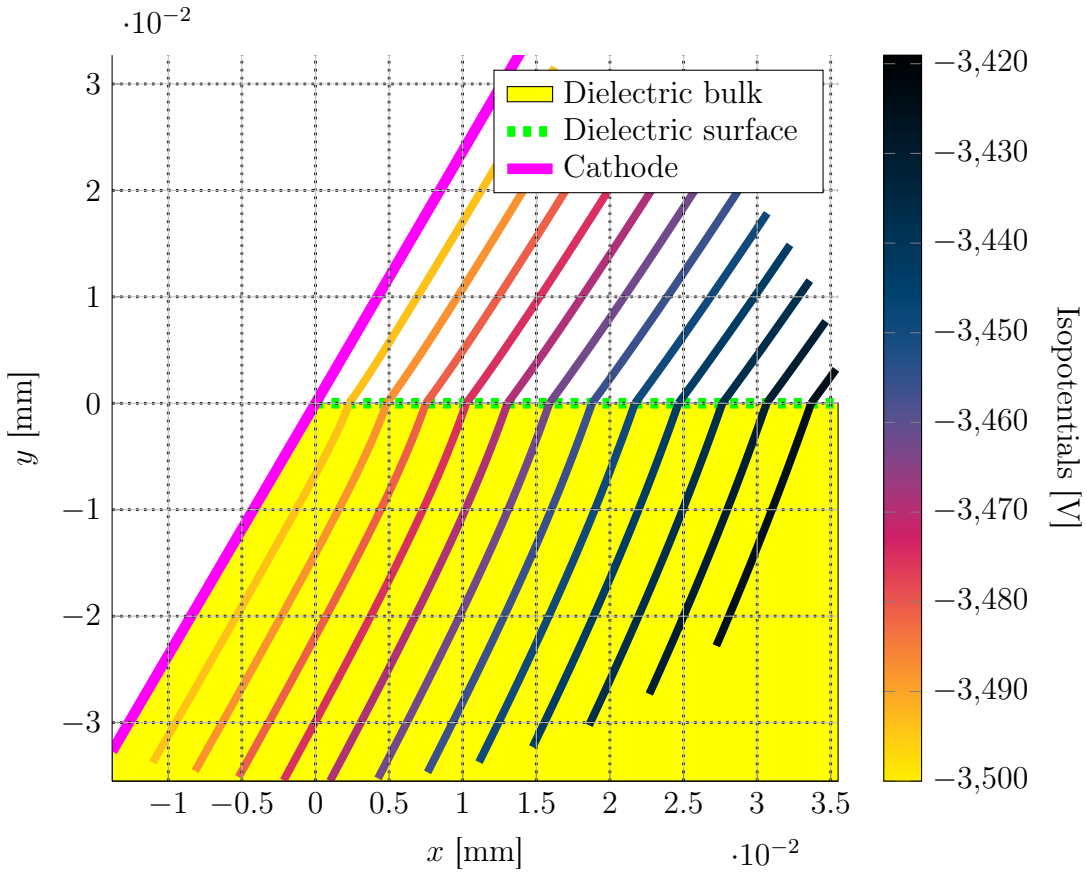


Figure 2.16: Equipotentials near the triple-point for $\alpha = 6.12°$. $-3500\,\text{kV}$ applied at the cathode. The lower half-space (yellow shaded) is the bulk dielectric, and the upper half-space is vacuum.

### 2.A.3 The Triple-Point Fields and Charge

Following from the potential form in Equation (2.36), the electric field takes the form:

$$\vec{E} = -\vec{\nabla}\Phi = \begin{cases} -A_1\nu \sin\left(\nu\left[\phi - \frac{\pi}{2} + \alpha\right]\right) r^{\nu-1}\hat{r} - \\ \quad A_1\nu \cos\left(\nu\left[\phi - \frac{\pi}{2} + \alpha\right]\right) r^{\nu-1}\hat{\phi} & 0 < \phi < \frac{\pi}{2} - \alpha \\ -A_2\nu \sin\left(\nu\left[\phi + \frac{\pi}{2} + \alpha\right]\right) r^{\nu-1}\hat{r} - \\ \quad A_2\nu \cos\left(\nu\left[\phi + \frac{\pi}{2} + \alpha\right]\right) r^{\nu-1}\hat{\phi} & -\frac{\pi}{2} - \alpha < \phi < 0. \end{cases} \tag{2.42}$$

The displacement field for a linear medium in this configuration is given by:

$$D_\phi = \varepsilon E_\phi = -\begin{cases} \varepsilon_0 A_1\nu \cos\left(\nu\left[\phi - \frac{\pi}{2} + \alpha\right]\right) r^{\nu-1} & 0 < \phi < \frac{\pi}{2} - \alpha \\ \varepsilon_0\varepsilon_r A_2\nu \cos\left(\nu\left[\phi + \frac{\pi}{2} + \alpha\right]\right) r^{\nu-1} & -\frac{\pi}{2} - \alpha < \phi < 0. \end{cases} \tag{2.43}$$

The charge on the electrode can then be written as:

$$Q = \oint_S \vec{D} \cdot d\vec{a} = \oint_S \vec{D}_\phi \cdot da\hat{\phi}. \tag{2.44}$$

The charge on the top electrode for a finite cylinder of height $\Delta_z$ is:

$$\begin{aligned} Q_{\text{top}} &= \int_{\frac{-\Delta_z}{2}}^{\frac{\Delta_z}{2}} \int_0^R \vec{D} \cdot \left(-drdz\hat{\phi}\right) = -\Delta_z \int_0^R drD_\phi \left(r, \frac{\pi}{2} - \alpha\right) \\ &= \Delta_z \varepsilon_0 \nu A_1 \frac{R^\nu}{\nu} = \Delta_z \varepsilon_0 R^\nu A_1. \end{aligned} \tag{2.45}$$

while the charge on the bottom electrode is:

$$\begin{aligned} Q_{\text{bottom}} &= \int_{\frac{-\Delta_z}{2}}^{\frac{\Delta_z}{2}} \int_0^R \vec{D} \cdot \left(drdz\hat{\phi}\right) = \Delta_z \int_0^R drD_\phi \left(r, -\frac{\pi}{2} - \alpha\right) = \\ &= -\Delta_z \varepsilon_0 \varepsilon_r A_2 \nu \frac{R^\nu}{\nu} = -\Delta_z \varepsilon_0 \varepsilon_r R^\nu A_2. \end{aligned} \tag{2.46}$$

and, finally, the total charge for a finite cylinder of height $\Delta_z$ is:

$$Q_{\text{total}} = Q_{\text{top}} + Q_{\text{bottom}} = \Delta_z \varepsilon_0 R^\nu A_1 - \Delta_z \varepsilon_0 \varepsilon_r R^\nu A_2 = \Delta_z \varepsilon_0 R^\nu \left(A_1 - \varepsilon_r A_2\right). \tag{2.47}$$

### 2.A.4 Electrostatic Energy Around the Triple Point

The electrostatic energy by integrating the energy density:

$$W_E = \frac{1}{2} \int \vec{D} \cdot \vec{E} d\tau = \frac{1}{2} \int \varepsilon \vec{E} \cdot \vec{E} d\tau, \tag{2.48}$$

where the last equality assumes a linear dielectric so that the constitutive relation, $\vec{D} = \varepsilon \vec{E}$ applies. Noting that the field is piecewise for this configuration, so that the integral of Equation (2.48) also requires piecewise treatment, where the energy density for the vacuum region is:

$$\frac{\varepsilon_0}{2} \vec{E}_1 \cdot \vec{E}_1 = \frac{\varepsilon_0}{2} \begin{pmatrix} \left[-A_1 \nu \sin\left(\nu \left[\phi - \pi/2 + \alpha\right]\right) r^{\nu-1}\right]^2 + \\ \left[-A_1 \nu \cos\left(\nu \left[\phi - \pi/2 + \alpha\right]\right) r^{\nu-1}\right]^2 \end{pmatrix} = \frac{\varepsilon_0}{2} A_1^2 \nu^2 r^{2\nu-2}, \tag{2.49}$$

and the energy density for the linear dielectric region is:

$$\frac{\varepsilon}{2} \vec{E}_2 \cdot \vec{E}_2 = \frac{\varepsilon}{2} \begin{pmatrix} \left[-A_2 \nu \sin\left(\nu \left[\phi + \pi/2 + \alpha\right]\right) r^{\nu-1}\right]^2 + \\ \left[-A_2 \nu \cos\left(\nu \left[\phi + \pi/2 + \alpha\right]\right) r^{\nu-1}\right]^2 \end{pmatrix} = \frac{\varepsilon}{2} A_2^2 \nu^2 r^{2\nu-2}. \tag{2.50}$$

Integrating over the finite cylinder noted at the beginning of this development and expanding $\varepsilon = \varepsilon_0 \varepsilon_r$:

$$\begin{aligned} W_E &= \left[ \frac{1}{2} \int_{-\frac{\Delta_z}{2}}^{\frac{\Delta_z}{2}} \int_0^{\frac{\pi}{2}-\alpha} \int_0^R \varepsilon_0 E_1^2 drrd\phi dz + \frac{1}{2} \int_{-\frac{\Delta_z}{2}}^{\frac{\Delta_z}{2}} \int_{-\frac{\pi}{2}-\alpha}^0 \int_0^R \varepsilon_0 \varepsilon_r E_2^2 drrd\phi dz \right] \\ &= \frac{1}{2} \varepsilon_0 \nu^2 \left[ A_1^2 \left(\Delta_z\right) \left(\frac{\pi}{2} - \alpha\right) \frac{r^{2\nu}}{2\nu}\bigg|_0^R + \varepsilon_r A_2^2 \left(\Delta_z\right) \left(\frac{\pi}{2} + \alpha\right) \frac{r^{2\nu}}{2\nu}\bigg|_0^R \right], \end{aligned} \tag{2.51}$$

and finally:

$$W_E = \frac{1}{4}\varepsilon_0 \nu \Delta_z R^{2\nu} \left[ \left( \frac{\pi}{2} - \alpha \right) A_1^2 + \left( \frac{\pi}{2} + \alpha \right) \varepsilon_r A_2^2 \right]. \tag{2.52}$$

### 2.A.5 Capacitance of the Triple-Point Region

The capacitance is defined by:

$$C = \frac{Q_{\text{total}}^2}{2W_E}. \tag{2.53}$$

Pulling in Equation (2.47) and Equation (2.52) gives:

$$\begin{aligned} C &= \frac{\left[\Delta_z \varepsilon_0 R^\nu \left(A_1 - \varepsilon_r A_2\right)\right]^2}{2\left[\frac{1}{4}\varepsilon_0 \nu \Delta_z R^{2\nu} \left( \left[\frac{\pi}{2} - \alpha\right] A_1^2 + \left[\frac{\pi}{2} + \alpha\right] \varepsilon_r A_2^2 \right)\right]} \\ &= \frac{2}{\nu} \frac{\left(\varepsilon_0 \Delta_z\right)^2}{\varepsilon_0 \Delta_z} \frac{R^{2\nu}}{R^{2\nu}} \frac{A_2^2 \left( \frac{A_1}{A_2} - \varepsilon_r \right)^2}{A_2^2 \left( \left[\frac{\pi}{2} - \alpha\right] \frac{A_1^2}{A_2^2} + \left[\frac{\pi}{2} + \alpha\right] \varepsilon_r \right)}. \end{aligned} \tag{2.54}$$

Recalling the boundary conditions from Equations (2.37) and (2.38), the constants can be defined as a ratio of sinusoidal terms:

$$\frac{A_1}{A_2} = \varepsilon_r \left[ \frac{\cos\left(\nu \left[\frac{\pi}{2} + \alpha\right]\right)}{\cos\left(\nu \left[\frac{\pi}{2} - \alpha\right]\right)} \right] = -\frac{\sin\left(\nu \left[\frac{\pi}{2} + \alpha\right]\right)}{\sin\left(\nu \left[\frac{\pi}{2} - \alpha\right]\right)}. \tag{2.55}$$

In particular, using the sinus ratio, i.e. the tangential boundary condition:

$$\begin{aligned} C &= \frac{2\varepsilon_0 \Delta_z}{\nu} \frac{\left( -\frac{\sin\left[\nu\left(\frac{\pi}{2} + \alpha\right)\right]}{\sin\left[\nu\left(\frac{\pi}{2} - \alpha\right)\right]} - \varepsilon_r \right)^2}{\left( \left[\frac{\pi}{2} - \alpha\right] \left[ -\frac{\sin\left(\nu\left[\frac{\pi}{2} + \alpha\right]\right)}{\sin\left(\nu\left[\frac{\pi}{2} - \alpha\right]\right)} \right]^2 + \left[\frac{\pi}{2} + \alpha\right] \varepsilon_r \right)} \\ &= \frac{2\varepsilon_0 \Delta_z}{\nu} \frac{\left( -\frac{1}{\sin\left[\nu\left(\frac{\pi}{2} - \alpha\right)\right]} \right)^2 \left( \sin\left[\nu\left(\frac{\pi}{2} + \alpha\right)\right] + \varepsilon_r \sin\left[\nu\left(\frac{\pi}{2} - \alpha\right)\right] \right)^2}{\left( \frac{1}{\sin\left[\nu\left(\frac{\pi}{2} - \alpha\right)\right]} \right)^2 \left( \begin{array}{l} \left[\frac{\pi}{2} - \alpha\right] \left[\sin\left(\nu\left[\frac{\pi}{2} + \alpha\right]\right)\right]^2 + \\ \left[\frac{\pi}{2} + \alpha\right] \varepsilon_r \left[\sin\left(\nu\left[\frac{\pi}{2} - \alpha\right]\right)\right]^2 \end{array} \right)} \end{aligned} \tag{2.56}$$

and finally:

$$C = \frac{1}{\nu} \varepsilon_0 \Delta_z \frac{2\left( \sin\left[\nu\left(\frac{\pi}{2} + \alpha\right)\right] + \varepsilon_r \sin\left[\nu\left(\frac{\pi}{2} - \alpha\right)\right] \right)^2}{\left(\frac{\pi}{2} - \alpha\right) \sin^2\left(\nu\left[\frac{\pi}{2} + \alpha\right]\right) + \left(\frac{\pi}{2} + \alpha\right) \varepsilon_r \sin^2\left(\nu\left[\frac{\pi}{2} - \alpha\right]\right)}. \tag{2.57}$$

It should be noted that following this treatment using the geometry from Schächter leads to a form for Equation (2.57) that does not include the $1/\nu$ factor, which is apparently a mistake on the part of the formulation in [4]. This work will follow the formulation here to maintain consistency.

### 2.A.6 The Effective Voltage of the Triple-Point Region

The effective voltage in the region is defined by:

$$V_{\text{eff}} \equiv \frac{Q_{\text{total}}}{C}, \tag{2.58}$$

where the total charge in the triple-point region is from Equation (2.47), and the capacitance is from Equation (2.57). Substituting into Equation (2.58) gives:

$$V_{\text{eff}} = \frac{\Delta_z \varepsilon_0 R^\nu \left(A_1 - \varepsilon_r A_2\right)}{\frac{1}{\nu}\varepsilon_0 \Delta_z \frac{2\left(\sin\left[\nu\left(\frac{\pi}{2}+\alpha\right)\right] + \varepsilon_r \sin\left[\nu\left(\frac{\pi}{2}-\alpha\right)\right]\right)^2}{\left(\frac{\pi}{2}-\alpha\right)\sin^2\left(\nu\left[\frac{\pi}{2}+\alpha\right]\right) + \left(\frac{\pi}{2}+\alpha\right)\varepsilon_r \sin^2\left(\nu\left[\frac{\pi}{2}-\alpha\right]\right)}}. \tag{2.59}$$

The majority of the denominator in Equation (2.59) can be collected into a function $\xi(\nu)$:

$$\xi\left(\nu\right) = \frac{\left(\frac{\pi}{2}-\alpha\right)\sin^2\left(\nu\left[\frac{\pi}{2}+\alpha\right]\right) + \left(\frac{\pi}{2}+\alpha\right)\varepsilon_r \sin^2\left(\nu\left[\frac{\pi}{2}-\alpha\right]\right)}{2\nu\left(\sin\left[\nu\left(\frac{\pi}{2}+\alpha\right)\right] + \varepsilon_r \sin\left[\nu\left(\frac{\pi}{2}-\alpha\right)\right]\right)^2}, \tag{2.60}$$

so that:

$$\begin{aligned} V_{\text{eff}} &= A_1 \nu^2 R^\nu \left(1 - \frac{A_2}{A_1}\varepsilon_r\right) \xi\left(\nu\right) \\ &= \nu^2 A_1 R^\nu \left(1 - \left[-\frac{\sin\left(\nu\left[\frac{\pi}{2}-\alpha\right]\right)}{\sin\left(\nu\left[\frac{\pi}{2}+\alpha\right]\right)}\right]\varepsilon_r\right) \xi\left(\nu\right) \\ &= \nu^2 A_1 R^\nu \frac{\sin\left(\nu\left[\frac{\pi}{2}+\alpha\right]\right) + \varepsilon_r \sin\left(\nu\left[\frac{\pi}{2}-\alpha\right]\right)}{\sin\left(\nu\left[\frac{\pi}{2}+\alpha\right]\right)} \xi\left(\nu\right), \end{aligned} \tag{2.61}$$

where the tangential boundary condition from Equation (2.55) was employed again. In keeping with the definitions in [4], another function, $\chi(\nu)$, can be defined:

$$\chi\left(\nu\right) = \frac{1}{\xi\left(\nu\right)} \frac{\sin\left(\nu\left[\frac{\pi}{2}+\alpha\right]\right)}{\sin\left(\nu\left[\frac{\pi}{2}+\alpha\right]\right) + \varepsilon_r \sin\left(\nu\left[\frac{\pi}{2}-\alpha\right]\right)}. \tag{2.62}$$

Finally, the effective voltage can be written simply as:

$$V_{\text{eff}} = \frac{\nu^2 A_1 R^\nu}{\chi\left(\nu\right)}, \tag{2.63}$$

This, again, differs from the developments in [4] by a factor of $\nu$ due to the initial error in the formulation of capacitance.

### 2.A.7 Integrated Current with Constant Charge

The current itself will take the form of a Fowler-Nordheim (FN) source with constant coefficients using the field calculated directly from Equation (2.42), rather than the fields by finite difference solution, in which the spatial discretization always models the metal boundary as orthogonal or conformal to the dielectric at the intersection of the boundaries. The FN form used here is:

$$J \simeq k_1 E^2 \exp\left(-\frac{k_2}{E}\right), \tag{2.64}$$

where the coefficients are:

$$k_1 = \frac{1.54 \times 10^{-6}}{\phi_w}\left[\frac{\mathrm{A}}{\mathrm{V}^2}\right]; k_2 = 6.83 \times 10^9 \phi_w^{1.5}\left[\frac{\mathrm{V}}{\mathrm{m}}\right]; \phi_w \equiv \text{work function } [\mathrm{eV}]. \tag{2.65}$$

The work function, $\phi_w$, is for the cathodic material where emission occurs, and is typically assumed a metal such as copper with $\phi_w = 4.4\,\mathrm{eV}$. The total integrated current over the cathodic region in the finite region mentioned at the beginning of this section is given by:

$$\begin{aligned} I_{\text{top}}^{Q_{\text{top}}} &= k_1 \int_{-\Delta_z/2}^{\Delta_z/2} \int_0^R E_1^2 \exp\left(-\frac{k_2}{E_1}\right) dr dz \\ &= k_1 \Delta_z \int_0^R A_1^2 \nu^2 r^{2\nu-2} \exp\left(-\frac{k_2}{\sqrt{A_1^2 \nu^2 r^{2\nu-2}}}\right) dr \\ &= A_1^2 \nu^2 k_1 \Delta_z \int_0^R r^{2\nu-2} \exp\left(-\frac{k_2}{A_1 \nu}\frac{1}{r^{\nu-1}}\right) dr. \end{aligned} \tag{2.66}$$

Only the field in the vacuum region is required for the integrated current in Equation (2.66). A few substitutions are used for non-dimensionalization:

$$a_0\,[\text{unitless}] = \frac{k_2}{E_{\text{eff,Q}}}, \tag{2.67}$$

$$E_{\text{eff,Q}}\left[\frac{\mathrm{V}}{\mathrm{m}}\right] = \frac{Q_{\text{top}}}{\varepsilon_0 R \Delta_z}, \tag{2.68}$$

$$Q_{\text{top}}\,[\mathrm{C}] = A_1 \varepsilon_0 \Delta_z R^\nu. \tag{2.69}$$

This development will use two, more-direct substitutions. The first is a minor manipulation of Equation (2.67):

$$a_0 = \frac{k_2}{E_{\text{eff,Q}}} \Rightarrow \frac{a_0}{\nu} = \frac{k_2}{\nu E_{\text{eff,Q}}} = \frac{k_2}{\nu}\frac{\varepsilon_0 R \Delta_z}{Q_{\text{top}}} = \frac{k_2}{\nu}\frac{\varepsilon_0 R \Delta_z}{A_1 \varepsilon_0 \Delta_z R^\nu} = \frac{k_2}{A_1 \nu}\frac{R}{R^\nu}$$

$$\Rightarrow \frac{a_0}{\nu}\,[\text{unitless}] = \frac{k_2}{A_1 \nu}\frac{R}{R^\nu}, \tag{2.70}$$

and the other is a multiplicative factor in units of current:

$$I_0 = \Delta_z R k_1 E_{\text{eff,Q}}^2 = \Delta_z R k_1 \left(\frac{Q_{\text{top}}}{\varepsilon_0 R \Delta_z}\right)^2 = \Delta_z R k_1 \left(\frac{A_1 \varepsilon_0 \Delta_z R^\nu}{\varepsilon_0 R \Delta_z}\right)^2$$
$$= \Delta_z R k_1 \left(\frac{A_1 R^\nu}{R}\right)^2 = \Delta_z R k_1 \frac{A_1^2 R^{2\nu}}{R^2}$$

$$\Rightarrow I_0\,[\text{A}] = A_1^2 k_1 \Delta_z \frac{R^{2\nu}}{R}, \tag{2.71}$$

Schächter also employs a substitution of the form:

$$-\frac{k_2}{A_1 \nu} \frac{1}{r^{\nu-1}} = -\frac{a_0}{\nu} y, \tag{2.72}$$

where $y$ is simply a non-dimensionalized radius, i.e.:

$$y = \frac{k_2}{A_1 \nu} \frac{r}{r^\nu} \frac{\nu}{a_0} = \frac{k_2}{A_1 \nu} \frac{r}{r^\nu} \frac{A_1 \nu R^\nu}{k_2 R} = \frac{k_2}{k_2} \frac{A_1 \nu}{A_1 \nu} \frac{r}{r^\nu} \frac{R^\nu}{R} = \frac{r}{R} \frac{R^\nu}{r^\nu} = \frac{r^{1-\nu}}{R^{1-\nu}}. \tag{2.73}$$

The differential on Equation (2.73) is:

$$dy = (1-\nu) \frac{r^{-\nu}}{R^{1-\nu}} dr = (1-\nu) \frac{R^\nu}{R} \frac{1}{r^\nu} dr, \tag{2.74}$$

and to get rid of the $r$ on the right-hand side of Equation (2.74), simply rearrange Equation (2.73) to get:

$$y = \frac{r^{1-\nu}}{R^{1-\nu}} \Rightarrow r^{1-\nu} = R^{1-\nu} y \Rightarrow r = \left(R^{1-\nu} y\right)^{\frac{1}{1-\nu}} = R^{\frac{1-\nu}{1-\nu}} y^{\frac{1}{1-\nu}} = R y^{\frac{1}{1-\nu}}. \tag{2.75}$$

Substituting Equation (2.75) into Equation (2.74) and rearranging to obtain $dr$ directly:

$$dy = (1-\nu) \frac{R^\nu}{R} \frac{1}{r^\nu} dr \Rightarrow dr = \frac{1}{1-\nu} \frac{R}{R^\nu} r^\nu dy = \frac{1}{1-\nu} \frac{R}{R^\nu} R^\nu y^{\frac{\nu}{1-\nu}} dy = \frac{R}{1-\nu} y^{\frac{\nu}{1-\nu}} dy$$

$$dr = \frac{R}{1-\nu} y^{\frac{\nu}{1-\nu}} dy. \tag{2.76}$$

Going back to the current in Equation (2.66) and padding with unit terms for normalization:

$$I_{\text{top}}^{Q_{\text{top}}} = A_1^2 k_1 \Delta_z \nu^2 \int_0^R \frac{r^{2\nu}}{r^2} \left(\frac{R^2}{R^{2\nu}} \frac{R^{2\nu}}{R^2}\right) \exp\left(-\frac{k_2}{A_1 \nu} \frac{R}{R^\nu} \frac{R^\nu}{R} \frac{r}{r^\nu}\right) dr, \tag{2.77}$$

and substituting with Equations (2.69) to (2.72) and (2.76):

$$\begin{aligned} I_{\text{top}}^{Q_{\text{top}}} &= \underbrace{\left(A_1^2 k_1 \Delta_z \frac{R^{2\nu}}{R}\right)}_{\equiv I_0} \frac{\nu^2}{R} \int_0^R \underbrace{\frac{r^{2\nu}}{r^2}\frac{R^2}{R^{2\nu}}}_{\equiv 1/y^2} \exp\left(-\underbrace{\frac{k_2}{A_1\nu}\frac{R}{R^\nu}}_{\equiv a_0/\nu}\underbrace{\frac{r}{r^\nu}\frac{R^\nu}{R}}_{\equiv y}\right) dr \\ &= I_0 \frac{\nu^2}{R} \int_0^R y^{-2} \exp\left(-\frac{a_0}{\nu}y\right) \underbrace{\left(\frac{R}{1-\nu} y^{\frac{\nu}{1-\nu}} dy\right)}_{dr} \\ &= I_0 \frac{\nu^2}{R} \frac{R}{-(\nu-1)} \int_0^R y^{\frac{-2(1-\nu)+\nu}{1-\nu}} \exp\left(-\frac{a_0}{\nu}y\right) dy \\ &= -I_0 \frac{\nu^2}{\nu-1} \int_{y=0}^{y=1} y^{\frac{3\nu-2}{1-\nu}} \exp\left(-\frac{a_0}{\nu}y\right) dy. \end{aligned} \tag{2.78}$$

Classically integrating by parts with:

$$\int udv = uv - \int vdu \begin{cases} u = \exp\left(-\frac{a_0}{\nu}y\right) & dv = y^{\frac{3\nu-2}{1-\nu}} dy \\ du = -\frac{a_0}{\nu}\exp\left(-\frac{a_0}{\nu}y\right) dy & v = \left(\frac{1-\nu}{2\nu-1}\right) y^{\frac{2\nu-1}{1-\nu}} \end{cases} . \tag{2.79}$$

After some manipulation of terms, the integration produces:

$$I_{\text{top}}^{Q_{\text{top}}} = I_0 \frac{\nu^2}{2\nu-1} \left[\exp\left(-\frac{a_0}{\nu}\right) + \frac{a_0}{\nu} \int_0^1 y^{-\frac{2\nu-1}{\nu-1}} \exp\left(-\frac{a_0}{\nu}y\right) dy\right]. \tag{2.80}$$

It should be noted that this is precisely the form presented in [4]; however, the form for the current by effective voltage has a slightly different form as a result of the error in the capacitance which was not used in the form of the current by constant charge on the electrode.

### 2.A.8 Integrated Current with Constant Effective Voltage

The electric field in this case is defined in terms of constant $V_{\text{eff}}$ from Equation (2.63), which can be rewritten as:

$$V_{\text{eff}} = \frac{\nu^2 A_1 R^\nu}{\chi(\nu)} \Rightarrow A_1\nu = \frac{V_{\text{eff}}\chi(\nu)}{\nu R^\nu},$$

so that the electric field can be written:

$$E_1 = A_1 \nu r^{\nu-1} = \frac{V_{\text{eff}}\chi(\nu)}{\nu R^\nu} r^{\nu-1}. \tag{2.81}$$

Recalling the normalization from Equation (2.73), Equation (2.81) can be multiplied by $R/R$ to give:

$$\begin{aligned} E_1 &= \frac{V_{\text{eff}}\chi(\nu)}{\nu R^{\nu}} r^{\nu-1}\frac{R}{R} = \frac{V_{\text{eff}}}{R}\frac{\chi(\nu)}{\nu}\frac{r^{\nu-1}}{R^{\nu}/R} \\ &= \frac{V_{\text{eff}}}{R}\frac{\chi(\nu)}{\nu}\frac{r^{-(1-\nu)}}{R^{-(1-\nu)}} = \frac{V_{\text{eff}}}{R}\frac{\chi(\nu)}{\nu}\left(\underbrace{\frac{r^{1-\nu}}{R^{1-\nu}}}_{\equiv y}\right)^{-1} \\ &= \frac{V_{\text{eff}}}{R}\frac{\chi(\nu)}{\nu}y^{-1}. \end{aligned} \tag{2.82}$$

Using two additional definitions for constants:

$$I_1 = \Delta_z R k_1 \left(\frac{V_{\text{eff}}}{R}\right)^2, \tag{2.83}$$

$$b_0 = \frac{k_2}{V_{\text{eff}}/R}, \tag{2.84}$$

the FN current density from Equation (2.64) can be integrated again using the substitutions from Equation (2.82) and Equation (2.76) for the differential:

$$\begin{aligned} I_{\text{top}}^{V_{\text{eff}}} &= k_1 \int_{-\Delta_z/2}^{\Delta_z/2}\int_0^R E_1^2 \exp\left(-\frac{k_2}{E_1}\right) dr dz \\ &= k_1\Delta_z \int_{y=0}^{y=1} \left(\frac{V_{\text{eff}}}{R}\frac{\chi(\nu)}{\nu}y^{-1}\right)^2 \exp\left(-\frac{k_2}{\frac{V_{\text{eff}}}{R}\frac{\chi(\nu)}{\nu}y^{-1}}\right)\frac{R}{1-\nu}y^{\frac{\nu}{1-\nu}}dy \\ &= \underbrace{\Delta_z R k_1\left(\frac{V_{\text{eff}}}{R}\right)^2}_{\equiv I_1}\frac{\chi^2(\nu)}{\nu^2(1-\nu)}\int_0^R y^{\frac{\nu}{1-\nu}-2}\exp\left(-\underbrace{\frac{k_2}{V_{\text{eff}}/R}}_{\equiv b_0}\frac{\nu}{\chi(\nu)}y\right)dy \\ &= I_1\frac{\chi^2(\nu)}{\nu^2(-[\nu-1])}\int_0^R y^{\frac{\nu}{1-\nu}-\frac{2-2\nu}{1-\nu}}\exp\left(-b_0\frac{\nu}{\chi(\nu)}y\right)dy \\ &= -I_1\frac{\chi^2(\nu)}{\nu^2(\nu-1)}\int_0^R y^{\frac{3\nu-2}{1-\nu}}\exp\left(-b_0\frac{\nu}{\chi(\nu)}y\right)dy. \end{aligned} \tag{2.85}$$

Again, classical integration by parts as in Equation (2.79):

$$\begin{aligned} u &= \exp\left(-\frac{b_0\nu}{\chi(\nu)}y\right), & dv &= y^{\frac{3\nu-2}{1-\nu}}dy, \\ du &= -\frac{b_0\nu}{\chi(\nu)}\exp\left(\frac{b_0\nu}{\chi(\nu)}y\right)dy, & v &= \left(\frac{1-\nu}{2\nu-1}\right)y^{\frac{2\nu-1}{1-\nu}}, \end{aligned} \tag{2.86}$$

and with some manipulation of terms, integration gives:

$$I_{\text{top}}^{V_{\text{eff}}} = I_1 \frac{\chi^2(\nu)}{\nu^2(2\nu-1)} \left[ \exp\left(-\frac{b_0\nu}{\chi(\nu)}\right) + \frac{b_0\nu}{\chi(\nu)} \int_0^1 y^{-\frac{2\nu-1}{\nu-1}} \exp\left(-\frac{b_0\nu}{\chi(\nu)} y\right) dy \right]. \quad (2.87)$$

Again, it must be stressed that this form differs from that presented in [4] as a result of an error in the capacitance calculation, which shows in both Equation (2.87) and the definition of $\chi(\nu)$ in Equation (2.62).

## 2.B Diffusion Model

The theory presented herein will formulate a basic first-principles assessment of diffusive transport of a fixed-flux outgassing species with constant flux from a surface, with the possibility of further outgassing from electron bombardment, and a single loss term in the form of ionization of the outgassing species. Ionized species will be subject to electromagnetic forces that are of greater significance than diffusive processes in cases of interest, and so ions will be considered a loss in the frame of the diffusive species. The procedure consists of the following:

1. Assume a constant flux from a plane dielectric surface following insights and developments from [13, 24, 64, 65]. (Other boundary conditions should be set as appropriate, e.g. open boundary conditions at the semi-infinite boundary.)

2. Apply diffusivity forms from [64].

3. Find Fick's second law analog: the time derivative of the density is the negative of the gradient of the particle flux rate minus any losses and plus any gains. This development will not consider gains, but will consider ionization losses.

4. Find Fick's first law analog for a gaseous discharge by looking at the concentration-basis flux relations for a 1-D plane in a 2-D volume [63].

5. Add relations for outgassing by electron bombardment following [70].

The diffusion coefficient from Item 2 is spatially dependent due to the variation in pressure (and possibly gas constituents depending on model; this study assumes diffusivity based on binary species) and therefore will generally require a gradient treatment that will be addressed numerically, but theoretical treatment will neglect this for tractability. The sink term used herein is also spatially dependent but will be averaged out in theoretical treatment. Item 3 is formulated by looking at the particle continuity through a volume. Item 4 is technically just applied following classical treatment, e.g. [63], with the added assumption that diffusivity is spatially dependent. Finally, Item 5 is just a straightforward application of emission models following bombardment. The numerical treatment takes a two-step approach that is not strictly equivalent to the typical reaction-diffusion model discussed here since densities are not updated synchronously; furthermore, the approach of using a loss rate dependent on distribution-average quantities might have difficulty modeling large local gradients, and will presume a Maxwellian distribution that is known

to not hold generally. In principle, a basic assumption for this treatment is that the gradients are sufficiently resolved over a grid size, and care will simply be taken to ensure that this condition is true for operating conditions of interest such that arguments for linearity may be applied.

### 2.B.1 Derivation of a 1-D Diffusion Relation

Returning to Item 3, and restricting this treatment to 1-D diffusion for now, Fick's second law for the typical configuration and physics processes considered here is derived from particle continuity through a volume, in this case taken as $A{\cdot}\delta y$, with the area-normal conformal with the $y$ axis as per Figure 4.20:

$$\delta n_{\text{diff}} \left[\frac{\text{particles}}{\text{m}^3}\right] = \left( \begin{array}{c} \dfrac{\left[j_{\text{diff}}\left(y\right) - j_{\text{diff}}\left(y+\delta y\right)\right]\left[\dfrac{\text{particles}}{\text{m}^2\cdot\text{s}}\right]\cdot\delta t\,[\text{s}]\cdot A\,[\text{m}^2]}{A\,[\text{m}^2]\,\delta y\,[\text{m}]} \\ -K_L\left[\dfrac{\text{m}^3}{\text{s}}\right] n_e\left[\dfrac{\text{electrons}}{\text{m}^3}\right] n_{\text{diff}}\left[\dfrac{\text{particles}}{\text{m}^3}\right]\delta t\,[\text{s}] \end{array} \right), \tag{2.88}$$

where $n_{\text{diff}}$ is the number density of diffusing species, $j_{\text{diff}}$ is the flux across an areal region, $A$, in a volume with with thickness $\delta y$, $K_L$ is the reaction rate constant for the loss term, assuming reaction of the diffusing species with electrons only, hence $n_e$. The change in flux across the volume faces is:

$$j_{\text{diff}}\left(y+\delta y\right) = j_{\text{diff}}\left(y\right) + \frac{\partial j_{\text{diff}}}{\partial y}\delta y. \tag{2.89}$$

The reaction rate constant for the loss term is taken as the distribution-averaged reaction rate constant following classical treatment, e.g. [34], limiting to ionization:

$$K_L = K_{iz} = \left\langle \sigma_{iz} v \right\rangle. \tag{2.90}$$

Particle continuity from Equation (2.88) then reduces to:

$$\delta n_{\text{diff}} = \frac{\left[-\dfrac{\partial j_{\text{diff}}}{\partial y}\delta y\right]\cdot\delta t\cdot A}{A\delta y} - \left\langle \sigma_{iz} v \right\rangle n_e n_{\text{diff}}\delta t. \tag{2.91}$$

Moving $\delta t$ and taking limits of $\delta$ quantities to differential quantities, Equation (2.91) becomes the form of Fick's second law for use herein:

$$\frac{\partial n_{\text{diff}}}{\partial t} = -\frac{\partial j_{\text{diff}}}{\partial y} - n_e n_{\text{diff}}\left\langle \sigma_{iz} v \right\rangle. \tag{2.92}$$

In the event that Fick's first law is written for homogeneous, isotropic diffusion such that:

$$j_{\text{diff}} = -\mathscr{D}_{\text{diff}}\frac{dn}{dy}, \tag{2.93}$$

so that Equation (2.92) becomes:

$$\frac{\partial n_{\text{diff}}}{\partial t} = \mathscr{D}_{\text{diff}}\frac{\partial^2 n_{\text{diff}}}{\partial y^2} - n_e n_{\text{diff}}\left\langle \sigma_{iz} v \right\rangle. \tag{2.94}$$

Equation (2.94) is the so-called Malthus reaction-diffusion equation, accounting for a single loss term via ionization, no gain term (although the boundary conditions can introduce a constant flux of $n$), and, again, homogeneous, isotropic diffusion conditions. This form is most valid at higher background pressures where the introduction of additional gaseous species via outgassing does not significantly alter the local diffusion constant. At low pressures, Equation (2.94) will likely be a problem vis-à-vis Equation (2.93), typically derived from free-energy formulations and, again, tacitly assuming homogeneity. The diffusivity is evaluated using [64], Equation 16.3-1, as noted in Section 2.4, c.f. Equation (2.27), although Lennard-Jones might be more accurate if parameters are available as per [64]. Figure 2.17 shows the diffusion constant normalized to the diffusivity at atmospheric pressure, i.e. 760 Torr. From 100 Torr and up, the gradient is shallower, dropping by less than a decade from 100 Torr to atmosphere, while the gradient climbs relatively quickly at lower pressures, and becomes exacerbated when moving from vacuum to regions suddenly populated by (relatively) high-density outgassed diffusive species.

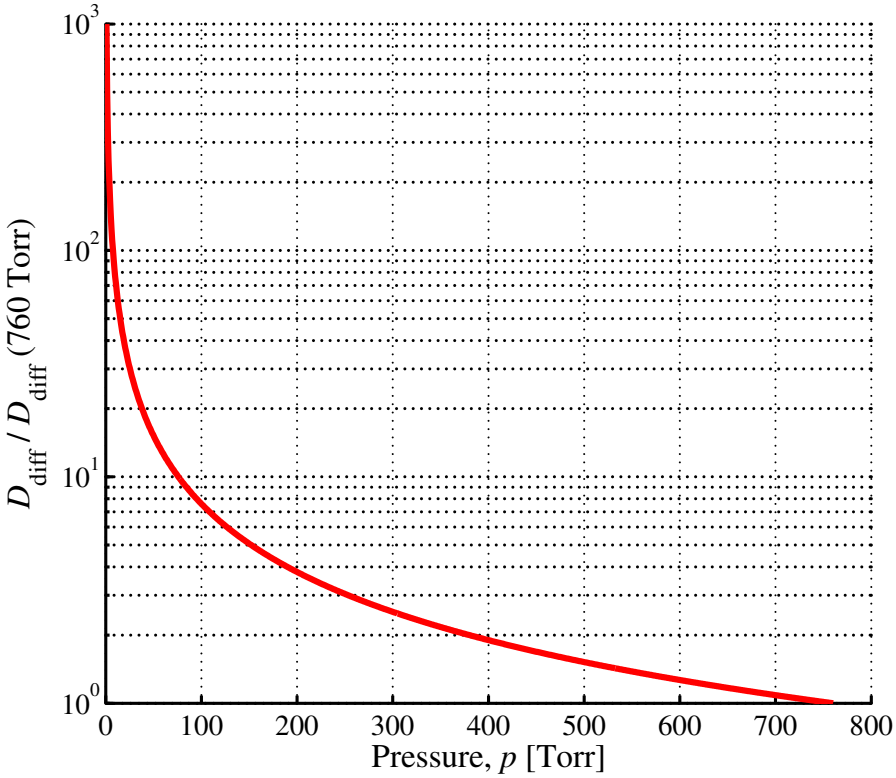


Figure 2.17: Diffusivity vs. pressure, normalized to diffusivity at atmospheric pressure. This study is particularly interested in vacuum to lower pressures, where the gradient is much steeper. From vacuum to 100 Torr and up, the diffusivity reduces by roughly two orders of magnitude. From 100 Torr and up, the diffusivity decreases by less than an order of magnitude. Arbitrarily using values for argon diffusing through argon.

### 2.B.2 Crank-Nicolson in 1-D

A common technique used to obtain a numerical solution to parabolic PDE's is to mix explicit and implicit discretization, covered extensively in standard texts such as [47, 71]:

$$\frac{\mathbf{n}_{\text{diff}}^{i+1} - \mathbf{n}_{\text{diff}}^{i}}{k} = \mathscr{D}_{\text{diff}} \sum_{\beta} D_{+\beta} D_{-\beta} \left( \gamma \mathbf{n}_{\text{diff}}^{i+1} + [1-\gamma]\, \mathbf{n}_{\text{diff}}^{i} \right) - L, \tag{2.95}$$

where superscripted $i$'s are time indices; $k$ is the time-step; the summation is done over all directions, $\beta$, in an orthogonal coordinate system; $D_{+\beta}$ is the forward finite-difference scheme in the direction $\beta$; and $D_{-\beta}$ is the backward finite-difference scheme in the direction $\beta$. Using $\gamma = 1/2$ in Equation (2.95) gives the so-called "Crank-Nicolson" (CN) scheme:

$$\left( \mathbf{I} - \mathscr{D}_{\text{diff}} \frac{k}{2} \sum_{\beta} D_{+\beta} D_{-\beta} \right) \mathbf{n}_{\text{diff}}^{i+1} = \left( \mathbf{I} + \mathscr{D}_{\text{diff}} \frac{k}{2} \sum_{\beta} D_{+\beta} D_{-\beta} \right) \mathbf{n}_{\text{diff}}^{i} - kL, \tag{2.96}$$

where $\mathbf{I}$ is the identity matrix. The loss term for ionization can be written:

$$L \equiv n_e\left(\vec{r}, t\right) \mathbf{n}_{\text{diff}} \sigma_{iz}\left(v_{\text{rel}}\right) v_{\text{rel}} \approx n_e\left(\vec{r}, t\right) \left( \frac{\mathbf{n}_{\text{diff}}^{i+1} + \mathbf{n}_{\text{diff}}^{i}}{2} \right) \sigma_{iz}\left(v_{\text{rel}}\right) v_{\text{rel}}, \tag{2.97}$$

where $\mathbf{n}_{\text{diff}}$ was written as a time average, $n_e$ is the electron density, $\sigma_{iz}$ is the ionization cross section, and $v_{\text{rel}}$ is the relative velocity between projectile and target particles. This study assumes $v_{\text{rel}} = v_e$ in common practice for cases where electron velocities are much larger than ion or neutral background gas velocities, i.e. $v_e >> v_i > v_{\text{bg}}$.

$D_{+\beta} D_{-\beta}$ in Equation (2.96) can be written more explicitly with the forward/backward shift operators, $S_{\pm\beta}$ in the direction $\beta$, e.g. $S_{+x} u \equiv u_{j+1,x} - u_{j,x}$. Equation (2.96), plugging in Equation (2.97) and rearranging, is then written:

$$\begin{pmatrix} \mathbf{I} + \frac{k n_e \sigma_{iz} v_e}{2} + \\ -\mathscr{D}_{\text{diff}} \frac{k}{2} \sum_{\beta} \frac{S_{+\beta} - 2\mathbf{I} + S_{-\beta}}{h_\beta^2} \end{pmatrix} \mathbf{n}_{\text{diff}}^{i+1} = \begin{pmatrix} \mathbf{I} - \frac{k n_e \sigma_{iz} v_e}{2} + \\ \mathscr{D}_{\text{diff}} \frac{k}{2} \sum_{\beta} \frac{S_{+\beta} - 2\mathbf{I} + S_{-\beta}}{h_\beta^2} \end{pmatrix} \mathbf{n}_{\text{diff}}^{i}. \tag{2.98}$$

where $h_\beta$ is the spatial discretization in the direction $\beta$. Implicit and explicit matrix operators can be defined to write Equation (2.98) in the following manner:

$$\mathbf{A}_{\text{impl}} \mathbf{n}_{\text{diff}}^{i+1} = \mathbf{B}_{\text{expl}} \mathbf{n}_{\text{diff}}^{i} \tag{2.99}$$

$\mathbf{A}_{\text{impl}}$ and $\mathbf{B}_{\text{expl}}$ are defined to denote the implicit and explicit matrix operators. For further notional simplicity define $\lambda_\beta \equiv k/(2h_\beta^2)$ in the direction $\beta$, and $\kappa_{iz} \equiv k n_e \sigma_{iz} v_e/2$. Writing Equation (2.96) in the $y$ direction only gives, for the implicit matrix:

$$\mathbf{A}_{\text{impl},y} \equiv \begin{bmatrix} 1 & & & & \\ \lambda_y & (1 + \kappa_{iz} + 2\lambda_y) & -\lambda_y & & \\ & \ddots & \ddots & \ddots & \\ & & \lambda_y & (1 + \kappa_{iz} + 2\lambda_y) & -\lambda_y \\ & & & & 1 \end{bmatrix}, \tag{2.100}$$

and the explicit matrix is:

$$\mathbf{B}_{\text{expl},y} \equiv \begin{bmatrix} 1 & & & & \\ -\lambda_y & (1-\kappa_{iz}-2\lambda_y) & \lambda_y & & \\ & \ddots & \ddots & \ddots & \\ & & -\lambda_y & (1-\kappa_{iz}-2\lambda_y) & \lambda_y \\ & & & & 1 \end{bmatrix}, \tag{2.101}$$

and the density vectors at current and forward time, respectively are:

$$\mathbf{n}^i = \begin{bmatrix} n_0^i \\ n_1^i \\ \vdots \\ n_{N-1}^i \\ n_N^i = n_B \end{bmatrix}; \; \mathbf{n}^{i+1} = \begin{bmatrix} n_0^{i+1} = n_0^i + \dfrac{\Gamma_{y0}}{\mathscr{D}_{\text{diff}}} \\ n_1^{i+1} \\ \vdots \\ n_{N-1}^{i+1} \\ n_N^{i+1} = n_B \end{bmatrix}. \tag{2.102}$$

Note $\mathbf{A}_{\text{impl},y}$ and $\mathbf{B}_{\text{impl},y}$ are written for Dirichlet conditions at the boundary, and $n_B$ is the boundary value at the semi-infinite boundary , and the dielectric-boundary value, $n_0$, is set at the forward time to be the previous boundary value with the addition of the flux, $\Gamma$, from the boundary, assumed constant for this study. Inverting the implicit matrix gives the solution at the next time step, i.e. Equation (2.29).

### 2.B.3 Extending to 2-D with ADI

The extension to 2-D is done in typical manner following the standard treatment [47] by applying a Crank-Nicolson implicit operator in the spatial finite-difference scheme, expanding, and ignoring terms of higher order in $k$:

$$\begin{aligned} \mathbf{I} \pm \frac{k}{2}\sum_\beta D_{+\beta}D_{-\beta} &= \prod_\beta \left(\mathbf{I} + \frac{k}{2}D_{+\beta}D_{-\beta}\right) + \frac{k^2}{4}\prod_{\substack{\beta,\gamma \\ \beta\neq\gamma}} D_{+\beta}D_{-\beta}D_{+\gamma}D_{-\gamma} + \cdots \\ &\approx \prod_\beta \left(\mathbf{I} + \frac{k}{2}D_{+\beta}D_{-\beta}\right). \end{aligned} \tag{2.103}$$

Neglecting higher orders of $k$ maintains the same order of truncation, but allows the matrix operation for each direction to be separated and applied individually in tri-diagonal form, similar to Equations (2.100) and (2.101):

$$\prod_\beta \mathbf{A}_{\text{impl},\beta} n_{\text{diff}}^{i+1} = \prod_\beta \mathbf{B}_{\text{expl},\beta} n_{\text{diff}}^{i} \tag{2.104}$$

Furthermore, it is common to write the scheme with the operators explicitly separated, operating on meta-vectors over $\beta$ directions:

$$\left\{\begin{array}{rcl} \left(I-\frac{k}{2}D_{+2}D_{-2}\right)u^{n+\frac{1}{\beta}} &=& \left(I+\frac{k}{2}D_{+1}D_{-1}\right)u^{n} \\ \left(I-\frac{k}{2}D_{+3}D_{-3}\right)u^{n+\frac{2}{\beta}} &=& \left(I+\frac{k}{2}D_{+2}D_{-2}\right)u^{n+\frac{1}{\beta}} \\ & \vdots & \\ \left(I-\frac{k}{2}D_{+\beta}D_{-\beta}\right)u^{n+\frac{\beta-1}{\beta}} &=& \left(I+\frac{k}{2}D_{+[\beta-1]}D_{-[\beta-1]}\right)u^{n+\frac{\beta-2}{\beta}} \\ \left(I-\frac{k}{2}D_{+1}D_{-1}\right)u^{n+1} &=& \left(I+\frac{k}{2}D_{+\beta}D_{-\beta}\right)u^{n+\frac{\beta-1}{\beta}} \end{array}\right\}. \tag{2.105}$$

This is the general form of the so-called alternating directions implicit (ADI) scheme, which is an unconditionally stable method, amounting to a Crank-Nicolson method in multiple dimensions consisting of a half explicit operator and half implicit operator on the solution.

### 2.B.4 Extending to Spatially-Varying Diffusivity

Finally, the particular form of ADI used for this implementation is attributed to Dendy [66]:

$$\begin{aligned} \left(I-\frac{k}{2}A_x^n\right)\left(n_{\text{diff}}\right)_{i,j}^{(n+1)^*} &= kf_{i,j}^n + kA_y^n\left(n_{\text{diff}}\right)_{i,j}^n + \left(I+\frac{k}{2}A_x^n\right)\left(n_{\text{diff}}\right)_{i,j}^n, \\ \left(I-\frac{k}{2}A_y^n\right)\left(n_{\text{diff}}\right)_{i,j}^{n+1} &= \left(n_{\text{diff}}\right)_{i,j}^{(n+1)^*} - \frac{k}{2}A_y^n\left(n_{\text{diff}}\right)_{i,j}^n, \end{aligned} \tag{2.106}$$

where $(n+1)^*$ is a meta-vector. For this study, the forcing function, $f$ (relating to the ionization losses, in this case), is shown in Equation (2.106) for completion, but will be set to zero and treated via a separate MCC module for this study; this technique could pose problems if the diffusion mechanism is too quick such that the rate of diffusion and the rate of reaction become highly disparate in a single time step. This will not be a problem for the modest rates expected in this study, but in cases where this does become an issue, typical techniques such as reducing the time step or spatial scales can mitigate some of these concerns at the expense of computational efficiency. The method in Equation (2.106) accounts for the variable diffusivity, i.e. variable coefficients, by applying a weighted backward difference in time and an average in space in the parameters for the functional form of diffusivity. Defining directional operators:

$$\begin{aligned} A_x^n &= D_x^+\left(\bar{\mathscr{D}}_{\text{diff}}^x\left(\tilde{n}_{\text{diff},i,j}^n\right)D_x^-\cdot\right), \\ A_y^n &= D_y^+\left(\bar{\mathscr{D}}_{\text{diff}}^y\left(\tilde{n}_{\text{diff},i,j}^n\right)D_y^-\cdot\right), \end{aligned} \tag{2.107}$$

where:

$$\left(\tilde{n}_{\text{diff}}\right)_{i,j}^n = \frac{3}{2}\left(n_{\text{diff}}\right)_{i,j}^n - \frac{1}{2}\left(n_{\text{diff}}\right)_{i,j}^{n-1}, \tag{2.108}$$

is a weighted backward difference in time (via the index $n$) at each node point (via the indices $[i, j]$), accounting for the temporal variability in the coefficients. Spatial variability is treated via an average of the pressure in each direction using a one-step method, which is then used as a parameter for the diffusivity:

$$\begin{aligned} \bar{\mathscr{D}}^{x}_{\text{diff}}\left(n_{\text{diff}}\right) &= \mathscr{D}_{\text{diff}}\left(\frac{1}{2}\left[\left(n_{\text{diff}}\right)_{i,j} + \left(n_{\text{diff}}\right)_{i-1,j}\right]\right) \\ \bar{\mathscr{D}}^{y}_{\text{diff}}\left(n_{\text{diff}}\right) &= \mathscr{D}_{\text{diff}}\left(\frac{1}{2}\left[\left(n_{\text{diff}}\right)_{i,j} + \left(n_{\text{diff}}\right)_{i,j-1}\right]\right). \end{aligned} \tag{2.109}$$

Noting:

$$\left(n_{\text{diff}}\right)^{n}_{i,j} = n_{\text{diff}}\left(ih, jh, nk\right), \tag{2.110}$$

the first step is done using the differential equation itself in standard practice:

$$\begin{aligned} \left(n_{\text{diff}}\right)^{1}_{i,j} = \left(n_{\text{diff}}\right)^{0}_{i,j} + k \left[\begin{array}{c} D^{+}_{x}\left(\bar{\mathscr{D}}^{x}_{\text{diff}}\left[\left(n_{\text{diff}}\right)^{0}_{i,j}\right] D^{-}_{x}\left[n_{\text{diff}}\right]^{0}_{i,j}\right) + \\ D^{+}_{y}\left(\bar{\mathscr{D}}^{y}_{\text{diff}}\left[\left(n_{\text{diff}}\right)^{0}_{i,j}\right] D^{-}_{y}\left[n_{\text{diff}}\right]^{0}_{i,j}\right) \end{array}\right] + \\ kf\left(ih, jh, t = 0, \left[n_{\text{diff}}\right]^{0}_{i,j}, D^{0}_{x}\left[n_{\text{diff}}\right]^{0}_{i,j}, D^{0}_{y}\left[n_{\text{diff}}\right]^{0}_{i,j}\right). \end{aligned} \tag{2.111}$$

# Chapter 3

# Vacuum and Ultra-low Pressure Breakdown

This chapter focuses on the treatment of discharges in vacuum through ultra-low pressure (VULP) of a background gas up to a few hundred mTorr with weak collisionality, leading to a discharge dominated by single-surface multipactor with minor space-charge effects.

## 3.1 Ideal Multipactor Breakdown

The early theoretical development in this chapter regarding ideal multipactor breakdown in VULP focuses on single-particle dynamics; therefore, the schematic of Figure 1.3 for a dielectric-loaded diode is most relevant to the following treatment and is reproduced in Figure 3.1b using the geometry for this chapter. A more general schematic is provided in Figure 3.1a to accommodate additional discussion in Section 3.1.1, particularly with respect to Equation (3.13) describing a source-sink treatment of the anode current.

### 3.1.1 VULP Theoretical Gain

The process of VULP breakdown is largely dominated by the single-surface multipactor for the geometry of Figure 3.1. Typically, multipactor is driven by an external RF source [9], but the underlying phenomena, particularly the physics described in Section 1.3.2 and Section 2.3, are relevant to VULP DC discharges. The extension from RF to DC can be understood as the limit at which a particle undergoes unidirectional transit and does not experience an applied retarding/reversing potential during its excursion in an RF system; in terms of the parameters relevant to this work, the equivalent RF system would have a characteristics length, $L = v_{\text{avg}} \cdot (T_{\text{RF}}/2)$, where $v_{\text{avg}}$ is the average particle speed, and $T_{\text{RF}}$ is the RF period.

This section will develop the expected theoretical gain by distilling a number of nonlinearities near the dielectric surface to simpler single-particle physics, starting with the electrostatic forces on a particle, separating into component directions perpendicular and parallel to the dielectric surface for convenience. Assuming static fields, neglecting space charge and magnetic fields, and treating collisionality as negligible, the forces on a particle

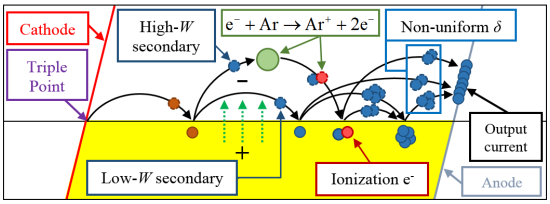


(a) Generalized multipactor schematic for source-sink formulation.

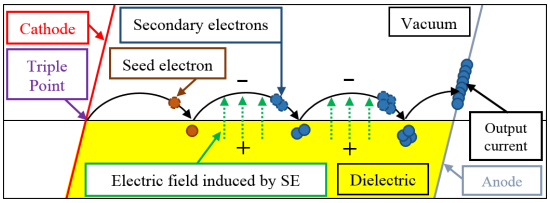


(b) Reproduction of Figure 1.3 for simplified source-output formulation.

Figure 3.1: Generalized single-surface multipactor schematic for VULP breakdown, with reproduction of Figure 1.3 for convenience. The more general schematic of (a) suggests a source-sink perspective would be more useful in characterizing the discharge behavior and output current. Considerations for ionization electrons, the energy distribution of emitted secondaries, and the variation in $\delta$ per impact are explicitly shown. In the case of a constant-waveform (CW) current with uniform $\delta$ for all impacts, the simplified schematic of (b) is sufficient to characterize the output-current relation.

near the dielectric surface subjected to an applied DC field for the schematic of Figure 3.1 are:

$$\vec{F} = m\vec{a} = q\vec{E} = q\left(\vec{E}_{\perp} + \vec{E}_{\parallel}\right). \tag{3.1}$$

The lifetime of the particle, $t_{\text{life}}$, is found from the perpendicular force:

$$F_{\perp} = qE_{\perp} = m\frac{dv_{\perp}}{dt} \Rightarrow \int_{v_{\perp 0}}^{-v_{\perp 0}} dv_{\perp} = \int_{0}^{t_{\text{life}}} \frac{q}{m} E_{\perp} dt \Rightarrow v_{\perp 0} = -\frac{1}{2}\int_{0}^{t_{\text{life}}} \frac{q}{m} E_{\perp} dt,$$

where the limits on perpendicular velocity are equal and opposite, assuming conservative forces only with, again, negligible collisional effects. Also, assuming quasistatic conditions (slowly varying perpendicular fields):

$$t_{\text{life}} = -\frac{2mv_{\perp 0}}{qE_{\perp}}. \tag{3.2}$$

The force parallel to the dielectric surface provides the energy gain in vacuum:

$$\int_{v_{\parallel 0}}^{v_{\parallel f}} dv_{\parallel} = \int_{0}^{t_{\text{life}}} \frac{q}{m} E_{\parallel} dt,$$

where the assumption of quasistatic fields, again, simplifies the particle energy gain as:

$$v_{\parallel f} - v_{\parallel 0} = \frac{q}{m} E_{\parallel} t_{\text{life}}. \tag{3.3}$$

Combining the quasistatic solutions above gives:

$$\begin{aligned} v_{\parallel f} - v_{\parallel 0} &= \frac{q}{m} E_{\parallel} \left( -\frac{2m}{q} \frac{v_{\perp 0}}{E_{\perp}} \right) = -2v_{\perp 0} \frac{E_{\parallel}}{E_{\perp}} \\ \Rightarrow v_{\parallel f} &= v_{\parallel 0} - 2v_{\perp 0} \frac{E_{\parallel}}{E_{\perp}}, \end{aligned} \tag{3.4}$$

for which the impact energy is:

$$\begin{aligned} W_{\text{imp}} &= \frac{1}{2} m \left( v_{\parallel f}^2 + v_{\perp f}^2 \right) = \frac{1}{2} m \left[ \left( v_{\parallel 0} - 2v_{\perp 0} \frac{E_{\parallel}}{E_{\perp}} \right)^2 + v_{\perp 0}^2 \right] \\ &= \frac{1}{2} m \left[ \left( v_{\parallel 0} - \frac{2v_{\perp 0}}{\tan\left(\chi_E\right)} \right)^2 + v_{\perp 0}^2 \right], \end{aligned} \tag{3.5}$$

and the impact angle, *with respect to the surface normal*, is:

$$\theta_{\text{imp}} = \tan^{-1} \left( \frac{v_{\parallel f}}{v_{\perp f}} \right). \tag{3.6}$$

The impact energy and angle ultimately determine the number of secondaries emitted per impact, as discussed in Section 2.3. Equation (3.5) states that the impact energy is related only to the initial energy of *emitted* secondaries (mostly a material property unless secondaries are scattered or reflected) and the surface-field angle. It must be stressed that the impact energy is related to the *ratio* of the surface-field components (i.e. the surface-field angle relative to the surface tangent), suggesting that the influence of parallel and perpendicular fields on particle dynamics are coupled and their individual magnitudes are insufficient to characterize VULP breakdown behavior.

Returning to Equation (3.5), additional insight can be gained by assuming initial emission with velocity only in the perpendicular direction, i.e. $v_{\perp 0} = v_0$ so that lifetime is maximized:

$$W_{\text{imp}}^{\text{max-life}} = \frac{1}{2} m \left[ \left( 0 - \frac{2v_0}{\tan\left(\chi_E\right)} \right)^2 + v_0^2 \right] = W_0 \frac{4 + \tan^2\left(\chi_E\right)}{\tan^2\left(\chi_E\right)}, \tag{3.7}$$

where $W_0 = \frac{1}{2} m v_0^2$ is the initial energy of emitted secondaries. In the interest of developing a sense for the distribution behavior, representative metrics for the emitted distribution are chosen as characteristic in an average or most-probable sense. The choice of normal emission is further justifiable with this consideration, since the emission-angle spectrum is peaked normal to the surface in a cosine distribution, effectively condensing emission characteristics in the sense of most-probable characteristics. A typical value for $W_0$ in Equation (3.7) can be taken to be the most-probable energy of the emitted distribution; for PTFE, $W_{\text{emit}}^{\text{mode}} = 1.85\,\text{eV}$ [57].

The impact energy of Equation (3.7) can now be plotted as a function of the electric-field angle, $\chi_E$, as in Figure 3.2. $\chi_E$ in Figure 3.2 ranges from 0° to 90° with respect to the $-x$ direction for the typical configuration as in the schematic of Figure 3.1, looking only at downstream-oriented forces that return electrons to the surface; the full domain of $\chi_E$ is, of

course, 0° to 360°. It must be stressed that $\chi_E$ is the electric-field angle at the surface of the dielectric, it is *not* the dielectric angle with respect to the electrode, $\alpha$, nor is it the impact angle with respect to the dielectric normal, $\theta_{\text{imp}}$; furthermore, $\chi_E$ is *not* generally related to $\alpha$ and $\theta_{\text{imp}}$ past the initial conditions. The effect of scattered and reflected particles is neglected. Figure 3.2 shows Equation (3.7) plotted with $W_1$ and $W_2$ for PTFE [2, 3, 57] from normal through grazing incidence (regions noted as "$\delta = 1$"), denoting field-angle regions in which multipactor may or may not occur depending on downstream surface conditions coupled with characteristics of the impacting distribution. The region noted as the "multiplicative region" is bounded by the $\delta = 1$ regions, and illustrates impact energies for which multipactor conditions are met for all impacts. "Absorption regions" are noted for cases when impact energies are too low or too high to generate net secondaries. Below $W_1$, multiplicative growth is not expected and steady-state dark-current can develop with sufficient time. A saturated state with impact energies averaging $W_2$ is not observed since surface conditions do not support lifetimes and energy gains sufficient to push particles to $W_2$ at the discharge onset. For an electron impacting the dielectric at normal incidence, i.e. $\theta_{\text{imp}} = 0$ *with respect to the surface normal*, $W_1(\theta_{\text{imp}} = 0) = 38.45\,\text{eV}$ and the field angle necessary for the model electrons to impact with $W_1$ is $\chi_E = \chi_1(\theta_{\text{imp}} = 0) = 24.20°$. For an electron impacting the dielectric at grazing incidence, $W_1(\theta_{\text{imp}} = \pi/2) = 6.24\,\text{eV}$ and $\chi_1(\theta_{\text{imp}} = \pi/2) = 24.88°$. High-energy analogs for normal and grazing incidence are $W_2(\theta_{\text{imp}} = 0) = 2165.2\,\text{eV}$ and $W_2(\theta_{\text{imp}} = \pi/2) = 5007.7\,\text{eV}$, respectively; the required $\chi_E$ can be read from Figure 3.2a to be $< 5°$.

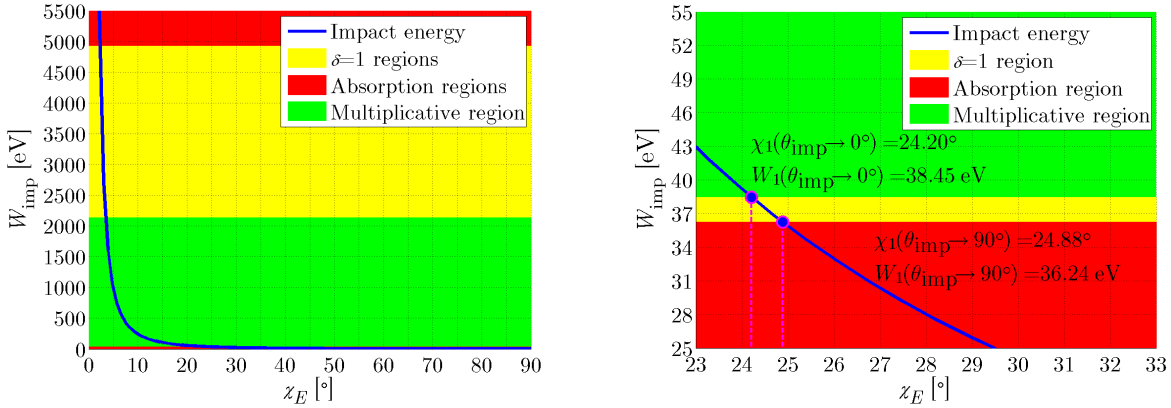


(a) Showing $W_1$ and $W_2$ regions.

(b) Enlarged $W_1$ region for illustration.

Figure 3.2: Impact energy, $W_{\text{imp}}$, vs. electric-field angle, $\chi_E$, for VULP breakdown. Model secondary-emission electrons are at $\theta_{\text{emit}}^{\text{mode}} = \pi/2$ *with respect to the surface tangent*, with $W_{\text{emit}}^{\text{mode}} = W_0 = 1.85\,\text{eV}$. $\chi_E = [0°, 90°]$ for this plot, overlaid on regions demarcated by $W_1$ and $W_2$. The intersection of $W_{\text{imp}}$ with $W_1$ and $W_2$ for grazing and normal incidence indicate crossover points into various operating regions noted in the legend and further delineated in the text. (b) is provided to clarify the small $W_1$ region in (a) since it is most relevant to phenomena discussed in this chapter.

Equation (3.5) suggests a strong dielectric-material dependence on VULP breakdown, since the emission energy of secondaries and initial surface-field angle are material-dependent. In principle, VULP can therefore be predicted by the solution of the gen-

eralized Poisson equation with the dielectric boundary conditions ultimately dictating surface-field conditions:

$$\begin{aligned}
&\nabla^2\phi\left(x,y\right)+\underbrace{\frac{\left(\nabla\cdot\varepsilon\left[x,y\right]\right)\nabla\phi\left(x,y\right)}{\varepsilon\left(x,y\right)}}_{\rho_{s,\text{bound}}}=-\frac{\rho_{s,\text{free}}\left(x,y\right)}{\varepsilon\left(x,y\right)}-\frac{\rho_{\text{vol}}\left(x,y\right)}{\varepsilon\left(x,y\right)},\\
&\lim_{y\to0}\left(D^{\perp}_{y>0}-D^{\perp}_{y<0}\right)=\rho_{s,\text{free}},\\
&\lim_{y\to0}\left(D^{\parallel}_{y>0}-D^{\parallel}_{y<0}\right)=P^{\parallel}_{y>0}-P^{\parallel}_{y<0},
\end{aligned}\tag{3.8}$$

where this study is concerned with linear dielectrics with polarization, $\vec{P}=\varepsilon_0(\varepsilon_r-1)\vec{E}$, and the constitutive relation, $\vec{D}=\varepsilon\vec{E}$. The boundary condition for the field parallel to the surface then simplifies to the familiar form: $\lim_{y\to0}\left(\vec{E}^{\parallel}_{y>0}-\vec{E}^{\parallel}_{y<0}\right)=0$. Equation (3.8), of course, simplifies to the Laplace form in the absence of volume charge, $\rho_{\text{vol}}$, and free surface charge, $\rho_{s,\text{free}}$, prior to the discharge onset, although bound charge, $\rho_{s,\text{bound}}$, in the presence of applied potential still remains, manifesting as net charge at the boundaries of dielectric media by the usual dipole alignment. With such simplifications, Equation (3.8) can be solved easily with simple numerical relaxation techniques in steady-state conditions; XOOPIC can be readily employed for more complex, dynamic conditions, although the same error restrictions across angles as described in Section 2.2.2 apply.

Returning to Equation (3.1) assuming quasistatic fields, the perpendicular-field relation with initial conditions $v_\perp(t=0)=v_{\perp0}$ and $y(t=0)=y_0$ gives the displacement in $y$:

$$F_\perp=qE_\perp=m\frac{dv_\perp}{dt}\Rightarrow y(t)-y_0=\frac{qE_\perp}{2m}t^2+v_{\perp0}t,\tag{3.9}$$

and the parallel field with $v_\parallel(t=0)=v_{\parallel0}$ and $x(t=0)=x_0$ gives the range:

$$F_\parallel=qE_\parallel=m\frac{dv_\parallel}{dt}\Rightarrow x(t)-x_0=\frac{qE_\parallel}{2m}t^2+v_{\parallel0}t.\tag{3.10}$$

The usual configuration for this study sets $y_0=0$. Since the early-transient field conditions are similar over the whole surface, the total excursion, $x-x_0$, is uniform as measured from all downstream impact points *for the characteristic particle* through a particle lifetime at both the early transient and at steady state. $x-x_0$ is more useful expressed as the excursion over the particle lifetime, recalling $t_{\text{life}}$ from Equation (3.2):

$$x\left(t_{\text{life}}\right)-x_0=\frac{2mv_{\perp0}}{qE_\perp}\left(v_{\perp0}\frac{E_\parallel}{E_\perp}-v_{\parallel0}\right).\tag{3.11}$$

For the gains in this ideal example, particle populations are relatively low in the early discharge (typically less than a few hundred picoseconds for systems in this study); consequently, subsequent generations of particles in unsaturated regions will be influenced largely by the applied potential. The number of impacts during transit to the anode can therefore be calculated trivially with the background fields by:

$$\begin{aligned}
N_{\text{imp}}&=\frac{\text{dielectric surface length}}{\text{single-particle excursion length}}=\frac{D/\cos\left(\alpha\right)}{x\left(t_{\text{life}}\right)-x_0}\\
&=\frac{qE_\perp D}{2mv_{\perp0}\cos\left(\alpha\right)\left(v_{\perp0}\frac{E_\parallel}{E_\perp}-v_{\parallel0}\right)}.
\end{aligned}\tag{3.12}$$

Knowing the number of impacts allows for the calculation of the idealized theoretical gain for the initial discharge conditions. The electric-current gain must be quantified at this point, but since $\delta$ is a function of the impacting particle characteristics, not the impacting current, the development of electric-current gain starts from the development of the particle population across boundaries and should apply distribution metrics where appropriate. A general formulation of the output current at the anode as a summation of particle sources and sinks at the dielectric boundary is employed and detailed in Section 3.A with the aid of Figure 3.1a. Note particularly that this treatment is primarily valid for the initial discharge conditions, which saturate quickly as shown in Section 3.4.1. The working form for the anodic current used in this study is:

$$I_{\text{anode}} = \left[ \begin{array}{l} \overbrace{I_0}^{\substack{\text{source} \\ \text{via seed}}} + \overbrace{\sum_{1}^{N_{\text{imp}}} \delta_i \left(W_{\text{imp}}, \theta_{\text{imp}}\right) I_{i-1}}^{\substack{\text{source via secondaries, } I_m, \\ \text{traceable to seed}}} + \overbrace{\left( - \sum_{1}^{N_{\text{imp}}} \left(1 - f_{\text{SRP}}\right) I_{i-1} \right)}^{\substack{\text{sink via dielectric absorption, } I_a, \\ \text{traceable to seed}}} + \\ \underbrace{I_0^*}_{\substack{\text{source via} \\ \text{ionization}}} + \underbrace{\sum_{1}^{N_{\text{loci}}^*} \sum_{1}^{N_{\text{imp}}^*} \delta_i^* \left(W_{\text{imp}}, \theta_{\text{imp}}\right) I_{i-1}^*}_{\substack{\text{source via secondaries, } I_m^*, \\ \text{traceable to ionization loci}}} + \underbrace{\left( - \sum_{1}^{N_{\text{imp}}^*} \left(1 - f_{\text{SRP}}\right) I_{i-1}^* \right)}_{\substack{\text{sink via dielectric absorption, } I_a^*, \\ \text{traceable to ionization loci}}} \end{array} \right], \tag{3.13}$$

where $I_{\text{anode}}$ is the anodic output current; $I_0$ is the seed current from the cathode; the $i$th impact consists of a secondary-emission coefficient dependent on $W_{\text{imp}}$ and $\theta_{\text{imp}}$ as per Section 2.3; $f_{\text{SRP}} = f_{\text{scattered}} + f_{\text{reflected}}$ is the total fraction of scattered and reflected particles (SRP) per impact, which reduces the number absorbed per impact sink; and $N_{\text{imp}}$ is the number of generational particle impacts on the dielectric. Equation (3.13) includes two terms for multiplicative current growth: $I_m$ accounts for contributions via pure-multipactor growth that are traceable back to the seed with no contributions from ionization, and $I_m^*$ accounts for currents traceable to ionization locus points (ILP's) in the volume. Current impact sinks are similarly divided into $I_a$ traceable to the seed and $I_a^*$ traceable to ILP's. In the vacuum case, the growing current from impacting particles can be approximated by a localized current, $I_i = \delta_i I_{i-1}$, where the $i$th impacting current is dependent on the previous generation, or $(i-1)$th current. In practice, this study assumes that $I^*$ is negligible compared to the overall multiplicative growth. For the limited ionization that does occur in VULP, particularly with the relatively low energy of secondaries in the distribution such that only high-energy electrons will contribute significantly to ionization, treatment of generations $I_{i-1}^* \rightarrow I_i^*$ can be written similar to those from pure multipactor, i.e. $I_i^* = \delta_i I_{i-1}^*$ in the limit of weak collisionality. A more thorough development of $I^*$ is presented in Section 4.1. Another simplifying assumption can be made noting that $v_{\parallel f} >> v_{\perp f}$ for practically all impacts in weak-collisionality discharges, corroborated in Figure 3.8b for vacuum and in Figure 3.21b for ultra-low pressure, where the impact angle is largely grazing, i.e. $v$ is mostly in the direction parallel to the surface. $v_{\parallel f} >> v_{\perp f}$ means Equation (3.6) can be taken to the maximum $\theta_{\text{imp}}$, i.e. $\theta_{\text{imp}} = \pi/2$ or $90°$ from the surface normal, letting all impacting particles emit secondaries according to the grazing-incidence curve of Figure 2.9. In the case of a continuous-waveform (CW) current for the $i_{\text{th}}$ impact, the $i_{\text{th}}$ current can be written

as $I_i = \prod_1^i \delta_j(W_{\text{imp}}, \theta_{\text{imp}}) I_0$. With all the assumptions above, Equation (3.13) ultimately reduces to a pure multipactor current in the following form:

$$I_{\text{anode}} = I_0 \prod_1^{N_{\text{imp}}} \delta_{\text{i}} \equiv I_m. \tag{3.14}$$

In the case of a uniform distribution for $\delta$ at all impacts, Equation (3.14) reduces to an exponential form that is readily pulled from the schematic of Figure 3.1b:

$$I_m = I_0 \delta^{N_{\text{imp}}}. \tag{3.15}$$

General characteristics of discharge behavior can now be considered with the aid of Equation (3.15). Average behavior can be studied in terms of an ensemble-average secondary-emission coefficient, $\delta_{\text{avg}}^{\text{ens}}$. In practice, $\delta_{\text{avg}}^{\text{ens}}$, would be calculated at simulation time since it necessarily evolves with the growing ensemble in time, but Equation (3.15) can be leveraged a-posteriori to calculate $\delta_{\text{avg}}^{\text{ens}}$ at peak current, $t = t_{\text{peak}}$, which is the edge of when $N_{\text{imp}}$ from Equation (3.12) is still relevant:

$$\delta_{\text{avg}}^{\text{ens}}(t_{\text{peak}}) = \left[\frac{I_m(t_{\text{peak}})}{I_0}\right]^{\frac{1}{N_{\text{imp}}}}. \tag{3.16}$$

As will be shown, impact energies in discharges of interest to this study typically asymptote to the first crossover, $W_1$; consequently, $\delta_{\text{avg}}^{\text{ens}}$ asymptotes to unity and the output current similarly asymptotes to $I_0$. Formally:

$$\lim_{\delta_{\text{avg}}^{\text{ens}} \to 1} I_{m,\text{avg}} = \lim_{\delta_{\text{avg}}^{\text{ens}} \to 1} I_0 (\delta_{\text{avg}}^{\text{ens}})^{N_{\text{imp}}^{\text{ss}}} = I_0, \tag{3.17}$$

where the number of impacts is represented by $N_{\text{imp}}^{\text{ss}}$ to emphasize that the discharge is approaching steady-state; the number of impacts at steady state is generally not equivalent to the number of impacts at the initial transient, noting that the growth of surface charge and volume charge in the multipactor front effectively decreases particle lifetime and range, which *increases* $N_{\text{imp}}$ while *decreasing* $\delta_{\text{avg}}^{\text{ens}}$. Although not explicitly treated, $N_{\text{imp}}$ is an implicit function of time since the single-particle excursion length of Equation (3.12) is a function of time, depending on the evolution of the near-surface fields. The maximum emission of secondaries for grazing incidence can be used in Equation (3.15) to facilitate discussion of the gain limit, although it must be understood that the distribution of energies for generated secondaries and the drive to saturation will generally not lead to impacting secondaries with maximum gain. Some generality can be gained by effectively dividing out the integration time for the current:

$$I_{\text{max}}/I_0 = N_{\text{sec}}^{\text{max}}/N_0^{\text{max}} = (\delta_{\text{max}}^{\text{ens}})^{N_{\text{imp}}}, \tag{3.18}$$

where $N_0^{\text{max}}$ is the maximum number of primaries over a normalized seed-current integration time, $N_{\text{sec}}^{\text{max}}$ is the maximum number of secondaries over the same integration time, and $\delta_{\text{max}}^{\text{ens}}$ is the ensemble gain coefficient, which may be replaced with $\delta_{\text{max}}^{\text{global}} = \delta_{\text{max}}(\theta_{\text{imp}} = 90°)$ (explicitly taking the global maximum of the Vaughan model) if interested in the gain

limit. Information about local electric-current magnitudes is lost in the form of Equation (3.18), but since Equation (3.18) is simply counting particles, the relation should hold for all scenarios. Note particularly that the development of Equations (3.13) to (3.15) tacitly assumes that all electrons from a given generation are absorbed at the same boundary per impact, i.e. only the dielectric or only the anode as per the schematic of Figure 3.1b. Further note that the neglected energy and spatial spread of the particle distributions will markedly affect the output current, particularly over local integration times. Inclusion of the distribution is best represented by $\delta_{\text{avg}}^{\text{ens}}$ in this framework.

A typical discharge case for this study includes a dielectric-loaded diode with gap-width $D = 2\,\text{mm}$, dielectric permittivity $\varepsilon_r = 2.1$, dielectric angle $\alpha = 6.12°$, and applied voltage of $V = -3500\,\text{V}$; the largely uniform initial surface fields as calculated with XOOPIC are $E_\perp = 2.54 \times 10^5\,\text{V/m}$ and $E_\parallel = -1.75 \times 10^6\,\text{V/m}$, taken at the center of the dielectric. The largest variation in the fields occur near the electrodes ($\sim 30\,\%$ of $E_0$ at maximum for 6.12° with typical parameters) largely a result of the discretization and necessarily stair-stepped Dirichlet condition at the electrode boundaries, as well as the influence of the wedge characteristics (outlined in Appendix 2.A via theoretical considerations for the Schächter source). Assuming all of the secondary-electron emission energy is associated with the perpendicular velocity to give the longest lifetime and setting the most-probable emission energy $W_{\text{emit}}^{\text{mode}} = 1.85\,\text{eV} \Rightarrow v_{\perp 0} = 8.07 \times 10^5\,\text{m/s}$, the number of impacts over the surface is:

$$N_{\text{imp}} = \frac{(-1.602 \times 10^{-19}\,\text{C})\left(2.54 \times 10^5\,\frac{\text{V}}{\text{m}}\right)(0.002\,\text{m})}{\left[2\left(9.11 \times 10^{-31}\,\text{kg}\right)\left(8.07 \times 10^5\,\frac{\text{m}}{\text{s}}\right)\cos(6.12°)\cdot\left(\left[8.07 \times 10^5\,\frac{\text{m}}{\text{s}}\right]\frac{-1.75 \times 10^6\,\frac{\text{V}}{\text{m}}}{2.54 \times 10^5\,\frac{\text{V}}{\text{m}}} - 0\right)\right]} \sim 10 \text{ impacts.} \tag{3.19}$$

The limiting particle gain can be calculated from Equation (3.18) using a $\delta_{\text{max}}^{\text{global}} \sim 4$ for PTFE:

$$N_{\text{sec}}^{\text{max}}/N_0^{\text{max}} = \left(\delta_{\text{max}}^{\text{global}}\right)^{N_{\text{imp}}} = (4)^{10} \sim 1 \times 10^6. \tag{3.20}$$

As will be described in Section 3.4.1, Equation (3.20) really applies to a region in the discharge described in this study as the "multipactor front", where the calculation for $N_{\text{imp}}$ largely holds until saturation cuts off the front. As parts of the dielectric approach steady state, field conditions evolve to support impact energies at $W_1$, $N_{\text{imp}}$ reaches a steady-state as noted previously, and output current saturates to the input current in typical cases.

### 3.1.2 Single-Particle Test

To verify the behavior of the single-particle approximation of Section 3.1.1, a simple test at 6.12° is conducted in XOOPIC for a current low enough to ensure that any arcs will be completed before the next primary is injected; for this particular case, the number of particles injected is one (macro)particle every nanosecond. Parameters specific to this section are summarized in Table 3.1, and otherwise standard parameters are listed in Table 2.7.

Table 3.1: General parameters for single-particle verification test in vacuum through ultra low pressure (VULP) conditions. These parameters are used to illustrate agreement with ideal gain described in Section 3.1.1. Other parameters are taken from Table 2.7.

| Physical Parameter | Symbol | Value |
|---|---|---|
| Dielectric angle (with respect to electrode normal) | $\alpha$ | 6.12° |
| Global max SE coefficient | $\delta_{\text{max}}^{\text{global}}$ | 4 |
| $\delta_{\text{max}}$ at normal incidence (for variable $\delta$ test) | $\delta_{\text{max}}$ | 2.95 |
| Cathode voltage | $V_{\text{cathode}} = -V_0$ | $-3500\,\text{V}$ |
| Gap width | $D_{\text{gap}}$ | $2\,\text{mm}$ |
| Background pressure | $p_{\text{bg}}$ | $0\,\text{mTorr}$ |
| Source current | $I_0$ | $1.602 \times 10^{-10}\,\text{A}$ |
| Fraction scattered | $f_{\text{Scattered}}$ | 0 |
| Fraction reflected | $f_{\text{Reflected}}$ | 0 |

| Numerical Parameter | Symbol | Value |
|---|---|---|
| Macro-particle weighting | np2c | 1 |

| Growth characteristic | Symbol | Value |
|---|---|---|
| Number of impacts (Equation (3.12)) | $N_{\text{imp}}$ | 10 |
| Theoretical max gain (Equation (3.18)) | $N_{\text{sec}}^{\text{max}}/N_0^{\text{max}}$ | 1048576 |

The most pertinent diagnostics are summarized in Figure 3.3: number plots as a function of time are shown for a number of cases to verify Section 3.1.1, particularly Equation (3.18) and Equation (3.20). The closest to the ideal setup of Section 3.1 is Figure 3.3a, with vertically emitted, monoenergetic secondaries ($W_{\text{emit}}^{\text{mode}} = 1.85\,\text{eV}$) and a constant $\delta = \delta_{\text{max}}^{\text{global}}$ for all impacts. A slight variation on the ideal case is shown Figure 3.3b with vertically emitted, monoenergetic secondaries emitted according to the Vaughan model as a function of impact energy and angle, $\delta = \delta(W_{\text{imp}}, \theta_{\text{imp}})$ using $\delta_{\text{max}}$ at normal incidence as a parameter. Secondaries in Figure 3.3c are vertically emitted, Maxwellian-flux secondaries with $\delta = \delta(W_{\text{imp}}, \theta_{\text{imp}})$, adding particle-distribution characteristics in energy and space. Finally, the most general case of semi-isotropic, Maxwellian-flux secondaries are shown in Figure 3.3d, adding additional spatial distribution via a range of emission angles. Note that in cases of Maxwellian-flux secondaries, a random sampling of a Maxwellian distribution is implemented, which could require longer observation times to generate a full arc; consequently, all plots are shown for $1\,\mu\text{s}$ to facilitate reasonable statistics. In all cases, the characteristics of a fully developed arc can be directly compared to Equation (3.20), or more generally with Equation (3.18) to gain insight into the sensitivity of ideal results to increasingly general forms of secondary emission.

Recall that the analysis in Section 3.1 neglects particle distributions, which invariably affects the growth rate and subsequent current via emission energy and energy gain/loss

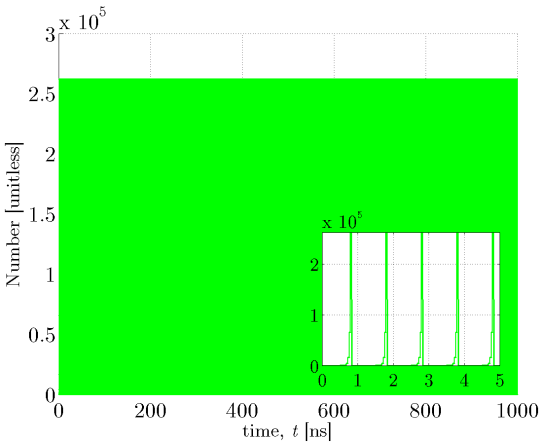


(a) Vertical emission, monoenergetic, $\delta = \delta_{\max}$.

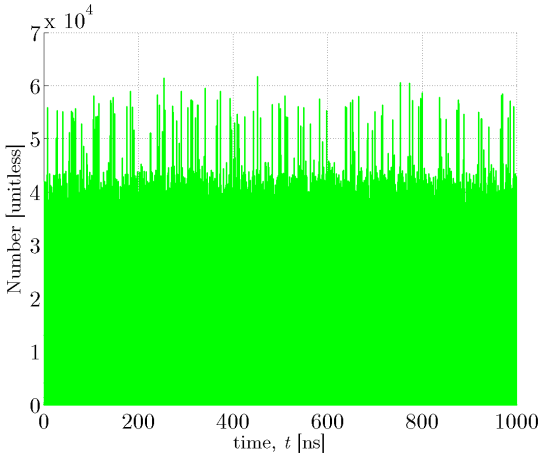


(b) Vertical emission, monoenergetic, $\delta = \delta(W_{\text{imp}}, \theta_{\text{imp}})$.

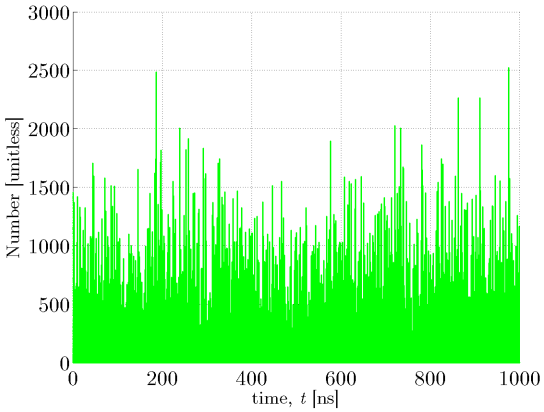


(c) Vertical emission, Maxwellian flux, $\delta = \delta(W_{\text{imp}}, \theta_{\text{imp}})$.

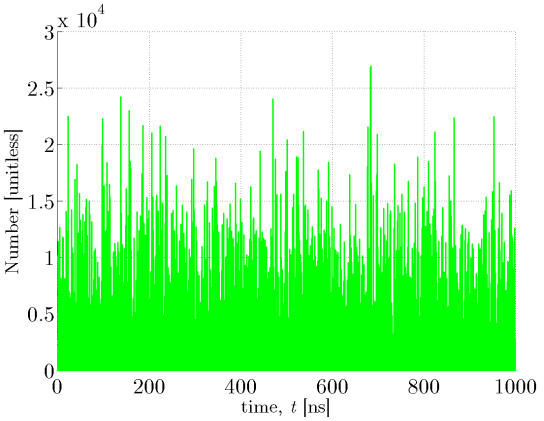


(d) Semi-isotropic emission, Maxwellian flux, $\delta = \delta(W_{\text{imp}}, \theta_{\text{imp}})$.

Figure 3.3: Low-current multipactor test for a multiplicative discharge at 6.12°. Number plots are shown for: [Note bold text below indicates the change from the previous subfigure.] (a) vertically emitted, monoenergetic (1.85 eV) secondaries at constant $\delta = \delta_{\max}^{\text{global}}$, with inset showing details of growth through initial 5 ns; (b) vertically emitted, monoenergetic secondaries at **variable** $\delta = \delta(W_{\mathbf{imp}}, \theta_{\mathbf{imp}})$; (c) vertically emitted, **Maxwellian-flux secondaries** at variable $\delta = \delta(W_{\text{imp}}, \theta_{\text{imp}})$; (d) **semi-isotropic**, Maxwellian-flux secondaries at variable $\delta = \delta(W_{\text{imp}}, \theta_{\text{imp}})$.

during excursion. It is clear that Figure 3.3a is in good agreement with the results of Equation (3.18) to within a factor of four (pertinent growth characteristics are listed at the bottom of Table 3.1), or more specifically by a factor of $\delta = \delta_{\text{max}}^{\text{global}|N_{\text{imp}}^{\text{actual}} - N_{\text{imp}}^{\text{estimate}}|}$ as the number of impacts was overestimated by one impact (not shown, but evident when tracing the configuration-space plots) as a result of near-electrode fields elongating early and late trajectories due to the expected aberration in the fields approaching the electrodes, resulting from the metallic boundary conditions and wedge characteristics of the triple-point [4, 12] noted above. The agreement of Figure 3.3a with Equation (3.18) is expected since this run directly uses ideal parameters. For the discharge represented by Figure 3.3b, $\delta_{\text{avg}}^{\text{ens}} \sim 3.21$ (not shown explicitly) at the peak anodic current, which marks quenching of upstream growth. $\delta_{\text{avg}}^{\text{ens}}$ is measured from code diagnostics, where $\delta$ is now determined by the characteristics of particles impacting the surface rather than being set to a constant as in Figure 3.3a. Equation (3.18) for 10 bounces then gives $\sim 1.17 \times 10^5$, which is consistent with the maximum gain in Figure 3.3b to within a factor of two, while comparison with ideal growth from Figure 3.3a shows a reduction by $\sim 1 - 3$ orders of magnitude, depending on comparison with measured or theoretical gain. It is apparent that multipactor gain is highly sensitive and non-linear with respect to distribution characteristics where slight variations can alter both the number of impacts and $\delta_{\text{avg}}^{\text{ens}}$ from ideal. Particles are still emitted vertically with the same energy, and particle secondary yield is now a function of impacting characteristics. Low space-charge is not expected to affect trajectories with the modest gains here, as per Equation (3.27). For the case of vertically emitted, Maxwellian-flux secondaries in Figure 3.3c, $\delta_{\text{avg}}^{\text{ens}} \sim 3.07$ for a fully developed discharge, so the expected gain is $\sim 7.44 \times 10^4$, which overestimates the peak growth in Figure 3.3c by about an order of magnitude. After sufficient statistics build up, the ratio of the number of particles emitted with energies greater than kinetic temperature (most-probable energy) to the number of particles emitted with energies less than kinetic temperature is about three. $\delta_{\text{avg}}^{\text{ens}}$ is expected to vary considerably from the characteristics of Figures 3.3a and 3.3b, where particles are emitted with the equivalent of most-probable energy, or half kinetic temperature in 2-D, for the distribution used in Figure 3.3c. The large reduction of particle gain from ideal gain despite a comparable $\delta_{\text{avg}}^{\text{ens}}$ at peak current is a useful illustration of the sensitivity of multipactor characteristics to $N_{\text{imp}}$. With more particles emitted with higher energies, $N_{\text{imp}}$ is reduced on average, so gain is reduced. For the case of semi-isotropic, Maxwellian-flux secondaries in Figure 3.3d, $\delta_{\text{avg}}^{\text{ens}} \sim 2.12$ for a fully developed discharge, so the expected gain is $\sim 1.83 \times 10^3$, which is about an order of magnitude below theoretical estimates but roughly consistent with the average peak gain per growth period. The wide domain of emission angles maps to a larger trajectory space, which, in the case of Figure 3.3d, leads to reduced $\delta_{\text{avg}}^{\text{ens}}$ and a range of $N_{\text{imp}}$ that is convoluted with each generation's spatial trajectory. It must be stressed that non-linear effects, e.g. space-charge and variations from particle distributions, introduced upstream are amplified when they occur nearer the cathode since these variations will experience more of the exponential characteristic for growth during a longer downstream excursion. Finally, note that Figure 3.3a illustrates the gain limit in Equation (3.20), serving as an upper bound for the other cases.

## 3.2 Pressure Limits of VULP Breakdown

As will be shown, the general phenomena seen in vacuum discharges and described in Section 3.4 is valid through ultra-low pressures up to a few hundred mTorr. This treatment will concentrate on the ionization of background gas in the Thomson model for generalization, although individual gas cross sections may be used for specific applications. In particular, single-ionization of an argon (Ar) background will be considered in simulation, and comparison with the Thomson model is provided in Section 3.B.

The limit between VULP breakdown and low-pressure breakdown (when collisionality can no longer be neglected) is determined by comparing multipactor growth rates to other growth mechanisms. In the ideal case, the front growth as a function of $x$ along the dielectric is readily obtained from Equation (3.18). The multipactor growth rate $R_m$ under negligible contributions from ionization is:

$$R_m = \frac{I\left(x\right)}{q_e} = \frac{I_0}{q_e}\left(\delta_{\text{avg}}^{\text{ens}}\right)^{N_{\text{imp}}}. \tag{3.21}$$

The largest growth rate will be downstream towards the anode, so a lower limit can be obtained by using $N_{\text{imp}}$ as calculated with Equation (3.12) and looking for a sufficient background-gas pressure to match the near-anode growth rate. A general ionization-collision rate can be calculated by integrating the usual Thomson cross section:

$$\sigma_{iz}\left(W\right) = \begin{cases} \pi\left(\dfrac{e^2}{4\pi\varepsilon_0}\right)^2 \dfrac{1}{W}\left(\dfrac{1}{U_{iz}} - \dfrac{1}{W}\right) & W \geq U_{iz} \\ 0 & W < U_{iz} \end{cases}, \tag{3.22}$$

where $U_{iz} \equiv$ ionization energy and $W = (1/2)mv^2$.

The collision frequency, $\nu_{iz}$ is the ionization rate to be equated to the multipactor growth rate:

$$\nu_{iz} = K_{iz} n_g = \sigma_0 \bar{v}_e \left(1 + \frac{2\mathrm{T}_e}{\mathcal{E}_{iz}}\right) \exp\left(-\frac{\mathcal{E}_{iz}}{\mathrm{T}_e}\right) n_g, \tag{3.23}$$

where $K_{iz} = \sigma_{iz}\left(v\right) v$ is the ionization coefficient, and $n_g$ is the neutral-gas density. Note that this treatment characterizes discharge behavior in an average sense, and that Equation (3.23) is a function of temperature, having integrated over energies of the particle distribution. Setting Equation (3.21) equal to Equation (3.23) and solving for density gives the critical density at which anodic ionization starts to become appreciable, on the order of multipactor growth:

$$n_g^{\text{crit}} = R_m / K_{iz} = \frac{\dfrac{I_0}{q_e}\left(\delta_{\text{avg}}^{\text{ens}}\right)^{N_{\text{imp}}(x)}}{\sigma_0 \bar{v}_e \left(1 + \dfrac{2\mathrm{T}_e}{\mathcal{E}_{iz}}\right) \exp\left(\dfrac{\mathcal{E}_{iz}}{\mathrm{T}_e}\right)}. \tag{3.24}$$

The typical parameters from Section 3.3 give a $\delta_{\text{avg}}^{\text{ens}} \sim 1.095$ at current onset, and assuming most particles undergo the impacts calculated from Equation (3.19), the multipactor growth rate in the ideal case is $R_m \sim 2.58 \times 10^{13}\,\text{s}^{-1}$. It is observed that the average energy for electrons in the volume is $\sim 130\,\text{eV}$. Assuming a 2-D Maxwellian

distribution in the volume, the temperature is the distribution average and the most-probable energy is $\sim 65\,\text{eV}$; however, it should be noted that while emission is Maxwellian, bulk-volume characteristics are not generally Maxwellian, so distribution quantities are not necessarily related to each other in the way that is being assumed here. The ionization constant with an ionization energy of $15.79\,\text{eV}$ is $K_{iz}\sim 111.73$. The critical gas density is $n_g^{\text{crit}}\sim 7.11\times10^{17}\,\text{m}^{-3}$ and, assuming ideal gas, a critical gas pressure of $\sim 1.28\times10^{5}\,\text{mTorr}$. This is about two orders of magnitude higher than pressures observed at which large oscillatory behavior due to space-charge coupling starts to become significant, observed at $< 1000\,\text{mTorr}$ and illustrated in Chapter 4. Much of the discrepancy is attributable to space-charge effects, which were neglected in the theoretical gain. Additionally, knowledge of growth-sensitive quantities such as $\delta_{\text{avg}}^{\text{ens}}$ (provided above via in-situ diagnostics in simulation) are difficult to obtain a-priori. $R_m$ and $\nu_{iz}$ can be estimated directly in simulation using the usual parameters from Section 3.3 and a $500\,\text{mTorr}$ background gas for electron growth rate near the anode, giving $R_m\sim 9.65\times10^{13}\,\text{s}^{-1}$ and $\nu_{iz}\sim 2.65\times10^{13}\,\text{s}^{-1}$. Using these measured values, the critical gas density is $n_g^{\text{crit}}\sim 1.01\times10^{17}\,\text{m}^{-3}$. Assuming ideal gas, this represents a critical gas pressure of $\sim 1821\,\text{mTorr}$. This is about a factor of two from the nominal $1000\,\text{mTorr}$ crossover observed in simulations.

## 3.3 VULP General Parameters

The general phenomenology of VULP breakdown will be described through a few examples using the parameters listed in Table 2.7. This section will focus on two dielectric angles, 6.12° and 22.9°, representing multiplicative breakdown and a dark-current steady-state breakdown, respectively, where dark-current steady-state breakdown is defined as a non-multiplicative arc with an average output-current magnitude equal to the seed-current magnitude for an unperturbed seed source. Extending the following results to other angles listed in Section 2.2.2 is straightforward, with the main differences across angles being the initial conditions over the dielectric surface and the length of the surface over which breakdown occurs, which affects the gain magnitude and time to steady-state.

Dielectric properties and secondary-emission properties are taken for polytetrafluoroethylene (PTFE), largely because it is a common material that would be suitable for extending these results to benchtop experiments. Applied voltages were chosen to ensure initial multiplication upon first impact as well as uniform initial conditions, eliminating concerns for delay times. The gap width is arbitrarily set to $2\,\text{mm}$, providing sufficiently large fields over moderate voltage drops; results can be linearly extended to variable gap widths in the operating regimes presented in this section. The seed source is a specified continuous-waveform (CW) injection with a 1-A magnitude at standard room temperature ($0.025\,\text{eV}$). This source provides sufficient current to measure the gain in reasonable simulation time. The reflected and scattered fractions have been set to zero for most cases, as they have been observed to provide minor influence to general phenomenology. For cases that treat SRP, the scattered and reflected fractions are set to typical values of 7% and 3%, respectively [45].

### 3.3.1 Grid Resolution in Vacuum

The original grid described in Section 2.2 was developed largely under the assumption of linear variation across a sufficiently resolved spatial grid. The assumption of linearity is certainly valid at the beginning of all discharges (when charged-particle populations are low) for the modest permittivities studied here. Linearity is also likely to remain valid at saturation assuming relatively small saturated populations and uniform densities everywhere. However, during the transient phase, the growth of particle populations (with distributions in energy and space) and the inclusion of space-charge could lead to significant nonlinearities near the surface and therefore a markedly different gain than that suggested by Section 3.1.1 treating single-particle motion in vacuum. The gain of six orders of magnitude suggested by Equation (3.20) is reduced for typical parameters in simulation by $\sim 1-2$ orders of magnitude, c.f. Figure 3.11, due to similar contributions from energy and spatial distributions seen in Section 3.1.2, while some low-pressure gas cases show a gain of up to 2 orders of magnitude with slower rise-times to peak current due to space-charge effects creating more distributed volume characteristics, covered in detail in Chapter 4. An analysis of particle excursions through the grid suggest that better resolution could be required, particularly where larger voltages are needed to be able to produce an adequate seed with sufficient energy to generate net secondaries on first impact, and where sufficient near-surface plasma cause significant shielding and under-resolved, small-scale trajectories, e.g. gyro-motion, that are not represented by the applied field. This section details some considerations regarding the grid.

For an idealized single-particle implementation of the typical system using the parameters of Table 2.7, the number of grid cells traversed for the maximum vertical excursion is shown in Figure 3.4, where additional simplifying assumptions include: vertical emission from the dielectric surface with an energy of 1.85 eV, no space charge, and no spatial or energy distribution. Figure 3.4 shows that as the field angles get larger, the particle does not sample the grid often for a parameter set that would allow the largest sampling in the vertical direction, i.e. with all initial velocity in the vertical direction only. The horizontal trajectory samples the grid infrequently with increasing field angle as well. While this does not pose a particular problem for VULP where the influence of space charge is relatively small, particularly at the start of the discharge and during saturation, there could be issues in resolving local field and particle behaviors that do not conform with the initial assumption of linearity. This problem could be more considerable in gaseous discharges, when space charge is both non-linear and non-uniform. As in [5], a grid size of at least one-third the Debye length for a gaseous discharge is typically recommended to capture the relevant local physics. Further comments regarding resolution of particle excursions in higher pressure regimes are provided in Section 4.2. Of course, a reduction in the grid size will require consideration of the particle-Courant condition for the leap-frog method, written for 2D discrete problems:

$$C = \frac{u_{x,\max}\Delta t}{\Delta x} + \frac{u_{y,\max}\Delta t}{\Delta y} < C_{\max}. \tag{3.25}$$

where $C_{\max} = 1$ for leap-frog, allowing the particle to sufficiently sample the grid in a timestep.

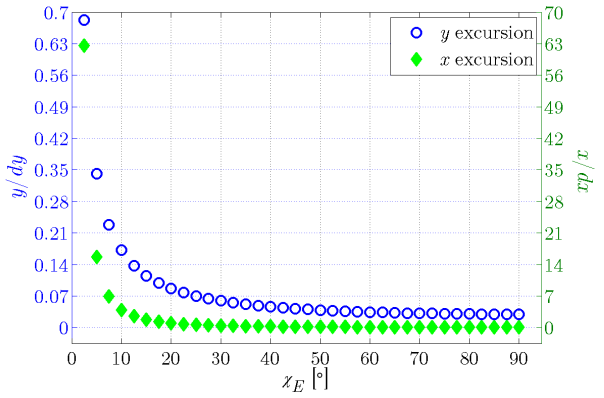


Figure 3.4: Maximum excursions of electrons in Cartesian coordinates, normalized to standard grid size. Applied voltage is 3500 V, initial velocity is only in the vertical direction, and emission energy is 1.85 eV. The grid sampling in $y$ can be small with increasingly orthogonal field angle, $\chi_E$, which could pose problems when nonlinear effects become significant. Horizontal sampling is finer than vertical sampling, but could also suffer from undersampling at higher $\chi_E$.

### 3.3.2 Quasistatic Considerations

The development of Section 3.1.1 assumes quasistatic conditions where a simple metric to ensure such conditions can be written as:

$$\phi_{qs} = \frac{1}{E}\frac{\partial E}{\partial t} t_{\text{life}} << 1, \tag{3.26}$$

expressing the normalized change in the field over a particle lifetime. Assuming a 1-D Poisson equation solved over the width of the multipactor front, $w_{\text{front}} = x_2 - x_1$, an approximation can be made of the required density for the background field to be influenced by a fraction $p$, assuming uniform charge density over $w_{\text{front}}$:

$$\rho_p(x_2) = -\frac{2p(x_2)\varepsilon_0 E_0}{x_2 - x_1}. \tag{3.27}$$

Setting a desired fractional change, $p(x_2)$, in $E_0$ at $x_2$ will allow Equation (3.27) to be written:

$$\phi_{qs}(x_2) = \frac{1}{E_0(p+1)}\left[-\frac{\rho\,(x_2)}{\varepsilon_0}\left(\left[\frac{x_2 - x_1}{2}\right]\frac{\delta - 1}{t_{\text{life}}} + v_{\text{avg}}^{\text{front}}\right)\right] t_{\text{life}}. \tag{3.28}$$

As a benchmark consideration, for $p = 1\,\%$, $\phi_{qs}(x_2) \sim 0.04$, and Equation (3.27) gives an electron number density, $n = \rho/q_e \sim 5 \times 10^{15}/\text{m}^3$. For the configurations used in this chapter at $\alpha = 6.12°$ and standard parameters from Table 2.7, this $n$ is typical for the densities produced by the seed-current. For the secondaries, low-density early transients lead to $n \sim 5 \times 10^{16}/\text{m}^3$, affecting the field by $\sim 10\,\%$ and giving $\phi_{qs} \sim 0.3$. At steady-state, $\phi_{qs} = 0$, of course. At the front, $n \sim 3 \times 10^{17}/\text{m}^3$ and $\phi_{qs} \sim 1.5$ near the anode and rapidly reverts to steady-state as the front passes. As expected, quasistatic conditions hold much better for early transients than at the fully developed front due to the density gain that changes rapidly over a particle lifetime. Typically, $\phi_{qs}$ *at the front* starts to climb

significantly above early-transient values after about half the time to the fully developed front; however, it will be shown that the front has a relatively small width, isolating the phenomenon to a short time (less than $\sim 100\,\text{ps}$) relative to the time for the front to fully develop ($\sim 500\,\text{ps}$ to peak current). The analysis of Section 3.1 therefore remains applicable through roughly 80% of the discharge time.

Further details on Equations (3.27) and (3.28) are provided in Section 3.C.

## 3.4 VULP General Phenomenology

This section will detail the behavior of typical operating regimes in vacuum through ultra-low pressures of weakly collisional discharges, including: (1) a transient, multiplicative regime in vacuum, (2) a non-multiplicative, dark-current regime in vacuum, and (3) parametric variations of (1) and (2) with scattered and reflected particles (SRP) and increased pressure up to a few hundred mTorr of stationary background Ar gas.

A particularly important point to note is that these simulations are seeded so that the energy of the *initial* primary impact produces net emission from the dielectric for all cases. This procedure provides uniform initial conditions, which facilitates direct comparison of surface physics across various angles without convoluting the delay time resulting from increasingly oblique angles. Setting the initial impact characteristics in this way should not be construed as a necessary condition for breakdown; if the initial impact characteristics do not support a multipactor avalanche, negative charging will occur near the triple-point, resulting in elongated lifetimes until the *initial* impact energy is pushed to at least $W_1$ or above. Once a seed is achieved, either multiplicative or non-multiplicative arcs are possible depending on the downstream surface conditions, as will be shown. Applied voltage can then be adjusted and observed to identify the representative regime. While these considerations are necessary to generate an appropriate seed for general comparison across angles, enforcing the seed condition exacerbates the grid problems delineated in Section 3.3.1 since larger applied voltages lead to reduced grid sampling. Again, while grid sampling does not pose a significant problem in the linear regime, space-charge and rapid development of the multipactor front could lead to insufficient resolution of the near-surface dynamics and must be accounted for on a case-by-case basis. For the cases shown in this chapter, the effect of grid resolution is minimal.

### 3.4.1 Multipactor-Dominated Breakdown

Multipactor dominates discharge physics for pressures up to a few hundred mTorr where interactions with background gas are small compared to surface phenomena. If the discharge is seeded with a current and field geometry that favors secondary emission, an electron cloud will develop over the dielectric surface and leave behind a positive charge on the surface. With sufficient positive surface charge coupled with the negative secondary-electron cloud, the strength of the electric field normal to the dielectric surface increases and ultimately shortens the lifetimes of new, low-energy (on average) secondaries which do not gain sufficient energy in transit to further multiply. Multipactor is reduced to a

steady-state non-multiplicative arc as secondaries impact with energies around the first-crossover energy. The following section details the factors driving this phenomenology.

Snapshots of the typical configuration-space for primary electrons and secondary electrons for a system with dielectric angle $\alpha = 6.12°$ are shown in Figure 3.5. The fast transient is shown in Figure 3.5a, taken at 100 ps (peak anode current occurs at $\sim 300$ ps), while steady-state is shown in Figure 3.5b, taken at 5 ns. Primaries impact the dielectric, and if their energies are between $W_1$ and $W_2$, as described in Section 2.3, then at least one electron will be emitted per absorbed electron, leading to the possibility of multipactor if downstream surface-field conditions support multiplication, as they do at $\alpha = 6.12°$, discussed later in the context of Figure 3.10 for the electric-field angle. The transient is characterized by a growing-density front followed by a steady-state tail. The configuration-space plot in Figure 3.5a does not show particularly pronounced variations in the field, as they do in Figure 3.12a for the dark-current case, and it is difficult to see the formation of the front in the view presented; however, further exposition below will make the formation of the front more apparent. The particle excursion in $y$ is clearly larger in Figure 3.5a than in Figure 3.5b, which is a subtle but non-trivial difference that will be evident in the discussion of near-surface fields vis-á-vis Figure 3.10.

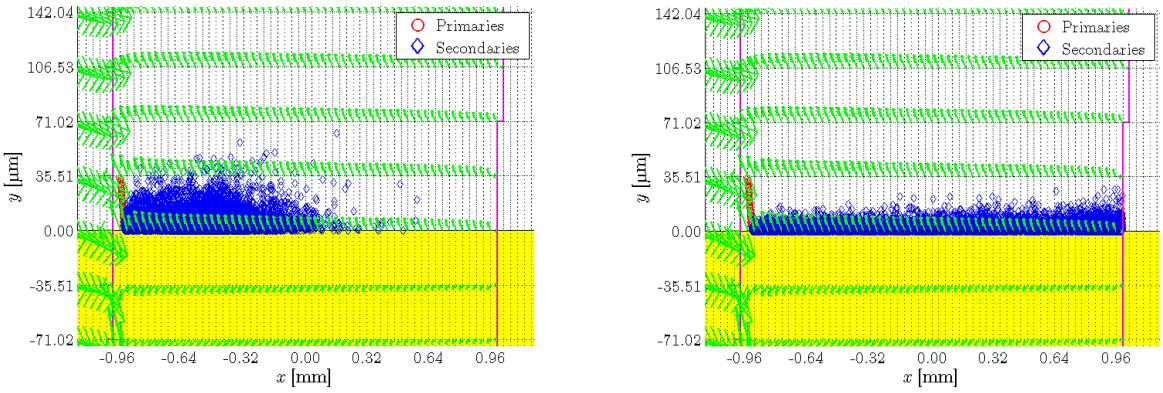


(a) Growing discharge, $t = 0.1$ ns.

(b) Steady-state discharge, $t = 5$ ns.

Figure 3.5: Configuration-space example of VULP breakdown at 6.12°. Primary and secondary electrons moving from the lower cathode potential on the left to higher anode potential on the right. Primary electrons are absorbed at the dielectric (shaded region, $y < 0$), emitting secondaries according to the theory outlined in Section 2.3. Time in (a) is 100 ps, and time in (b) is 5 ns. The grid shown corresponds to the numerical grid, with a square-grid spacing of 35.5 µm in $x$ and $y$. Green arrows correspond to the magnitude and direction of $\vec{E}$ at the displayed time. No SRP.

The dielectric surface charging for a discharge at $\alpha = 6.12°$ through 5 ns is shown in Figure 3.6. Figure 3.6b is a contour view of the dielectric charging, emphasizing the dominant positive charging for most of the surface for the full discharge time. The relatively large positive charging localized near the cathode is the initial-impact region for primaries, which has some finite width due to the beam characteristics of the seed current. The region immediately downstream of the initial-impact region is typically characterized as a charge sink relative to the initial-impact region; in Figure 3.6a, this

region is characterized by obviously reduced charge by an order of magnitude compared to the initial-impact region, and often charges negatively due to short-lived secondaries that do not gain sufficient energy in their excursion to further multiply. The characterization of the immediate-downstream region can be defined by the maximum range for a particle with the most-probable characteristics in vacuum fields to impact with energy just below $W_1$, where details are provided in Section 3.D. In short, $W_{\text{emit}}^{\text{mode}}$ is sufficient to define the width of immediate-downstream region, giving $\sim 73\,\mu\text{m}$ by leveraging Equation (3.4) and Equation (3.11) with fields taken from diagnostics. Although not shown, after $\sim 12\,\text{ns}$, the reduced-charged region from the diagnostic of Figure 3.6 develops a negative charge that is localized around $70\,\mu\text{m}$ from the initial-impact peak, with a width of $< 100\,\mu\text{m}$, consistent with the width noted above using $W_{\text{emit}}^{\text{mode}}$. Sufficient charging immediately downstream the initial-impact region could lead to migration of the initial-impact region upstream as a result of space-charge interaction between the negative surface charge and the beam source. This particular configuration does not see significant migration of the initial-impact region. In the presence of upstream migration, the immediate-downstream region would also migrate up, reducing the positive charge at the original region of initial impact. The effect of initial-impact-region migration could lead to reduced steady-state current if electrons are collected at the cathode as a result of upstream trajectories, although this is not explicitly shown in this exposition; parameters could be set to effectively demonstrate this effect, most easily by manually shifting the location of the seed and initial-impact region further upstream.

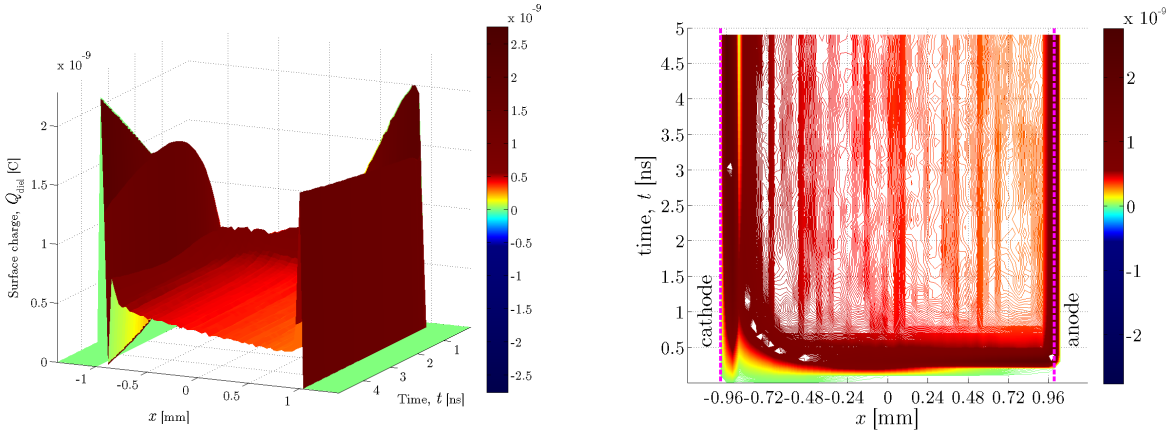


(a) Dielectric-charge full profile.

(b) Dielectric charge contour in $x$ against $t$.

Figure 3.6: Characteristic dielectric-surface charging for a multipactoring discharge at 6.12°. Positive charging is shown over a large region of the dielectric, indicating surface characteristics sufficient for multiplicative breakdown.

Figure 3.6a shows a large positive charging near the anode at $\sim 1\,\text{mm}$; this is a result of net emission from the dielectric near the anode that is simply collected at the anode boundary without returning to the dielectric. The near-anode positive charge could serve as a potential well for some particles with sufficient charge, but excessive electron collection in the positive region is not observed for this configuration. Furthermore, the charge at the near-anode region is not expected to be significant to the discharge characteristics

because a sufficiently positive charge that reduces near-anode lifetimes will eventually collect sufficient electrons to increase lifetimes again. In principle, the near-anode dielectric charge could fluctuate with long-enough discharge times, but this is not observed for the configurations studied. Also of note is that the exponential growth along the path as a function of the number of impacts means that the growth rate is itself exponential, so downstream growth rates and dielectric-charging rates are generally larger than upstream rates with the possible exception of the initial-impact region, which has a growth rate and dielectric-charging rate proportional to the seed current and initial $\delta$, recalling that the primary impact is specified to emit near $\delta_{\max}(\theta_{\text{imp}})$, with $\theta_{\text{imp}} \sim 30°$.

Figure 3.7a shows the primary impact energy distribution over the dielectric surface, indicating sufficient energy to be near the maximum secondary emission for the initial impact angle, in this case, $\theta_{\text{imp}} \sim 30°$ from the dielectric normal; in Figure 3.8, the primaries are essentially all particles clustered near the peak of the secondary-emission line plotted at $\theta_{\text{imp}} = 32.0°$. Subsequent impacts from secondaries on the dielectric cover a range of energies due to the thermal distribution of emission energies and associated range of energy gains for the various lifetimes experienced by individual particles in the distribution, illustrated in Figure 3.7b. Figure 3.8 further indicates that most of the secondary impacts approach grazing incidence as most of the energy is attributed to gains from fields parallel to the dielectric surface; consequently, most secondaries are following the curve associated with the global maximum yield from Figure 2.9, justifying the approximation with $\delta_{\max}^{\text{global}}$ in Equation (3.18). However, it must be noted that, while secondaries follow the near-grazing curve, the majority of particles do not emit at $\delta_{\max}^{\text{global}}$ due to limited gain. Further note that much of the spread in the angular distribution shown in Figure 3.8 is occurring at the low-energy end, and is about five orders of magnitude smaller than the peak at $\theta_{\text{imp}} = 80°$.

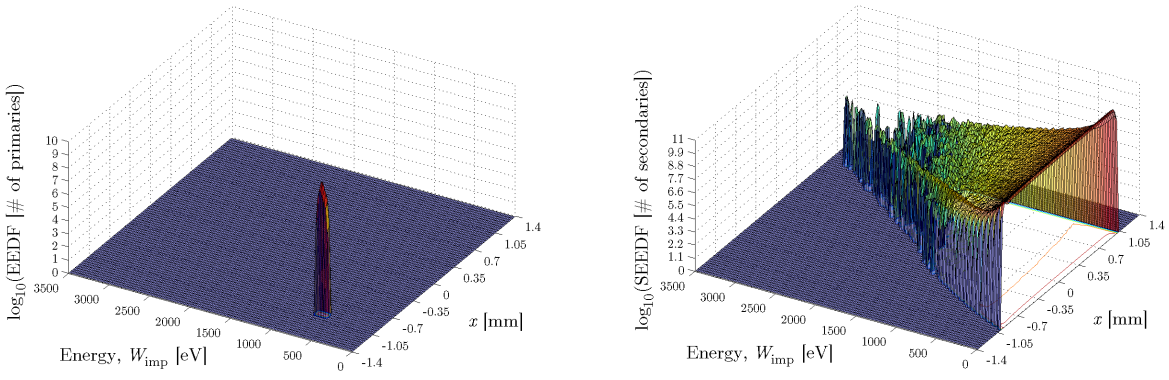


(a) Primary-electron EDF.

(b) Secondary-electron EDF.

Figure 3.7: Primary-electron and secondary-electron energy distributions functions (EDFs) on the dielectric surface for 6.12°. These plots are cumulative over the whole discharge. (a) shows the primaries impact nearly monoenergetically. (b) shows secondaries impact with a range of energies due to the initial distribution and lifetime ranges.

Figure 3.9 illustrates the formation of the multipactor front via the weighted average

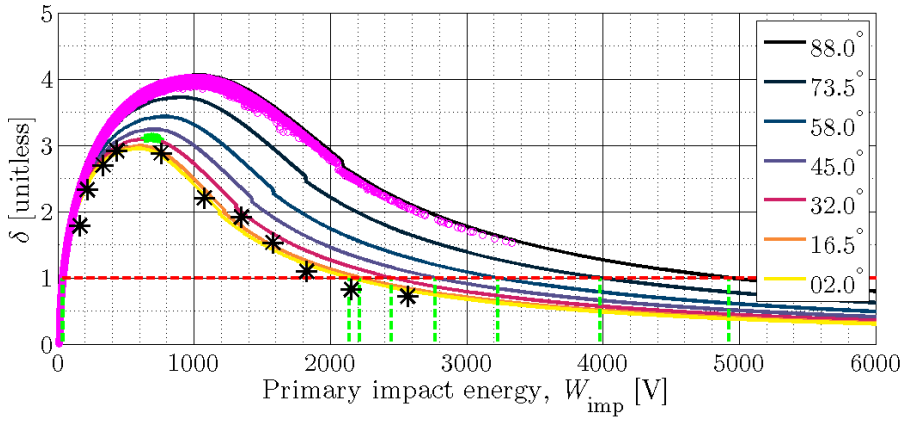


(a) Secondary-emission coefficient vs. impact energy at various impact angles.

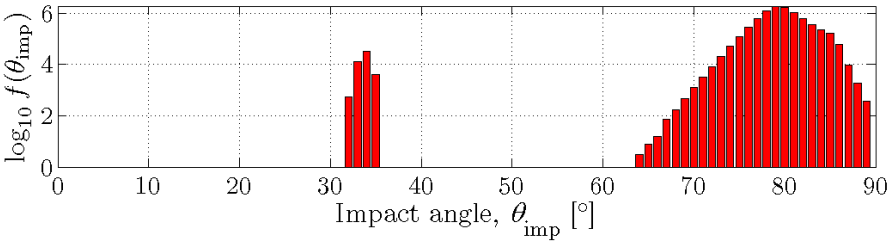


(b) Impact angular distribution.

Figure 3.8: Reconstructed secondary-emission curve from simulation for 6.12°. Simulation time is 5 ns. (a) shows the impacting energies for primaries (green) and secondaries (magenta) in the circular (o) marker plotted against the theoretical Vaughan curve [2] at various angles. (b) shows the impact angular distribution, where the peak near 32.0° is largely composed of primaries while the rest of the distribution is composed of secondaries.

density for secondary electrons over the dielectric surface as a function of time:

$$n_w(x,t)\left[\mathrm{m}^{-3}\right] = \frac{\int \frac{n(x,y,t)}{\Gamma}\exp(-y/\Gamma_w)dy}{\int \exp(-y/\Gamma_w)dy}, \tag{3.29}$$

where $y$ is in m. The weighting scheme was chosen to emphasize near-surface contributions to the volume density using the empirical factor $\Gamma_w$. Since growth can be exponential within a small volume, linear weighting over all $y$ would lead to excessive smoothing of density data, incorrectly showing uniform density over the surface with time. $\Gamma_w$ is varied from large values (excessive smoothing) and reduced until the observed near-surface structure in time is returned. A factor of $\Gamma \sim 1/1000$ m is found to be sufficient for the purposes of this study, which may be interpreted as indicating the influence of near-surface phenomena is limited to an effective depth of 1 mm in this metric, noting that this is only for diagnostic purposes and not a strict definition of the sphere of influence of near-surface phenomena. Further note that this study does not use the weighted diagnostic for physical applications. If such an application is desired, mass must be considered in the grid scheme so that proper weighting is applied without destroying mass or improperly locating mass on the grid. Since physical application of this scheme is not treated in this study, grid correction is not applied.

The multipactor front develops from an initially growing electron density, leaving positive charge on the dielectric surface that subsequently leads to unfavorable surface conditions for secondary emission due to a coupling of the positive surface charge with the negative secondary-electron cloud, creating a growing, peaked secondary density front with steady-state wake. Lifetimes of new secondaries and the amount of energy new secondaries can gain in a lifetime are ultimately reduced in the wake of the front. Following time in Figure 3.9a, the secondary density markedly increases across the dielectric surface, with a weighted density ranging over about five orders of magnitude between minimum ($10^{11}\,\mathrm{m}^{-3}$) and maximum ($10^{16}\,\mathrm{m}^{-3}$), and roughly one order of magnitude between steady-state average ($10^{15}\,\mathrm{m}^{-3}$) and maximum. When surface-field angles are saturated consistent with Figure 3.2b, further multipactor growth is quenched and steady-state dark current develops over the surface with $\delta_{\mathrm{avg}}^{\mathrm{ens}} \sim 1$ and roughly uniform secondary-electron density over the dielectric surface as in Figure 3.9 past 1000 ps with the fully developed front evacuating at the anode; after 1000 ps, the system has reached the steady-state described in Equation (3.17), with $N_{\mathrm{imp}}^{\mathrm{ss}} \sim 33$, showing the expected increase compared to Equation (3.19). Figure 3.9b shows the fast development and quenching of the multipactor front, with most of the front dumping on the anode in less than $\sim 100$ ps. The speed of the front is largely defined by the average velocity tangential to the surface for multipactor secondaries in the system; the bulk-volume velocity is a weak function of the emission energy and angle, and a strong function of applied voltage and surface-field conditions. Assuming quasi-static fields and recalling the low average emission energies, most of the energy is attributed to the tangential velocity, and the average total energy can therefore be used to estimate the speed of the front. For the case shown, simulation-time diagnostics show secondaries have an average, bulk-volume energy of $\sim 136.5$ eV during the transient (peaked in the average, before the steady-state wake starts contributing significantly to the average), for a multipactor-front velocity of $\sim 6.9 \times 10^6$ m/s, roughly equivalent to that shown in Figure 3.9b, estimated to be about $v_{\mathrm{front}} = 2.0\,\mathrm{mm}/320\,\mathrm{ps} = 6.3 \times 10^6$ m/s using the time to peak density as labeled.

The drive to saturation can also be shown via surface electric-field diagnostics as shown in the representative case of Figure 3.10, plotting the surface-field angle for the center of the dielectric. The field shows a slight initial dip resulting from the buildup of the multipactor front upstream of the dielectric center. The development of a minimum field angle shown around 0.13 ns is indicative of an upstream multipactor front; after 0.13 ns, the front has passed the dielectric center and the field angle increases until saturation at $\sim 1$ ns. Figure 3.2b suggests the expected saturation field angle, $\chi_{E,\mathrm{center}}$, should range from 24.20° to 24.88°; Figure 3.10 corroborates the expected general trend with a saturation around $\chi_{E,\mathrm{center}} \sim 20.8°$, albeit roughly $\sim 20\,\%$ off from theoretical limit. It should be noted that one of the main contributors to this discrepancy is the assumption that secondaries in the volume are Maxwellian. Observation of the secondary distribution during simulation will show that this is not the case; however, the general trend in this framework is captured, suggesting the distribution is at least "close to" Maxwellian. Another contributor to the $\sim 20\,\%$ discrepancy is related to the distributed steady-state density near the surface, averaging $\sim 10^{15}\,\mathrm{m}^{-3}$. As the secondaries are weighted to the grid, the calculation of the field angle sees most of the particles weighted towards the surface rather than the grid-points above, meaning the calculation of field angles will bias

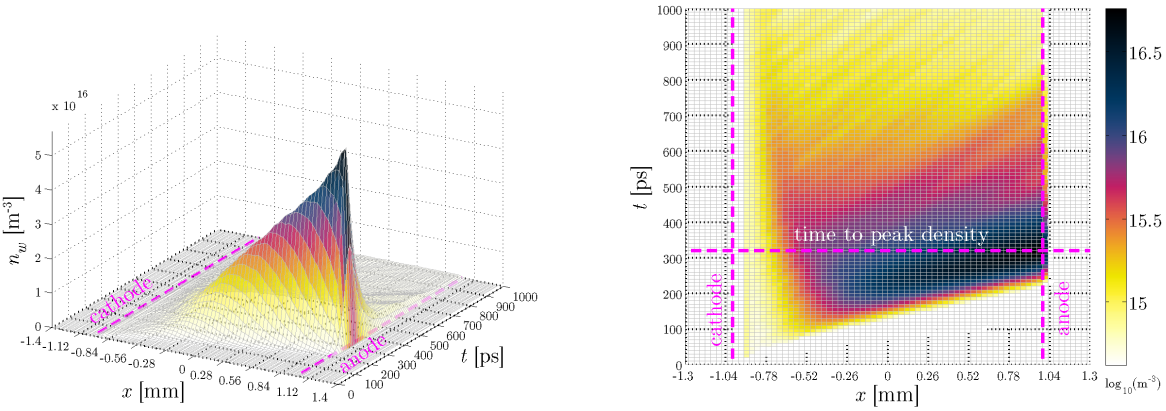


(a) Number-density surface plot.

(b) Number-density plot, $x$ vs. $t$.

Figure 3.9: Plots of the weighted-average density,$n_w$, for secondary electrons over the dielectric surface at $\alpha = 6.12°$. (a) clearly shows the evolution of the multipactor front as it grows from discharge onset until the front evacuates at the anode around $\sim 300\,\text{ps}$ with a slow decay until $\sim 2\,\text{ns}$. The cathode is at $\sim -1\,\text{mm}$ and the anode is at $\sim 1\,\text{mm}$. (b) clearly shows the speed of the front, which can be characterized by the average energy of the ensemble (at the front).

towards *smaller* $\chi_E$. It should be noted that the saturation angle is expected to approach the grazing limit at 24.88°, saturating slightly lower considering the average impact is closer to $\theta_{\text{imp}} \sim 80°$ from Figure 3.8. The saturation field-angle would move to the left along the curve of Figure 3.2b.

Figure 3.11b shows the characteristic markers for a multipactoring discharge with $\alpha = 6.12°$, showing $\delta_{\text{avg}}$ (the secondary-emission coefficient averaged over all impacting electrons) in the solid line and the anode (output) current in the dashed line. Figure 3.11b effectively summarizes Figure 3.9 in terms of the output current. $\delta_{\text{avg}}$ shows an initial spike followed by a slowly decaying tail. The anodic current develops with $\delta_{\text{avg}} > 1$, indicating a multiplicative discharge has developed as a result of secondary emission from the dielectric; a slowly decaying $\delta_{\text{avg}}$ is therefore a good indicator that a multipactor current will be observed. The anodic-current peaks at $\sim 0.3\,\text{ns}$ with a magnitude $\sim 250\times$ larger than the 1 A seed current at the cathode, indicating significant multiplicative growth at "modest" input voltage of 1.75 MV/m (compared to typical breakdown voltages of $> 10\,\text{MV/m}$ for common systems and studies [20]). The multipactor current is seen as a fast-growing initial current spike, with most of the current rise-time integrating over $\sim 50\,\text{ps}$ with the standard 10 % to 90 % rise-time definition. The current decays over $\sim 50\,\text{ps}$ as well, with a 90 % to 10 % fall-time definition, and continues to decay until $\sim 1\,\text{ns}$. After $\sim 1\,\text{ns}$, surface field angles have saturated, leading to the steady-state dark current with average current-magnitude equal to the seed (input) current and $\delta_{\text{avg}}$ asymptotically approaching unity, as described in Section 3.1.1. The maximum gain in terms of particle number is roughly conformal with Figure 3.3d, although the current at the anode is reduced by $\sim 2-3$ orders of magnitude from the maximum gain seen in Figure 3.3d. Equation (3.18) suggests the gains in number and current should be comparable, but the basic assumption made in Equation (3.18) that number and current growth comprises a single generation collected

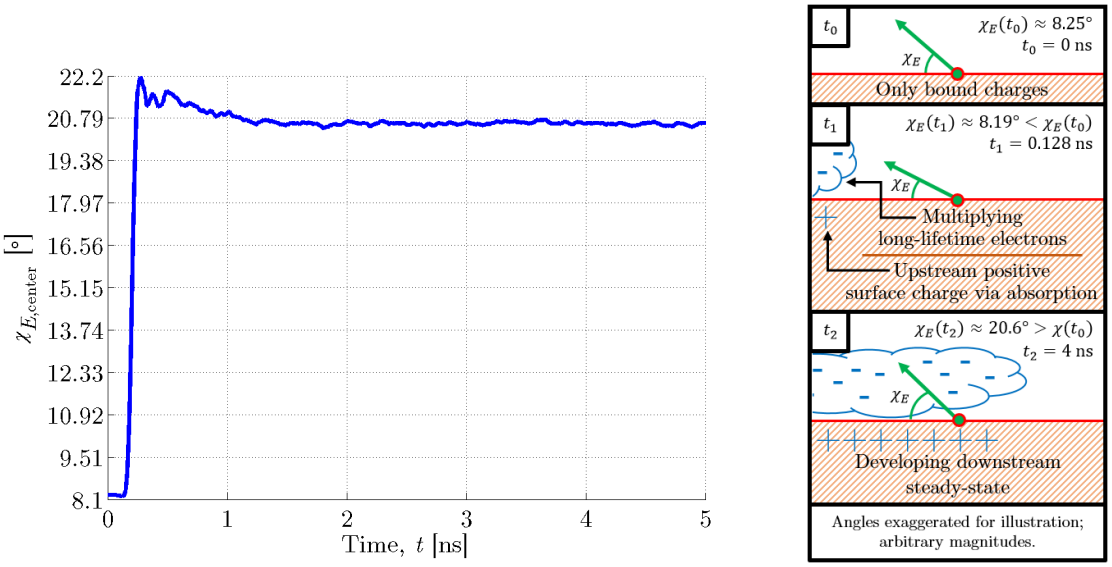


(a) Electric-field plot. (b) Electric-field schematic.

Figure 3.10: Electric-field angle, $\chi_E$ at the center of the dielectric surface vs. time for 6.12 deg. The minimum in (a) is indicative of an approaching multipactor front, and $\chi_E$ grows after the front passes the center until saturation is reached around 1.5 ns, consistent with Figure 3.11.

at a single surface does not hold for a general discharge with distributions in energy and space; consequently, the gain seen in number is reduced down when integrating over finite time, consisting of a variety of generations at varying energies. The initial seeding is a broad beam (in both energy and space) rather than the single-particle seed used in Figure 3.3.

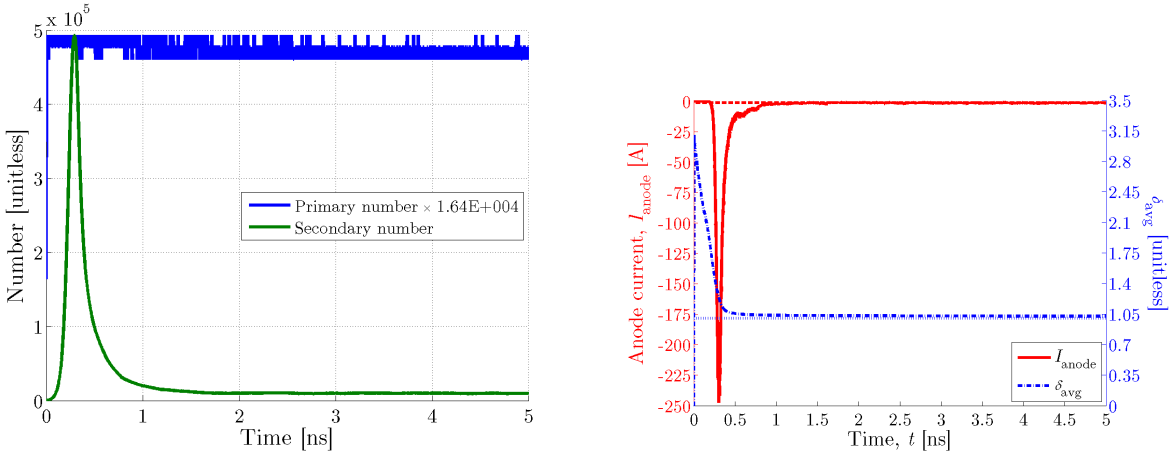


(a) Scaled number (of computational particles). (b) Anode current and $\delta_{\text{avg}}$.

Figure 3.11: Particle number plots and average secondary-emission coefficient, $\delta_{\text{avg}}$, and anode current, $I_{\text{anode}}$, for the case of $\alpha = 6.12°$ in VULP breakdown. Note the time;scale is from 0 ns to 5 ns for later comparison.

### 3.4.2 Dark-Current Steady-State

Increasing the angle of the dielectric will eventually lead to surface-field conditions that cannot support net multiplicative growth past the seeding of a discharge, solely by the field geometry downstream of the initial impact region. Such surface conditions are noted by all regions excluding the "multiplicative region" of Figure 3.2a. In such cases, it is observed that the dielectric charges negative due to the coupled conditions of short lifetimes and low impact energies for emitted secondary electrons, even if there is positive charging enforced upon initial impact. Sufficient negative surface charging results in field reversal and surface-charge repulsion of newly generated secondaries immediately downstream of the initial impact region, leading to highly elongated lifetimes; an arc is formed as evident in the configuration-space plots of Figure 3.12. Figure 3.12a is taken at 4 ns (peak output current starts at $\sim 18$ ns), and Figure 3.12b is taken at 50 ns, showing the fully developed steady-state discharge. Unlike the characteristics of Figure 3.5, it is apparent that the conditions of the discharge significantly affect the field characteristics much earlier than dark-current develops, and trajectory evolution is highly apparent.

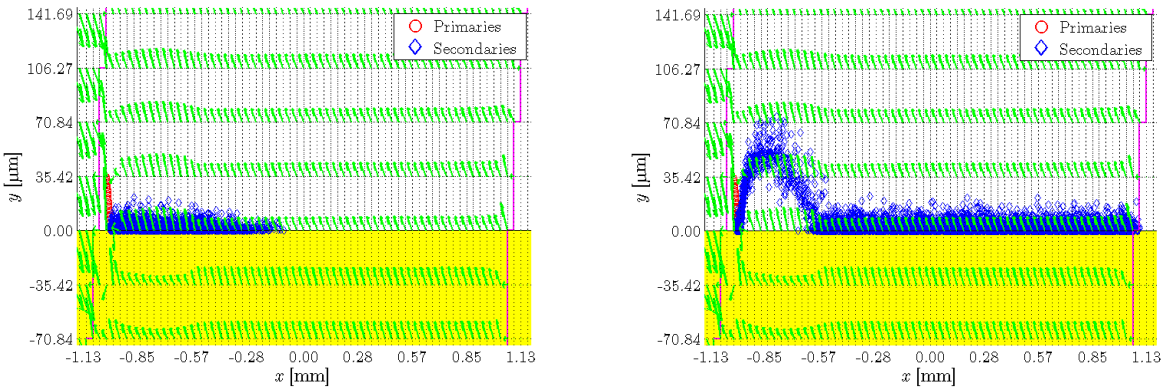


(a) Initial, non-multiplicative discharge.

(b) Steady-state discharge.

Figure 3.12: Configuration-space example of VULP breakdown at 22.9°. Primary and secondary electrons move from the lower cathode potential on the left to higher anode potential on the right. Primary electrons are absorbed at the dielectric (shaded region, $y < 0$), emitting secondaries according to the theory outlined in Section 2.3. Time in (a) is 8 ns, and time in (b) is 50 ns. The grid shown corresponds to the numerical grid, with a square-grid spacing of 35.5 µm in $x$ and $y$. No SRP.

Figure 3.13 illustrates the positive charging at the initial-impact site, and the more obvious existence of the negatively charged immediate-downstream region noted in Figure 3.13 for 6.12°, followed by largely negative surface charging for the remainder of the dielectric. The charging behavior near initial impact is dependent on the initial conditions of the seed, so there will be similarities in the early features in Figure 3.13 (at the picosecond scale) compared with Figure 3.6. Field reversal at the initial-impact region generates an arc over the surface with a width of $\sim 0.5$ mm at 50 ns, interestingly flanked by the immediate-downstream region of the initial-impact on the upstream side, and an analogous region of low-energy absorption that migrates with the arc on the downstream side. The arc generally consists of longer-lived particles with higher energies, so

distributed particles outlying the main arc that impact the dielectric will likely lead to positive charging, hence the region below the arc is positively charged. Past the arc, downstream surface-field conditions dominate discharge evolution, and the remainder of the surface charges negatively due to short lifetimes with minimal energy gain, consistent with the predictions of Figure 3.2a.

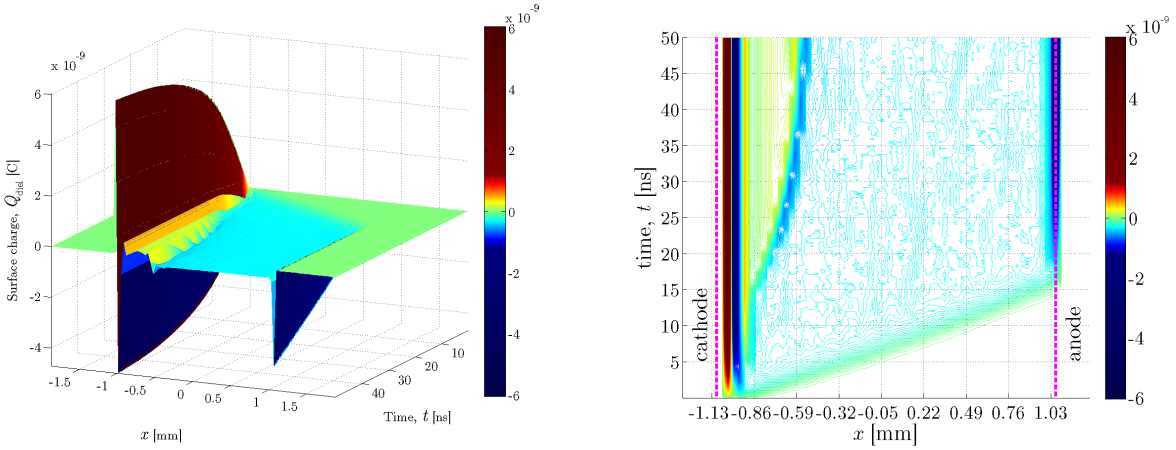


(a) Dielectric-charge full profile.

(b) Dielectric charge contour in $x$ against $t$.

Figure 3.13: Characteristic dielectric-surface charging for a non-multipactoring discharge at 22.9°. Parameters from Table 2.7 are used. 50 ns are plotted. Negative charging is shown for most of the dielectric, indicating surface characteristics that are insufficient for multiplicative breakdown. This plot is the analog to Figure 3.6 for the case of non-multiplicative, dark-current steady-state discharge.

Figure 3.14 shows the electron energy distribution functions for the discharge at 22.9°. Figure 3.14a simply confirms the initial conditions where the seed is guaranteed to generate secondaries upon initial impact. Figure 3.14b is the analog to Figure 3.7b, showing significant variations in energy characteristics as initial downstream conditions differ substantially. Secondary energy distributions at emission are specified, so the differences in secondary EDF's are a function of surface conditions. The conditions for the discharge in Figure 3.7b allow for longer secondary lifetimes and consequent energy gain, producing secondaries with energies up to applied voltage. The highest energies in Figure 3.14 are a result of the arc, mentioned above, while the remainder of the downstream surface corroborates the limited lifetimes and consequent energy gain. In principle, sufficient surface charge could create an arc from initial impact directly to the anode, or from cathode seed directly to anode (leading to a vacuum arc); however, neither of these effects have been observed in typical configurations for this study.

Analogous to Figure 3.8, Figure 3.15 shows the primary cluster around the peak of the $\delta(\theta_{\text{imp}} = 32.0°)$ curve, while the secondaries are impacting largely at grazing incidence. The angular distribution characteristics in Figure 3.15 are very similar to that shown in Figure 3.8, with most secondary impacts approaching grazing incicidence, primaries impacting at $\sim 30°$, and a similar spread down to smaller angles as in Figure 3.8 occurring at the low-energy end, about five orders of magnitude smaller than the peak at $\theta_{\text{imp}} = 80°$. Similarities are largely a consequence of low emission energy, again, typically in the eV

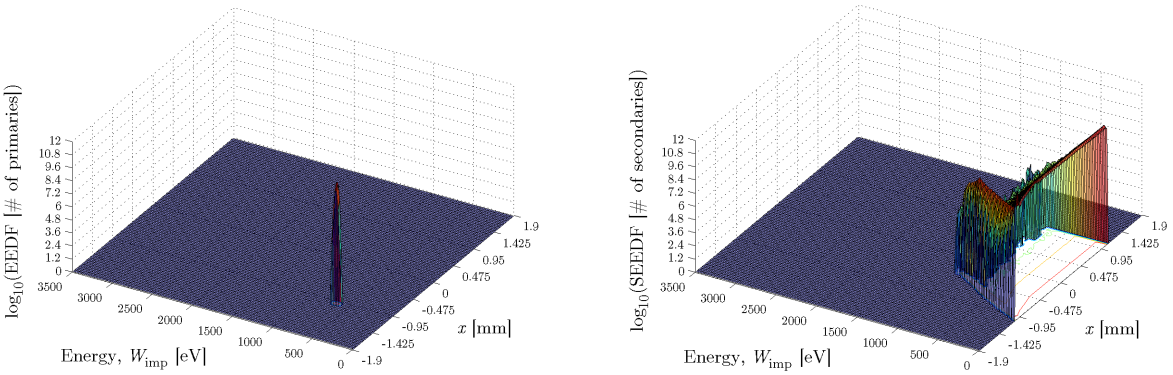


(a) Primary-electron EDF.

(b) Secondary-electron EDF.

Figure 3.14: Primary-electron and secondary-electron energy distributions functions (EDFs) on the dielectric surface for 22.9°. The primary EDF in (a) shows the largely monoenergetic beam consistent with initial conditions. The secondary EDF in (b) is more distributed than the primaries, similar to Figure 3.7b since secondaries are emitted with the same distribution parameters.

range for dielectrics so that typical energy gains are often translated to grazing incidence.

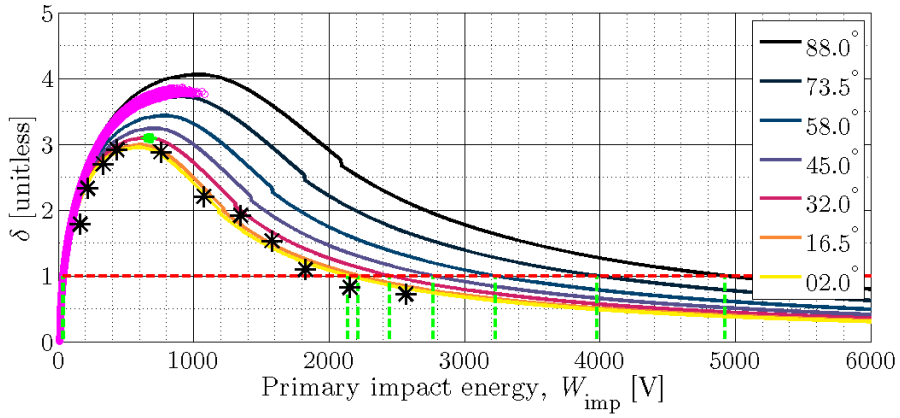


(a) Secondary-emission coefficient vs. impact energy at various impact angles.

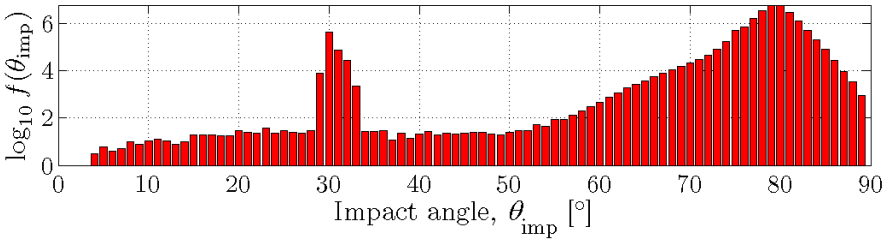


(b) Impact angular distribution.

Figure 3.15: Reconstructed secondary-emission curve from simulation for 22.9°. This plot is the dark-current analog to Figure 3.8, plotted for a simulation time of 50 ns (10× longer than Figure 3.8).

Figure 3.16 illustrates the formation of the near-surface secondary-electron density,

which remains relatively low throughout the discharge by about two orders of magnitude at peak compared to the $\alpha = 6.12°$ case of Figure 3.11. Net negative charging results from impact energies with $\delta < 1$ along the surface until surface-field angle conditions are reduced sufficiently in accordance with the discussion of Section 3.1.1. The non-multiplicative, negative-charge front slowly creeps downstream as the surface is saturated until $\sim 20$ ns when steady-state dark current has fully developed. The influence of the arc characteristic in Figure 3.12 are also observable in Figure 3.16b with the evacuated density region between that grows along $x$ and shows a saturating characteristic with a width of $\sim 0.41$ mm (between $\sim -1$ mm and $\sim -0.59$ mm) at 50 ns. Similar to the 6.12° discharge, the system eventually reaches a steady-state over the surface with roughly uniform secondary-electron density (albeit, past the arc), but the discharge takes significantly longer to reach steady-state conditions; the fully saturated surface conditions in Figure 3.16 after 20 ns have similar magnitudes to the fully developed dark-current steady state after 2 ns in Figure 3.9, averaging $\sim 10^{15}$ m$^{-3}$, as should be expected for an ensemble unit gain of a similar seed. It is obvious that the multipactor front of Figure 3.9 does not form in cases of larger dielectric angles, as in Figure 3.16, but is replaced by a creeping front that is effectively pushed downstream after sufficient upstream charge has pushed fields to support emission at unit gain.

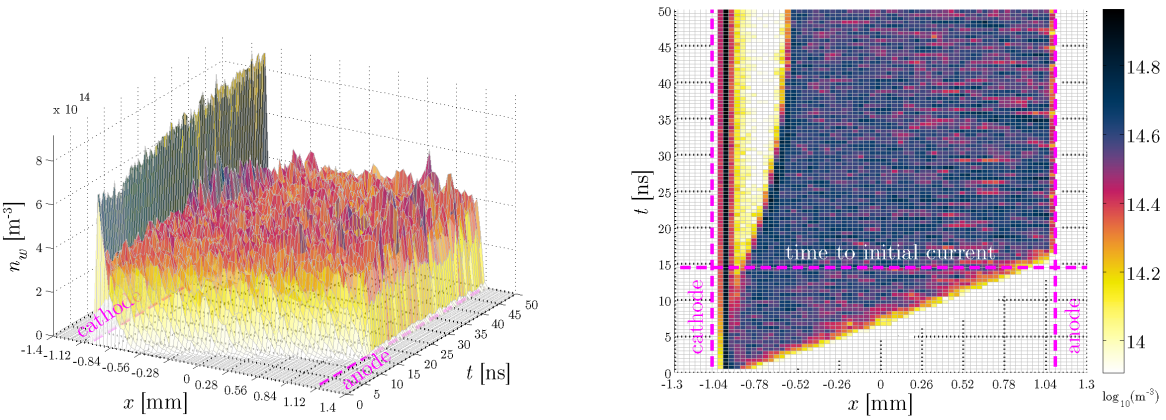


(a) Number-density surface plot.

(b) Number-density plot, $x$ vs. $t$.

Figure 3.16: Plots of the weighted average density, $n_w$, for secondary electrons over the dielectric surface at $\alpha = 22.9°$. Notice the lack of a multipactor front development and evolution as there was for $\alpha = 6.12°$ in Figure 3.9. The cathode is at $\sim -1.1$ mm and the anode is at $\sim 1.1$ mm. The appearance of a clear front is not seen in (a) nor in (b), and the development of anodic current can be seen in (b) to start at $\sim 15$ ns, reaching peak steady-state current at $\sim 20$ ns.

It is, again, possible to visualize the drive to steady-state via surface-field diagnostics as shown in Figure 3.17, plotting the temporal evolution of the surface-field angle at the center of the dielectric analogous to Figure 3.10. It is evident that the initial surface-field angle is well within the "absorption region" of Figure 3.2. The discharge evolution brings the field angle down until saturation is reached at $\chi_{E,\text{center}} \sim 20.5°$, where most secondaries are impacting with energies around $W_1$. Again Figure 3.2 suggests saturation around $\chi_{E,\text{center}} \sim 24.88°$, for grazing-impact characteristics. As is the case for 6.12°, the

saturation angle in Figure 3.17 is otherwise lower than formally expected from, considering the average impact is similarly closer to $\theta_{\text{imp}} \sim 80°$ from Figure 3.15. Similar to the 6.12°-case, the saturation field angle would be slightly larger than $\chi_{E,\text{center}} \sim 20.5°$, again, moving to the right along the curve of Figure 3.2b. The contributors to this discrepancy remains the same as the 6.12°-case, i.e. secondaries are not Maxwellian in the volume, and weighting of secondaries to the grid leads to a field biased towards smaller $\chi_E$.

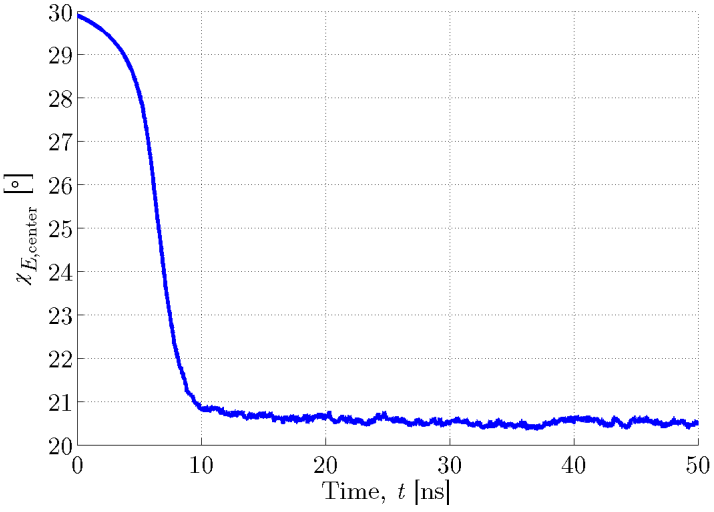


(a) Electric-field plot.

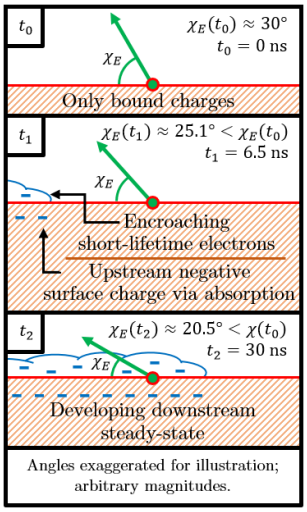


(b) Electric-field schematic.

Figure 3.17: Electric-field angle, $\chi_E$ at the center of the dielectric surface vs. time for 22.9 deg. This temporal profile is characteristic of much of the dielectric, where the field starts off well in the region of non-multiplicative conditions as noted in Figure 3.2. As the dielectric is charged more negatively, the field angle is reduced, creating longer lifetimes and saturating impact energies at $W_1$ once the (slow, non-multiplicative) front passes at $\sim 10$ ns.

Figure 3.18b for $\alpha = 22.9°$ shows the characteristic markers for a discharge dominated by a non-multiplicative dark-current steady-state. Dielectric-surface field conditions lead to short lifetimes for the, on average, low-energy secondaries, resulting in rapid decay times for the $\delta_{\text{avg}}$ diagnostic that quickly decays below unity due to short-lived secondaries. Low-energy secondaries are absorbed almost immediately at the dielectric, noting that much of the surface is in the "absorption region" of Figure 3.2. $\delta_{\text{avg}}$ is slowly driven up with sufficient negative charging on the dielectric surface, leading to longer lifetimes and higher energy gain. A dark current is eventually observed at the anode, saturating with an average magnitude equal to the seed current. A multipactor front never forms in this case, but a non-multiplicative front slowly creeps towards the anode as the surface field angles reduce to support secondary emission at $\delta \sim 1$ with impact energies at $W_1$. The immediate drop of $\delta_{\text{avg}}$ below unity as in Figure 3.18b is a good indicator that this discharge will not undergo multipactor growth.

It is of interest to note that the drive to steady-state in the 6.12° case is faster than the 22.9° case, paying particular attention to the time scales between Figure 3.11 and Figure 3.18. This difference is a result of faster surface charging in multipactor, proportional

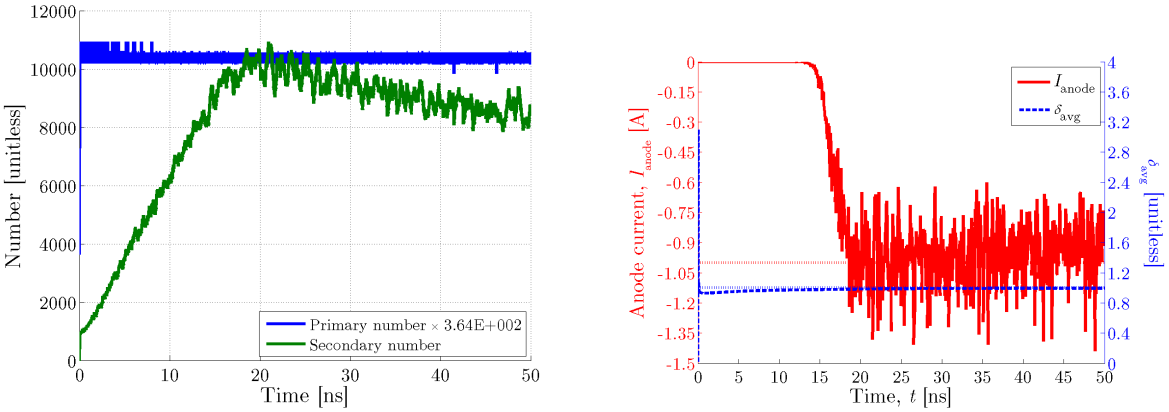


(a) Scaled number (of computational particles).

(b) Anode current and $\delta_{avg}$.

Figure 3.18: Particle number plots and average secondary-emission coefficient, $\delta_{avg}$, and anode current, $I_{anode}$, for the case of $\alpha = 22.9°$ in VULP breakdown. Analogous plot to Figure 3.11 for a dielectric angle $\alpha = 22.9°$. Note the time scale is from 0 ns to 50 ns, ten times as long as for Figure 3.11.

to both the seed current and an exponential growth factor with $\delta_{avg} > 1$, as in Equation (3.18), rather than, effectively, just the seed current in the dark-current dominated regime.

## 3.5 The Influence of Scattered and Reflected Particles

As per [45], the SRP fractions are set to 7 % and 3 %, respectively. SRP is important because of the myriad of possible influences downstream as a result of larger average energies in the SRP group with associated longer lifetimes and larger impact energies. SRP can initiate microsites of multiplication and dielectric charge forward of the main multipactor front while also carrying significant energy downstream. SRP carry a spectrum of energies that can lead to positive or negative charging of the dielectric depending on subsequent impact characteristics. Reflected particles will carry the full energy of the original particle, which can be relatively high (continually gaining energy via effectively prolonged excursions in the applied field) and is more likely to contribute to ionization and outgassing further downstream (treated in Chapter 4) that seeds additional reactions. In the case of VULP, the phenomenological influence of SRP is minimal, leading to minor variations in key characteristics. Figure 3.19 shows $\delta_{avg}$ with the anode current, showing similar characteristics to Figure 3.11b but with a smaller peak magnitude and a slightly longer rise time. The peak current is reduced by $\sim 25$ %, largely explained by an overall reduced density in the peak since the multipactoring population is reduced by the percentage of particles undergoing scattering and reflection. Effectively, the secondary population is more distributed spatially and energetically, with 10 % of the population effectively integrated over a different temporal range than their otherwise low-energy analogs in Figure 3.11b.

The electric-field angle is shown in Figure 3.20, to be compared directly to Figure 3.10. The minimum field angle and time-to-minimum are similar, while moving into a steady-

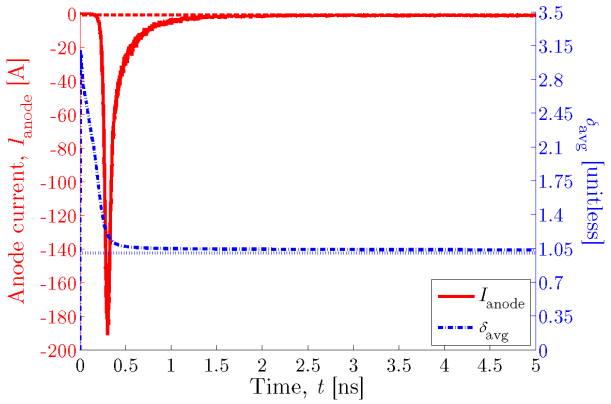


Figure 3.19: Average secondary-emission coefficient, $\delta_{\text{avg}}$, and anode current, $I_{\text{anode}}$, for the case of $\alpha = 6.12°$ in VULP breakdown with SRP. Note the time scale is from 0 ns to 5 ns.

state discharge shows some minor variations in field-angle magnitude and saturation characteristics around 5 % with respect to the case without SRP. Interestingly, the saturation angle in Figure 3.20 with SRP is slightly higher than in Figure 3.10 without SRP. This is likely a numerical effect where an increased number of particles in the SRP case are further away from the dielectric surface in the volume and accordingly weighted to the grid, increasing the field angle; this is in the same vein as the generally reduced angles from that predicted in Figure 3.2b, resulting from numerical weighting to the surface that biases all angles down.

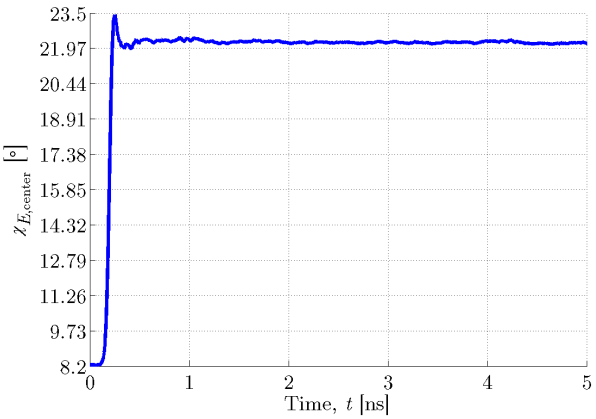


Figure 3.20: Electric-field angle, $\chi_E$ at the center of the dielectric surface vs. time for 6.12 deg with SRP. The minimum is indicative of an approaching multipactor front, and $\chi_E$ grows after the front passes the center until saturation is reached around 1.5 ns, consistent with Figure 3.11b.

## 3.6 The Influence of Ionization on VULP Breakdown

As noted in Section 3.3, the background pressure for the discharges in this section is $p_{\text{bg}} = 500\,\text{mTorr}$. For Section 3.6.1 and Section 3.6.2 ion collisions are neglected, but

reintroduced for discussion in Section 3.6.3.

### 3.6.1 Multiplicative Transient

Similar to Section 3.4.1, this section details discharges with an early, fast transient largely composed of multipactoring electrons via the seed, followed by a slower transient composed of both multipactoring electrons via the seed and additional ionization electrons. Dielectric-surface field conditions during the early transient are similar to those encountered in Section 3.4.1 even with low collisionality inducing some minor space-charge variations. As will be shown, field conditions are in the multiplicative region of Figure 3.2 through the early transient until space-charge becomes significant with sufficient ionization, leading to additional ionization-assisted multiplication until saturation.

Ionization introduces charged-particle species into the bulk volume that, of course, have implications for space charge and local-field variations not seen in the pure vacuum case; additionally, new electrons from ionization can contribute to secondary-emission growth at all surfaces. Unlike the multipactor front coupled to the initial seed, ionization electrons have a broader impact-energy spectrum with trajectories that differ significantly from the trajectories of electrons coupled to the initial seed. Figure 3.21 most importantly illustrates that although the impact angular space is sampled more than in Figure 3.8 (i.e. particles impact with a broader spectrum in $\theta_{\text{imp}}$), the majority of secondaries impacting the surface still approach grazing incidence (upwards of two orders of magnitude larger in $f(\theta_{\text{imp}})$) and the discharge evolution is largely understood through the mechanisms encountered and discussed in Section 3.4. There is a clear upper limit for the secondaries in terms of impact energy, which is the order of the applied voltage, since secondaries typically start with energies in the eV range; on the other hand, primaries are injected with a few hundred eV, so deflected primaries that span the full gap width can reach an upper energy limit of the injected energy plus applied voltage.

The evolution of the electric-field angle, shown in Figure 3.22 for a characteristic surface point at the dielectric center, is consistent with the theory of Section 3.1.1. Similar to Figure 3.10, the early transient shows a slight, initially increased favoring of multipactoring conditions prior to $\sim 150\,\text{ps}$ due to an upstream increase in electrons and consequent reduction of $\chi_E$ that can push the discharge further into the multiplicative region of Figure 3.2. Figure 3.10 past 2 ns is in saturation (recalling that the saturation angle is roughly consistent with the expected angle in Figure 3.2 at grazing incidence), with similar characteristics for the initial transient in Figure 3.22a up to 5 ns. Past 5 ns in Figure 3.22b, ions have built significant momentum towards the cathode, and the coupling of the evacuating ion cloud (via the cathode) with positive charging on the surface results in surface-field conditions that move towards the multiplicative region in Figure 3.2, and can approach initial conditions with sufficient ion momentum. Ion-assisted multiplication follows, leading to additional anodic current past the initial transient as shown in Figure 3.23b, where the current past 5 ns is not seen in Figure 3.11b for vacuum at 6.12°. Particle fluxes to the boundaries eventually equilibrate with particle sources in the volume, leading to population saturation after $\sim 200\,\text{ns}$ as in Figure 3.24; additionally, the electric-field angle in Figure 3.22 saturates at $\sim 20.7°$ as it does for Figure 3.10. Of note is the tracking of electron population with ion species after the initial fast transient in Figure 3.24a, even in the case of primaries, which results from collisions spreading the spatial distribution

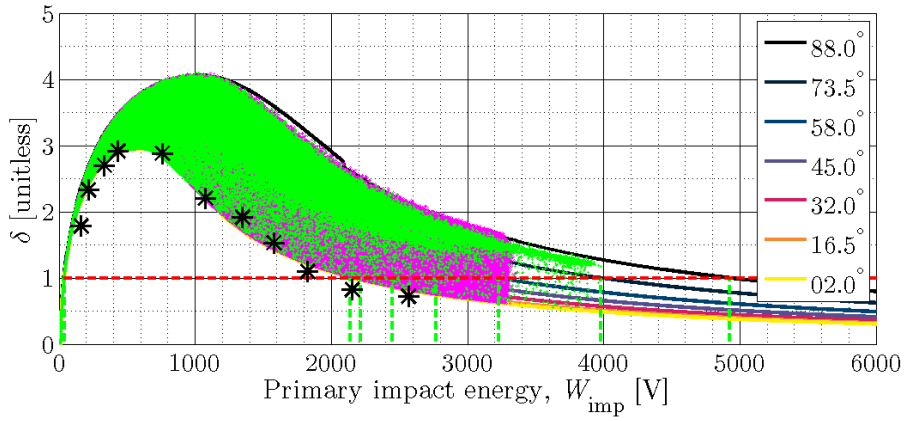


(a) Secondary-emission coefficient vs. impact energy at various impact angles.

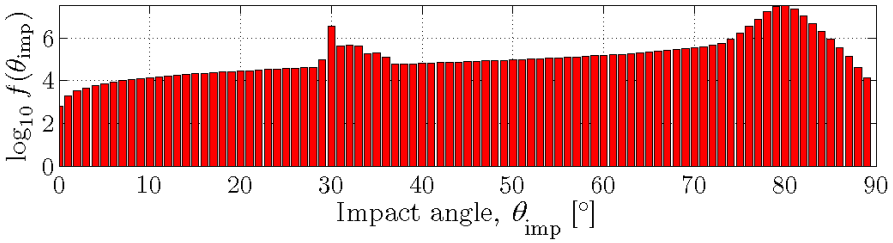


(b) Impact angular distribution.

Figure 3.21: Reconstructed secondary-emission curve from simulation for 6.12° with background pressure of 500 mTorr. Simulation time is 5 ns. Analogous to Figure 3.8 for higher collisionality, but still negligible compared to the multipactor effect in the early transient. (b) shows that $\theta_{\text{imp}}$ clearly samples more of the impact-angle domain than in Figure 3.8, but most particles are still impacting with grazing incidence.

of primaries and growing local space charge near the cathode elongating lifetimes. An envelope function is fitted to the peaks using non-linear regression, following a simple exponential model with non-zero steady-state tail:

$$N = N_0 \exp\left(-\frac{t}{\tau}\right) + N_{\text{ss}} \tag{3.30}$$

The fit is plotted in Figure 3.24b. The pre-exponential, $N_0$, is $2.318 \times 10^5$, the steady-state constant, $N_{\text{ss}}$, is $1.022 \times 10^5$, and the damping time constant, $\tau$, is $\sim 92.91$ ns. It is clear that the 6.12° discharge is underdamped about the steady-state number in Figure 3.24b.

Finally, it must be noted that the oscillations are driven by the ion momentum and ion plasma frequency, as evidenced by Figure 3.25. Figure 3.25a shows the Fourier-transformed number plot, showing primary frequencies in the MHz range, while Figure 3.25b shows that electron plasma frequencies are in the GHz range and Ar plasma frequencies are in the MHz range.

### 3.6.2 Non-Multiplicative Transient

Similar to Section 3.4.2, this section details discharges lacking early, fast transients that are typical of the discharges in Section 3.4.1 and Section 3.6.1. Noted in Section 3.4.2, the

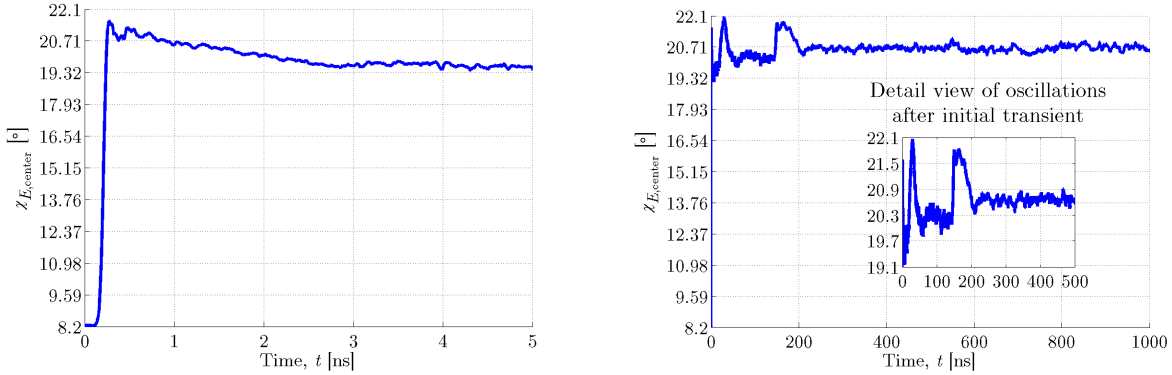


(a) Up to 5 ns. (b) Up to 1000 ns = 1 µs.

Figure 3.22: Electric-field angle, $\chi_E$ at the center of the dielectric surface vs. time for 6.12 deg, 500 mTorr. No ion collisions. These plots are analogous to Figure 3.10 for the vacuum case. Saturation characteristics are to be compared to Figure 3.2 in Section 3.1.1.

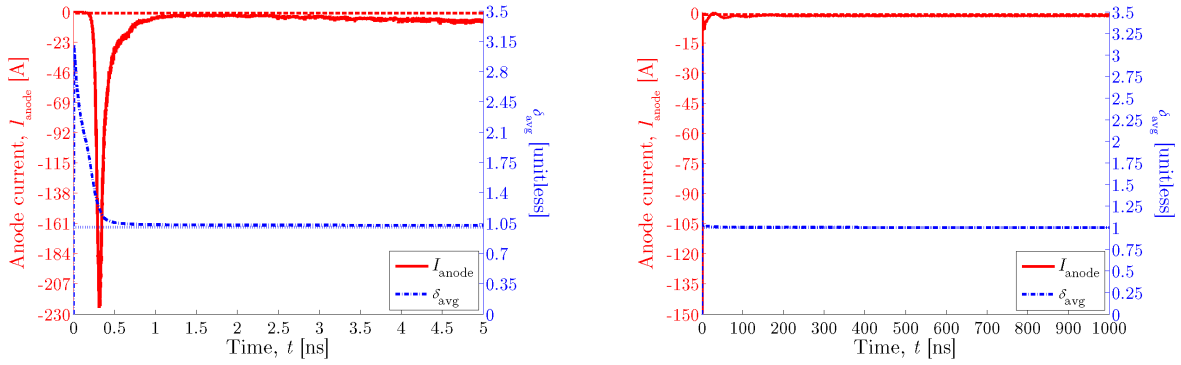


(a) Up to 5 ns. (b) Up to 1000 ns = 1 µs.

Figure 3.23: Average secondary-emission coefficient, $\delta_{\text{avg}}$, and anode current, $I_{\text{anode}}$, for the case of $\alpha = 6.12°$ in VULP breakdown, 500 mTorr. No ion collisions. Note the time scale for (a) is from 0 ns to 5 ns, to be compared directly to Figure 3.11. The time scale for (b) is from 0 ns to 1 µs to illustrate ion-assisted multiplicative growth.

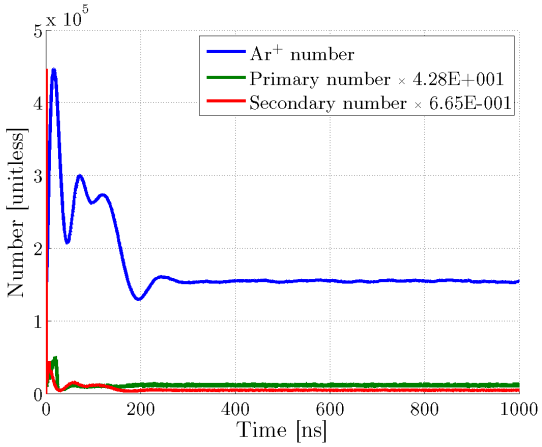


(a) Scaled number (of computational particles).

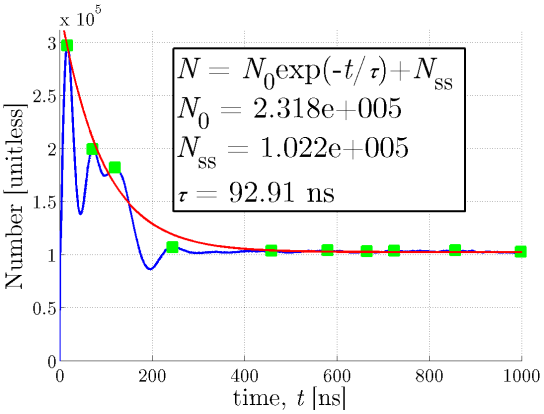


(b) Argon with fit.

Figure 3.24: Particle number plots for computational particles from simulation for 6.12° with background pressure of 500 mTorr. No ion collisions. Oscillations driven by ion momentum and population. Saturation after 600 ns results from equilibrated particle creation (via seed, secondary emission, and ionization) with particle losses to the boundaries. Damping is characterized in (b), using Ar number since oscillations are driven by the Ar plasma frequency. Oscillations in number for 6.12° are underdamped.

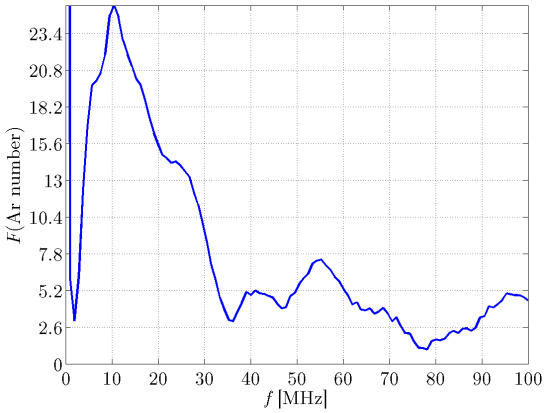


(a) Ar number in frequency space.

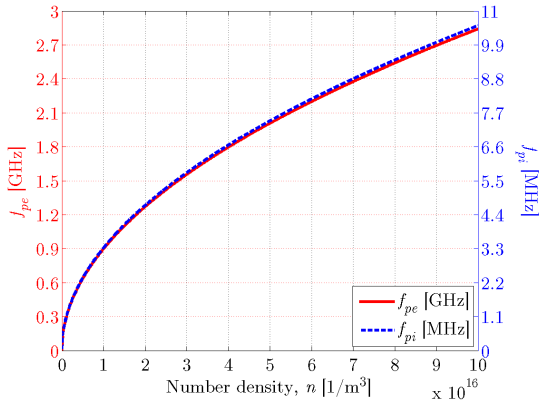


(b) Electron and ion plasma frequencies.

Figure 3.25: Fourier transform of $Ar^+$ number history compared to electron and ion plasma frequencies. Neutral argon pressure is 500 mTorr, with no ion collisions, and $\alpha = 6.12°$. Characteristic frequencies in Figure 3.25a match the ion plasma frequency in Figure 3.25b; therefore, oscillations are driven by ion momentum and population.

initial dielectric-surface field conditions do not favor surface growth, with field angles in the non-multiplicative regions of Figure 3.2. With sufficient ionization and subsequent ion momentum leading to distributed space-charge, field conditions evolve to allow dielectric-surface multiplication through a slow transient, similar to the slow transient seen in Section 3.6.1 past 2 ns when the early, fast transient has effectively saturated out.

Figure 3.26 is the analog to Figure 3.15 at 500 mTorr. Some similarities in impact characteristics are seen compared to Figure 3.21 at 6.12°, such as a larger impact-angle spectrum compared to the analogous plot without ionization (Figure 3.15) while maintaining mostly grazing incidence. However, the early discharge characteristics at 22.9° are dominated by non-multiplicative conditions with particles in the absorption regions of Figure 3.2, corroborated with Figure 3.27a. Coupling of surface charge and ionization (with momentum) pushes the dielectric-surface field conditions into the multiplicative regions of Figure 3.2 in a similar way to that shown in Figure 3.22b; however, the time to the slow-transient, ion-assisted buildup takes longer than the analogous buildup in Figure 3.22b due to reduced gain from surface multipactor at 22.9°, hence fewer electrons at the surface to seed ion-assisted gain in the volume.

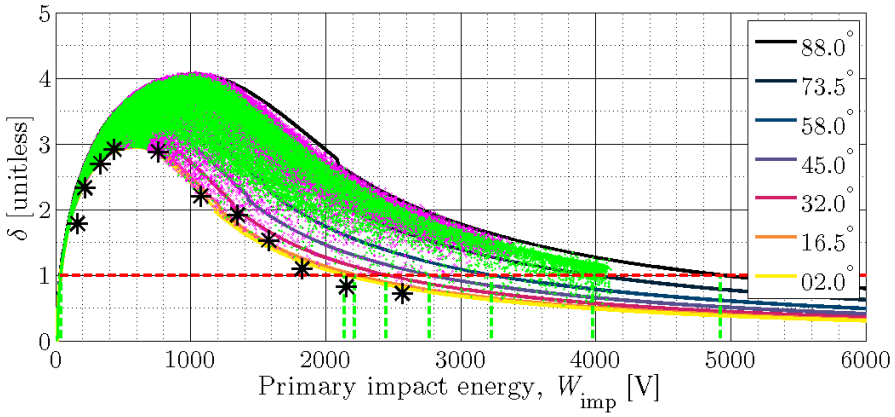


(a) Secondary-emission coefficient vs. impact energy at various impact angles.

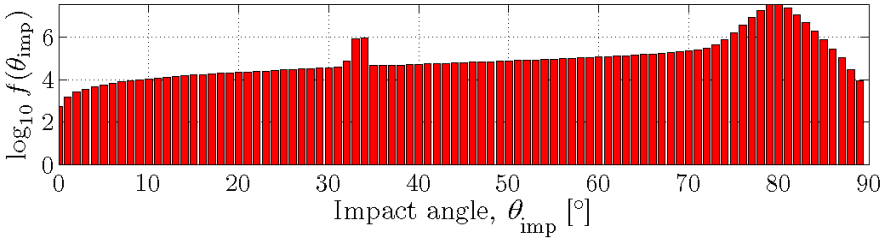


(b) Impact angular distribution.

Figure 3.26: Reconstructed secondary-emission curve from simulation for 22.9° with background pressure of 500 mTorr. Simulation time is 50 ns. Analogous to Figure 3.15 for higher collisionality, but still negligible compared to the multipactor effect in the early transient. $\theta_{imp}$ is more distributed here than in Figure 3.15, but most particles are impacting with grazing incidence.

Again, similar to Figure 3.18, the output current in Figure 3.28a does not show an early transient with $\delta_{avg}^{ens} < 1$ still applicable to the early discharge characteristics without being

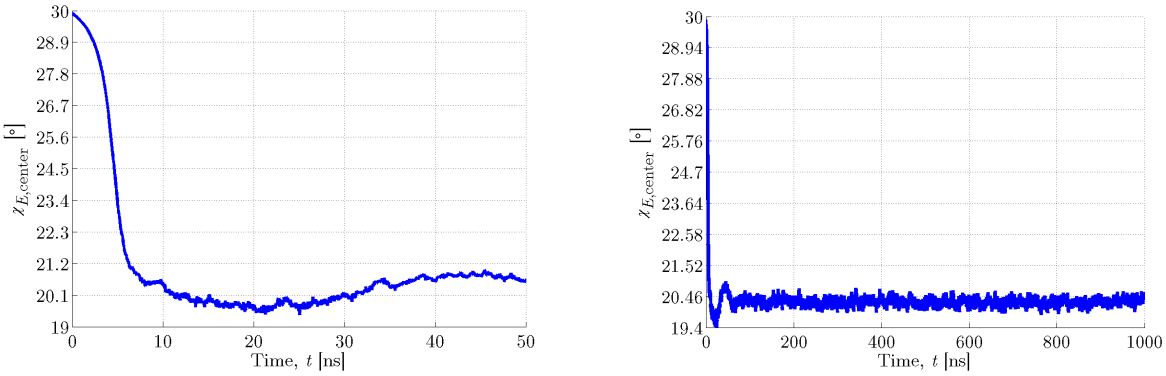


(a) Up to 50 ns. (b) Up to 1000 ns = 1 µs.

Figure 3.27: Electric-field angle, $\chi_E$ at the center of the dielectric surface vs. time for 22.9 deg, 500 mTorr. No ion collisions. These plots are analogous to Figure 3.17 for the vacuum case. Saturation characteristics are to be compared to Figure 3.2 in Section 3.1.1.

dominated by ion-assisted growth. Ion-assisted current does develop in this discharge with sufficient time ($\sim$ 18 ns to peak current), and experiences smaller oscillatory behavior than that shown at 6.12°. The output current saturates to the input current with sufficient time as in Figure 3.28b with population saturation as in Figure 3.29, occurring with equilibrated ionization and removal at the boundaries.

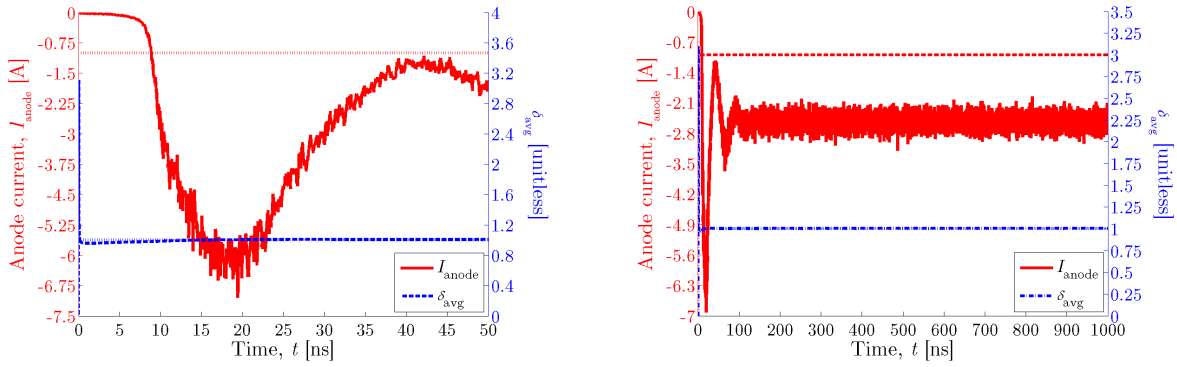


(a) Up to 50 ns. (b) Up to 1000 ns = 1 µs.

Figure 3.28: Average secondary-emission coefficient, $\delta_{\text{avg}}$, and anode current, $I_{\text{anode}}$, for the case of $\alpha = 22.9°$ in VULP breakdown, 500 mTorr. No ion collisions. Note the time scale for (a) is from 0 ns to 50 ns, to be compared directly to Figure 3.18b. The time scale for (b) is from 0 ns to 1 µs to illustrate ion-assisted multiplicative growth.

As in Figure 3.24a, the tracking of electron population with the ions, particularly noting the primaries, is evident in Figure 3.29a and incidentally clearer due to the lack of the fast transient. An envelope function is, again, fitted to Ar number peaks using non-linear regression, following Equation (3.30). The fit is plotted in Figure 3.24b, with $N_0 = 2.435 \times 10^5$, $N_{\text{ss}} = 2.687 \times 10^3$, and $\tau = 25.64$ ns. The 22.9° discharge is underdamped about the steady-state number in Figure 3.29b, taking shorter time to approach $N_{\text{ss}}$ than at 6.12°.

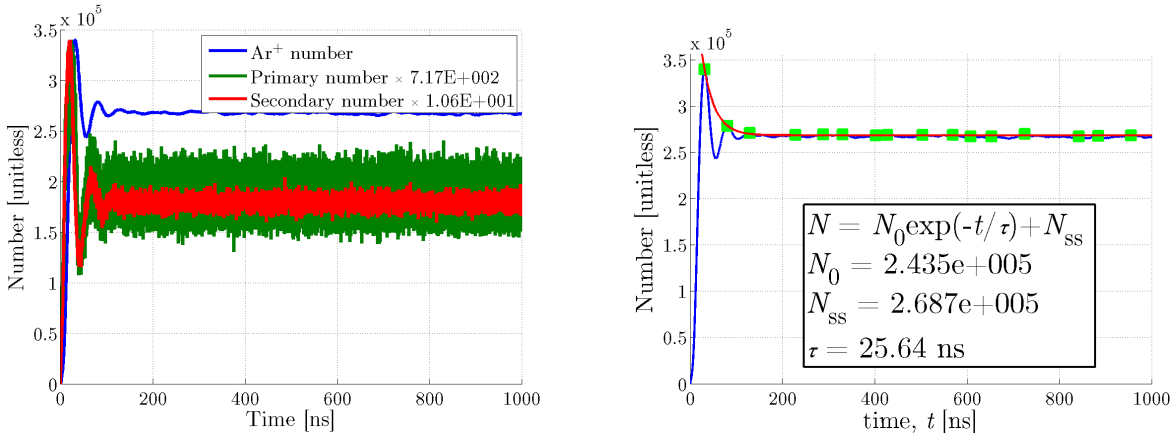


(a) Scaled number (of computational particles).

(b) Argon with fit.

Figure 3.29: Particle number plots for computational particles from simulation for 22.9° with background pressure of 500 mTorr. No ion collisions. Large amplitude driven by ion momentum and population. Although not apparent at the scale shown, the temporal characteristic of each number plot is a highly damped oscillation. Damping is characterized in (b), using Ar number since oscillations are driven by the Ar plasma frequency; 22.9° is underdamped as in 6.12°, c.f. Figure 3.24b.

### 3.6.3 The Effect of Ion Collisions

Ion collisions effectively create a drag on ion momentum, reducing the magnitude of the oscillatory transient, but overall maintaining the general behavior described in Section 3.6.1 and Section 3.6.2. In the case of $\alpha = 6.12°$, plots analogous to Figure 3.24 but including $Ar^+$ collisions (elastic scattering and charge-exchange) are shown in Figure 3.30. As expected, magnitudes in the number plot of Figure 3.30a with ion collisions are slightly larger at all times compared to the collisionless case since reduced ion momentum allows more ions to remain in the volume longer. From the characteristics of the envelope function in Figure 3.30b, steady-state number is increased by roughly a factor of two while the decay time constant in the envelope function is also increased significantly as the reduced momentum pulls decay further out in time.

Similarly analogous plots to Figure 3.29 but including $Ar^+$ collisions are shown in Figure 3.31. As with Figure 3.31, the case of $\alpha = 22.9°$ shows increased overall magnitudes of the total electron and $Ar^+$ number in the volume, increased steady-state values by a similar factor of two as was the case for 6.12°, and increased decay time-constant in the envelope function consistent with reduced ion momentum.

One final note is that the inclusion of drag breaks the simple model of Equation (3.30). Peaks in Figure 3.31b are markedly harder to identify, so the decay constant should be taken with some caution.

## 3.7 Comments on Methods for VULP Suppression

Although this study will not directly address suppression, it must be emphasized that the results in this chapter indicate that the dielectric-surface conditions are the driving

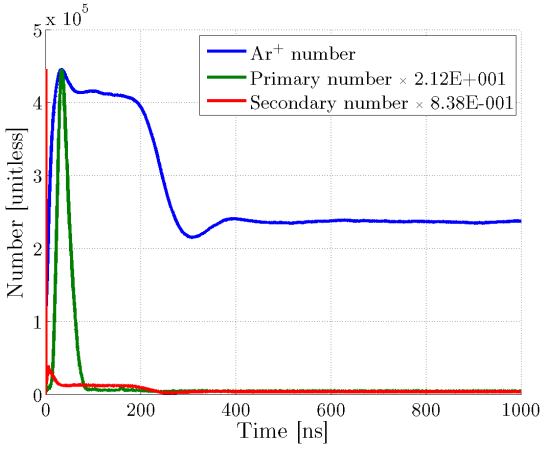


(a) All species, scaled.

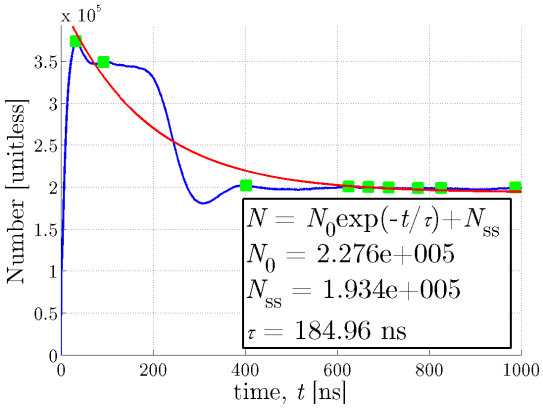


(b) Argon with fit.

Figure 3.30: Particle number plots from simulation for 6.12° with background pressure of 500 mTorr, including ion collisions. Analogous plot to Figure 3.24, but including $Ar^+$ elastic collision and charge exchange. Damping is characterized in (b), showing reduced damping resulting from slower ion momentum. 6.12° still remains underdamped compared to 22.9°, c.f. Figure 3.31b.

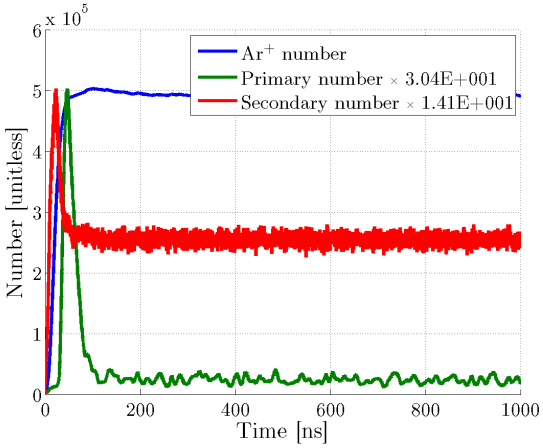


(a) All species, scaled.

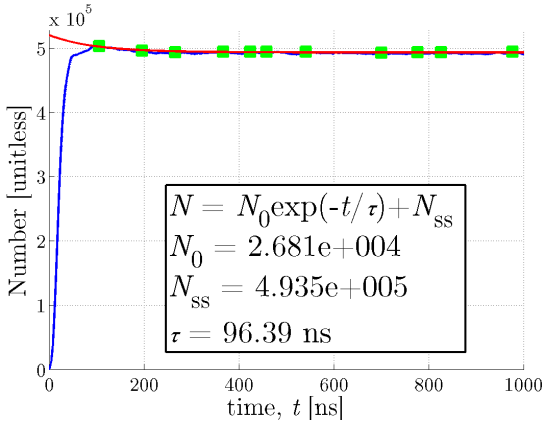


(b) Argon with fit.

Figure 3.31: Particle number plots from simulation for 22.9° with background pressure of 500 mTorr, including ion collisions. Analogous plot to Figure 3.29, but including $Ar^+$ elastic collision and charge exchange. Damping is characterized in (b), showing reduced damping resulting from slower ion momentum. 22.9° is underdamped as in 6.12°, c.f. Figure 3.24b.

factor of multiplicative discharges with negligible collisionality compared to multipactor growth. The nature of the imposed beam-like seed current suggests that the seed can initially impact anywhere along the dielectric, and as long as dielectric-surface field conditions are sufficient for growth according to Section 3.1.1, particularly Figure 3.2, multipactor will occur. In principle, this is a more general condition than that presented in [12], which focused on field conditions and characteristics near the triple-point to determine likelihood of breakdown as discussed in Section 1.3.1.

From considerations in Section 3.1.1, these results support techniques for surface-charge preconditioning whereby either positive or negative initial surface charge can be used to push the system into non-multiplicative regimes of Figure 3.2. $W_1$-saturation would be achieved with an initial positive-charge preconditioning over the surface that shortens lifetimes and reduces energy gains to accelerate saturation to $W_1$ while $W_2$-saturation would be achieved with an initial negative-charge preconditioning over the dielectric surface that elongates lifetimes and increases energy gain. Surface preconditioning extends to discharges with background gas in low collisionality as long as surface conditions are met; however, as seen in Figure 3.22b, sufficient ionization with longer discharge times could lead to ion-assisted multiplication due to field variations via ion momentum and population. In principle, ion-assisted multiplication would be pushed out further in time with surface preconditioning since electron populations would be reduced. Ion-population saturation can then be forced into saturation as in Figure 3.24 by engineering methods, reducing the likelihood of ion-assisted growth. Recombination can be leveraged to reduce ion populations, or a bleed to the boundaries might be induced to quickly equilibrate population growth rates.

## 3.8 Chapter 3 Conclusions

A vacuum multipactor discharge is characterized by a multiplicative front that quickly saturates early in the discharge. Lifetimes and impact energies of new secondaries are coupled via surface fields, and discharges of interest tend to evolve towards impact energies averaging first crossover. Since secondary-emission characteristics, particularly at first crossover, do not vary significantly for dielectric materials of interest to this study [57], the observation that steady-state impacts average first crossover means there is relatively little dependence on material; this is less true of second crossover, which tends to have a larger range, but this characteristic is largely not applicable since discharges of interest do not steady-state to second crossover. In cases dominated by dark-current discharges, the multipactor front does not form and saturation times are much longer than cases dominated by multipactor. Section 3.3 outlined specific conditions and parameters to be included in this study in an attempt to define fundamental contributions to breakdown; therefore, it should be clear that steady-state conditions are limited to that described by Equation (3.17) by virtue of the restricted inclusion of various effects. Equation (3.17) is, by no means, a general condition for all discharges, particularly being valid for conditions of low collisionality with minor volume-charge build-up and assuming additional effects are negligible, e.g. outgassing.

As noted, previous studies have focused largely on the triple-point conditions for breakdown [12], whereas this chapter shows that more emphasis should be on the sur-

face conditions and secondary-emission characteristics to understand the physical limit of breakdown. Breakdown can be seeded by any source as long as downstream surface-field conditions provide adequate multiplication given the conditions of secondary emission, e.g. dielectric secondary-emission characteristics and typical impacting characteristics for new generations. In other words, a seed source is a necessary but insufficient condition for breakdown to occur, and the nature of the seed can be anything that does not immediately affect the downstream conditions even if upstream conditions are altered during an early transient. A distributed seed source (discussed further in Chapter 6) might interact with a larger portion of the upstream surface than the beam source used here, but it does not alter downstream conditions prior to the seeding of the first multipactor generation. As long as the source can seed the first secondary generation under the surface conditions outlined in this chapter, multipactor, will occur, hence breakdown. The CW source of this chapter is related to thermally emitted sources in that the seed is not affected by the local fields, but the relatively high and uniform energies of the injected electrons means the injected source is more typical of external injection of accelerated particles into the configuration volume.

An important corollary result to the deterministic characterization of breakdown presented in this chapter is that there will be no breakdown voltage curve as typically presented in works such as [20]. More details of this characteristic are treated in Chapter 5. The results delineated here are therefore to be interpreted as conditions on the discharge physics rather than conditions on operating conditions of real systems. The source used in this study isolates the fundamental discharge characteristics without convoluting other intricacies typical of real systems, such as delay times that would result from distributed or low-energy sources that otherwise do not have the required initial characteristics to seed the first secondary generation, but might gain them with, for example, sufficient negative charging. Such operating characteristics ultimately distract from the principal contributors to breakdown, and are therefore separated from this study.

Finally, suggestions for further study include variations of the dielectric material, inclusion of an RF field in place of or on top of the DC applied field, a study of discharge delay times with beam-like sources that are not deliberately injected with sufficient energy to multiply, and testing of the notes and suggestions on multipactor suppression in Section 3.7.

## 3.A Source-Sink Simplification

Since the secondary-emission coefficient, $\delta$, depends on particle characteristics at the boundaries, the initial development for the electric-current gain should start with discrete particle counting across boundaries. In this case, the anode is chosen as the reference boundary, and sources and sinks are developed to account for contributing particles to the net current *at the anode*. Counting all relevant sources and sinks as a result of interaction with the dielectric over a finite time, $\Delta t$, gives a finite charge, $\Delta Q$, summed

over all boundaries:

$$\frac{\Delta Q}{\Delta t} = \frac{q_e N_{\text{anode}}}{\Delta t} = \left[ \begin{array}{c} \overbrace{\frac{q_e N_0}{\Delta t}}^{\substack{\text{source} \\ \text{via seed}}} + \overbrace{\sum_{1}^{N_{\text{imp}}} \delta_i \left(W_{\text{imp}}, \theta_{\text{imp}}\right) \frac{q_e N_{i-1}}{\Delta t}}^{\text{source via secondaries traceable to seed}} + \\ \underbrace{\left( - \sum_{1}^{N_{\text{imp}}} \left(1 - f_{\text{SRP}}\right) \frac{q_e N_{i-1}}{\Delta t} \right)}_{\text{sink via dielectric absorption traceable to seed}} + \\ \overbrace{\frac{q_e N_0^*}{\Delta t}}^{\substack{\text{source via} \\ \text{ionization}}} + \overbrace{\sum_{1}^{N_{\text{loci}}^*} \sum_{1}^{N_{\text{imp}}^*} \delta_i^* \left(W_{\text{imp}}, \theta_{\text{imp}}\right) \frac{q_e N_{i-1}^*}{\Delta t}}^{\text{source via secondaries traceable to ionization loci}} + \\ \underbrace{\left( - \sum_{1}^{N_{\text{imp}}^*} \left(1 - f_{\text{SRP}}\right) \frac{q_e N_{i-1}^*}{\Delta t} \right)}_{\text{sink via dielectric absorption traceable to ionization loci}} \end{array} \right], \tag{3.31}$$

where $N_{\text{anode}}$ is the total particle count at the anode via multipactor gain or direct arc, all $N_i$ terms including $N_0$ are electron population counts traceable to the seed, $N_{\text{imp}}$ is the number of impacts on the dielectric, $N_{\text{loci}}^*$ is the number of ionization locus points (ILP's), all $N_i^*$ terms including $N_0^*$ are electron population counts traceable to ILP's , $N_{\text{imp}}^*$ is the number of impacts on the dielectric by primaries and secondaries traceable to ILP's, $W_{\text{imp}}$ and $\theta_{\text{imp}}$ is the impact energy and angle, respectively, for the impacting electron, and $f_{\text{SRP}} = f_{\text{scattered}} + f_{\text{reflected}}$ is the fraction of scattered and reflected particles (SRP) per impact. Note that ionization quantities can be written in terms of cross sections, which will be further discussed in Chapter 4, where first-order approximations in the limit of weak collisionality are made for this chapter. It must also be stressed that while quantities in Equation (3.31) are tracked via interactions at the *dielectric*, the summation of all sources and sinks occurs at the *anode*. Noting that secondary-emission coefficients and SRP fractions are not functions of time, assuming $\delta$ represents the secondary-emission coefficient for the population impacting the boundary over small $\Delta t$, and taking $\Delta$ quantities sufficiently small to produce differentials in charge and time

will give the current at the anode:

$$\lim_{\substack{\Delta Q\to dQ\\ \Delta t\to dt}} \frac{\Delta Q}{\Delta t} = \left[\begin{array}{c} I_0 + \sum_{1}^{N_{\text{imp}}} \delta_i \left(W_{\text{imp}}, \theta_{\text{imp}}\right) I_{i-1} + \\ \left(-\sum_{1}^{N_{\text{imp}}} \left(1 - f_{\text{SRP}}\right) I_{i-1}\right) + \\ I_0^* + \sum_{1}^{N_{\text{loci}}^*} \sum_{1}^{N_{\text{imp}}^*} \delta_i^* \left(W_{\text{imp}}, \theta_{\text{imp}}\right) I_{i-1}^* + \\ \left(-\sum_{1}^{N_{\text{imp}}^*} \left(1 - f_{\text{SRP}}\right) I_{i-1}^*\right) \end{array}\right] = I_{\text{anode}} \tag{3.32}$$

In principle, all currents could be functions of time; however, this analysis will typically assume uniform current, constant-waveform (CW) current.

Consider Equation (3.32) without ionization, some notable limiting cases are: (1) no dielectric impacts leads to a vacuum arc: $I_{\text{anode}} = I_0$; (2) no secondaries with primary impact and $f_{\text{SRP}} = 0$ leads to zero anodic current: $I_{\text{anode}} = I_0 - (1 - f_{\text{SRP}})I_0 = 0$; (3) no secondaries with primary impact and $f_{\text{SRP}} = 1$ leads to a scattered arc: $I_{\text{anode}} = I_0 - (1 - f_{\text{SRP}})I_0 = I_0$. Further simplifying Equation (3.32) by neglecting SRP reduces to Equation (3.13):

$$I_{\text{anode}} = \underbrace{\overbrace{I_0}^{\text{primary current}} + \overbrace{\sum_{1}^{N_{\text{imp}}} \delta_i \left(W_{\text{imp}}, \theta_{\text{imp}}\right) I_{i-1}}^{\text{emitted secondary current, } I_e}}_{\text{source}} + \underbrace{\overbrace{\left(-\sum_{1}^{N_{\text{imp}}} I_{i-1}\right)}^{\substack{\text{absorbed current,}\\ I_a\text{, at dielectric}}}}_{\text{sink}}.$$

The assumption of CW current for all impacts alluded to above allows expansion of all currents in terms of $I_0$:

$$\begin{aligned} I_{\text{anode}} &= I_0 + \left(\delta_1 I_0 + \delta_2 I_1 + \cdots + \delta_{N_{\text{imp}}} I_{N_{\text{imp}}-1}\right) - \left(I_0 + I_1 + I_2 + \cdots + I_{N_{\text{imp}}-1}\right) \\ &= \left[\begin{array}{c} I_0 + \left( \delta_1 I_0 + \delta_2 \left[\delta_1 I_0\right] + \cdots + \delta_{N_{\text{imp}}} \left[\prod_{1}^{N_{\text{imp}}-1} \delta_i\right] I_0 \right) \\ - \left( I_0 + \delta_1 I_0 + \delta_2 \delta_1 I_0 + \cdots + \left[\prod_{1}^{N_{\text{imp}}-1} \delta_i\right] I_0 \right) \end{array}\right] \\ &= I_0 \left[\begin{array}{c} 1 + \delta_1 + \delta_2 \left[\delta_1\right] + \cdots + \left[\prod_{1}^{N_{\text{imp}}-1} \delta_i\right] + \prod_{1}^{N_{\text{imp}}} \delta_i \\ - 1 - \delta_1 - \delta_2 \delta_1 - \cdots - \left[\prod_{1}^{N_{\text{imp}}-1} \delta_i\right] \end{array}\right]. \end{aligned}$$

Clearly, all but one of the product terms in the brackets cancels, leaving a pure multipactor current:

$$I_{\text{anode}} = I_{\text{multipactor}} = I_0 \prod_{1}^{N_{\text{imp}}} \delta_{\text{i}}. \tag{3.33}$$

If all $\delta_i$ terms are set to $\delta_{\max}$ for all impacts, Equation (3.14) further simplifies to:

$$I^{\max}_{\text{multipactor}} = I_0 \prod_{1}^{N_{\text{imp}}} \delta_{\max} = I_0 \left(\delta_{\max}\right)^{N_{\text{imp}}}, \tag{3.34}$$

which is Equation (3.18) in Section 3.1.1, used to facilitate discussion of maximum gain. Similarly, in the limit that $\delta$ can be written as an average of the particle ensemble impacting the dielectric, Equation (3.14) can be written in terms of an ensemble-average secondary-emission coefficient for all impacts:

$$I^{\text{avg}}_{\text{multipactor}} = I_0 \prod_{1}^{N_{\text{imp}}} \delta^{\text{ens}}_{\text{avg}} = I_0 \left(\delta^{\text{ens}}_{\text{avg}}\right)^{N_{\text{imp}}}. \tag{3.35}$$

It must be stressed that Equation (3.35) is very sensitive to $N_{\text{imp}}$, and the temporal characteristics of the discharge will vary $N_{\text{imp}}$ appreciably; Equation (3.35) therefore has limited use in the transient, but does asymptotically represent the steady-state limit with appropriately tracked $N_{\text{imp}}$ and $\delta^{\text{ens}}_{\text{avg}}$.

## 3.B Thomson-Model Ionization and VULP Pressure Limit

The classic Rapp-Golden empirical model [72] for Ar ionization used in XOOPIC is:

$$\sigma_{iz}\left(E\right) = \begin{cases} 2.648 \times 10^{-18} \left(\dfrac{\mathcal{E} - \mathcal{E}_{iz}}{\mathcal{E}^2}\right) \log\left(0.0344\mathcal{E}\right) & \mathcal{E} \geqslant \mathcal{E}_{\text{upper}} \\ 1.7155 \times 10^{-18} \left(\dfrac{\mathcal{E} - \mathcal{E}_{iz}}{\mathcal{E}^2}\right) \log\left(0.0634\mathcal{E}\right) & \mathcal{E}_{\text{upper}} > \mathcal{E} \geqslant \mathcal{E}_{iz} \\ 0 & \mathcal{E} < \mathcal{E}_{iz} \end{cases}, \tag{3.36}$$

where the ionization cross section, $\sigma_{iz}$, is in $\text{m}^2$, energy units are in eV, $\mathcal{E}_{iz} = 15.79\,\text{eV}$, and $\mathcal{E}_{\text{upper}} = 79\,\text{eV}$. Cross sections for alternative gases should be used when needed. The Thomson model is an otherwise appropriate collisional model to use for general, first-order treatment of ionization processes as found in Section 3.2 to find the pressure limit between vacuum-like behavior and the space-charge coupled behavior discussed in Chapter 4, i.e. the upper limit where the discussions in this chapter remain valid [34]. The Thomson cross section is given by:

$$\sigma_{iz}\left(\mathcal{E}\right) = \begin{cases} \pi \left(\dfrac{e}{4\pi\varepsilon_0}\right)^2 \dfrac{1}{\mathcal{E}} \left(\dfrac{1}{\mathcal{E}_{iz}} - \dfrac{1}{\mathcal{E}}\right) & \mathcal{E} \geq \mathcal{E}_{iz} \\ 0 & \mathcal{E} < \mathcal{E}_{iz} \end{cases}, \tag{3.37}$$

As integration of Equation (3.37) in the equation for the reaction-rate constant likely leads to a form with an exponential integral, expansions of Equation (3.37) are employed to attain a tractable, analytic solution. The $n$th-order Taylor expansion for Equation (3.37) around $\mathcal{E}_{iz}$ can be written in the following form:

$$\begin{aligned}
\sigma_{iz} &= \pi\left(\frac{e}{4\pi\varepsilon_0}\right)^2 \frac{1}{\mathcal{E}}\left(\frac{1}{\mathcal{E}_{iz}} - \frac{1}{\mathcal{E}}\right) \\
&= \sigma_{iz}\left(\mathcal{E}_{iz}\right) + \frac{\sigma'\left(\mathcal{E}_{iz}\right)}{1!}\left(\mathcal{E} - \mathcal{E}_{iz}\right) + \frac{\sigma''\left(\mathcal{E}_{iz}\right)}{2!}\left(\mathcal{E} - \mathcal{E}_{iz}\right)^2 + \cdots \\
&= 0 + \underbrace{\pi\left(\frac{e}{4\pi\varepsilon_0}\right)^2 \frac{1}{\mathcal{E}_{iz}^2}}_{\equiv\sigma_0} \frac{\left(\mathcal{E} - \mathcal{E}_{iz}\right)}{\mathcal{E}_{iz}} + \frac{1}{2}\left[-4\,\underbrace{\pi\left(\frac{e}{4\pi\varepsilon_0}\right)^2 \frac{1}{\mathcal{E}_{iz}^2}}_{\equiv\sigma_0}\right] \frac{\left(\mathcal{E} - \mathcal{E}_{iz}\right)^2}{\mathcal{E}_{iz}^2} + \cdots \\
&= \sum_{j=1}^{\infty} (-1)^{n-1} j\sigma_0 \frac{\left(\mathcal{E} - \mathcal{E}_{iz}\right)^j}{\mathcal{E}_{iz}^j}
\end{aligned} \tag{3.38}$$

The first-order approximation is therefore:

$$\sigma_{iz} \approx \sigma_0\left(\frac{\mathcal{E} - \mathcal{E}_{iz}}{\mathcal{E}_{iz}}\right) \tag{3.39}$$

The variations between Rapp/Golden, full Thomson, and first-order Thomson cross-sections are shown in Figure 3.32a, and the relative error with respect to the Rapp/Golden empirical model is shown in Figure 3.32b. While the cross sections themselves can vary significantly, the reaction-rate constants are not necessarily affected by the cross-section errors at higher energies since contributions can be small as a result of distribution characteristics. It should be cautioned that the use of a higher-order expansion from Equation (3.38) could lead to larger errors at higher energies as a result of slow convergence of the Taylor expansion about $\mathcal{E}_{iz}$ and subsequent divergent error in higher orders terms that could grow faster than the exponentially decaying term in Equation (3.40).

This study deals with distributions of particles, so the reaction-rate constant, $K$, for a reaction with cross-section, $\sigma(\mathcal{E})$, can be calculated by taking the average over the distribution [34].

$$K\left(T\right) = \left(\frac{m}{2\pi kT}\right)^{3/2} \frac{8\pi}{m^2} \int_0^{\infty} \sigma\left(\mathcal{E}\right) \exp\left(-\frac{e\mathcal{E}}{kT}\right) e\mathcal{E}d\left(e\mathcal{E}\right). \tag{3.40}$$

Again, expansions on the cross section are typically required to obtain tractable analytic solutions to Equation (3.40). Applying Equation (3.39) for ionization, replacing the lower

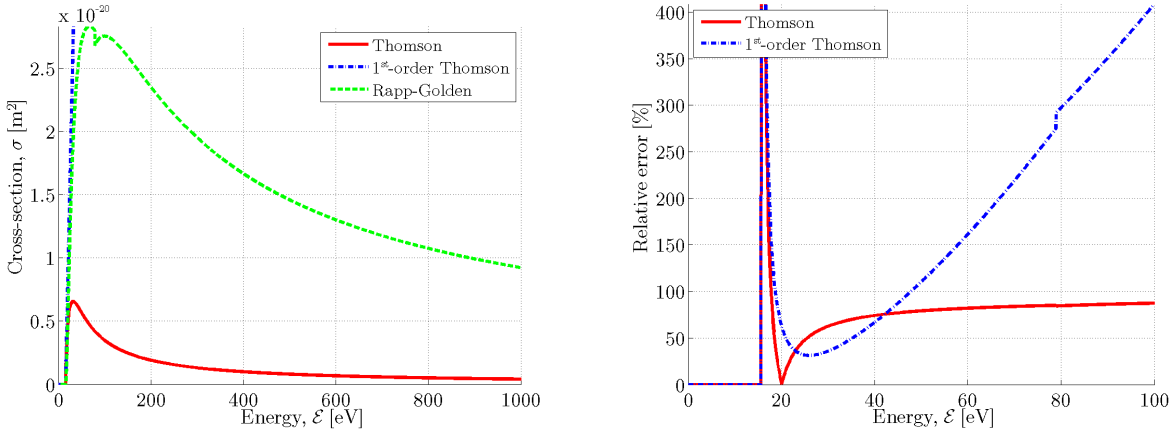


(a) Cross sections.

(b) Relative errors.

Figure 3.32: Comparison of Thomson, first-order Thomson, and Rapp/Golden ionization cross sections for Ar. First-order Thomson is expanded about the ionization energy, $\mathcal{E}_{iz}$. Errors in (b) are with respect to the Rapp/Golden empirical model.

limit with $\mathcal{E}_{iz}$, and integrating over energy in a straightforward manner gives:

$$\begin{aligned} K_{iz}\left(\mathrm{T}\right) &= \left(\frac{m}{2\pi e\mathrm{T}}\right)^{3/2} \frac{8\pi}{m^2} \int_{\mathcal{E}_{iz}}^{\infty} \sigma_0 \left(\frac{\mathcal{E}-\mathcal{E}_{iz}}{\mathcal{E}_{iz}}\right) \exp\left(-\frac{e\mathcal{E}}{e\mathrm{T}}\right) e\mathcal{E}\, d\left(e\mathcal{E}\right) \\ &= \sigma_0 \sqrt{\frac{m^3}{2^3\pi^3 e^3 \mathrm{T}^3} \frac{8^2\pi^2}{m^4} e^4} \frac{\mathrm{T}}{\mathcal{E}_{iz}} \left(\mathrm{T}\mathcal{E}_{iz} + 2\mathrm{T}^2\right) \exp\left[-\frac{\mathcal{E}_{iz}}{\mathrm{T}}\right] \\ &= \sigma_0 \underbrace{\sqrt{\frac{8e\mathrm{T}}{\pi m}}}_{\equiv \bar{v}_e} \left(1 + \frac{2\mathrm{T}}{\mathcal{E}_{iz}}\right) \exp\left[-\frac{\mathcal{E}_{iz}}{\mathrm{T}}\right]. \end{aligned} \tag{3.41}$$

Assuming the emission temperature for secondary electrons is the volume temperature (while also noting that this is not generally the case) so that $e\mathrm{T} = 1.85\,\mathrm{eV}$, the reaction-rate constants are given in Table 3.2, using Equation (3.41) for first-order Thomson and a simple composite-Simpson integrator on Equation (3.40) for the full Thomson form and Rapp/Golden . The constant calculated with the first-order expansion of the Thomson cross section differs from the constant calculated with Rapp/Golden by a reasonably small factor of $\sim 2$. At least 99.7 % of the integral for all cross sections is captured with an upper integral limit of less than $\sim 35\,\mathrm{eV}$, corroborated with Figure 3.33a. Although the Rapp/Golden cross section can be larger than the Thomson models at higher energies, the typical energies accessed for this simple test are in the low-energy region where Thomson happens to be higher than Rapp/Golden, where Figure 3.33b shows the integrands of Equation (3.40) for the various models in Figure 3.33b.

Table 3.2: Comparison of reaction-rate constants, $K_{iz}$ using Equation (3.40) with Thomson, first-order Thomson, and Rapp/Golden. Relative error in the reaction-rates using the specified cross-section model are given with respect to the Rapp/Golden empirical model. This error is not to be confused with the errors in cross sections from Figure 3.32b.

| Cross-section model | $K_{iz}$ [1/s/m$^3$] | Relative error [%] |
|---|---|---|
| Thomson | $1.017 \times 10^{-8}$ | 33.2 |
| First-order Thomson | $1.509 \times 10^{-8}$ | 97.7 |
| Rapp/Golden | $7.630 \times 10^{-9}$ | 0 |

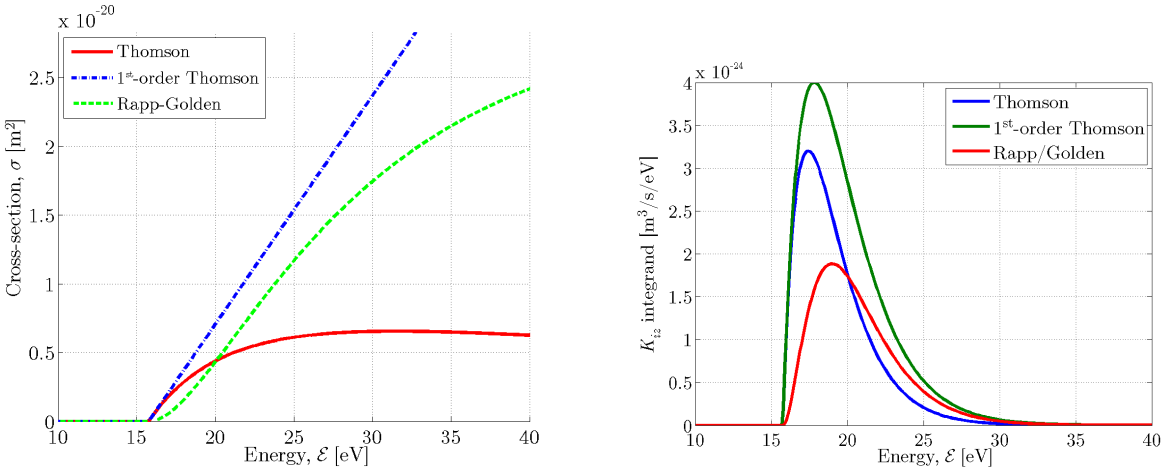


(a) Cross sections at low energy.

(b) Integrands for various models.

Figure 3.33: Cross sections at low energies with reaction-rate constant integrands from Equation (3.40) for Ar. Reaction rates are dominated by contributions at energies less than $\sim 35\,\text{eV}$. Despite the overall larger cross sections for Rapp/Golden at higher energies compared to the full Thomson model, Rapp/Golden reaction rates are smaller due to the electrons' accessible energy domain.

## 3.C 1-D Fractional Change in $E$

For an arbitrary width of the multipactor front, $w_{\text{front}} = x_2 - x_1$, assuming uniform density across a typically small $w_{\text{front}}$, the 1-D potential is:

$$\phi = -\left(\frac{\rho x^2}{2\varepsilon_0} + C_1 x + C_2\right). \tag{3.42}$$

Letting $\phi(x_1) = -V_1$ and $\phi(x_2) = -V_2$:

$$\begin{aligned}
&\phi\left(x = x_1\right) = -V_1 = -\left(\tfrac{\rho}{2\varepsilon_0}\left(x_1\right)^2 + C_1\left(x_1\right) + C_2\right) \\
&\Rightarrow -V_1 = -\tfrac{\rho}{2\varepsilon_0}x_1^2 - C_1 x_1 - C_2 \Rightarrow C_2 = V_1 - \tfrac{\rho}{2\varepsilon_0}x_1^2 - C_1 x_1, \\
&\phi\left(x = x_2\right) = -V_2 = -\left(\tfrac{\rho}{2\varepsilon_0}\left(x_2\right)^2 + C_1\left(x_2\right) + C_2\right) \\
&\Rightarrow -V_2 = -\tfrac{\rho}{2\varepsilon_0}x_2^2 - C_1 x_2 - C_2 \Rightarrow C_2 = V_2 - \tfrac{\rho}{2\varepsilon_0}x_2^2 - C_1 x_2.
\end{aligned} \tag{3.43}$$

The integration constants are then:

$$\begin{aligned} C_1 &= \left[\tfrac{V_2-V_1}{x_2-x_1} - \tfrac{\rho(x_2+x_1)}{2\varepsilon_0}\right], \\ C_2 &= V_1 - \tfrac{\rho}{2\varepsilon_0}x_1^2 - \left[\tfrac{V_2-V_1}{x_2-x_1} - \tfrac{\rho(x_2+x_1)}{2\varepsilon_0}\right] x_1. \end{aligned} \tag{3.44}$$

and the 1-D potential over the multipactor front is:

$$\phi = -\left( \begin{array}{c} \tfrac{\rho x^2}{2\varepsilon_0} + \left[\tfrac{V_2-V_1}{x_2-x_1} - \tfrac{\rho(x_2+x_1)}{2\varepsilon_0}\right] x + \\ V_1 - \tfrac{\rho}{2\varepsilon_0}x_1^2 - \left[\tfrac{V_2-V_1}{x_2-x_1} - \tfrac{\rho(x_2+x_1)}{2\varepsilon_0}\right] x_1 \end{array} \right). \tag{3.45}$$

The electric field is then:

$$E = \frac{d\phi}{dx} = -\left(\frac{\rho}{\varepsilon_0}\left[x - \frac{x_2+x_1}{2}\right] + \frac{V_2-V_1}{x_2-x_1}\right). \tag{3.46}$$

A simplifying approximation can also be made by assuming that the initial-transient and steady-state potential profiles are roughly similar so that $x_1$ and $x_2$ bound, i.e. define, the front with $E(x_1) \approx E_0(x_1)$ and $E(x_2) \approx E_0(x_2)$. Observing that the notation here means that a finite-difference approximation to the electric field would be:

$$E \approx \left(\frac{-V_i - (-V_{i-1})}{x_i - x_{i-1}}\right) = -\left(\frac{V_i - V_{i-1}}{x_i - x_{i-1}}\right) \Rightarrow E_0 \approx -\left(\frac{V_2 - V_1}{x_2 - x_x}\right).$$

The interest is in how the field at the edge of the front, $x_2$ (presumably where the highest density is located, although this formulation does assume uniform density through $w_{\text{front}}$):

$$E\left(x_2\right) = -\left(\frac{\rho}{\varepsilon_0}\left[x_2 - \frac{x_2+x_1}{2}\right] + \frac{V_2-V_1}{x_2-x_1}\right) = -\left(\frac{\rho}{\varepsilon_0}\left[\frac{x_2-x_1}{2}\right] - E_0\right). \tag{3.47}$$

The fractional change in $E$ from the background applied field, $E_0$, is defined by:

$$p(x_2) = \frac{E\left(x_2\right) - E_0}{E_0} = -\frac{\rho}{\varepsilon_0 E_0}\left[\frac{x_2-x_1}{2}\right]. \tag{3.48}$$

Equation (3.48) can be rearranged to get the density required to change the field by a fraction $p$:

$$\rho_p(x_2) = -\frac{2p(x_2)\varepsilon_0 E_0}{x_2 - x_1}. \tag{3.49}$$

The temporal change in the electric field, applied to Equation (3.46), is given by:

$$\begin{aligned} \frac{dE}{dt} &= -\frac{\partial}{\partial t}\left(\frac{\rho}{\varepsilon_0}\left[x - \frac{x_2+x_1}{2}\right] + \frac{V_2-V_1}{x_2-x_1}\right) \\ &\approx -\left(x - \frac{x_2+x_1}{2}\right)\frac{1}{\varepsilon_0}\frac{\partial\rho}{\partial t} + \frac{\rho}{\varepsilon_0}\frac{dx}{dt}. \end{aligned} \tag{3.50}$$

Equation (3.50) is in the lab frame, so $dx/dt$ can be approximated as the average velocity of the front, $v_{\text{front}}^{\text{avg}}$, which can further be calculated from the (non-relativistic) average

emission energy for secondaries. Additionally, from Equation (3.48), the electric field after a fractional gain of $p$ can be written as:

$$E\left(x_2\right) = E_0\left(p+1\right). \tag{3.51}$$

Finally, for any $p$, the quasistatic metric at the multipactor front edge, $x_2$, can be written as:

$$\frac{1}{E(x_2)}\frac{dE(x_2)}{dt}t_{\text{life}} \approx \frac{1}{\left(E_0 p(x_2)+1\right)}\left[-\frac{\rho_p(x_2)}{\varepsilon_0}\left(\left[\frac{x_2-x_1}{2}\right]\frac{\delta-1}{t_{\text{life}}}+v_{\text{front}}^{\text{avg}}\right)\right]t_{\text{life}}. \tag{3.52}$$

## 3.D Definition of the Immediate-Downstream Region

The characteristics of initial impact for the typical beam-like source used in this chapter are specified to guarantee net emission and subsequent positive dielectric charge for the discharges in this chapter. Low-energy impacts from the distributed secondaries emitted after initial impact do not generate net secondaries in a region "immediately downstream" of the initial-impact region leading to a pocket of negative charge near initial impact as in Figure 3.6 and Figure 3.13. The interest here is to characterize the typical emission energy of the first generation of secondaries from the initial impact that would lead to a subsequent impact at first crossover, $W_1$. The energy will then give the range from the single-particle treatment in Section 3.4.1. The impact energy has to be less than or equal to first crossover, $W_{\text{imp}} \leq W_1$, where $W_{\text{imp}}$ is found with Equation (3.4); it is still valid to assume that most of the *impact* energy is from the velocity parallel to the surface when considering impact at $W_1$, despite a relatively low energy of $W_1(\theta_{\text{imp}} = 0°) = 38.45\,\text{eV}$. Assuming all the *impact* energy is attributable to parallel velocity at impact while all the *emission* energy is attributable to normal velocity at emission, Equation (3.4) gives:

$$\frac{1}{2}mv_{\parallel f}^2 = \frac{1}{2}m\left([0]-2v_{\perp 0}\frac{E_\parallel}{E_\perp}\right)^2 \Rightarrow W_f = 4W_{\text{init}}\left(\frac{E_\parallel}{E_\perp}\right)^2 \approx W_{\text{imp}}, \tag{3.53}$$

Setting Equation (3.53) equal to $W_1$ gives the required initial energy, $W_{\text{init}}$:

$$W_{\text{init}} + \Delta W = W_1 \Rightarrow W_{\text{init}} = \frac{W_1}{\left[4\left(\frac{E_\parallel}{E_\perp}\right)^2+1\right]}. \tag{3.54}$$

Having obtained $W_{\text{init}}$, the range is simplified from Equation (3.11):

$$\Delta x = \frac{4W_{\text{init}}}{qE_\perp}\frac{E_\parallel}{E_\perp} \tag{3.55}$$

Equation (3.55) does have a range since there is a range for the first-crossover energies; the range in $W_1$ is only $\sim 10\,\%$, so the variation in immediate-downstream width using Equation (3.55) is the same order. As an example, returning to typical conditions for the discharge at $\alpha = 6.12°$ described in Section 3.4.1, initial vacuum fields are $E_{\parallel 0} = -1.76\,\text{MV/m}$ and $E_{\perp 0} = 0.42\,\text{MV/m}$, and assuming $W_1 = W_1(\theta_{\text{imp}} = 90°) = 6.24\,\text{eV}$,

Equation (3.54) gives $W_{\text{init}} \sim 1.40\,\text{eV}$, amounting to an excursion of $\sim 55\,\mu\text{m}$ from Equation (3.55). The energies returned from Equation (3.54) are sufficiently close to the specified most-probable energy, $W_{\text{emit}}^{\text{mode}}$, for the emitted distribution, so it is sufficient to characterize the range for the immediate-downstream region using $W_{\text{emit}}^{\text{mode}}$ rather than Equation (3.54) for the typical emission parameters of this study.

Finally, the common assumption made in this chapter of grazing impact is not particularly true at the early discharge near initial impact since lower-energy emitted particles do not gain sufficient parallel velocity in their relatively short lifetimes to make the assumption of grazing impact valid. This discrepancy does not affect the calculation for the range, but is worth noting.

# Chapter 4

# Gaseous Breakdown and Diffusion in Multipactor

This chapter will focus on gaseous breakdown (GB) as it pertains to the evolution of multipactor discharges heretofore discussed. Effects in low pressure (nominally, $\sim 1$ Torr) are covered in this chapter. This document will *not* treat general gaseous breakdown, which may be reviewed in any of the standard texts [8, 9, 34, 73] and which was discussed briefly in Section 1.3.3. Discharges beyond low pressure and approaching atmospheric pressure (760 Torr) will be dominated by volume effects, where surface multipactor may seed volume breakdown but will not drive growth since surface effects are generally lower order compared to volume effects. An assessment of the critical pressure past which volume effects dominate surface growth was given in Section 3.2, which can be used to clearly illustrate the dominance of volume growth rates beyond the critical pressure. Again, it was shown in Chapter 3 that there is no Paschen-like curve in the surface-dominated breakdown regime, while volume growth at pressures approaching atmospheric can be modeled with the classical Paschen curve. Recall the exposition of Chapter 3 focused on pure vacuum discharges to communicate general phenomenology, but the results of that chapter are valid in any pressure regime where surface effects dominate up to a few hundred mTorr; consequently, the more general phrase "vacuum-like effects" will be used when referencing results of Chapter 3 to encompass the extended validity of those results.

A discussion extending VULP effects into the gaseous regime is given in Section 4.1.1, including delineation of the gain characteristics in Section 4.1, and considerations for the grid in Section 4.2 following from Section 3.3.1. General parameters for this chapter are discussed in Section 4.3. The bulk of this chapter will detail discharge behavior near the critical pressure at 1 Torr in Section 4.4. Finally, summary treatment of diffusive outgassing is given in Section 4.5.

## 4.1 Theoretical Gain in Gaseous Discharges

Gaseous collisional effects studied herein are limited to excitation and single ionization of neutral background argon (Ar) gas. Generalization to other species and reactions will require incorporating additional considerations for growth characteristics that will not be covered here, but may be considered extensions of considerations for sources and sinks

added to the formulations of Section 3.A. For example, in cases including oxygen gas, volume recombination reduces space charge and alters the coupling characteristics between surface charge and space charge (to be discussed in this chapter), requiring treatment of space-charge characteristics that essentially evolve with opposing gradients compared to discharges studies herein. In principle, it is difficult to obtain an *a-priori* estimate of the gain for the gaseous discharges studied in this chapter due to the inclusion of space charge effects and distribution characteristics of all species in the discharge. Multipactor seeds volume growth while space charge couples to the saturated surface to induce non-linear effects not otherwise seen treated in classical formulations of diode-type problems. With these considerations in mind, this section will provide an upper estimate of the expected gain characteristics, making a number of assumptions about the interacting species to make such a formulation tractable.

### 4.1.1 Extension from VULP

As was thoroughly delineated in Chapter 3, single-surface multipactor discharges are forward peaked with a downstream densities at least two orders of magnitude larger than the upstream tail, c.f. Figure 3.9 in the 6.12° case. It is sufficient to follow the front to get an estimate of the growth, particularly through the fast transient phase, where surface multipactor is clearly dominant, as will be shown. The ionization reaction rate will vary according to the local density and energy of electrons, the density of neutral gas species, and the type of gas present. The ionization rate at the multipactor peak, limiting to single ionization of neutral background argon, is:

$$R_{iz} = K_{iz} n_{e,\text{front}}(t) n_g, \tag{4.1}$$

where $n_{e,\text{front}}(t)$ is the time-dependent electron density (at the multipactor front); $n_g$ is the neutral background density, typically treated with ideal gas so that 1 Torr Ar gas $= 3.329 \times 10^{22}\,1/\text{m}^3$; and the ionization rate constant, $K_{iz}$, is distribution averaged, where it is assumed electron velocity is much larger than the neutral velocity:

$$K_{iz} = \langle \sigma_{iz} v_e \rangle = \int_{-\infty}^{\infty} d^3 v_e \left(\sigma_{iz} v_e\right) f_{en}\left(v_e\right) = 4\pi \int_{-\infty}^{\infty} v_e^2 dv_e \left(\sigma_{iz} v_e\right) f_{en}\left(v_e\right). \tag{4.2}$$

Equation (4.1) can be integrated over the time for volume electrons to traverse the dielectric surface, giving an approximate total gain from multipactor and ionization events, where the time for front propagation is simply the time for average secondaries to reach the anode at average secondary velocity:

$$t_{\text{front}} = \frac{D_{\text{gap}}}{\cos(\alpha)} \cdot \frac{1}{\langle v_{\text{sec}} \rangle}, \tag{4.3}$$

where $\langle v_{\text{sec}} \rangle$ is the distribution average velocity of emitted secondaries. At this point, the difficulties with identifying *a-priori* metrics becomes apparent with consideration of $\langle v_{\text{sec}} \rangle$. One of the major assumptions made throughout this document is that the secondaries in the volume are Maxwellian, which is known to be inaccurate by observation of simulation. Injection of secondaries is via a Maxwellian flux, but exposure to the gap potential causes

the initial Maxwellian distribution to deviate towards smaller energies due to varying (and largely short) lifetime and gain characteristics. For tractability, this study will simply assume a measured average kinetic energy of $\sim 25\,\mathrm{eV}$, observed in simulation for the both multiplicative and non-multiplicative discharges, c.f. Figures 4.9 and 4.17. Consequently, the numbers in this treatment are not general, but will provide necessary foundation to discuss the results of Section 4.4.

Recall that XOOPIC uses the Rapp-Golden ionization cross section for Ar, shown in Equation (3.36) and plotted in Figure 3.32a as a function of energy. For completion, the Rapp-Golden cross section is plotted against electron speed in Figure 4.1a. Also recall the normalized distribution function:

$$f_{en}\left(v_e\right) = \left(\frac{m_e}{2\pi kT}\right)^{3/2} \exp\left(-\frac{m_e v_e^2}{2kT}\right), \tag{4.4}$$

and the normalization criterion, $\int d^3v_e f_{en}\left(v_e\right) = 1$. Equation (4.4) is plotted in Figure 4.1b with the assumption of $\langle E \rangle \sim 25\,\mathrm{eV}$.

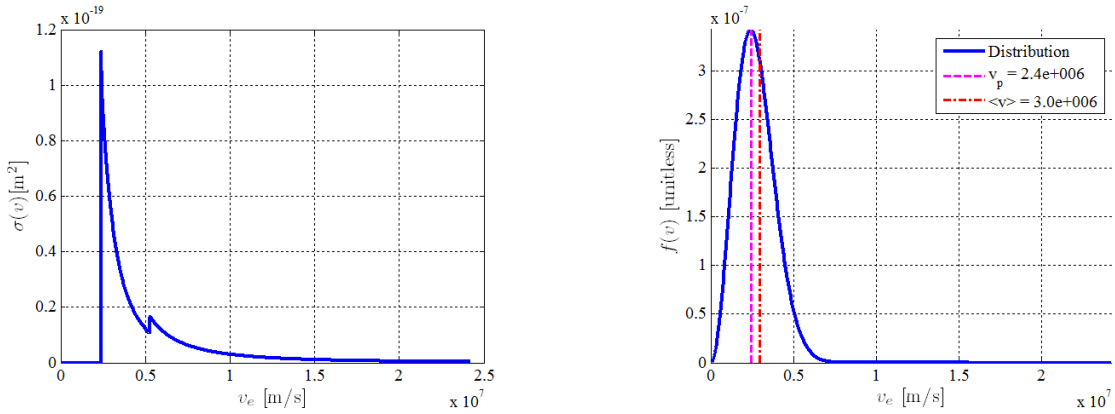


(a) Rapp-Golden vs. electron velocity.

(b) Normalized Maxwellian.

Figure 4.1: Ionization cross section and electron distribution for use in reaction rate calculations. (a) is the Rapp-Golden cross section from Equation (3.36), plotted against electron velocity, and (b) is the normalized Maxwellian speed distribution assuming an average energy of $\sim 25\,\mathrm{eV}$ as per observations of simulations, c.f. Figures 4.9 and 4.17.

With Equations (4.2) and (4.4), the reaction rate can be found with Equation (4.1) to be $R_{iz} = 1.837 \times 10^{36}\,1/\mathrm{m}^3/\mathrm{s}$. Rather than using Equation (4.3) directly, since initial secondary characteristics are relatively uniform through the fast transient, growth can be estimated per bounce, allowing for simple integration of ionization and multipactor contributions per bounce. With typical parameters used in the gaseous studies here (i.e. $p_{\mathrm{Ar}} = 1\,\mathrm{Torr}$ background gas at $V_0 = 8500\,\mathrm{V}$ applied voltage), the number of bounces at 6.12° is $\sim 24$, found from applying Equation (3.12) with measured values of the field in simulation. The time per bounce is then $t_{\mathrm{bounce}} = t_{\mathrm{front}}/24$. Assuming an initial electron density injection of $n_{e,0}$, which can be derived from the injected current, or simply measured via simulation, the gain at each bounce is given by:

$$\chi_i = \frac{n_e^i}{n_{e,0}} = \delta^i(1 + K_{iz} n_g \Delta t_{\mathrm{bounce}})^i, \tag{4.5}$$

for the $i$th bounce, relative to the initial (primary) injected density. It is assumed in Equation (4.4) that the fully realized secondary population is emitted at $i \times t_{\text{bounce}}$, and it is furthermore tacitly assumed that the volume into which density is integrated remains uniform at every bounce; due to the particle distribution, there will be a temporal and spatial spread through the bounce time that is neglected in this treatment. Furthermore, Equation (4.4) assumes that the whole ionization electron population undergo multipactor at the same gain as pure secondaries, which is not representative of ionization electrons in any regime, since impact energies will vary greatly from the secondary cascade; this is made clear in diagnostics for the average kinetic energy of the various electron populations, c.f. Figures 4.9 and 4.17. The assumption of maximum gain may be construed as having an large safety factor for engineering applications, or otherwise providing a necessary upper bound on gain characteristics.

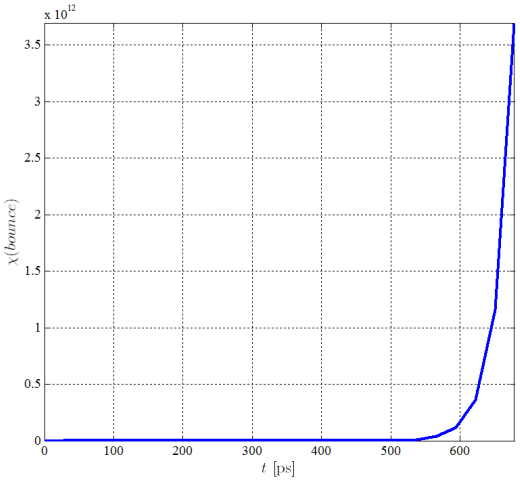


Figure 4.2: Ideal gaseous gain vs time. Total time is the required time for full dielectric-surface excursion of average fast-transient secondaries.

It will be shown that this estimate is several orders of magnitude ($\sim$ 15 orders) larger than observed in simulation, where the discussion in Section 3.1 can account for at least $\sim$ 6 orders of magnitude difference from pure surface growth, c.f. Figure 3.3 where ideal multipactor growth is suppressed with the introduction of the distribution. Assuming similar characteristics of secondary growth, where ideal growth was characterized by $\delta_{\text{avg}}^{\text{ens}} \sim 4$, and the fully implemented distribution was characterized by $\delta_{\text{avg}}^{\text{ens}} \sim 2.12$, the ratio of gains over 24 bounces gives $4^{24}/2.12^{24} \sim 4.1 \times 10^6$, hence the $\sim$ 6 orders of magnitude mentioned previously. A large part of the discrepancy in order of magnitude will be attributable to the aforementioned assumption of uniformity over the density volume from the primary source, which is known to be an inaccurate representation since primary injection properties are specified while secondary injection properties are determined by a Maxwellian flux over a finite integration time. Again, Equation (4.5) should be considered carefully, particularly when estimating gains based on densities, which may limit engineering applicability. Generality can be assumed in a similar way to Equation (3.18), where the integration time was integrated out to get to a ratio of particle numbers rather than current; the analog for Equation (4.5) would be to integrate out the density volume

to get back to number, i.e. $N = \int ndV$, where careful consideration of the integration operation will account for discrepancies to produce less conservative gain estimates for wider engineering applicability.

## 4.2 Grid Resolution in Gaseous Discharges

Pressure regimes for this study range from vacuum through low pressure, nominally 1 Torr. As noted in Section 3.3.1, the recommended grid-size limit for accurately capturing the local physics in a space-charge region is one-third of a Debye length [5]. Grid resolution must therefore be revisited to ensure that local fields are accurately sampled and represented. Figure 4.3 shows the Debye length over several decades of electron density, up to the maximum gain from Section 4.1. The Debye length in a (cold) plasma is typically written in the form:

$$\lambda_D = \sqrt{\frac{\varepsilon_0 k_B / q_e^2}{n_e / T_e}} = \sqrt{\frac{\varepsilon_0 k_B T_e\,[\mathrm{K}]\,/ q_e^2}{n_e}} = \sqrt{\frac{\varepsilon_0 e \mathrm{T}_e\,[\mathrm{eV}]\,/ q_e^2}{n_e}}, \tag{4.6}$$

where $\varepsilon_0$ is vacuum permittivity in SI units, $k_B$ is the Boltzmann constant in J/K, and $T_e$ is the electron temperatures in K. Recalling that typical parameters used herein result in a grid resolution of $\sim 35.5\,\mu\mathrm{m}$, it is clear that the maximum gain would not well resolved; however, observation of simulation results, c.f. Figures 4.8 and 4.16 suggests that electron densities peak around $1 \times 10^{16}\,1/\mathrm{m}^3$, giving a Debye length of 200 µm, within the suggested resolution limit of 66.7 µm by nearly a factor of two.

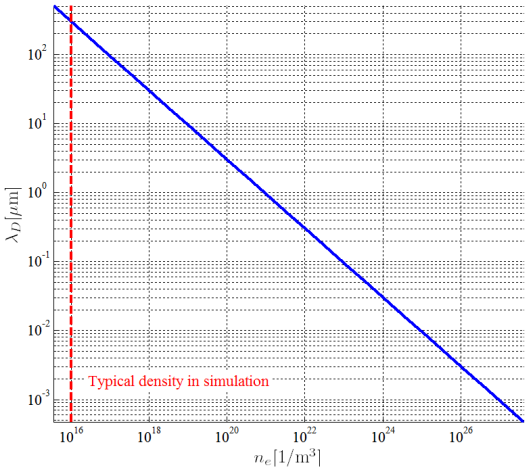


Figure 4.3: Debye length at various pressures. Maximum ionization rates are used for Ar background gas with a usual CW seed at 1 A.

## 4.3 Gaseous Breakdown General Parameters

The general phenomenology of gaseous breakdown will be described through a few examples using the general parameters listed in Table 2.7 for the 1 Torr case. As for the

VULP discharges, this chapter will focus on two angles, 6.12° and 22.9°, representing otherwise multiplicative surface breakdown and dark-current steady-state surface breakdown, respectively. All definitions remain the same, where multiplicative breakdown refers to surface-dominated growth only, and dark-current steady-state is defined as a non-multiplicative surface arc with an average magnitude equal to the seed-current magnitude for an unperturbed seed source. Similarly, extending the following results to other angles listed in Section 2.2.2 is straightforward, with the main differences across angles being the gain magnitude and time to steady-state, along with a change in the ratio of mean free path to excursion length.

## 4.4 Low-Pressure Breakdown

In low pressure breakdown, growth rates in surface multipactor are comparable to growth rates in the volume, previously shown in Section 3.2. It will be shown that the appreciable ionization at low pressures coupled with the surface charge resulting from multipactor leads to oscillatory effects in otherwise DC discharges, which are simply extensions of the underdamped oscillations studied in Section 3.6. The following results are valid for background-gas pressures $\sim 1\,\text{Torr}$, where collisional effects are comparable to surface growth rates, but do not dominate the discharge duration.

### 4.4.1 Multiplicative Breakdown in Low Pressure Gas

This section details a gaseous discharge at 1 Torr with surface field conditions that lead to multiplicative surface growth. Primary and secondary electrons from the surface seed volume growth, which affect the conditions of the surface fields, most importantly the field angle as a result of coupling between volume charge and surface charge.

This exposition will follow a format similar to Section 3.4.1. Figure 4.4 is a collection of snapshots in phase space illustrating the evolution of the discharge, similar to Figure 3.5, with electrons moving towards the positively biased anode at the right, and with the addition of slow ion species moving primarily to the negatively biased cathode at the left. Figure 4.4a at 100 ps shows the initially multiplicative discharge in near-vacuum conditions (where the background gas has not sufficiently ionized to affect the vacuum-like early transient), analogous to Figure 3.5a. Figure 4.4b at 5 ns shows the discharge past the early transient, towards what would otherwise be saturation of the discharge, analogous to Figure 3.5b. A vacuum-like discharge would simply stop evolving past Figure 4.4b, but the introduction of the volume ionic charge couples with the surface charge as ions move towards the cathode due to the potential across the gap. Figure 4.4c at 25 ns shows volume saturation of ions at roughly the peak of ionization events, just before ion momentum becomes appreciable. Finally, Figure 4.4d at 75 ns shows the end of the initial bulk ion evacuation cycle, with ions removed from the system at the cathode. Apparent ion striping (i.e. regions of varying ion density) is a result of field conditions through the volume that cause ions to gain more momentum in the striped region, which can be seen in the vector magnitude of the fields in Figure 4.4d, where the low argon ion density region is clearly larger than nearby fields up until the cathode region (left boundary). Field conditions are sufficiently restored into the multiplicative regime, starting a new multipactor cycle, albeit

with conditions that are not as favorable to growth as the initial discharge conditions, leading to reduced current and longer growth and decay times compared to the fast transient, but still appreciable growth characteristics that could be sufficiently large to require additional engineering consideration for failure modes.

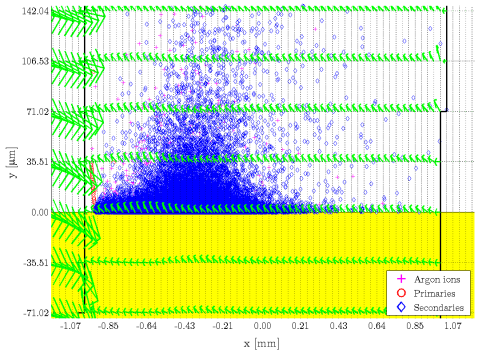


(a) Vacuum-like fast transient, $t = 100\,\text{ps}$.

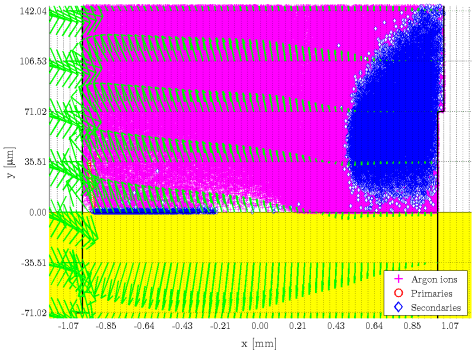


(b) Post fast transient, $t = 5\,\text{ns}$.

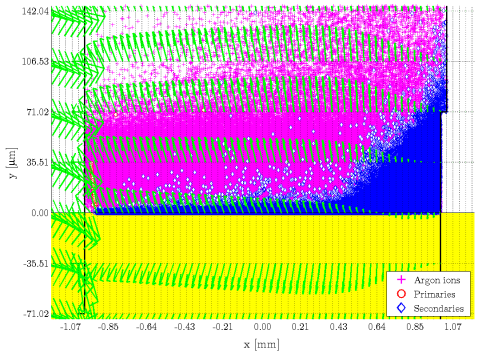


(c) Volume saturation, $t = 25\,\text{ns}$.

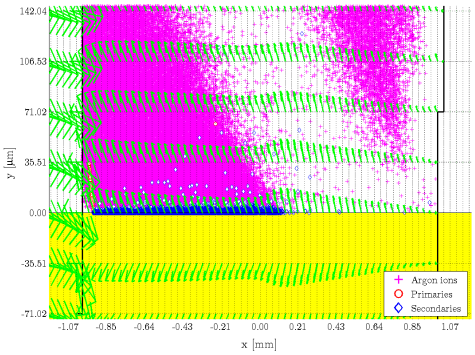


(d) Volume ion evacuation, $t = 75\,\text{ns}$.

Figure 4.4: Configuration-space example of VULP breakdown at 6.12° in 1 Torr background argon gas. Primary, secondary, and ionization electrons move from the lower cathode potential on the left to higher anode potential on the right. Primary electrons are absorbed at the dielectric (shaded region, $y < 0$), emitting secondaries according to the theory outlined in Section 2.3. Single ionization in argon produces additional volume electrons. The grid shown corresponds to the numerical grid, with a square-grid resolution of 35.5 µm in $x$ and $y$. Green arrows correspond to the magnitude and direction of $\vec{E}$ at the displayed time. No SRP.

Dielectric charging on the surface for the discharge is shown in Figure 4.5. Comparing Figure 3.6a for vacuum-like discharges to Figure 4.5a for low pressure shows similar positive charging characteristics for the initial-impact and immediate-downstream regions near the cathode. Oscillations present in Figure 4.5a are the result of coupling between volume charge due to ions and surface charge due to net emission of electrons (recall leading to positive surface charging), where ion momentum causes surface field conditions to fluctuate between into and out of multiplicative conditions, which will be more clear when looking at the surface field conditions in Figure 4.10, discussed further below. The con-

tour plot in Figure 4.5b shows the oscillations in surface-charge magnitude more clearly, which occur on the order of the ion plasma frequency, which is $\sim$ MHz.

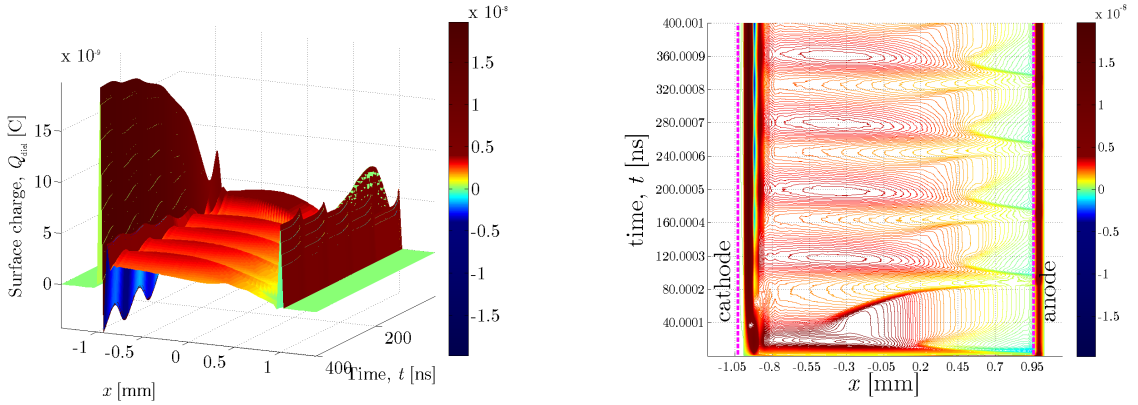


(a) Dielectric-charge full profile.

(b) Dielectric charge contour in $x$ against $t$.

Figure 4.5: Characteristic dielectric-surface charging for a multipactoring discharge at 6.12° in 1 Torr background argon gas. Positive charging is shown over a large region of the dielectric, indicating surface characteristics sufficient for multiplicative breakdown. Oscillations are a result of ionic volume charge coupling to positive surface charge, allowing the surface to go into and out of multiplicative conditions.

Figure 4.6a clarifies the impact characteristics for the primaries, showing a peak at the intended initial impact energy around $\sim$ 750 eV, which was a clearly more defined peak in the vacuum-like discharge of Figure 3.7a. Recall that the peak in the EEDF deliberately corresponds to the peak in the secondary-emission curve (at a specified impact angle of $\sim 32°$, although there is some spread due to space-charge interactions over time) to intentionally emit the maximum number of secondaries at first impact. This is clear for the vacuum-like discharges (c.f. Figure 3.8) since primaries remain largely monoenergetic through the discharge. The primaries are clearly more distributed in Figure 4.6a as a result of volume collisions and scattering leading to variations in lifetimes and impact energies. The primary electron distribution everywhere other than the peak is $\sim$ 4 orders of magnitude lower than the peak. The secondary electron distribution in Figure 4.6b is similarly more distributed than the vacuum-like discharges in Figure 3.7b due to volume collisions. Figure 4.7 is another view of the broader impact characteristics for these low pressure discharges, while retaining important metrics for growth. Figure 4.7a is the analogous secondary-emission curve from Figure 3.8a for 1 Torr. The secondary curve is clearly more sampled than previously seen.

Number density plots for secondary electrons are shown in Figure 4.8, showing similar development of the multipactor front through the early transient, followed by similarly oscillatory densities throughout the discharge time that mirrors the dielectric charging. The speed of the fast-transient multipactor front is determined as in Section 3.4.1, referencing Figure 3.9b and using the average velocity of the emitted secondary electrons. The average velocity of the emitted secondaries can be obtained by the average kinetic energy in the bulk volume, which is $\sim$ 140 eV from Figure 4.9, giving a front velocity of $\sim 4.962 \times 10^6$ m/s. The speed of the multipactor front is also readily estimated in Fig-

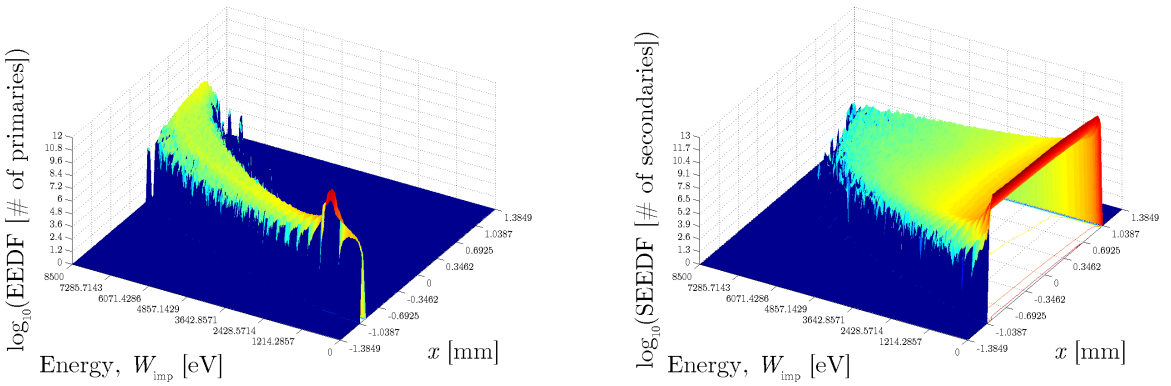


(a) Primary-electron EDF.

(b) Secondary-electron EDF.

Figure 4.6: Primary-electron and secondary-electron energy distributions functions (EDFs) on the dielectric surface for 6.12°. These plots are cumulative over the whole discharge. (a) shows a peak in the energy distribution, resulting from the specified injection, while the large spread is a result of interaction with space charge not present in Figure 3.7a. (b) shows secondaries impact with a range of energies due to the initial distribution and lifetime ranges, broader than the analogous Figure 3.7b.

ure 4.8b from the time to peak current across the full excursion length (i.e. the length of the dielectric surface), Figure 4.8b, as $2.002\,\text{mm}/211\,\text{ps} = 9.483 \times 10^6\,\text{m/s}$, which differs from the kinetic energy estimate by a factor of 2.

The electric field plot for what has been taken as the characteristic center point in this study shown in Figure 4.10 is an extension of what was shown in Figure 3.10 for vacuum-like discharges. Figure 4.10 has a characteristic "overshoot" in the field angle, approaching closer to orthogonal angles than vacuum-like discharges. Recall the expected saturation angle is $\chi_E = \chi_1(\theta_{\text{imp}} = \pi/2) = 24.88°$ for an electron at grazing incidence, discussed in Section 3.1.1 and valid here. The electric field angle in Figure 4.10 peaks at nearly double the saturation angle, well into the region of $\delta < 1$, assisted by the additional electron species from volume ionization. As the discharge evolves, the positive surface charging reduces from subsequent secondary electron impacts where field conditions support $\delta < 1$ (noting that this may not be the case for volume ionization electrons). For these parameters, electron population and average secondary electron energy are not sufficient to generate significant ions until ion momentum pushes fields into the multiplicative region, where new secondaries have sufficient lifetime to gain the required ionization energy while multiplying to sufficient quantities that support bulk ionization.

Finally, discharge evolution characteristics are clearly illustrated in Figure 4.11, where the species numbers oscillate in a closely coupled manner. Scaling for each species number in Figure 4.11a is the ratio of the species peak number to the secondary peak number, which conveniently gives the growth ratio from primaries to secondaries for the *fast transient*, since the peak secondary number occurs during the fast transient. As mentioned in Section 4.1.1, this gain is orders of magnitude smaller than the ideal gain from Equation (4.5), shown as $\sim 10 \times 10^{12}$ in Figure 4.2. Past the fast-transient ($\sim$ ps time frame), the secondaries precede the $Ar^+$ and ionization electrons, as expected, since the secondary

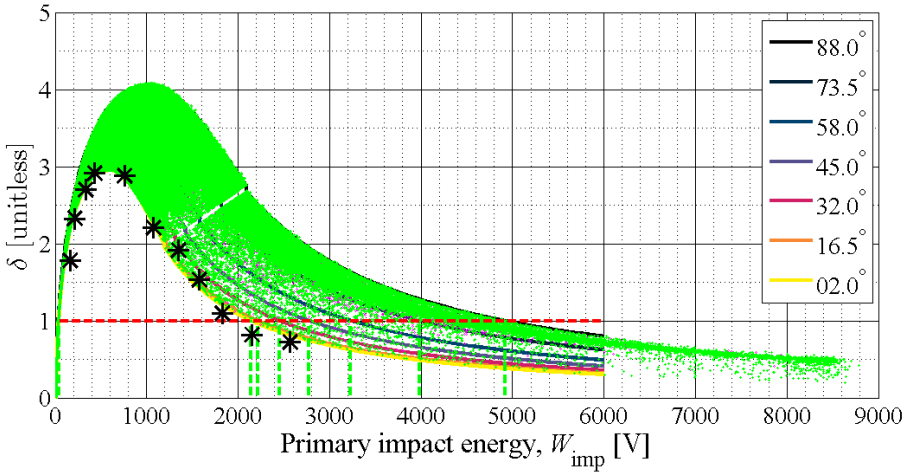


(a) Secondary-emission coefficient vs. impact energy at various impact angles.

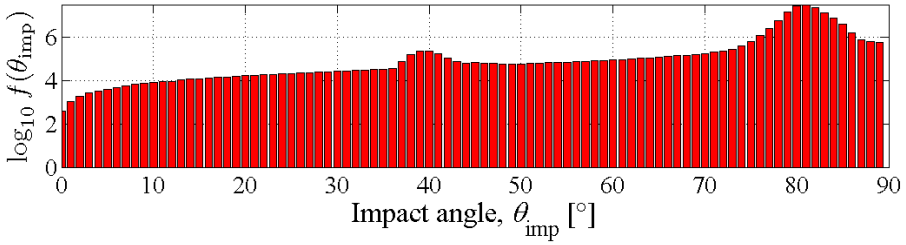


(b) Impact angular distribution.

Figure 4.7: Reconstructed secondary-emission curve from simulation for 6.12° at 1 Torr. Simulation time is 400 ns, showing only a fifth of the total impacts (memory limited). (a) shows the impacting energies for primaries (green) and secondaries (magenta) in the circular (o) marker plotted against the theoretical Vaughan curve [2] at various angles. (b) shows the impact angular distribution, where the peak near 39° (migrated from the initial specification of 32° due to space-charge) is largely composed of primaries while the rest of the distribution is composed of secondaries. Ionization electrons are not included.

avalanche is the dominant seed for bulk volume ionization with these parameters. Ionization electrons closely follow the $Ar^+$ number, but have a much faster decay time due to the large electron mobility. The decay time on the ionization electrons is $\sim 25$ ns, while $Ar^+$ decays with $\sim 50$ ns. Rise times for both the $Ar^+$ and ionization electron species is $\sim 20$ ns, as expected, since volume ionization creates both species at the same time. The characteristic behavior for the ensemble secondary emission coefficient, $\delta_{avg} > 1$, discussed in Section 3.4.1 vis-á-vis Figure 3.11b is still valid for Figure 4.11b during the fast transient time frames ($\sim$ ps) due to the dominance of surface growth. More precisely, the criterion for $\delta_{avg} > 1$ is valid in all cases where ionization has not reached significant coupling to the surface charge. Beyond the fast transient in low pressure cases, $\delta_{avg}$ is not a viable diagnostic since the discharge is not dominated by pure secondary-electron growth. Beyond the fast transient, ionization electrons are broadly distributed in energy such that growth characteristics are no longer *a-priori* with respect to surface fields. As seen in Figure 4.11b, oscillations are apparent, and although there is growth past the fast-transient, the criterion for $\delta_{avg} > 1$ does not hold beyond the fast transient.

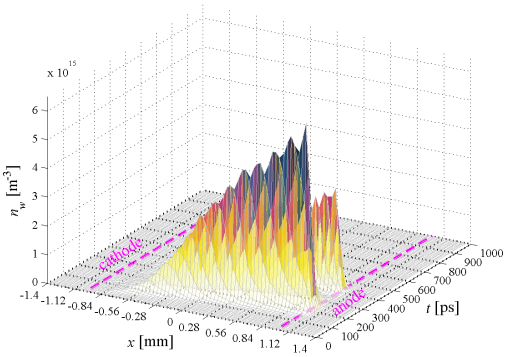


(a) Logarithmic surface plot, fast transient.

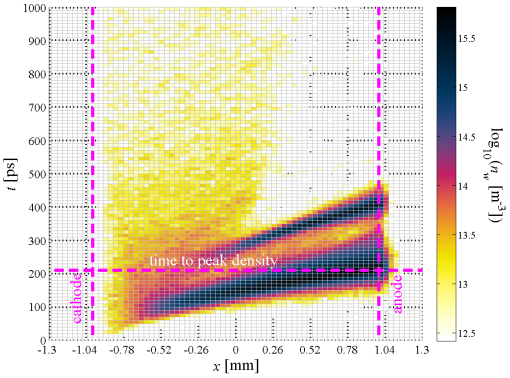


(b) Linear 3-D plot, fast transient.

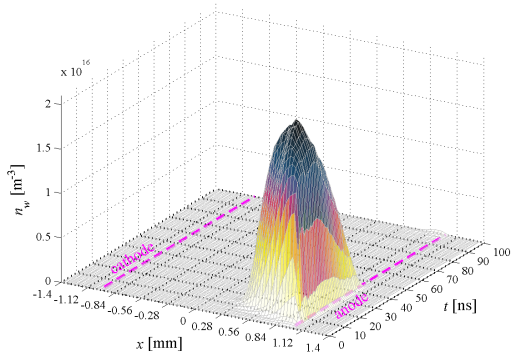


(c) Logarithmic surface plot, ion-assisted regime.

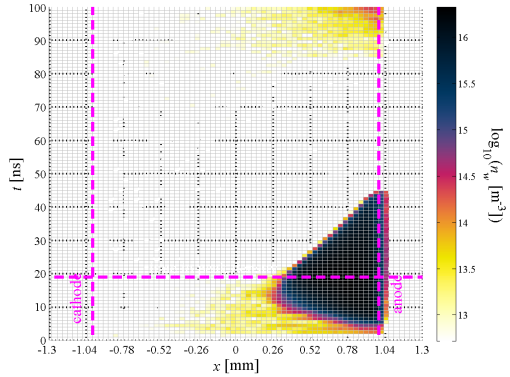


(d) Linear 3-D plot, ion-assisted regime.

Figure 4.8: Plots of the weighted-average density, $n_w$, for secondary electrons over the dielectric surface at $\alpha = 6.12°$ in 1 Torr background argon gas. (a) and (b) are plots for the fast transient regime. (c) and (d) are plots for the ion-assisted regime. Both plots show the evolution of the multipactor front as it grows from discharge onset until the front evacuates at the anode, $\sim 200\,\text{ps}$ for the fast transient and $\sim 20\,\text{ns}$ for the ion-assisted regime. Recalling the cathode is at $\sim -1\,\text{mm}$ and the anode is at $\sim 1\,\text{mm}$, the speed of the front can be calculated by inspection.

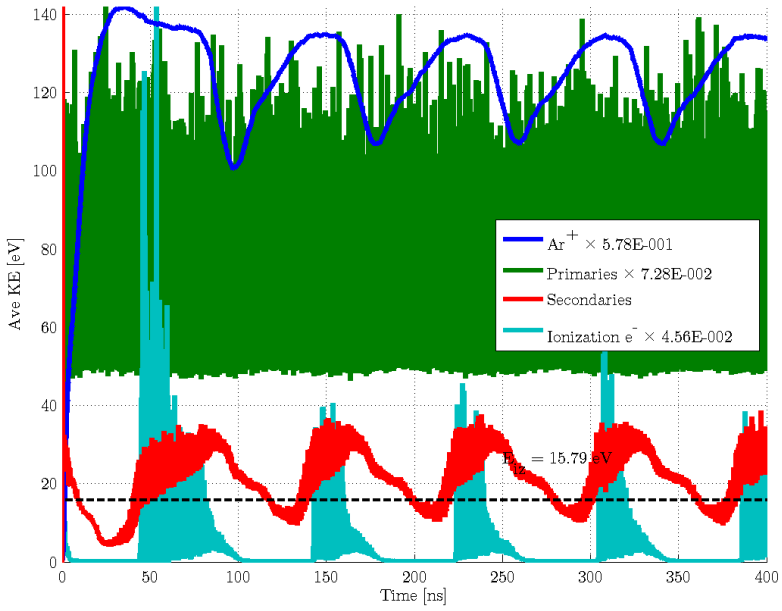


Figure 4.9: Plot of the species average kinetic energy for $\alpha = 6.12°$ in 1 Torr background argon gas. Appreciable ionization is induced with sufficient electron lifetime, but as the discharge evolves, there are time ranges in which field conditions can do not support secondary average energies to induce further volume growth. Ion momentum partially restores conditions supporting surface growth, elongating lifetimes and consequently producing average kinetic energies that support further ionization.

### 4.4.2 Dark-Current Multipactor in Low Pressure Gas

This section details gaseous discharges at 1 Torr with surface field conditions that would otherwise lead to the development of anodic dark-current. Electrons in the discharge can still seed volume growth, which can affect the conditions of the surface fields, most importantly the field angle. As for Section 4.4.1, this exposition will follow a format similar to the analogous Section 3.4.2 for vacuum-like discharges.

Figure 4.12 is a collection of snapshots in phase space, analogous to Figure 4.4, but for the case of a discharge that would otherwise result in dark-current steady-state conditions. The initial discharge clearly follows the vacuum-like characterization in Figure 4.12a, where the fast-transient does not occur over the early discharge. Again, electrons move towards the anode at the right, and slow ions primarily move to the cathode boundary at the left. Figure 4.12a at 100 ps is the phase space for 22.9° at a time analogous to Figure 4.4a. Similar to the vacuum-like case of Figure 3.12a, the initial discharge crawls towards the anode with $\delta_{\text{avg}} < 1$, which is still a valid diagnostic for the initial discharge as it was for the vacuum-like discharge of Section 3.4.2, noted further below. Figure 4.12b at 30 ns shows a time analogous to Figure 3.12b, which is well into a regime of ion-assisted growth that was simply not present in the vacuum-like discharges of Section 3.4.2. Figure 4.12c at 63 ns is towards the end of the ion-assisted growth phase, showing volume saturation of electrons and ions. A new growth cycle starts past 63 ns, where ions have suf-

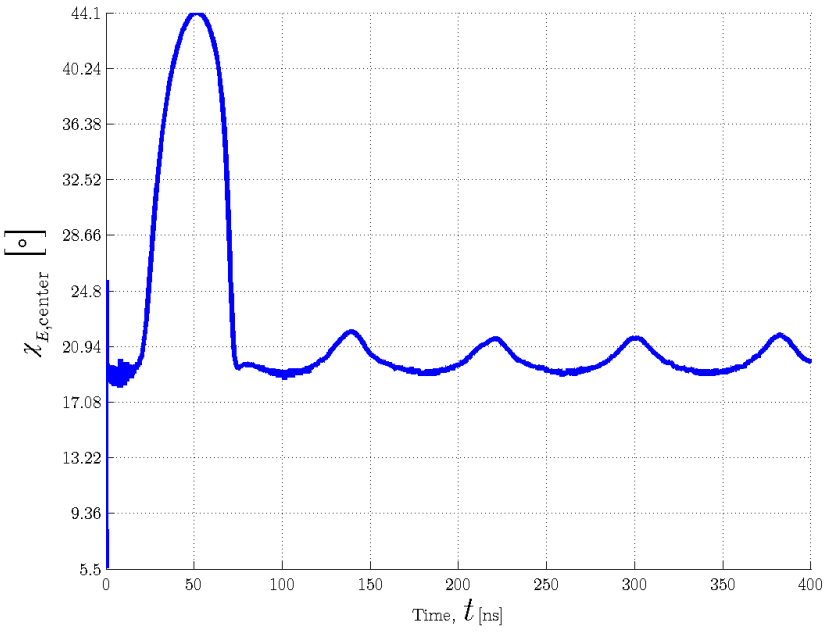


Figure 4.10: Electric-field angle, $\chi_E$ at the center of the dielectric surface vs. time for 6.12 deg in 1 Torr of background argon gas. Fast-transient characteristics are generally similar to Figure 3.10a, while post fast-transient field angles are pushed beyond the $\sim 22.2°$ maximum for the vacuum case due to the presence of further negative charging. Peak field angle is 44.1°, and oscillates about $\sim 20.2°$. The schematic behavior in the presence of volume charge is similar to Figure 3.10b, albeit with positive charge also existing in the volume.

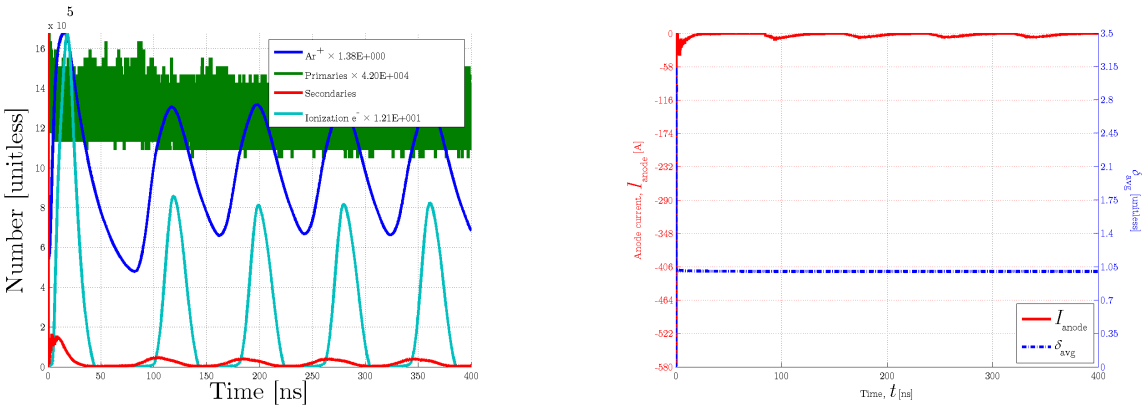


(a) Scaled number (of computational particles).

(b) Anode current and $\delta_{\text{avg}}$.

Figure 4.11: Particle number plots and average secondary-emission coefficient, $\delta_{\text{avg}}$, and anode current, $I_{\text{anode}}$, for the case of $\alpha = 6.12°$ in 1 Torr background argon gas. Note the time scale is from 0 ns to 400 ns, $\sim 100\times$ longer than the VULP analog in Figure 3.11.

ficiently evacuated such that the coupling of volume and surface charge has pushed surface fields into multiplicative growth, increasing the electron population and thus ionization.

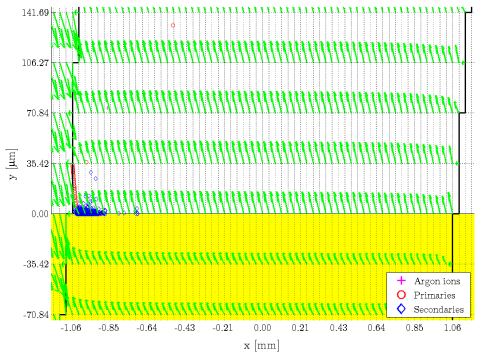


(a) Vacuum-like slow transient, $t = 100\,\text{ps}$.

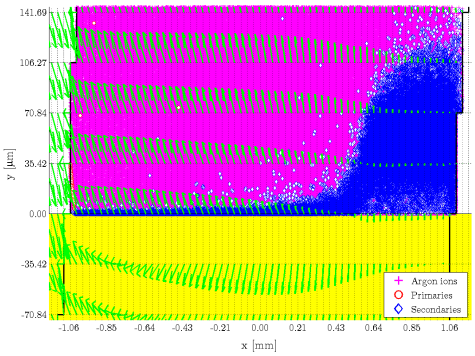


(b) Volume saturation, $t = 30\,\text{ns}$.

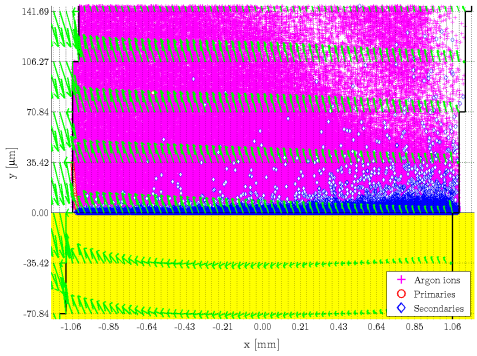


(c) Volume ion evacuation, $t = 63\,\text{ns}$.

Figure 4.12: Configuration-space example of VULP breakdown at 22.9° in 1 Torr background argon gas. Primary, secondary, and ionization electrons move from the lower cathode potential on the left to higher anode potential on the right. Primary electrons are absorbed at the dielectric (shaded region, $y < 0$), emitting secondaries according to the theory outlined in Section 2.3. Single ionization in argon produces additional volume electrons. The grid shown corresponds to the numerical grid, with a square-grid resolution of 35.5 μm in $x$ and $y$. Green arrows correspond to the magnitude and direction of $\vec{E}$ at the displayed time. No SRP.

Charging on the dielectric surface is shown in Figure 4.13. As for the vacuum-like discharges, the initial-impact region shows positive surface charging due to the intentional injection of primary electrons consistent with maximum secondary emission on first impact clearly shown in Figure 4.13a. The remainder of the surface is negatively charged during the early discharge (up to $\sim 20\,\text{ns}$), most apparent in Figure 4.13b. Past $\sim 20\,\text{ns}$), ion-assisted growth pushes the surface into a multiplicative discharge regime, leading to positive charging on the surface, although of smaller magnitude compared to the initial impact region and compared to the initially multiplicative discharge at 6.12° due to the initial negative charging. A similar oscillatory phenomenon is clearly present, with a periodicity of $\sim 70\,\text{ns}$, comparable to the $\sim 80\,\text{ns}$ in the 6.12° case. Again, oscillations present

in Figure 4.13a are the result of coupling between volume ionic charge due to ions and surface charge due to electrons. The coupling in the 22.9° case is slightly different in that the surface is negatively charged, but due to the strong applied bias, ion momentum is still towards the cathode, and the potential depression left behind as the saturated ion cloud evacuates the region near the surface leads to a similar effect as at 6.12°, where field conditions fluctuate into and out of the multiplicative regime near the first-impact energy.

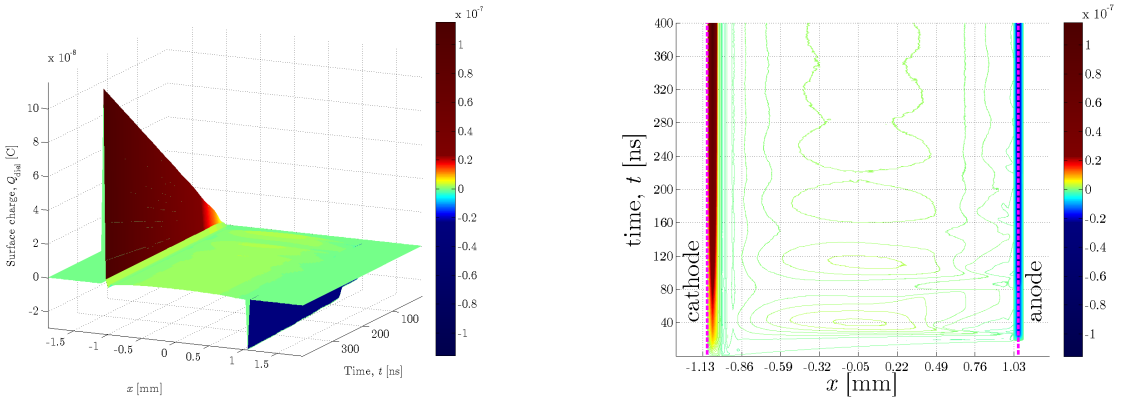


(a) Dielectric-charge full profile.

(b) Dielectric charge contour in $x$ against $t$.

Figure 4.13: Characteristic dielectric-surface charging for a multipactoring discharge at 22.9° in 1 Torr background argon gas. Negative charging dominates through the early discharge up to $\sim 20$ ns, although difficult to see in this scale. More importantly, positive charging is shown over a large region of the dielectric after the early discharge, when space charge alters near surface conditions to support surface characteristics sufficient for multiplicative breakdown. Oscillations are a result of ionic volume charge coupling to the now-dominant positive surface charge, allowing the surface to go into and out of multiplicative conditions.

Figure 4.14a clarifies the impact characteristics for the primaries, showing a peak at the intended initial impact energy around $\sim 800$ eV, which was a clearly more defined peak in the vacuum-like discharge of Figure 3.14a. Recall that the peak in the EEDF deliberately corresponds to the peak in the secondary-emission curve (at a specified impact angle of $\sim 32°$) to intentionally emit the maximum number of secondaries at first impact. Again, primaries in the vacuum-like discharges (c.f. Figure 3.15) are largely monoenergetic through the discharge, while collisions distribute the primaries in the low pressure case at all angles. As for the multiplicative case at 6.12°, the primary electron distribution everywhere other than the peak is $\sim 4$ orders of magnitude lower than the peak. The secondary electron distribution in Figure 4.14b is also distributed due to volume collisions. Figure 4.15 is another view of the broader impact characteristics for these low pressure discharges, but it is difficult to use this diagnostic due to the broad energy characteristics that are difficult to illustrate in this view.

Number density plots for secondary electrons are shown in Figure 4.16, showing the expected slow growth of electrons through the early discharge. Oscillatory behavior is evident in the electron population on similar scales seen in Figure 4.8, past the fast

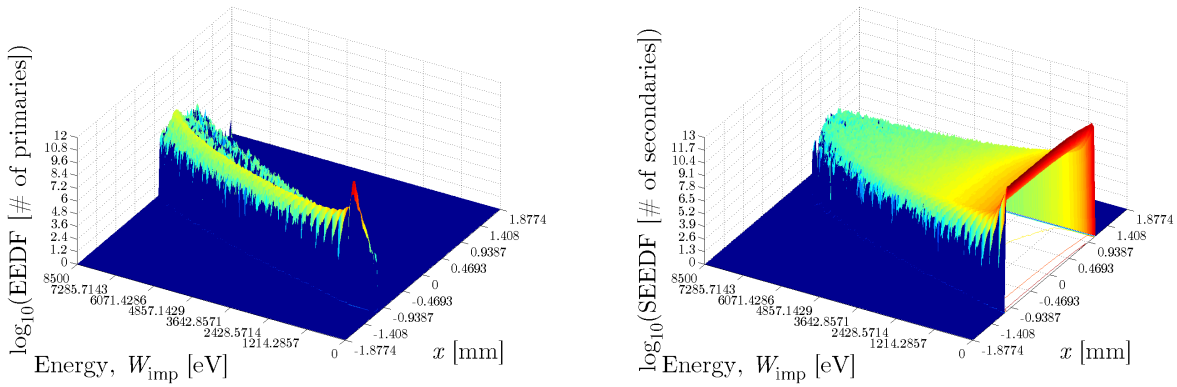


(a) Primary-electron EDF.

(b) Secondary-electron EDF.

Figure 4.14: Primary-electron and secondary-electron energy distributions functions (EDFs) on the dielectric surface for 22.9°. These plots are cumulative over the whole discharge. As was the case at 6.12° in Figure 4.6a, (a) shows a peak in the energy distribution, resulting from the specified injection, while the large spread is a result of interaction with space charge not present in Figure 3.14a. (b) shows secondaries impact with a range of energies due to the initial distribution and lifetime ranges, broader than the analogous Figure 3.14b.

transient for the 6.12° case; in the case of 22.9°, starting at $\sim 20\,\text{ns}$. As for the 6.12° case, the average velocity of the emitted secondaries can be obtained by the average kinetic energy in the bulk volume. While there is no multipactor front, there is a dark-current developing on the surface that creeps towards the anode following similar treatment of the average kinetic energy of the secondary species, which ranges significantly, but oscillates around $\sim 25\,\text{eV}$, giving a dark-current creep velocity of $\sim 2.97 \times 10^6\,\text{m/s}$.

Alternatively, the speed of the dark-current creep is readily estimated in Figure 4.16d from the time to initial current across the full excursion length (i.e. the length of the dielectric surface at 2.2 mm, giving $2.2\,\text{mm}/(15\,\text{ns} = 1.4 \times 10^5\,\text{m/s}$, which is an order of magnitude smaller, largely due to the treatment of the distribution, where a better estimate may be obtained by integrating the energy distribution function with time information, which is not readily available, but may be obtained. Similarly, the speed of the ion-assisted multipactor front is readily estimated by following the peak density across the full excursion length (again, 2.2 mm, assuming the discharge starts to multiply after $\sim 20\,\text{ns}$, giving $2.2\,\text{mm}/(42\,\text{ns} - 20\,\text{ns}) = 1.0 \times 10^5\,\text{m/s}$. Recall that the length of the dielectric is longer in the 22.9° case, i.e. $x_{\text{exc},22.9°}/x_{\text{exc},6.12°} = \cos(6.12°)/\cos(22.9°) = 1.0794$, or 7.9 % longer. For these parameters, ion population is initially limited by the small number of electrons in the system (due to the $\delta_{\text{avg}} < 1$), but ionization does occur in sufficient amounts to create significant space charge. Ionization is expected with these parameters since the average energy of bulk of electrons is greater than the ionization energy, i.e. $K_e > (\mathcal{E}_{iz} = 15.79\,\text{eV})$, for much of the discharge.

It is of interest to note that temporal gradient for the average kinetic energy ($d\text{KE}_{\text{ave}}/dt$) in the early discharge is negative for 6.12° (c.f. Figure 4.9, $\sim 0\,\text{ns}$ to $20\,\text{ns}$) and positive for 22.9° (c.f. Figure 4.17, $\sim 0\,\text{ns}$ to $20\,\text{ns}$). This is a consequence of field conditions

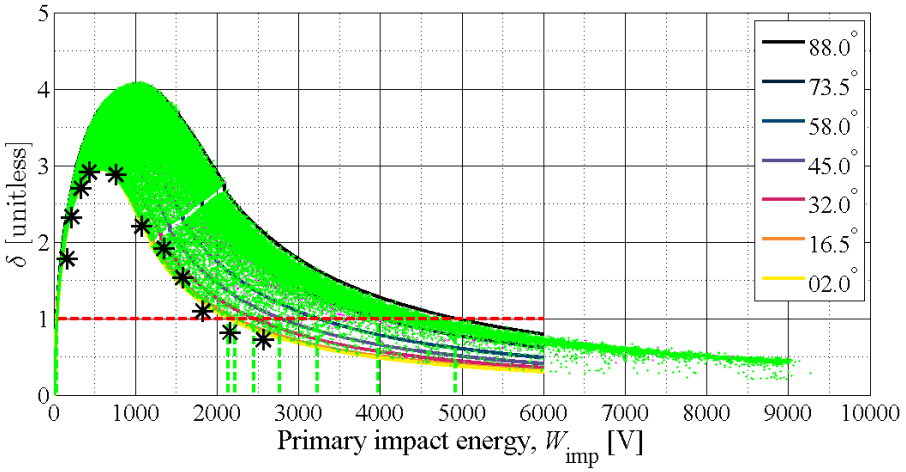


(a) Secondary-emission coefficient vs. impact energy at various impact angles.

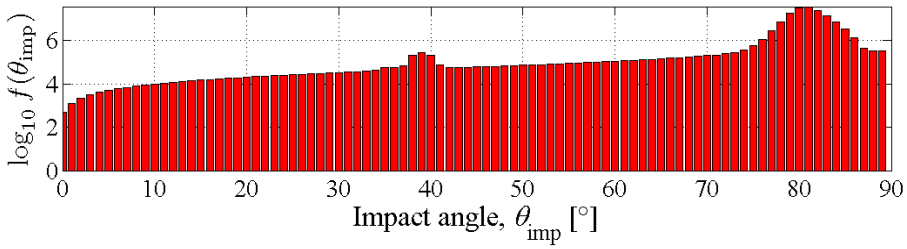


(b) Impact angular distribution.

Figure 4.15: Reconstructed secondary-emission curve from simulation for 22.9°. Simulation time is 5 ns. (a) shows the impacting energies for primaries (green) and secondaries (magenta) in the circular (o) marker plotted against the theoretical Vaughan curve [2] at various angles. (b) shows the impact angular distribution, where the peak near 32.0° is largely composed of primaries while the rest of the distribution is composed of secondaries.

evolving to support emission at first crossover in both cases, but from different sides of the secondary-emission curve. In the 6.12° case, secondaries have longer lifetimes and higher average energy during the fast transient until saturation in the wake of the multipactor front reduces particle lifetimes and energy, bringing the average kinetic energy down on the approach to saturation. In the 22.9° case, average kinetic energies are low because field conditions produce short-lived secondaries with low energy until sufficient negative surface charging elongates secondary lifetime and energy, bringing the average kinetic energy up.

As was the case for 6.12°, the electric field plot for the characteristic center point shown in Figure 4.18 is an extension of what was shown in Figure 3.17 for vacuum-like discharges. The field angle evolves in a similar way to the vacuum-like discharges due to the lack of surface growth and minimal ionization limited by the population of electrons. The field angle is well into the absorption region most easily seen in Figure 3.2b, and negative charging eventually brings field conditions into a regime where impact characteristics support growth about first crossover, i.e. $W_1$. As was the case with 6.12°, the expected saturation angle is $\chi_E = \chi_1(\theta_{\text{imp}} = \pi/2) = 24.88°$ for an electron at grazing incidence, since such energy treatments are independent of the dielectric angle. The electric field

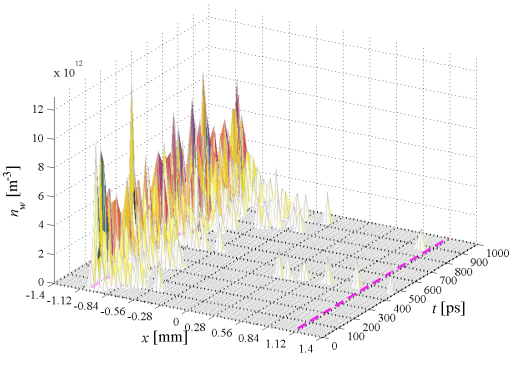


(a) Number-density surface plot.

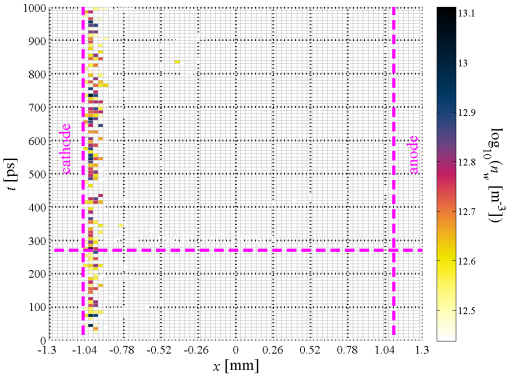


(b) Number-density plot, $x$ vs. $t$.

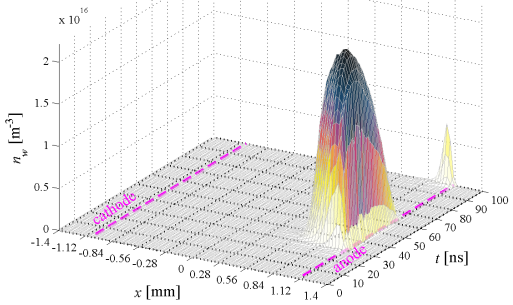


(c) Number-density surface plot.

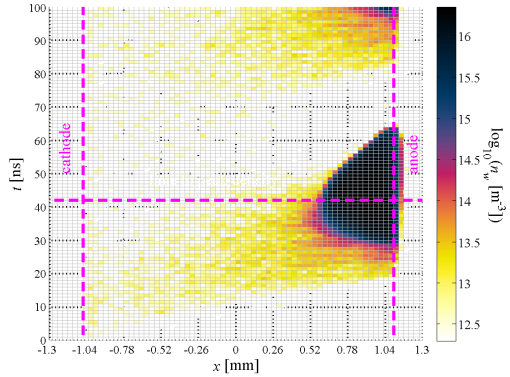


(d) Number-density plot, $x$ vs. $t$.

Figure 4.16: Plots of the weighted-average density,$n_w$, for secondary electrons over the dielectric surface at $\alpha = 22.9°$ in 1 Torr background argon gas. (a) and (b) show the equivalent of the fast-transient time frame at 6.12°, comparing with Figures 4.8a and 4.8b. (c) and (d) show the ion-assisted regime, to be compared with Figures 4.8c and 4.8d The cathode is at $\sim -1.063$ mm and the anode is at $\sim 1.098$ mm, where asymmetry is just due to the stair-stepped boundary representation which happens to vary by some multiple of the grid size, in this case $1 \times dx$. (d) clearly shows the speed of the ion-assisted front, which can also be characterized by the average energy of the ensemble (at the front).

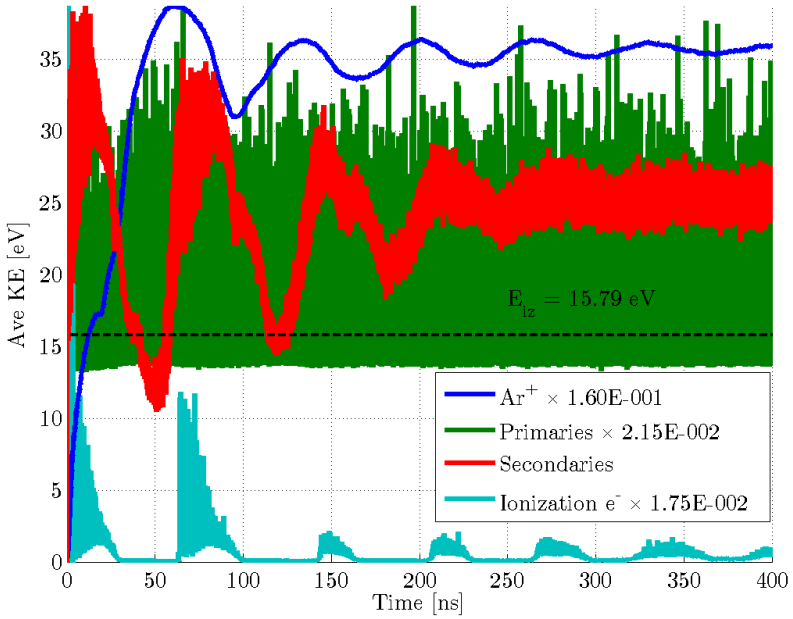


Figure 4.17: Plot of the species average kinetic energy for $\alpha = 22.9°$ in 1 Torr background argon gas. Appreciable ionization is induced with sufficient electron lifetime and secondary population. While energies are typically above the ionization threshold, electron population remains small due to the lack of surface growth. Growth starts to become appreciable at ($\sim$ 20 ns) when field conditions are at least favorable to unit secondary emission, c.f. Figure 4.18.

angle in Figure 4.18 is actually peaked at the initial conditions, and the total discharge experiences damped oscillations rather than the arguably uniform oscillations at 6.12° in 1 Torr, apparent in Figure 4.10. It is interesting to note that the average kinetic energy never drops below $\mathcal{E}_{iz}$ as it did for 6.12°, which can largely be understood by comparing Figure 4.10 and Figure 4.18. Overall, the 6.12° case sees larger field angles (i.e. field angles approaching orthogonal) compared to the 22.9° case, particularly in the early discharge prior to 100 ns. The 22.9° case sees generally shallower angles when ion-assisted growth becomes appreciable, which means longer lifetimes and larger average energy.

Finally, discharge evolution characteristics are clearly illustrated in Figure 4.19, where the species numbers oscillate in a closely coupled manner, approaching steady-state values in unison. Characteristics from 6.12° beyond the fast transient and initial ion-assisted growth (i.e. beyond 100 ns are otherwise similar, where secondaries precede the $Ar^+$ and ionization electrons, since secondaries are still seeding ionization for these parameters and are simply in insufficient numbers to cause appreciable ionization through the early discharge. Ionization electrons, again, closely follow the $Ar^+$ number, but mobility causes much faster decay times. As mobility is largely decoupled from local space charges in these parameters, the decay and rise times for the ionization species remains the same as the 6.12° case, i.e. ionization electron number decays over $\sim$ 25 ns, $Ar^+$ number decays with $\sim$ 50 ns, and rise times for both the ionization species is $\sim$ 20 ns. As for 6.12°, the characteristic behavior for the ensemble secondary emission coefficient, $\delta_{\text{avg}} < 1$,

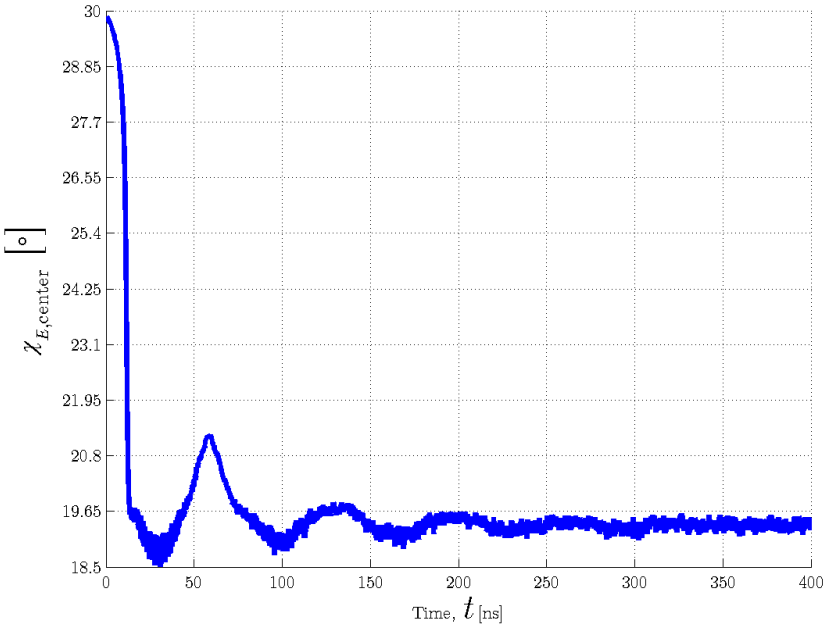


Figure 4.18: Electric-field angle, $\chi_E$ at the center of the dielectric surface vs. time for 22.9 deg in 1 Torr of background argon gas. Clearly, the initial field angle does not support multipactor growth, and oscillates around $\sim 19.4°$, tending to saturation. The schematic behavior in the presence of volume charge is similar to Figure 3.17b, albeit with positive charge also in the volume.

discussed in Section 3.4.2 vis-á-vis Figure 3.18b is still valid for Figure 4.19b during the initial discharge over the first $\sim 25$ ns. Again, when entering the ion-assisted regime, $\delta_{\text{avg}}$ is not a viable diagnostic since the discharge is not dominated by pure secondary-electron growth. It is worth noting that growth and decay times in the ion-assisted growth regions are comparable to the ion-assisted growth regions of Section 4.4.1. Ion-assisted oscillatory phenomena can be considered partially decoupled from the physical dielectric angle, while it should be clear that the phenomenon is not strictly decoupled since initial surface charging will influence the long-term oscillatory behavior evident in the damped oscillations at 22.9° that are not present at 6.12°.

## 4.5 Outgassing and Diffusion

This section discusses the effect of outgassing on the evolution of otherwise VULP discharges, where initially ultra-low pressures are targeted due to the relatively large diffusivities, the presence of variable diffusivity due to large pressure gradients, and the interest in discharges dominated by surface effects for this study. Outgassing can replenish gas species near the dielectric surface, where multipactoring cascades would be subjected to increased probability of ionization, further enhancing multiplication and altering the time to saturation depending on local electric-field characteristics. This treatment will focus on the fundamental effects of a diffusive outgassed source of neutral argon into a

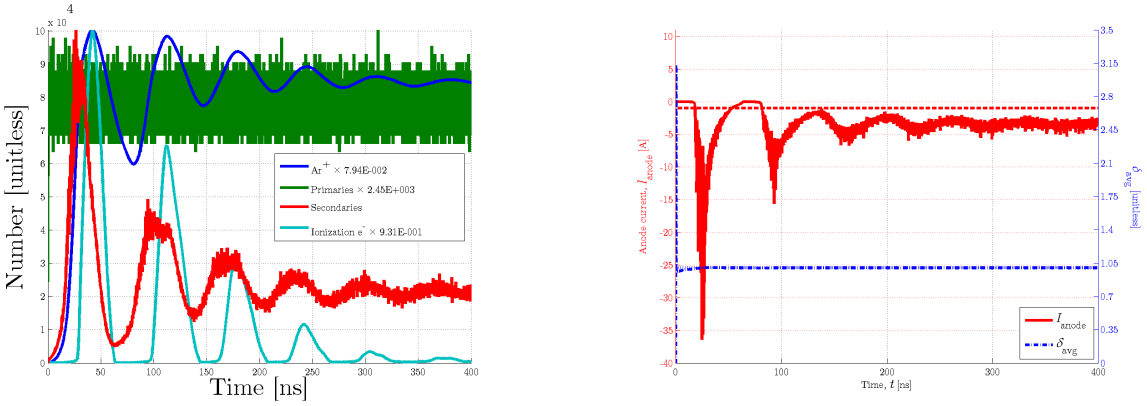


(a) Scaled number (of computational particles).

(b) Anode current and $\delta_{\text{avg}}$.

Figure 4.19: Particle number plots and average secondary-emission coefficient, $\delta_{\text{avg}}$, and anode current, $I_{\text{anode}}$, for the case of $\alpha = 22.9°$ in 1 Torr background argon gas. Note the time scale is from 0 ns to 400 ns.

neutral argon background. Outgassed species are best considered a desorbed source of argon, although the particular physics of adsorption/desorption, and the characteristic motion of outgassed species are not treated in this study. A corollary intent for this treatment is to lay the foundation for future work using XOOPIC to model a variety of outgassing effects.

Section 4.5.1 outlines a simplified application of the Malthus diffusion equation in 1-D for outgassed argon into background argon showing the baseline case for consideration where diffusion can penetrate deeply on time scales of interest to this study. Section 4.5.2 compiles the results of applying the outgassing formulation detailed in Section 2.4 to XOOPIC. Section 4.5.2.1 is the PIC treatment in 1-D for a constant-flux, zero-velocity source of argon into argon, analogous to the system described in Section 4.5.1, showing similar penetration characteristics. Section 4.5.2.2 extends the results of Section 4.5.2.1 to include an impact-dependent flux, showing a significantly altered profile for the outgassing species that expectedly tracks the multipactoring growth along the dielectric, and necessarily means diffusive processes will be stronger towards the anode, where the gaseous profile is of much higher density. Section 4.5.2.3 completes the treatment by including the second spatial dimension, which can have the effect of reducing ionization probability in some regions for otherwise similar outgassing conditions by expanding the spatial domain while also increasing interaction probabilities further upstream by enhancing the presence of gaseous species by diffusion of large downstream densities into the upstream region. Section 4.6 outlines additional considerations for outgassing and the expected behavior for the fully-realized discharge in 2-D, particularly noting that kinetic treatment should be implemented for future studies.

### 4.5.1 The Malthus Diffusion Equation

This section outlines a first-order, 1-D analysis of diffusive outgassing in the typical configurations for this study to develop an intuitive understanding of the behavior of

VULP discharges under diffusive conditions. A 1-D form of Equation (4.7) is used with $y$ as the spatial metric for a half-space slab with a one-way flux of electrons from the surface, with an ionization loss term and no gain term:

$$\frac{\partial n_{\mathrm{A}}(\vec{r},t)}{\partial t} = \mathscr{D}_{\mathrm{AB}}\left(\vec{r},t\right)\nabla^2 n_{\mathrm{A}}(\vec{r},t) - n_e\left(\vec{r},t\right)n_{\mathrm{A}}(\vec{r},t)\sigma(v_{\mathrm{rel}})v_{\mathrm{rel}}, \tag{4.7}$$

where $n_{\mathrm{A}}$ is the density of gas A (i.e. the diffusing gas); $\mathscr{D}_{\mathrm{AB}}$ is a diffusion coefficient denoting diffusion of gas A into another gas, B; and the right-most term represents a loss term for the diffusing species (gas A). $\mathscr{D}_{\mathrm{AB}}$ is generally state dependent, i.e. dependent on the local pressure, and implicitly dependent on space and time (but written here as explicitly dependent on space and time).

Consider the operating schematic of Figure 4.20. For this first-order analysis, a region near the surface is identified as an approximate multipactoring region of uniform electron density, typically up to a few tens of microns thick where electrons could be in sufficient density to cause significant ionization losses to the neutral population near the surface; this is typical of steady-state conditions in VULP discharges as outlined in Chapter 3. For the purposes of this study, the sink term is limited to ionization losses as written in Equation (4.7); neutral species undergoing ionization are thereafter strongly affected by local electrostatic forces and are thus removed from the diffusion process of the neutral species. Depending on rates of outgassing and ionization, sheath formation and steady-state conditions might also be affected. The velocity distribution of outgassed species is neglected, isolating purely diffusive processes. Electrons from the triple point will impact and multipactor along the dielectric, depositing energy on the serve and causing adsorbed species to be emitted. Increases in the surface temperature from electron impact are also neglected. There will, of course, be variability in the spatial profile of the diffusive gas since the multipactor profile is peaked toward the anode. The scenario of uniform gaseous profile is therefore more "severe", since densities will be increased towards the cathode where multiplication factors are low, i.e. there will be no loss in generality for this treatment. Consider the following boundary conditions:

$$\begin{aligned}
&\Gamma_y\left(y=0,t\right)\left[\frac{\text{neutrals}}{\text{m}^2\cdot\text{s}}\right] = \Gamma_{y0} = \mathscr{D}_{\mathrm{AB}}\left(y,t\right)\left.\frac{\partial n_{\mathrm{A}}}{\partial y}\right|_{y=0}\\
&n_{\mathrm{total}}\left(y,t=0\right)\left[\frac{\text{neutrals}}{\text{m}^3}\right] = n_{\mathrm{bg}}\\
&n_{\mathrm{total}}\left(y\to\infty,t\right)\left[\frac{\text{neutrals}}{\text{m}^3}\right] = n_{\mathrm{bg}}
\end{aligned} \tag{4.8}$$

$n_{\mathrm{bg}}$ is the background gas pressure. $\Gamma_y$ is the flux of particles from the dielectric surface, taken to be a one-way flux approximated from outgassing observations in [13]. $n_{\mathrm{total}}$ is the total neutral-gas density consisting of diffusive and background species, which is set everywhere to the background gas density, $n_{\mathrm{bg}}$, at the initial time, $t=0$. $n_{\mathrm{total}}(y\to\infty)$ is also set to $n_{\mathrm{bg}}$ for all time. Generally, the asymptotically-infinite distance is chosen with the practical considerations of Chapter 2, letting $y = n_{\mathrm{bdry}}D/2\cos(\alpha)$; for the test case to follow, $\alpha = 0$ and the boundary error index, $n_{\mathrm{bdry}}$, is set to 2.

$$\frac{\partial n_{\mathrm{total}}}{\partial y}\left(x=-\frac{D}{2}\sec\alpha,t\right)\left[\frac{\text{neutrals}}{\text{m}^3}\right] = \frac{\partial n_{\mathrm{total}}}{\partial y}\left(x=+\frac{D}{2}\sec\alpha,t\right) = 0 \tag{4.9}$$

Furthermore, gas molecules will be of relatively low energy, so assume gas molecules are reflected at the walls, so that the wall condition is a simple Neumann condition as in Equation (4.9). For simplicity, it will generally be assumed that the semi-infinite condition will be Dirichlet, set to the background gas density, which is equivalent to a bleed the boundary that maintains the pressure out at the semi-infinite boundary. The case of an open boundary condition may also be applied, and will generally just return the system to the behavior of Chapter 4 since sufficiently long times will approach saturated densities through the whole volume. It should be noted that the PIC treatment neglects electrode boundaries as a matter of time constraints and current lack of general tools in XOOPIC for dealing with non-orthogonal boundaries, but the effect should be minimal since reflected particles at the boundaries would preferentially diffuse *away* from the surface in any case that would reflect or scatter off boundaries.

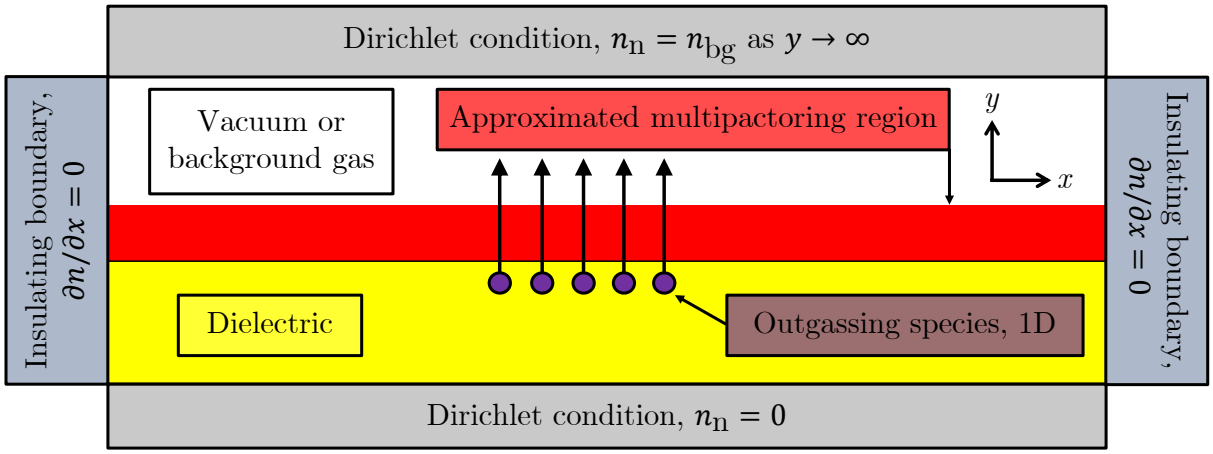


Figure 4.20: Simple 1-D test configuration for outgassing. Outgassed species interact with near-surface electrons, indicated schematically by the region labeled "approximated multipactoring region", over short time periods.

The diffusion coefficient is taken from [64], reproduced in Equation (4.10).

$$\mathscr{D}_{AB} = a\left(\frac{T}{\sqrt{T_{cA}T_{cB}}}\right)^{b}(p_{cA}p_{cB}))^{1/3}(T_{cA}T_{cB})^{5/12}\sqrt{\frac{1}{M_A}+\frac{1}{M_B}}\frac{1}{p} \tag{4.10}$$

For nonpolar gas pairs, $a = 2.745 \times 10^{-4}$ and $b = 1.823$. All quantities marked with a subscripted 'c' denote 'critical' values. Finally, note that the "diffusion depth" is defined as the location of the diffusion front, i.e. the spatial point closest to the surface where $n_{total}(t) = n_{bg}$.

While this study will largely concentrate on an argon outgassed species into an argon background (Ar-Ar), Figure 4.21 illustrates the differences between Ar-Ar and diatomic hydrogen outgassing into an argon background ($H_2$-Ar), showing penetration depths at various times. Parameters are listed in Table 4.1, and the simple Crank-Nicolson scheme from [47], detailed in Section 2.B.2, is used.

Figure 4.21, shows the Ar outgassing into Ar background penetrates the system up to $L/2$ after $\sim 1$ ns, which is on the order of the VULP discharge times seen in Section 3.4;

Table 4.1: Parameters for outgassing test problem.

| Parameter | Variable | Value |
|---|---|---|
| (Near-surface) electron density | $n_e$ | $1 \times 10^{14}$ electrons/m$^3$ |
| System length | $L$ | 2 mm |
| Outgassing flux | $\Gamma$ | $1 \times 10^{23}$ neutrals/m$^2$/s |
| Background gas density | $n_0$ | 1 mTorr $= 3 \times 10^{19}$ neutrals/m$^3$ |
| Collisional cross section | $\sigma$ | $2 \times 10^{-20}$ m$^2$ |

however, normalized density is not significant compared to background. The density of outgassed neutrals expectedly continues to increase near the surface up through $\sim 100$ ns shown in the plot. Since gaseous discharges can run up through several hundred ns, this suggests that the edge condition should be treated with a Neumann condition rather than the Dirichlet condition set for this test case in cases running out to such temporal conditions. This treatment is concerned with how diffusive effects influence the scale of the fast-transient time from Chapter 3, where growth characteristics are surface-dominated.

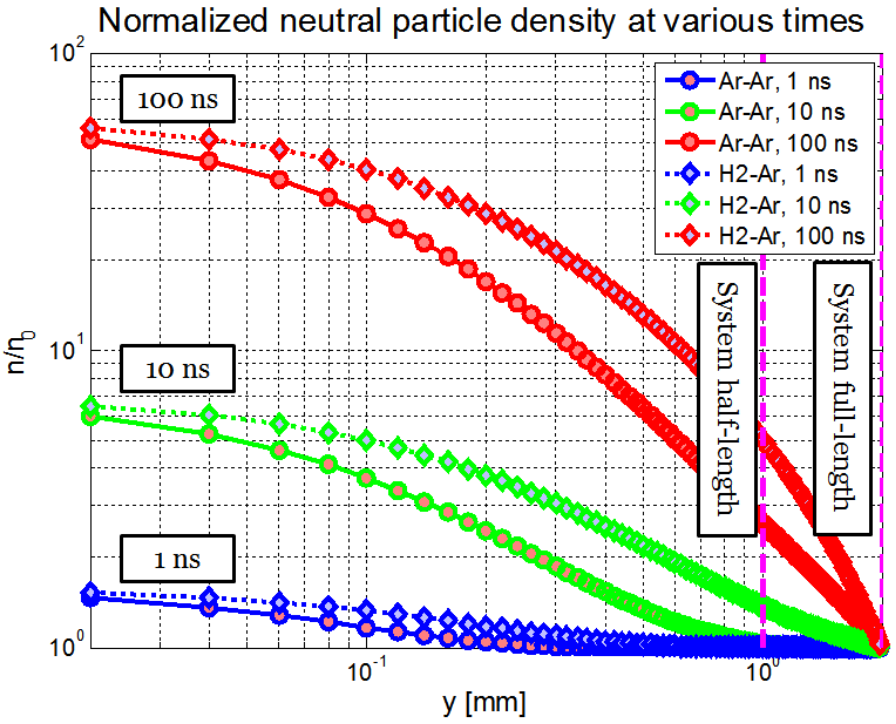


Figure 4.21: Crank-Nicolson solution to the 1-D Malthus diffusion equation, Equation (4.7), with no losses. Parameters used are those listed in Table 4.1. Ar-Ar and $H_2$-Ar are shown for various times, indicating significant diffusion through typical discharge times.

Figure 4.22 shows the effect of including electron interactions near the surface for a case with moderate electron population and interaction rates which do not significantly

affect the diffusion characteristics; however, at (uniform) densities equivalent to the *peak* multipactoring front, Figure 4.23 shows near-surface interactions could deplete neutrals in the multipactoring region, causing bi-directional diffusion near the dielectric surface in the worst case. Figure 4.23 is shown for illustrative purposes of the worst case scenario, which is not expected for operational densities in this study, but should be noted. The diffusivities are shown in Figure 4.22b and Figure 4.23b for the case of moderate loss and large loss, respectively. Consistent with the basic illustration of diffusivity properties in Figure 2.17, the higher the pressure, the lower the diffusivity. Flow will occur in the direction of the pressure gradient, and will occur more strongly in regions of higher diffusivity where pressure is low.

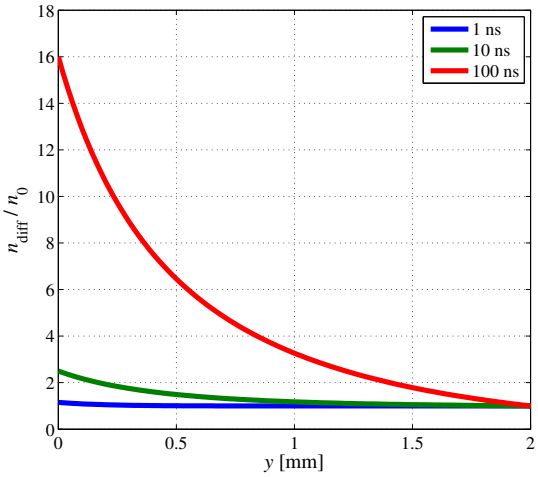


(a) Ar density through 100 ns

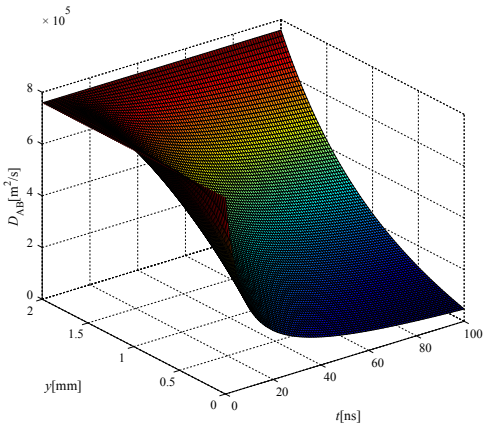


(b) Diffusivity at all points through 100 ns

Figure 4.22: Solution to the Malthus diffusion equation with moderate loss over 100 ns. The diffusion coefficient for each point at each time is shown.

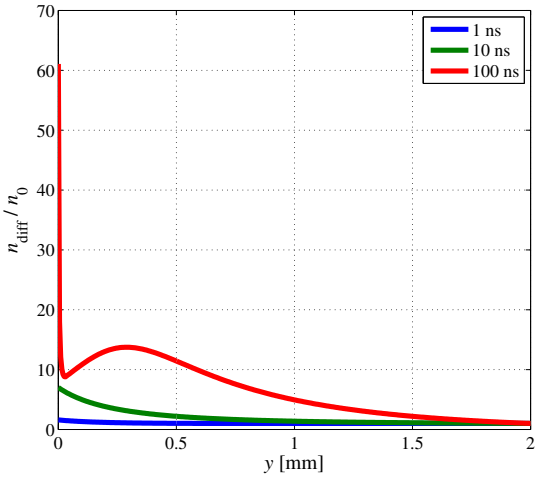


(a) $H_2$ density through 100 ns

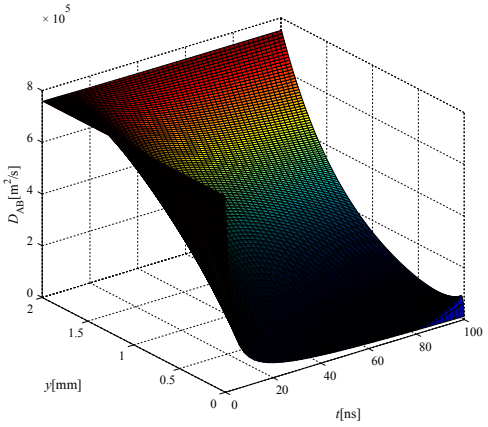


(b) Diffusivity at all points through 100 ns

Figure 4.23: Solution to the Malthus diffusion equation with significant loss over 100 ns. The diffusion coefficient for each point at each time is shown.

### 4.5.2 Diffusive Outgassing in PIC

As noted in Section 2.4, the implementation in PIC is a two-step approach, where diffusion is implemented first, and then collisions are implemented in the standard manner already developed as part of the PIC-MCC model. The separation of these effects is the primary distinction between the implementation in this section and the treatment in Section 4.5.1, but diffusive effects are expected to be slower than the fast-transient phenomena, so resolution of the fast transient (already established) is a sufficient condition to presume that the diffusive phenomena will be well-resolved in this treatment.

#### 4.5.2.1 Constant-Flux, 1-D Diffusive Outgassing

The case of constant-flux, diffusive outgassing is most similar to the studies of Section 4.5.1, and would be the limiting case for Sections 4.5.2.2 and 4.5.2.3 when taken to steady-state conditions with a sufficient uniform outgassed flux. Figure 4.24a shows the profile of the number density at the end of this run at 5 ns, using similar densities to the moderate ionization rates in Figure 4.22.

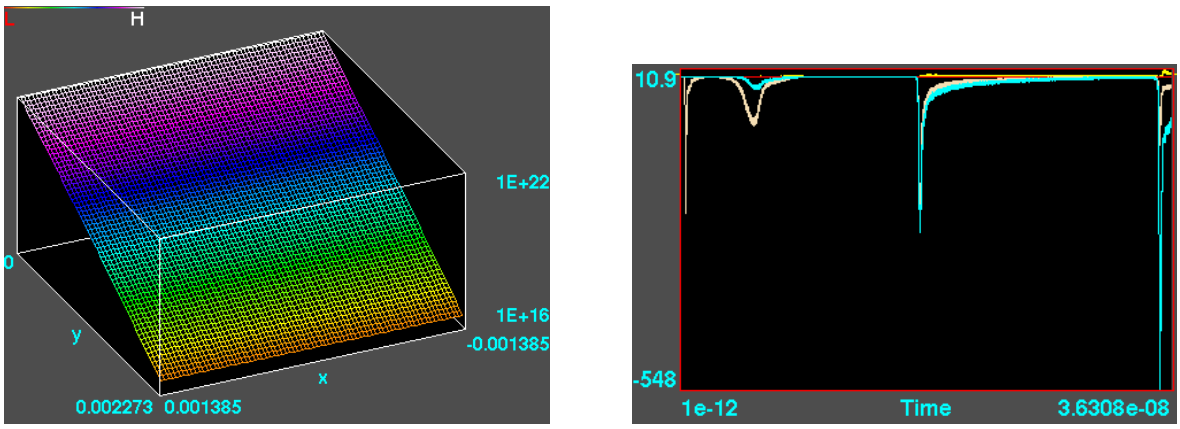


(a) Ar density. (b) Anode current.

Figure 4.24: Number density and anode current for constant flux of outgassed neutral density in 1-D diffusion. Expected uniform profile, consistent with the characteristics of Figure 4.22. Fast-transient and initial slow transient show similar characteristics to the discharges of Chapter 4, while new, fast rise-time pulses are generated here due to concentration of ionization near the surface and subsequent uniformity of multipactoring electrons. Using direct XOOPIC diagnostic output for the gaseous region only.

The behavior metrics of the constant-flux discharge through the fast-transient follow similar characteristics as the VULP discharges of Chapter 3 due to the relatively minor variation from vacuum characteristics on the time scale of the fast transient, $\sim 500$ ps. As shown in Figure 4.24b, there is clear contrast in the rise times of the anodic current post the initial fast transient and a slow current associated with the system in similar surface-field conditions from Chapter 4, where electrons prior to saturation are generated further away from the surface, leading to a broader energy spectrum. To recap Chapter 4, discharges resulted in an early fast transient associated with surface-dominated multipactor, followed by oscillations driven by ion momentum, where ionization occurred in a uniform

background gas. As the gas peeled away from the surface, a restorative feedback on the surface pushed the system back into a multiplicative regime, where electrons were interacting with bulk volume gas throughout the volume. In contrast, ionization profiles in this section are more concentrated towards the surface, which means the profile of electrons undergoing multiplication at the surface can be much more uniform, since more ionization events are closer to the surface. As was the case in Chapter 4, the frequency of oscillatory pulses are driven by the slow ions, but the shape of the pulse is driven by the electron profile through the volume. With higher concentrations of ionizations (thus electrons) nearer to the surface, the lifetimes of electrons in the bulk are much more uniform than in the cases in Chapter 4, leading to more uniform electron profiles on new multipactor fronts post fast-transient. Uniform lifetimes lead to uniform velocity distributions for the electrons, creating a faster pulse lead.

#### 4.5.2.2 Impact-Dependent, 1-D Diffusive Outgassing

The clearest illustrations of the influence of impact-dependent flux is shown in the profile of the neutral species and anode current, shown in Figure 4.25a and Figure 4.25b, respectively. The neutral density tracks the multipactoring electrons, as expected, causing a large density of neutrals at the anode to develop, increasing ionization towards the anode and proportionately increasing the current. The peak anode current shown in Figure 4.25b is higher by an order of magnitude than the case of Figure 3.11, which would be the most relevant comparison. The variation would be dependent on the characteristic of impact-dependent outgassing, but the main point is that the outgassing will track the multipactoring growth.

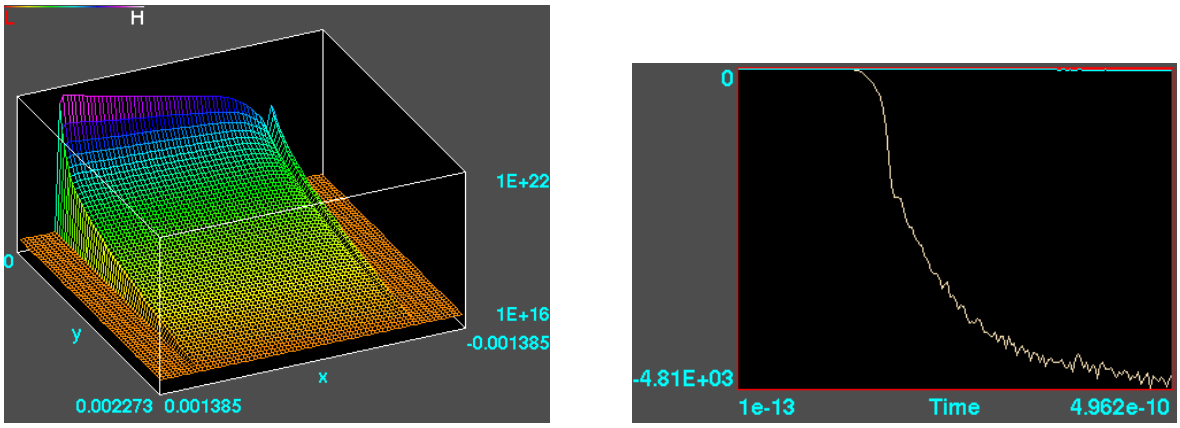


(a) Ar density.

(b) Anode current.

Figure 4.25: Number density and anode current for impact-dependent flux of outgassed neutral density in 1-D diffusion. Number density profile tracks the multipactoring electron density, as expected, peaking towards the anode. Fast-transient and initial slow transient show similar characteristics to the discharges of Chapter 4, with pulse shape differences due to ionization closer to the surface. Using direct XOOPIC diagnostic output for the gaseous region only.

#### 4.5.2.3 2-D Diffusive Outgassing

As alluded to earlier, the diffusive process is relatively slow compared to the fast transient, so the 2-D diffusive outgassing generally looks similar to the 1-D process through the fast transient. This is characteristic is most apparent comparing Figure 4.25a and Figure 4.26a, where the peak density is practically identical due to the minimal diffusive effects on the fast-transient time scale (noting the fact that the applied outgassing characteristics are, of course, identical). Similarly, the anode current, comparing Figure 4.25b and Figure 4.26b, shows comparable peak currents through the fast transient phase.

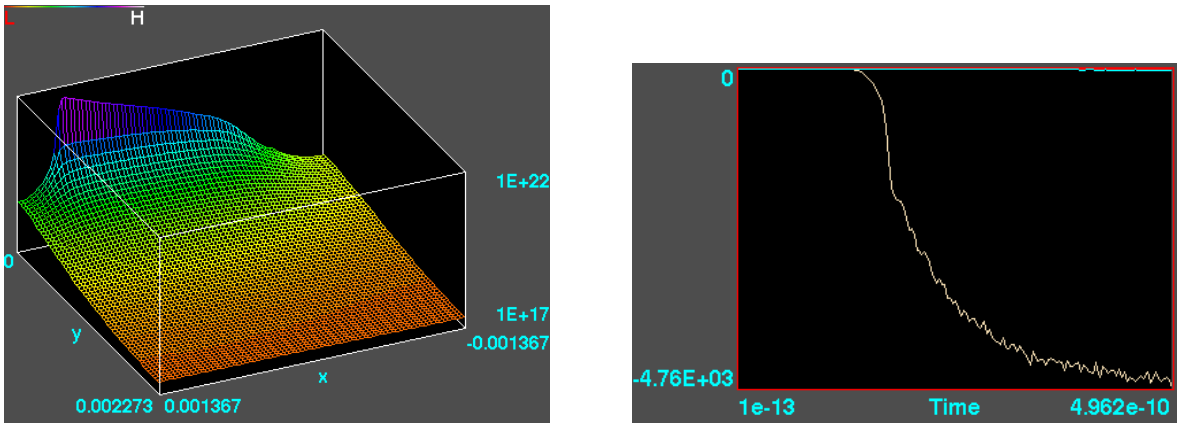


(a) Ar density.

(b) Anode current.

Figure 4.26: Number density and anode current for impact-dependent flux of outgassed neutral density in 2-D diffusion. Number density profile similarly tracks the multipactoring electron density, as in expected, peaking towards the anode. Fast-transient and initial slow transient show similar characteristics to the discharges of Chapter 4, with pulse shape differences due to ionization closer to the surface. Using direct XOOPIC diagnostic output for the gaseous region only.

#### 4.5.2.4 Continuing Work in Diffusive Outgassing

The work in diffusive outgassing is presented to lay the foundation for future study and further modeling, including kinetic collisions that have yet to be included in the XOOPIC framework. This section illustrates that diffusive outgassing leads to expected hybrid behavior, where the fast transient exists prior to sufficient outgassing, and the proximity of outgassed species to the surface can influence the average energy of electrons that impact the surface, causing altering ion-assisted growth to be characterized by faster pulse rise times than seen in previous sections.

## 4.6 Future Work

This implementation lays the groundwork for future studies with outgassing on dielectric surfaces. Much of the important phenomena have been neglected in order to generate a baseline study, isolating diffusive phenomena that parallels the Malthus diffusion form of

Equation (2.26). Future studies should implement complete physisorption and chemisorption models for extended applications. More complete models for electron-stimulated desorption should also be implemented. When applying temperature-dependent outgassing models, the diffusion of generated heat should also be diffused into the dielectric and vacuum, and direct application of the models developed here for neutral gas diffusion are, of course, directly applicable and simply need to be repurposed for a globally tracked heat variable. It was noted earlier that boundaries were neglected in the PIC treatment due to the current lack of tools to identify and appropriate the correct elements in the directional matrix operators, which just consist of unit elements at the appropriate points in the matrix.

Recall that this work extends existing models for collisions between a specified particle species and a fluid gas model where interactions are encapsulated in an MCC model. This approach works very well for interactions where new or modified particles are created, but is not suited for corollary interactions where particles are removed from simulation, e.g. recombination of ionized oxygen with electrons. It is not sufficient to treat the new ionized oxygen with a fluid model in this case due to the low statistical representation upon creation, and treating a charged species as a fluid would nullify the benefits of the PIC model by smoothing out kinetic effects. A proper kinetic, particle-particle treatment should be implemented for corollary effects to further extend the utility of diffusive models.

Finally, improved solvers should be implemented in the case of higher densities, where the matrices of Equation (2.106) can be poorly conditioned. This study limited to densities where matrix conditioning was not observed, but future studies may be interested in worst-case studies for operating conditions, e.g. cold shot operating conditions or conditions where bake-out is not an option.

## 4.7 Chapter 4 Conclusions

It should be noted that a number of simplifications were made in theoretical treatment to gain insight into the behavior of the system, including the lack of scattering, no gain terms, no absorptive loss terms, and the inclusion of a single loss term in the Malthus diffusion equation of Equation (4.7). Scattering is included in the standard MCC models for XOOPIC, and additional volumetric loss terms can be modeled in certain gases, but general theoretical treatment still requires a number of assumptions, e.g. isotropic scattering, to make solutions tractable. The theoretical treatment herein therefore covers the most fundamental effect of diffusive flow by gradient concentration with the most significant loss factor (ionization).

Uniform outgassing is typical of cold starts or dirty HPM systems where bake-out is not an available option. The uniform outgassing case suggests a bridge between the vacuum-like discharges of Chapter 3 and the oscillatory discharges of Chapter 4. Additional effects on the pulse shape become apparent with the variation in spatial variation in neutral density that causes near-surface electrons to add to the multipactoring electrons in a way that causes fast rise times in subsequent pulses that are otherwise driven by ion momentum.

The transition to impact-dependent outgassing turns out to be not as neatly consistent with previous developments due to the large density neutral density buildup near

the anode, tracking with the multipactor population. The increased neutral density near the anode increases the anodic current by a few orders of magnitude from the standard vacuum-like cases, but the overall characteristics still match the fast-transient characteristics of Chapter 3, but enhanced due to the increased-near-surface ionization. The same fast rise-time phenomenon seen in the late-stage 1-D uniform outgassing case is present in the impact-dependent outgassing case for the same reason that new ionizations occur close to the surface, leading to similar characteristics as the main multipactor seed and thus a fast pulse. The extension to 2-D does not affect the fast-transient phenomena due to the relatively slow characteristic of the diffusion process, but later times are affected by the inclusion of the additional degree of freedom.

Discharges are still well described by the DC susceptibility theory of Chapter 5, where surface effects are largely driving growth conditions in the early discharge. Susceptibility will capture the temporal hybrid characteristics noted above, transitioning between surface-dominated effects at early times as in Chapter 3 into the space-charge coupled discharges of Chapter 4, where oscillations develop dependent on ion characteristics. In keeping with *a-priori* metrics, it is still advised to operate with limit lines drawn according to the initial background density, which will generally overestimate the susceptibility characteristics. In principle, this hybrid condition is as expected, but the success of the DC susceptibility theory in describing discharge temporal evolution cannot be overstated, as it provides useful insights into how to leverage or mitigate growth from systems that experience outgassing on longer timescales than those seen in Chapter 5, and may also provide a diagnostic tool in cases of unexpected outgassing where the appearance of space-charge coupled phenomena might be correlated to oscillatory behavior in diagnostic susceptibility diagrams.

# Chapter 5

# DC Breakdown Susceptibility

## 5.1 RF Susceptibility

The technique of breakdown susceptibility (herein referred to as simply "susceptibility", not to be confused with the classical concept of "electrical susceptibility" describing the tendency for a dielectric to polarize under external fields) was originally developed under Dr. Y.Y. Lau via his former graduate student, Dr. R. Kishek, at the University of Michigan [1, 10] studying breakdown in RF for high-power microwave (HPM) transmission windows. The likelihood of discharges to undergo multiplicative breakdown in RF systems is well characterized in the so-called "susceptibility diagram", with the typical form shown in Figure 5.1, reproduced from [1], for various values of $\delta_{\max,0}$, roughly representing different materials for transmission windows. These diagrams show the limits of multiplicative discharges against normalized field metrics: the driving field (parallel to the surface in the typical configuration) plotted in the ordinate and the DC field (perpendicular to the surface) plotted in the abscissa. Typically, a single macroparticle injected with random energy from a predetermined distribution, typically Maxwellian, is tracked for baseline construction of susceptibility diagrams (although other studies may consider multiple-particle injection targeting bulk growth with consideration for associated statistics of the injected distribution). Particles are tracked via Monte-Carlo simulation over a statistically large number of injections to monitor exponential growth or decay of the charge on impact. A growth of zero over a large number of impacts indicates the location of the limits parameterized in $E_{\mathrm{DC}}$, $E_{\mathrm{RF}}$ and $\delta_{\max,0}$. Typically, these diagrams are plotted with the orientation of the target surface conformal to one of the axes so that the opposing axis is conformal to the surface normal; in this case, the dielectric is situated with the surface vertical in a Cartesian space, and the electric-field normal is conformal to the abscissa. This configuration rather conveniently gives the orientation of the field angle relative to the surface tangent, a characteristic not leveraged in typical studies for susceptibility, but does play a significant part in this study as Chapter 3 showed fundamental multipactor effects are strong functions of the dielectric-surface field angle.

RF susceptibility is successful in communicating the evolution of RF discharges by mapping field characteristics at the surface and tracing the evolution of the fields as markers for surface growth. The typical behavior of discharges oscillating into and out of breakdown is shown in Figure 5.2 (reproduced from [74] for a 1-D discharge with velocity

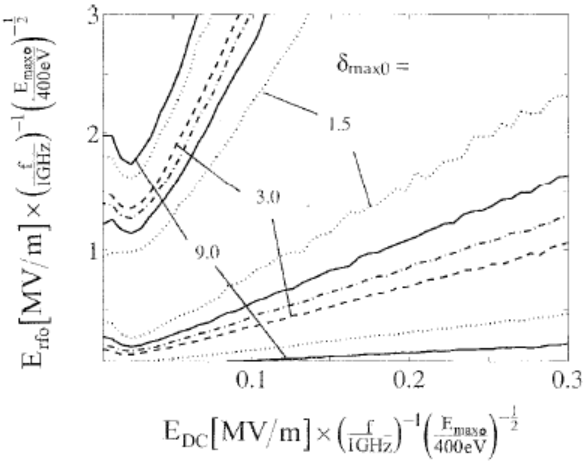


Figure 5.1: RF susceptibility diagram example. Reprinted figure with permission from [1]. Copyright 1998 by the American Physical Society. Limits are drawn by injecting a macroparticle into a system in a Monte-Carlo simulation, varying fields and secondary-emission yield, and tracing the macroparticle over a long time to measure exponential growth or decay. A growth of zero results in the limits shown.

components in 3-D), where a Lissajous trajectory of the surface field ratios develops. Outside the susceptibility limits at (1) in Figure 5.2, the applied RF driving field coupled with the small DC field provides excessive energy to secondaries such that particles would likely impact with energy above second crossover, causing net decay in charge and keeping surface DC fields low. When the applied field reduces in magnitude, particles start to impact with energies between first and second crossover. Near the first polar-reversed peak at (2), growth is rapid as a result of favorable lifetime and impact characteristics that support multiplicative secondary growth, and the surface DC field also grows accordingly with increasing positive surface charge coupled to the growing electron cloud. With excessively large DC fields at (3), lifetimes are reduced, moving particle impact energies from the second crossover to the first crossover (and below). Particle growth is stifled, pushing the system into a non-multiplicative region of the susceptibility plot (middle region) until negative surface charging reduces the DC field and the RF driving field adds sufficient energy to support impact at the first crossover (at minimum). Particles do not enter the multiplicative region until field polar reversal near (4), and the process of polar-peak rapid growth into DC saturation repeats beyond (4).

While RF susceptibility is successful in describing the evolution of RF-driven discharges in breakdown, the interest in this chapter is to tie susceptibility to existing theory via a-priori metrics on the distribution of emitted particles rather than to Monte-Carlo, parametric simulations. This study will not treat RF directly, but the characteristics developed here are directly applicable to RF in the same limit as previously described: the characteristic length of the system should be, at most, $L = v_{\text{avg}} \cdot (T_{\text{RF}}/2)$, where $T_{\text{RF}}$ is the RF period, and $v_{\text{avg}} = \langle|\vec{v}(t \in [n, n+1]T_{\text{RF}}/2)|\rangle$ for $n \in [0, \infty)$ is the average particle speed in a half period of non-retarding potential, limiting to unidirectional particle excursion.

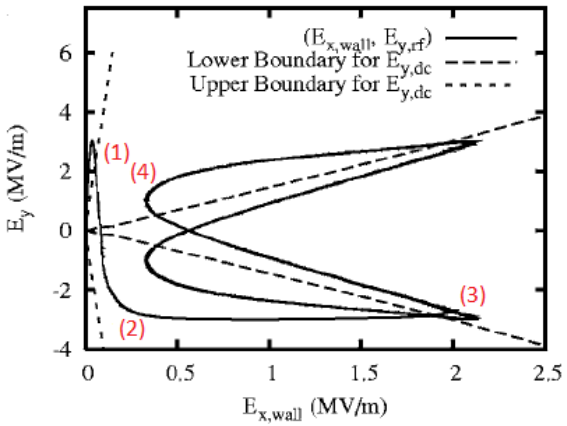


Figure 5.2: RF susceptibility example with field trace in breakdown. Reprinted with permission from [74] Copyright 2005, AIP Publishing LLC. RF driven at $f_{\mathrm{rf},0} = 1\,\mathrm{GHz}$ with amplitude $E_{\mathrm{rf},0} = 3\,\frac{\mathrm{MV}}{\mathrm{m}}$. Field tracing shows a Lissajous characteristic as the discharge moves into and out of a multiplicative regime. Variations on frequency and amplitude of the driving field will lead to lengthening or contracting of the drive to steady state out to larger DC values, but will typically lead to Lissajous characteristics at steady-state [74].

## 5.2 DC Susceptibility

The most obvious difference between RF discharges and DC discharges is the absence of the RF driving field, which can typically be treated as parameterized for a given study, and is often conformal to the transmissive surface (n.b. this is for typical configurations, and the transmissive surface could very well be situated at arbitrary angle to the RF component). The presence of an RF driving field allows the lifetime and energy gain to be effectively decoupled in typical configurations studied [1, 74], whereas the self-consistent DC field in the discharges studied herein are responsible for both lifetime and energy gain due to the angle of the dielectric, and the individual components typically do not evolve independently, nor can they be parameterized. As demonstrated in Section 3.1.1, particle dynamics are effectively defined by the field angle in Equation (3.5) for the ideal vacuum case, i.e. the impact energy is defined by the coupled field components and *not* the individual magnitudes.

This study flips the usual orientation for the fields on the axes. As noted previously, typical RF susceptibility diagrams plot the driving RF field amplitude on the ordinate and the otherwise DC field on the abscissa. In the modeled problem for this study, the orientation is rotated so that the dielectric surface is conformal with the orientation of the abscissa, and the field normal to the surface is plotted on the ordinate. The rotation maintains the orientation of the fields relative to the surface, again, readily providing the field angles with respect to the surface tangent. The fields are non-dimensionalized with the following factor:

$$s \equiv \frac{1}{\varepsilon_r E_0}. \tag{5.1}$$

where $\varepsilon_r$ is the relative permittivity of the dielectric material, and $E_0$ is the initial applied field. $sE$, where $E$ is the electric field, is therefore unitless. In principle, $s$ provides

a normalization against material, which will not be explored in this study, but should be noted for future work. Finally, time is normalized with a standard transit time for a characteristic electron with energy equal to the most-probable energy of an emitted secondary electron (a function of the dielectric material) across the full vacuum gap:

$$t_{\text{gap}}^{\text{trans}} = \frac{D_{\text{gap}}}{\sqrt{\frac{2W_p}{m_e}}}, \tag{5.2}$$

where $D_{\text{gap}}$ is the gap width, $W_p$ is the most-probable energy of the electron, and $m_e$ is the electron mass, taking non-relativistic relations, which is valid for parameters employed herein. For the typical vacuum parameters of Chapter 3, listed in Table 2.7, the standard transit time is $t_{\text{gap}}^{\text{trans}} \sim 2.5\,\text{ns}$. Note that $t_{\text{gap}}^{\text{trans}}$ is roughly five times longer than the typical fast-transient growth characteristic seen in breakdown discharges of Chapter 3.

The DC susceptibility of the dielectric surface to the formation of a multipactoring discharge is described by a region in the $E_\perp/E_\parallel$ plane over which a characteristic electron can gain sufficient energy during its lifetime such that the impact energy is between the first crossover, $W_1$, and second crossover, $W_2$, as described by Vaughan's theory on secondary emission outlined in Section 2.3. The following treatment will look at a general form for particle dynamics with a simple treatment of collisions:

$$m\frac{dv}{dt} = qE - mv\nu_\beta, \tag{5.3}$$

where $\nu_\beta = K_\beta n_g$ is the collision frequency related to some collisional event, $\beta$; $K_\beta$ is the collision rate coefficient; and $n_g$ is the neutral gas density. Note that the form of Equation (5.3) does not include space charge. Furthermore, it should be noted that the velocity in the collisional component should be the relative velocity between projectile and target particles, but the usual approximation that the electron speed is much greater than the typical gas speed is employed here so that $\lim_{v_e \gg v_n} (v_e + v_n) \to v_e = v$ is used in Equation (5.3), where $v_e$ is the electron speed and $v_n$ is the neutral speed. This treatment springboards off the usual analysis from Section 3.1, applying a number of simplifying assumptions to isolate the pertinent physics of various pressure regimes and to pull out lifetime and impact energy relations as outlined in the following sections. Discharge behavior will be described in terms of a characteristic particle encompassing distribution metrics used in this study.

It must be stressed that DC susceptibility limits are drawn according to the characteristic particle, but the limits are thereafter assumed to apply to the distribution as a whole, keeping with the logical extension of characteristic metrics, e.g. temperature in kinetic gas theory. This is a common source of confusion, as the characteristic particle will have a deterministic impact angle, but the distribution will not, and can be effectively parameterized with respect to the distribution. In principle, the limits drawn with respect to the characteristic particle may be construed as being "fuzzy" limits, but the intention of this study is to define a-priori behavior correlated to distribution metrics and *not* to reintroduce distribution statistics. That said, limits can be drawn assuming other characteristic quantities in the distribution functions, e.g. average velocity from $f(v)$, RMS average velocity from $f(E)$, averages in impact angle from $f(\theta_{\text{imp}})$, but the

most-probable metrics have been observed to serve the purposes of this development. The DC susceptibility regions defined here describe $E_\perp/E_\parallel$ regions that lead to multiplicative impact energies from the initial energy of the characteristic particle (again, representing the distribution) assuming a *single impact angle*. Varying the *field angle*, i.e. $E_\perp/E_\parallel$, is not to be construed as varying the *impact angle*, but merely varying the *impact energy*; the ability to do this is a product of the assumption that $E_\perp/E_\parallel$ limits are descriptive of the *distribution* and not any single particle in the distribution. The impact angle can now be parameterized to give the dependence on $\theta_{\text{imp}}$ as a theoretical limit. Recall the observations and physical understanding of typical discharge behavior from Chapters 3 and 4 with respect to impact angle, where the $\theta_{\text{imp}}$-space in vacuum cases is typically sampled in a sparse manner, e.g. Figure 3.8, while the $\theta_{\text{imp}}$-space for gaseous cases is sampled in a peaked-distribution manner, e.g. Figure 3.21. Previous observations suggest a wider variation in both the magnitude of $\theta_{\text{imp}}$ and in the temporal variation of $\theta_{\text{imp}}$ for gaseous cases.

### 5.2.1 Vacuum Susceptibility

In the limit of zero collisionality, i.e. $\nu_\beta = 0$ in Equation (5.3), the particle dynamics from Section 3.1 apply, where the forces in terms of perpendicular and parallel fields near the surface are reproduced here; the force due to the field perpendicular to the dielectric is:

$$F_\perp = qE_\perp = m\frac{dv_\perp}{dt} \Rightarrow \int_{v_{\perp 0}}^{-v_{\perp 0}} dv_\perp = \int_0^{t_{\text{life}}} \frac{q}{m} E_\perp dt, \tag{5.4}$$

and the force due to the field parallel to the dielectric surface is:

$$F_\parallel = qE_\parallel = m\frac{dv_\parallel}{dt} \Rightarrow \int_{v_{\parallel 0}}^{v_{\parallel f}} dv_\parallel = \int_0^{t_{\text{life}}} \frac{q}{m} E_\parallel dt. \tag{5.5}$$

Since much of the discharge remains close to the dielectric as illustrated in Section 3.4, the behavior of the discharge is dominated by the near-surface fields. As in Section 3.1, assuming quasi-static fields with negligible space-charge and no external effects, e.g. collisions, the perpendicular velocity at emission must be the (negated) perpendicular velocity at impact, so Equation (5.4) is readily integrated to give the lifetime of the particle as in Section 3.1:

$$t_{\text{life}} = -\frac{2mv_{\perp 0}}{qE_\perp}, \tag{5.6}$$

and the change in velocity is

$$v_{\parallel f} - v_{\parallel 0} = \frac{q}{m} E_\parallel t_{\text{life}}. \tag{5.7}$$

Plugging in for $t_{\text{life}}$ in Equation (5.7), and solving for the final velocity, $v_{\parallel f}$:

$$v_{\parallel f} = v_{\parallel 0} - 2v_{\perp 0}\frac{E_\parallel}{E_\perp}. \tag{5.8}$$

The impact energy is therefore:

$$W_{\text{imp}} = \frac{1}{2}m\left(v_{\parallel f}^2 + v_{\perp f}^2\right) = \frac{1}{2}m\left(\left[v_{\parallel 0} - 2v_{\perp 0}\frac{E_\parallel}{E_\perp}\right]^2 + v_{\perp 0}^2\right). \tag{5.9}$$

Rearranging gives the ratio of perpendicular fields to parallel fields:

$$\frac{E_\perp}{E_\parallel} = \frac{2v_{\perp 0}}{v_{\parallel 0} - \sqrt{\dfrac{2W_{\text{imp}}}{m} - v_{\perp 0}^2}}. \tag{5.10}$$

The limits of Equation (5.10) at which multipactor is expected to occur via the Vaughan model can be found by simply replacing $W_{\text{imp}}$ with $W_1$ and $W_2$. As shown in Section 3.4, particles in vacuum discharges impact with most of their energy associated with the velocity parallel to the surface so that most impacts are grazing; therefore, the construction of Figure 5.3 uses $W_1$ and $W_2$ for grazing impact. The region between the dashed lines representing the $W_1$ and $W_2$ limits indicates multipactor conditions while non-multiplicative conditions flank both sides of the multipactor region. A first-order interpretation of the non-multiplicative region above the $W_1$ limit is that lifetimes are too short with insufficient energy gain (i.e. larger $E_\perp$ coupled with smaller $E_\parallel$) to allow for multiplication, hence impact energies are below first crossover. Similarly, the region below the $W_2$ limit can be understood as providing particles with too much energy over longer lifetimes (i.e. smaller $E_\perp$ coupled with larger $E_\parallel$), hence impact energies are above second crossover. Near-surface electric fields from simulation can be plotted on top of Figure 5.3, showing the evolution of surface-field angle characteristics in time, e.g. Figure 5.11.

Figure 5.3 plots Equation (5.10) for a characteristic particle defined by the most-probable emission energy. The use of a characteristic particle is necessary to define the initial velocities in Equation (5.10). Emission is done by sampling a Maxwellian reservoir with most-probable emission energy $W_{\text{emit}}^{\text{mode}}$, where typical Maxwellian metrics apply over sufficient emission. Empirically, it is observed that defining distribution characteristics based on most-probable metrics allows temporal traces to approach closer to the limit lines, suggesting the tendency for multiplicative breakdown is driven more by particle population density rather than distribution moments (e.g. the first moment of the velocity distribution, the square-root of the second moment, or the square-root of the energy distribution, all giving various velocity averages, with the latter two being the root-mean square velocity). Note that these relations are relevant to the *emission* characteristics, which are, again, defined by the dielectric material. Furthermore, particles are emitted in a half-space cosine distribution, peaked at normal emission. The general behavior of a characteristic distribution may then be correlated to specific metrics, where proper treatment, again, requires the most-probable metrics of the energy distribution rather than average metrics. Some typical parameters for the target distribution are listed in Table 5.1.

Recall crossover energies, $W_1$ and $W_2$, are a function of impact angle as described in Section 2.3, so the limits drawn in Figure 5.3 should include the functional dependence on function of impact angle as well. Varying $W_1$ and $W_2$ with impact angle creates a surface as in Figure 5.4a. The susceptibility surface provides additional information about the characteristics of the impact distribution, but the time evolution of surface fields becomes

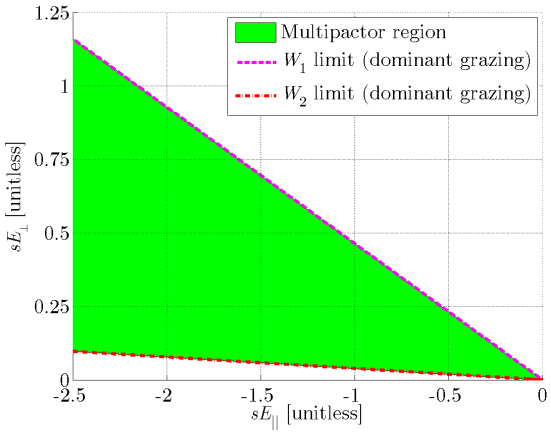


Figure 5.3: General form of a susceptibility diagram under vacuum conditions for grazing incidence. $E_\perp$ against $E_\parallel$ is plotted, showing the form of $W_1$ and $W_2$ for the most-probable particle with properties listed in Table 5.1. Note this diagram is the transpose of the usual RF susceptibility diagrams, c.f. Figure 5.1, to show the electric-field angles relative to the dielectric surface.

Table 5.1: Typical parameters used in constructing the baseline susceptibility curve.

| Parameter | Symbol | Value |
|---|---|---|
| Emission temperature | T | 1.85 eV |
| Particle mass (electron) | $m_e$ | $9.11 \times 10^{-31}$ kg |
| Most-probable emission energy | $W_{\text{mode}}^{\text{emit}}$ | 1.85 eV |
| Average speed | $\bar{v}$ | $9.4642 \times 10^5$ m/s |

more difficult to track if the impact characteristics are highly distributed. In cases where electrons are incident on the dielectric over a small range of impact angles, treatment can approach the simplified version above while retaining some information about the impact distribution with some modification to the interpretation of the susceptibility plot: to first-order, impact-angle information from Figure 5.4a can be collapsed into regions of probable multiplicative conditions as in Figure 5.4b rather than simply distinct lines separating multiplicative and non-multiplicative regions as in Figure 5.3. Limited ranges for impact angles can occur in vacuum discharges due to the relative uniformity of emission characteristics and volume discharge evolution, as in the discharges of Chapter 3. Collapsing the susceptibility surface of Figure 5.4a into the $E_\perp/E_\parallel$-space is therefore just a looser interpretation of the original susceptibility formulation above, defining three regions (rather than two) of: (1) definite multiplicative growth, (2) probable multiplicative growth, and (3) definite non-multiplicative growth.

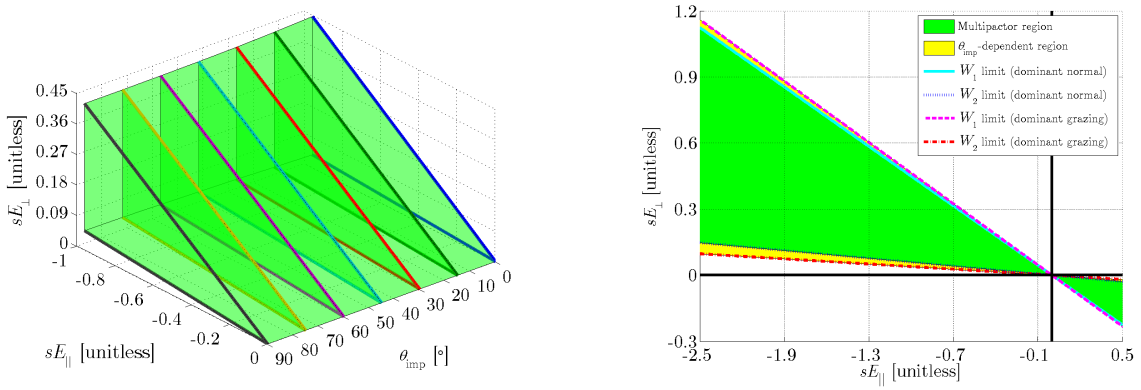


(a) Full susceptibility surface.

(b) Susceptibility surface, collapsing $\theta_{\text{imp}}$ effects.

Figure 5.4: Field ratios, $E_\perp/E_\parallel$, vs. impact angle, $\theta_{\text{imp}}$, in vacuum. (a) illustrates the minor dependence on $\theta_{\text{imp}}$. The green region indicates susceptibility to multipactor. Lines at select impact angles are for clarity. (b) is the reduced susceptibility surface, encompassing $\theta_{\text{imp}}$-dependence in the yellow regions, further illustrating the minor dependence on impact angle for typical parameters.

### 5.2.2 Low-Pressure Susceptibility

This section describes considerations for susceptibility at low pressures, on the order of 1 Torr. Increasing the pressure introduces collisional and localized space-charge effects that can invalidate the vacuum assumptions of quasi-static discharges influenced largely by near-surface fields. In the case of low-pressure discharges where collisions start to become appreciable while space-charge effects remain moderate (i.e. still assuming quasi-static fields over relatively short time scales), the kinetic equation must also account for collisional terms in the kinetic equations, i.e. Equation (5.3) must be used. Lifetimes and impact energies are significantly altered, most easily seen through impact diagnostics, e.g. Figure 3.21. Particle dynamics must therefore be treated more directly with more details on the following exposition are available in Appendix 5.A. The perpendicular velocity gives:

$$\begin{aligned} v_\perp(t) = \frac{dy}{dt} &= e^{-\nu_\beta t}\int_0^t e^{\nu_\beta s}\frac{q}{m}E_\perp ds + v_{\perp 0}e^{-\nu_\beta t} \\ \Rightarrow \int_0^y dr &= \int_0^t \left[\frac{qE_\perp}{m\nu_\beta}\left(1-e^{-\nu_\beta s}\right) + v_{\perp 0}e^{-\nu_\beta s}\right] ds, \end{aligned} \tag{5.11}$$

and the parallel fields gives:

$$\begin{aligned} v_\parallel(t) = \frac{dx}{dt} &= e^{-\nu_\beta t}\int_0^t \mathrm{e}^{\nu_\beta s}\,\frac{q}{m}E_\parallel ds + v_{\parallel 0}e^{-\nu_\beta t} \\ \Rightarrow \int_0^x dr &= \int_0^t \left[\frac{qE_\parallel}{m\nu_\beta}\left(1-e^{-\nu_\beta s}\right) + v_{\parallel 0}e^{-\nu_\beta s}\right] ds. \end{aligned} \tag{5.12}$$

It should be noted that the limits of the integrals are taken from 0 to the dimension of interest, implicitly stating that all impact points on the surface can be treated independently, particularly at the discharge onset when field conditions are uniform. Furthermore, the collision frequency was not split into component form, linearly affecting all directions equally. Equation (5.11) can be used to obtain the trajectory in $y$:

$$y = \frac{qE_\perp}{m\nu_\beta^2}\left(\nu_\beta t + e^{-\nu_\beta t} - 1\right) - \frac{v_{\perp 0}}{\nu_\beta}\left(e^{-\nu_\beta t} - 1\right). \tag{5.13}$$

Similarly, the particle range can be obtained from Equation (5.12):

$$x = \frac{qE_\parallel}{m\nu_\beta^2}\left(\nu_\beta t + e^{-\nu_\beta t} - 1\right) - \frac{v_{\parallel 0}}{\nu_\beta}\left(e^{-\nu_\beta t} - 1\right). \tag{5.14}$$

The lifetime of a typical particle can be found by setting $y(t_{\text{life}}) = 0$ in Equation (5.13), producing an implicit non-linear form for the particle lifetime:

$$\begin{aligned} 0 &= \frac{qE_\perp}{m\nu_\beta^2}\left(\nu_\beta t_{\text{life}} + e^{-\nu_\beta t_{\text{life}}} - 1\right) - \frac{v_{\perp 0}}{\nu_\beta}\left(e^{-\nu_\beta t_{\text{life}}} - 1\right) \\ &\Rightarrow e^{-\nu_\beta t_{\text{life}}} = 1 - \frac{qE_\perp \nu_\beta}{qE_\perp - m\nu_\beta v_{\perp 0}} t_{\text{life}}. \end{aligned} \tag{5.15}$$

At this point, it is necessary to outline gaseous discharge parameters to compute $\nu_\beta$. The most fundamental target collision for this study is single-ionization of ground-state argon background gas, i.e. $\nu_\beta = \nu_{iz}$, where $\nu_{iz}$ is the ionization frequency for single ionization of Ar:

$$\nu_{iz} = K_{iz}(\mathrm{T}_e) n_g, \tag{5.16}$$

where the ionization constant in the Thomson model [34] is:

$$K_{iz}\left(\mathrm{T}_e\right) = \sigma_0 \bar{v}_e \left(1 + \frac{2\mathrm{T}_e}{\mathcal{E}_{iz}}\right) e^{-\frac{\mathcal{E}_{iz}}{\mathrm{T}_e}}, \tag{5.17}$$

and the parameters in Equation (5.17) are:

$$\begin{aligned} \sigma_0 &= \pi \left(\frac{e}{4\pi\varepsilon_0 \mathcal{E}_{iz}}\right)^2, \\ \bar{v}_e &= \left(\frac{8e\mathrm{T}_e}{\pi m}\right)^{1/2}, \text{ and} \\ \mathcal{E}_{iz} &= 15.79 \text{ V for Ar.} \end{aligned}$$

Assuming ideal gas for a 1 Torr Ar background, $n_g = 3.33 \times 10^{22}\,\mathrm{m}^{-3}$, and $\nu_{iz} = 1.91 \times 10^5\,\mathrm{s}^{-1}$. It should be noted that the volume characteristic of the distribution is not well-represented by the Maxwellian distribution, and the Thomson model can overestimate reaction rates by at least a factor of two as shown in Appendix 3.B. In principle, a transfer function might be devised to represent the volume distribution from the emitted Maxwellian, but the evolution of the discharge is not well defined in the parameter space of interest, and seeking out a general transfer function is outside the scope of this work. Additionally,

seeking out a transfer function for a limited parameter set amounts to a-posteriori correlation that is not consistent the intent of this a-priori diagnostic.

Using a simple iterative Newton solver on Equation (5.15), lifetimes can be obtained from standard values used in this study. The lifetimes are shown in Figure 5.5 as a function secondary emission angle, $\theta_{\text{emit}}$, and surface field angle, $\chi_E$. The extremes of $\chi_E$ are not shown due to divergent lifetime calculations approaching infinity. Assuming constant $|\vec{E}|$, for a constant $\chi_E$, lifetimes should be *longest* at normal emission, i.e. $\theta_{\text{emit}} = 0°$, since the maximum energy is attributed to the vertical direction in such a case; alternatively, for a constant $\theta_{\text{emit}}$, lifetimes should be *shortest* for normal field angles, i.e. $\chi_E = 90°$, since the electron experiences the maximum force in the perpendicular direction in such a case.

The errors in expanding $e^{\nu_\beta t_{\text{life}}}$ to first order for the lifetimes plotted in Figure 5.5 are shown in Figure 5.6. The extremes of $\chi_E$ are not shown due to divergent values, since lifetimes approach infinity for $\chi_E \to 0°$ and $\chi_E \to 180°$ with respect to the surface tangent in the direction of the cathode. The max norm of the error is $< 1\,\%$ at $\chi_E \sim 0.18°$ and $\chi_E \sim 179.82°$. At atmospheric pressure, expansion errors grow considerably at the extremes. It is worth noting that expansion errors may be acceptable at field angles approaching normal to the surface ($\chi_E \to 90°$); however, it is not in the interest of this study to maintain field angles at a specified orientation, so limiting the expansion error by field angle is not an appropriate exploit here. The fact that the error is smallest at field angles normal to the surface could be applied to multiple-stack configurations as a means of simplifying theoretical dynamics near electrodes.

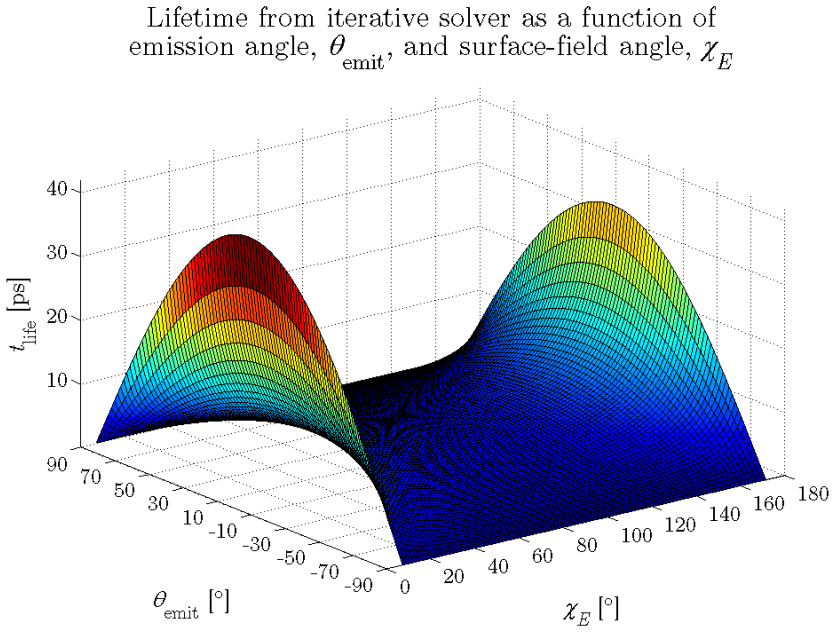


Figure 5.5: Low-pressure particle lifetimes from iterative solution of Equation (5.15), $p_{\text{bg}} = 1\,\text{Torr}$. Extreme values of $\chi_E$ are not shown due to divergent values of lifetime, i.e. lifetimes approach infinity with zero perpendicular fields as $\chi_E \to [0°, 180°]$, with respect to the surface tangent in the direction of the cathode.

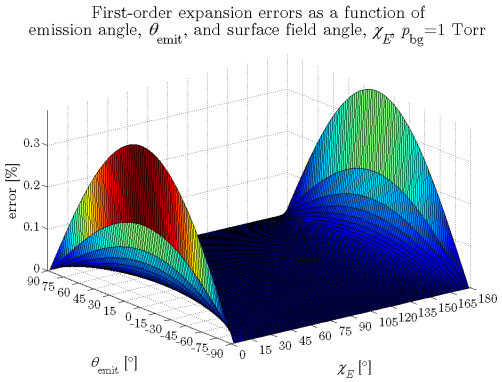


(a) $p_{bg} = 1\,\text{Torr}$.

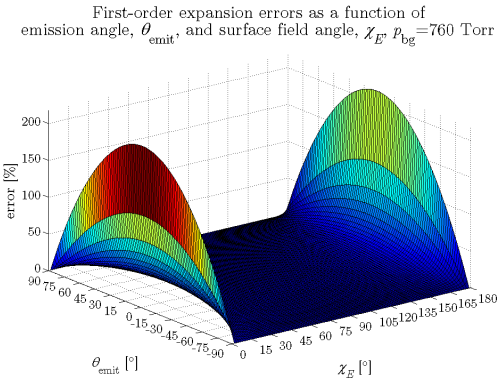


(b) $p_{bg} = 760\,\text{Torr}$.

Figure 5.6: Errors for the first-order expansion of the exponential term in Equation (5.15). N.b. this is the error in the *expansion*, not the particle lifetime, which is provided in Figure 5.8 for 1 Torr and in Figure 5.9 for 760 Torr.

The error from the first-order expansion is acceptably low (much less than 1 %) for most of the parameter space, with higher orders providing increasing smaller contributions to the error. Equation (5.15) can therefore be simplified, cutting off at the second-order term:

$$e^{-\nu_\beta t_{\text{life}}} = 1 + (-\nu_\beta t_{\text{life}}) + \frac{(-\nu_\beta t_{\text{life}})^2}{2!} + \cdots . \tag{5.18}$$

Plugging in the expansion reduces the lifetime to a tractable form:

$$t_{\text{life}} = \frac{2mv_{\perp 0}}{m\nu_\beta v_{\perp 0} - qE_\perp}. \tag{5.19}$$

The approximate lifetime values for the case of $p_{bg} = 1\,\text{Torr}$ are shown in Figure 5.7, and the error between Equation (5.15) and Equation (5.19) is shown in Figure 5.8a, i.e. the lifetime error as a function of emission angle, $\theta_{\text{emit}}$, and electric-field angle, $\chi_E$. From Figure 5.8a, the lifetime error is generally acceptable for all values of $\theta_{\text{emit}}$ and $\chi_E$, except at the extreme values, which correspond to the longest lifetimes. Since $\theta_{\text{emit}}$ is a cosine distribution in half-space emission, the lifetime error can be integrated with the normalized cosine distribution to get a weighted lifetime error as a function of the field angle, shown in Figure 5.8b. Errors in lifetime calculations are acceptably small for field angles ranging $|\chi_E^{1\,\%}| \sim [0.18°, 179.82°]$ for the case of 1 Torr. The divergence of the lifetime error for $|\chi_E| > |\chi_E^{1\,\%}|$ is, again, a consequence of divergent lifetimes calculated with fields parallel to the surface resulting in (locally) infinite lifetimes for emitted particles. For most typical discharge parameters, the surface does not experience fields tangent to the surface for most of the discharge time, unless the dielectric angle is orthogonal to the electrodes, i.e. $\alpha = 0°$. As discussed in Section 3.1.1, typical parameters in vacuum tend to saturate around the $\chi_E = 15.6°$ limit. The divergent errors at infinite lifetimes are therefore not expected to significantly influence the characterization of the discharge. Finally, Figure 5.9b shows the lifetime errors and weighted lifetime error for the case of $p_{bg} = 760\,\text{Torr}$, showing that errors can become appreciable with higher collisionality. Since fields evolve with the discharge, it is difficult to limit the error globally in time, but

from Chapters 3 and 4, up through low pressure, it is observed that systems of interest are not typically operating at field values consistent with divergent lifetime errors, so such errors are not of general concern. Furthermore, the expansion employed in Equation (5.19) provides a useful diagnostic to demarcate pressure regimes between what has ostensibly been referred to as "low-pressure breakdown" and "high-pressure breakdown" in this work. It is known that surface fields will tend to saturate to an equilibrium field angle, which is $\chi_E \sim 25°$ from Figure 3.2. Additionally, the initial conditions for the surface fields can be calculated or measured, as in Figure 3.10 and Figure 3.17, with the shallowest field angle at $\chi_E \sim 8°$. Limiting the expansion error to 1 percent at the shallowest angle will lead to a pressure limit of $\sim 50$ Torr by iterative solution. However, since much of the discharge time is not spent with $\chi_E$ at the shallowest angle, it will be sufficient to simply limit the lifetime error to 1 % at $\chi_E = 25°$, giving a pressure limit of $\sim 140$ Torr by iterative solution. Note that this limit, determined by Taylor expansion consideration, is similar to the limit in Section 3.2 determined by comparison of the ionization rate and the multipactor rate.

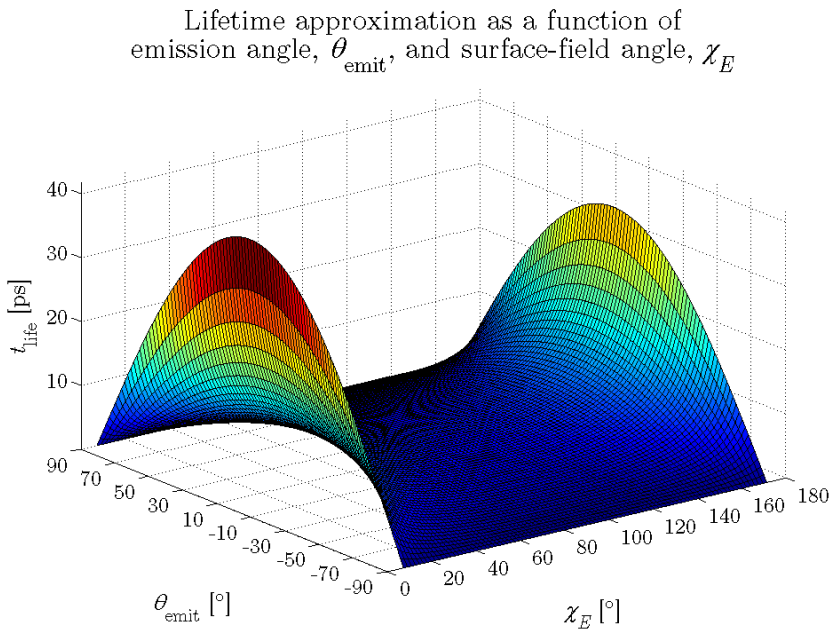


Figure 5.7: Low-pressure particle lifetimes from iterative solution of Equation (5.15), $p_{bg} = 1$ Torr. Extreme values of $\chi_E$ are not shown due to divergent values of lifetime, i.e. lifetimes approach infinity with practically zero perpendicular fields as $\chi_E \to 0°$ or $\chi_E \to 180°$, measured relative to the surface tangent in the direction of the cathode.

Impact velocities can also be simplified applying the same Taylor expansion, but this time to first-order to force a linear relation with respect to $t_{life}$:

$$\begin{aligned} v_{\parallel}\left(t_{life}\right) &= v_{\parallel 0} + \left(\frac{qE_{\parallel} - mv_{\parallel 0}\nu_{\beta}}{m}\right) t_{life}, \text{ and} \\ v_{\perp}\left(t_{life}\right) &= v_{\perp 0} + \left(\frac{qE_{\perp} - mv_{\perp 0}\nu_{\beta}}{m}\right) t_{life}. \end{aligned} \tag{5.20}$$

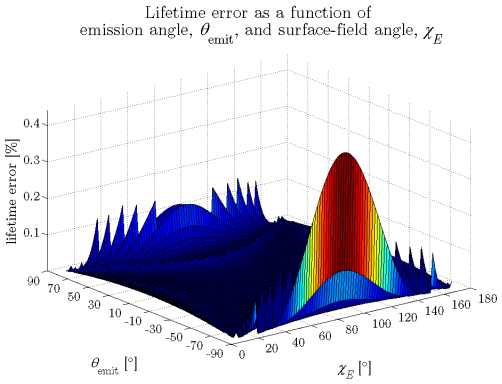


(a) Lifetime errors.

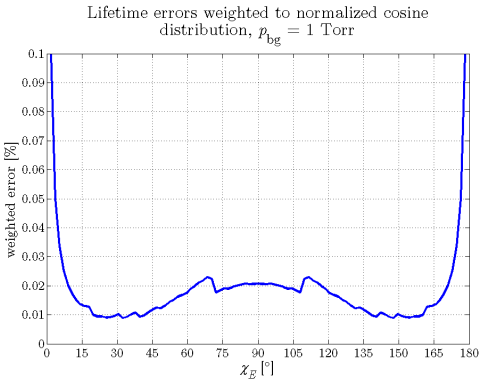


(b) Weighted lifetime error.

Figure 5.8: Lifetime errors and weighted lifetime error at 1 Torr. Approximate lifetimes are calculated with Equation (5.19) and exact lifetimes are taken from Equation (5.15). Extreme values at $\chi_E \to [0°, 180°]$ are not shown due to divergent values as a result of lifetimes approaching infinity.

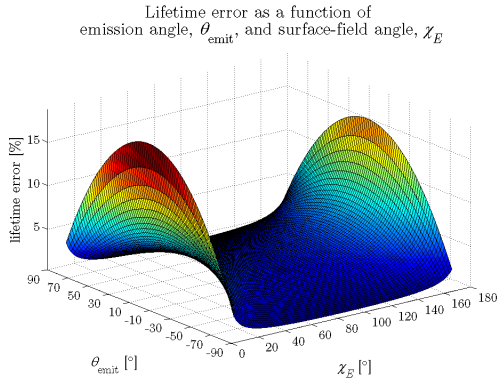


(a) Lifetime errors.

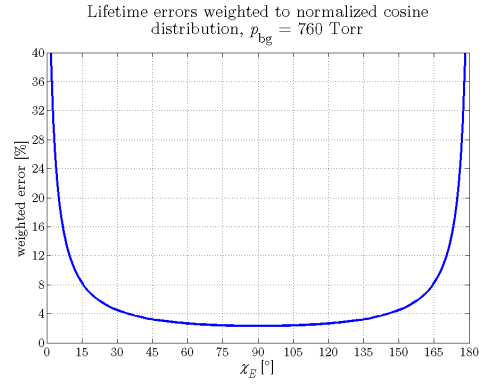


(b) Weighted lifetime error.

Figure 5.9: Lifetime errors and weighted lifetime error at 760 Torr. Analogous to Figure 5.8.

Finally, plugging in for $t_{\text{life}}$:

$$\begin{aligned} v_{\parallel}\left(t_{\text{life}}\right) &= v_{\parallel 0} + \frac{2v_{\perp 0}qE_{\parallel} - 2v_{\perp 0}mv_{\parallel 0}\nu_{\beta}}{m\nu_{\beta}v_{\perp 0} - qE_{\perp}}, \text{ and} \\ v_{\perp}\left(t_{\text{life}}\right) &= v_{\perp 0} + \frac{2v_{\perp 0}qE_{\perp} - 2v_{\perp 0}mv_{\perp 0}\nu_{\beta}}{m\nu_{\beta}v_{\perp 0} - qE_{\perp}}. \end{aligned} \tag{5.21}$$

With the velocities now in closed form, the impact energy can be written as:

$$W_{\text{imp}} = \frac{1}{2}m\left(\left[v_{\parallel}\left(t_{\text{life}}\right)\right]^2 + \left[v_{\perp}\left(t_{\text{life}}\right)\right]^2\right) = \frac{1}{2}m\left(\left[\frac{2v_{\perp 0}qE_{\parallel}}{m\nu_{\beta}v_{\perp 0} - qE_{\perp}} + v_{\parallel 0}\right]^2 + v_{\perp 0}^2\right). \tag{5.22}$$

The target metric is, again, the ratio of perpendicular to parallel fields, which is obtained by rearranging Equation (5.22):

$$\frac{E_{\perp}}{E_{\parallel}} = \frac{2v_{\perp 0}}{\left(v_{\parallel 0} - \sqrt{\frac{2W_{\text{imp}}}{m} - v_{\perp 0}^2}\right)} + \frac{m\nu_{\beta}v_{\perp 0}}{qE_{\parallel}}. \tag{5.23}$$

Comparison of Equation (5.23) with Equation (5.10) shows that the collisionless contribution of $E_{\perp}/E_{\parallel}$ is clearly retained, while low-pressure collisions introduce an additive term dependent on the field parallel to the dielectric, effectively moving the whole susceptibility plane up or down in the $E_{\perp}/E_{\parallel}$-space, as in Figure 5.10, which uses an uncharacteristically high pressure and temperature to enhance the effect. The dependence on the parallel field is sensible since collisions are highly dependent on the particle energy, which is largely driven by the parallel fields. It should be noted that this treatment will be applied to discharges in Chapter 4, while the remainder of this chapter will focus on applying developments in Section 5.2.1.

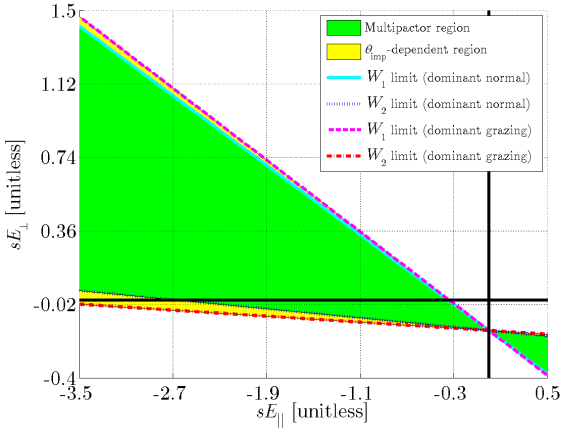


Figure 5.10: $E_{\perp}/E_{\parallel}$ vs. $\theta_{\text{imp}}$ for the low pressure case. Pressure, $p_{bg} = 10\,\text{Torr}$, with electrons assumed to be Maxwellian with a temperature at $T = 15.79\,\text{eV}$ to increase the ionization rate. N.b. the pressure and temperature are artificially increased in this plot for illustrative purposes.

### 5.2.3 Comments on High-Pressure Susceptibility

This work will not address DC susceptibility at higher pressures beyond the limits discussed in this chapter and in Section 3.2. The treatment of additional collisions requires using the full lifetime relation from Equation (5.15) without expansion, with the possible inclusion of additional space-charge effects when ionization and similar charge-producing effects become significant. This would require an iterative treatment at each time step, which would be computationally intensive in the aggregate. Velocities in Equations (5.11) and (5.12) were similarly expanded, and would need to be solved in-situ since quasi-static field arguments are less likely to apply with increased reaction rates. The most significant characteristic of this treatment up to this point is that DC susceptibility through low pressures is an *a-priori* metric, using known characteristics of the discharge to draw limit lines; going deeper into regimes dominated by volume effects removes the *a-priori* characteristic, and while DC susceptibility can provide useful insight into the discharge evolution by agglomerating a collection of metrics (field phase and magnitude, secondary impact and emission characteristics, etc.), it loses the predictive capability that makes DC susceptibility particularly useful and important as a diagnostic tool that can be leveraged to move a system into a desired operating regime.

## 5.3 VULP Susceptibility Diagrams

### 5.3.1 VULP in Multiplicative Breakdown

In general, fields can move into and out of the multipactor region similar to the characteristically Lissajous curves of Figure 5.2. A typical time-trace of the electric-field ratios for all points along the dielectric surface is shown in Figure 5.11. The colormapping of the scatter plot describes the evolution of the fields from $0{\times}t_{\text{gap}}^{\text{trans}}$ in yellow to $2{\times}t_{\text{gap}}^{\text{trans}}$ in black, noting that the time scale has been normalized to the standard transit time of Equation (5.2). The blue triangles indicate the fields at $0{\times}t_{\text{gap}}^{\text{trans}}$ along the dielectric surface. The direction towards the cathode and anode are specified, but the actual values are not plotted to allow for a cleaner plot where it should be noted that fields at the electrodes are specified. In principle, there is some error in the way electrode fields are represented with respect to the dielectric surface, related to the problems addressed in Section 2.2.1, particularly as the electrodes are stair-stepped. Since the metallic boundary condition forces fields normal to the electrode boundary, the fields at the intersection of the electrode and dielectric are either parallel or perpendicular depending on the orientation of the electrode segment intersecting with the dielectric. The binary field orientation (either perpendicular or parallel) with respect to the dielectric surface is a result of the stair-stepping errors, while the real configuration will generally result in an oblique field angle with respect to the dielectric surface. Furthermore, it should be noted that the fields on approach to the electrodes are theoretically subject to divergent characteristics from dielectric wedges [4, 69, 75], although this is not explicitly modeled in PIC. The triple-point fields are important to the seed, but not to the overall characteristic of field evolution further downstream, as the divergent characteristic quickly decays as noted in Section 2.A.3.

Recall the expected behavior for vacuum discharges in breakdown is described in

Section 3.4.1. In the context of Figure 5.11, the behavior of the discharge includes the following sequence: (1) the discharge starts within the multipactor region, indicated by the blue triangles; (2) the development of an upstream, multiplicative, negatively-charged cloud initially pulls surface field angles lower, mostly as a result of an increased field component parallel to the surface in response to the growing upstream cloud, effectively moving further into the multiplicative region; and (3) the discharge evolves towards the first crossover line once the multipactor front passes a specified downstream point as a result of increased perpendicular fields (reducing particle lifetimes) and reduced parallel fields (reducing particle energy gain). Points on approach to the cathode continue to evolve as a result of the unperturbed, CW, beam-like source used to seed these discharges. The drive towards first crossover is a result of the multipactor growth as surface fields respond to the front sweeping the surface; in the vacuum case, the front effectively snuffs further growth in its wake, consistent with observations in Section 3.4.1.

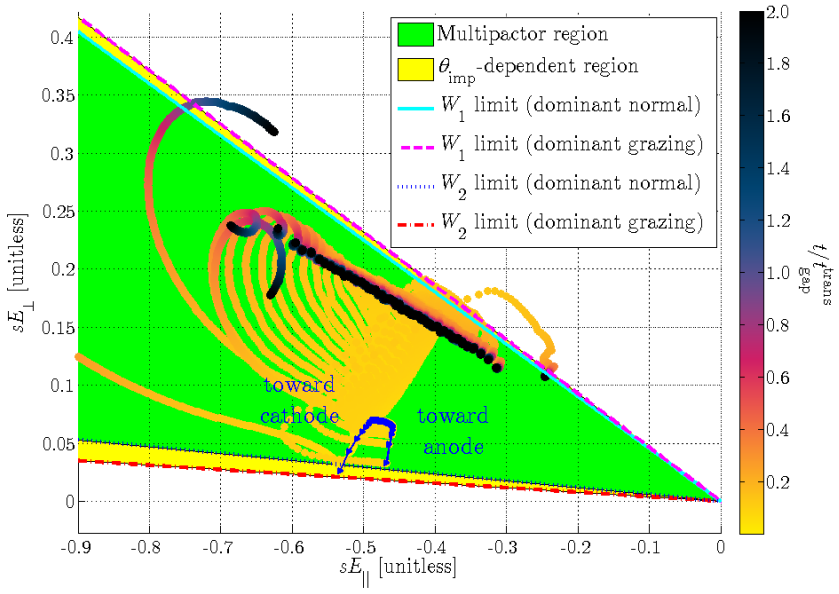


Figure 5.11: $E_\perp/E_\parallel$ plotted at the dielectric surface with $\alpha = 6.12°$ in vacuum. Field ratios are scattered as a function of time. Yellow is 0 ps and black is 5000 ps. The time-evolution scatter includes space charge, while the $W_1$ and $W_2$ limits do not.

Figure 5.12 shows more detailed temporal snapshots of the susceptibility diagram. The various times shown are a collection of three plots, comprising the susceptibility diagram for a characteristic point representative of most of the surface (chosen as the center of the dielectric surface for this study) shown as the main subplot, scaled number plots shown on the upper-right subplot, and a reproduction of the full-surface susceptibility in the bottom-right subplot. Note that the scaling in the number plots is arbitrary for ease of visualization, and the time scale is a moving window. The choice of the center is largely a matter of observation, serving as a point observed to be sufficiently far from localized effects of the initial-impact region such that near upstream and downstream impacts are roughly similar in time, noting particularly that this is not necessarily true for all variations on parameters. The dielectric center is furthermore an ideal choice as

the error was designed to be smallest there, c.f. Section 2.2. For all plots, the current time is identified by a white circle, matching the white bar on the temporal color-bar in the center. Figure 5.12a illustrates the initial fast growth up to $\sim 0.12 \times t_{\text{gap}}^{\text{trans}}$, i.e. a tenth of the standard transit time or $\sim 250\,\text{ps}$, showing the very-fast pull-up to the $W_1$-limit from well-within the multipactor region. Although not shown explicitly, the secondary peak is consistent with the ionization-electron peak, where most of the ionization occurs near the surface, with the ionization-electron density peaked near the anode during the fast-transient, allowing for the relatively fast decay of the ionization electrons. Evacuation of both secondaries and ionization electrons to the anode leaves behind an appreciable positive charge in the volume from the ions that will move slowly towards the cathode in the nanosecond time-scale. The full-surface diagram in the lower right of Figure 5.12a more clearly shows the ballooning of the field profile from a relatively concentrated (i.e. near uniform) field condition as the downstream fields respond to upstream growth that pulls downstream fields along as the front progresses over the surface. Figure 5.12b shows the initial drive to steady-state, which amounts to a relatively fast decay of the number where the leading edge of the decay is attributed to the maximum current gain of $\sim 250 \times I_0$ from Figure 3.11b. The full extent of the field ballooning is more apparent by this time, where it is most important to note that surface points are approaching a saturated angle everywhere, even if individual magnitudes might vary by $> 200\,\%$ at maximum comparing component field magnitudes in the main cluster (ignoring the outermost tendrils that are still affected by the electrode conditions). Finally, Figure 5.12c illustrates the sustained steady-state for the remainder of the discharge, where the lower-right full-surface diagram looks very similar to the full-surface diagram from Figure 5.12b. It is apparent that the field angle approached in Figure 5.12c is, indeed, a saturation angle, and is consistent with the location of the $W_1$ limit. Again, observing the full-surface plots in the lower-right subplots, most of the surface away from the electrodes behaves in a similar manner to the characteristic (dielectric center) susceptibility diagrams, with minor tugs in both directions along $E_{\parallel}$ in response to whether the traveling multipactor front is upstream or downstream of any point of interest on the surface. The pull-up to $W_1$ is similarly a response to the traveling front. The maximum variation in $E_{\parallel}$ is $\sim 15\,\%$ of the initial value while the maximum variation in $E_{\perp}$ is $\sim 150\,\%$ of the initial value, so most of the saturation phenomenon is coming from the perpendicular response, particularly since the parallel value seems to oscillate about the initial value, again, as a response to the traveling multipactor front and later as a response to the steady-state tail.

### 5.3.2 VULP in Dark-Current Steady-State

The time-trace for the electric-field ratios at $\alpha = 22.9°$ is shown in Figure 5.13, with the colormapping similarly showing the time-evolution of fields as for Figure 5.11, albeit for an order of magnitude longer time for the full discharge, noting the scales. The expected behavior for vacuum discharges in a creeping dark-current is described in Section 3.4.2. In the context of Figure 5.13, the discharge behavior includes the following sequence: (1) the discharge starts outside the multiplicative region; (2) the development of an upstream, non-multiplicative, negatively-charged creeping front, coupled with negative surface-charging, pulls surface field angles lower toward the edge of the multiplicative region, with particle lifetimes and energy gain increased; and (3) the discharge evolves to-

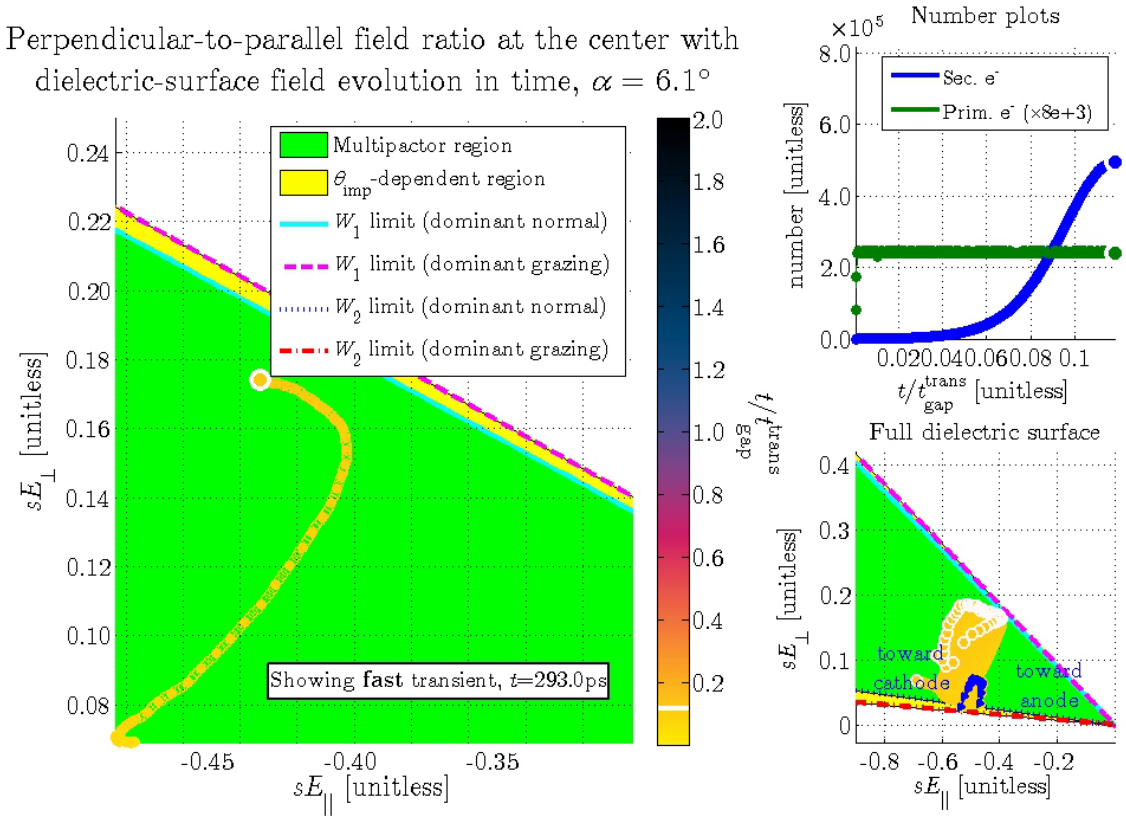


(a) Through peak transient.

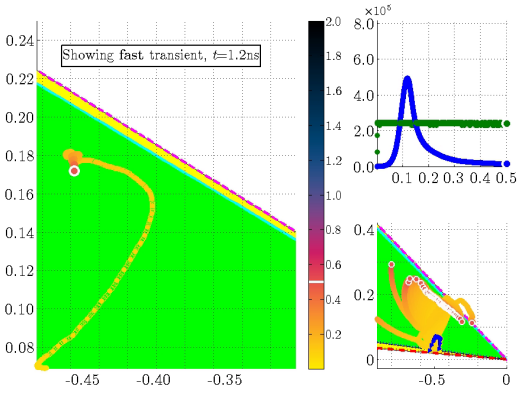


(b) Post peak-current.

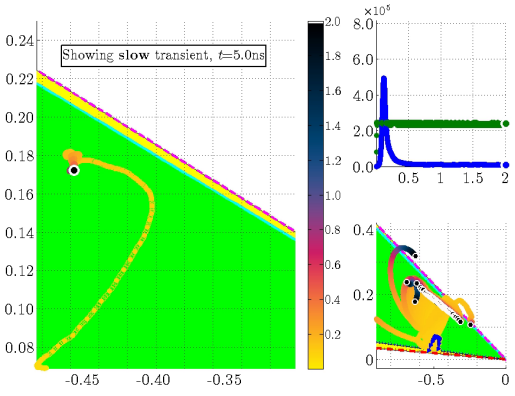


(c) Fully-developed steady-state.

Figure 5.12: Snapshots of $E_\perp/E_\parallel$ plotted at the dielectric surface with $\alpha = 6.12°$ in vacuum. Field ratios are scattered as a function of time. Yellow is 0 ps and black is 5000 ps. The time-evolution scatter includes space charge, while the $W_1$ and $W_2$ limits do not. A full video is available at as a supplement to this document.

wards the first crossover line with the dark-current front slowly creeping over downstream points with unit gain. There is a region near the cathode that experiences field-reversal as a result of excessive negative charging on the dielectric surface, leading to an arc that results in the field pull-up shown in the upstream evolution (toward the cathode) of Figure 5.13.

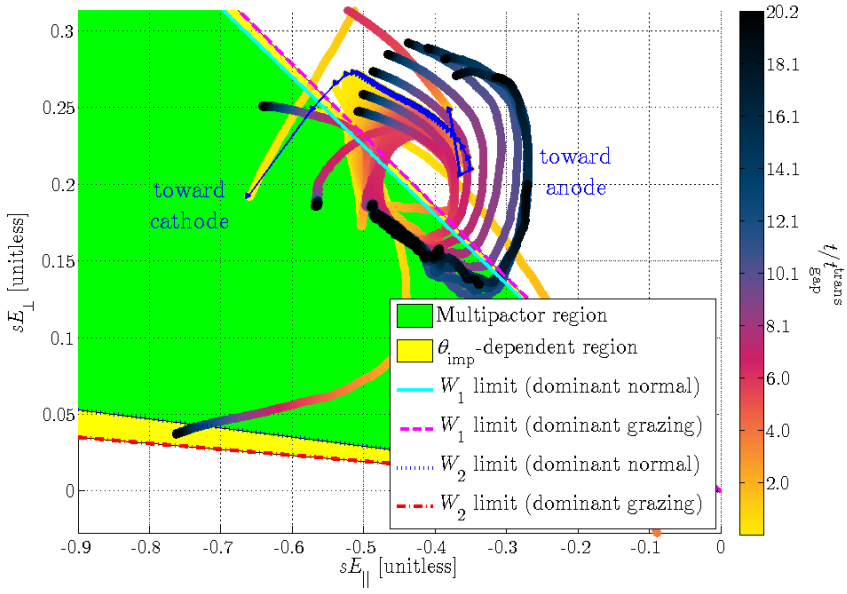


Figure 5.13: $E_\perp/E_\parallel$ plotted at the dielectric surface with $\alpha = 22.9°$ in vacuum. Field ratios are scattered as a function of time. Yellow is 0 ps and black is 50 ns. The time-evolution scatter includes space charge, while the $W_1$ and $W_2$ limits do not.

Figure 5.14 shows more detailed temporal snapshots of the susceptibility diagrams for $\alpha = 22.9°$, analogous to Figure 5.12 for the case of $\alpha = 6.12°$, including similarly associated characteristic (dielectric-center) susceptibility diagrams in the main subplot, (scaled) number plots in the upper-right subplot, and reproductions of the full-surface susceptibility diagrams in the lower-right subplot. The current time is, again, marked for all plots with a white circle, matching the white bar on the temporal color-bar. Figure 5.14a illustrates the slow pull-down through $\sim 5.0 \times t^{trans}_{gap}$, noting that this is, of course, slower than the standard transit time and occurs over a timescale that is $\sim 40\times$ longer than the timescale for dominant effects at $\alpha = 6.12°$. Figure 5.14a is roughly half the time to a relative steady-state, and the lower right graph showing the full surface illustrates that most points are pushing from well outside the multipactor region to the $W_1$-limit line. Figure 5.14b shows the initial drive to an otherwise steady-state regime, where the center point in the main diagram has not moved much, the remainder of the downstream surface has effectively saturated near the $W_1$-limit, but upstream points are showing a drive to field angles outside the multipactor region, responding to the previously-mentioned upstream charge near the initial-impact region. Figure 5.14c shows the full extent of the discharge out to $\sim 10\times$ the temporal extent in Figure 5.12. The volume charge does show some reduction, which is a function of near-electrode fields affecting particle losses to the electrode boundaries, and may fluctuate over very long time scales as fields re-

spond to near-electrode charges; nonetheless, but the overall steady-state characteristic will look like the lower-right, full-surface graph in Figure 5.14c, with most points away from electrodes responding as in the main center sample point in all main diagrams of Figure 5.14.

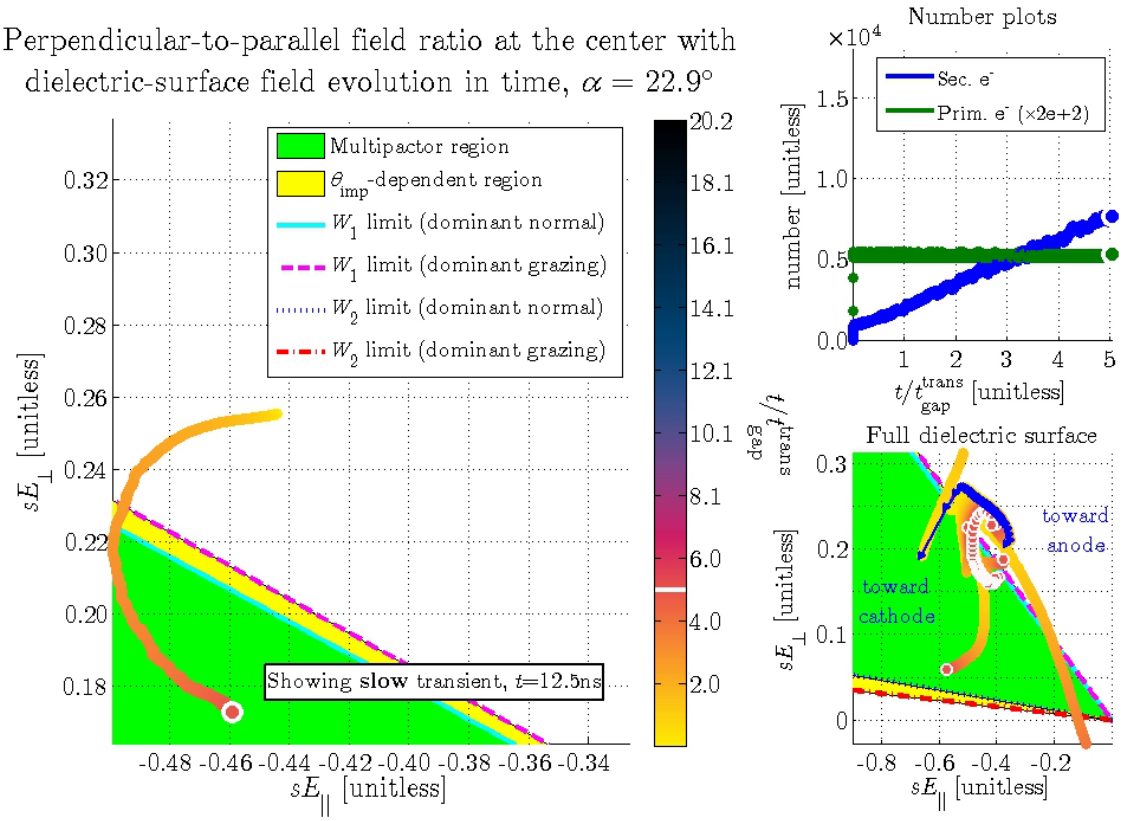


(a) Through slow transient.

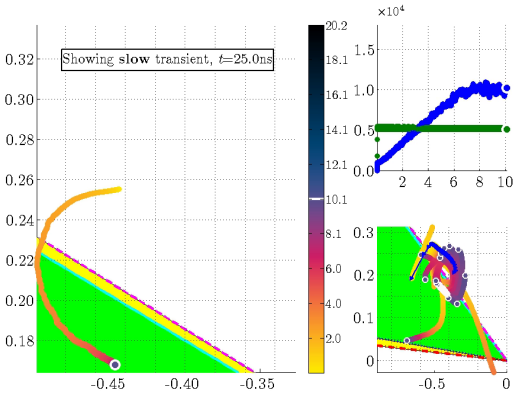


(b) Post peak-current.

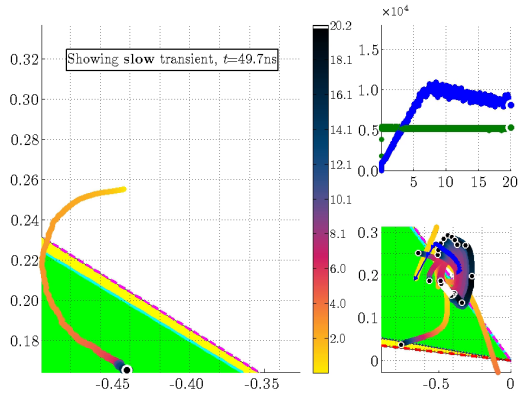


(c) Fully-developed steady-state.

Figure 5.14: Snapshots of $E_\perp/E_\parallel$ plotted at the dielectric surface with $\alpha = 22.9°$ in vacuum. Analogous to Figure 5.12, but for a non-multiplicative discharge. Yellow is 0 ps and black is 50 ns. A full video is available at as a supplement to this document.

## 5.4 Low-Pressure DC Susceptibility Diagrams

### 5.4.1 Low Pressure in Multiplicative Breakdown

Up to a few tens of Torr, the development of Section 5.2.2 is valid, and this section will detail a 1 Torr discharge consistent with low-pressure parameters encountered in cases of, for example, standard process plasmas [34]. Figure 5.15 shows the full-surface diagram, analogous to Figure 5.11. The fast, early transient, multiplicative growth from the VULP case is still present across the surface, but occurs over a very-short time frame compared to the overall time shown, which is $\sim 100\times$ longer in Figure 5.15 than in Figure 5.11. Clearly , much of the temporal characteristics are obscured by the broad movement of the fields compared to the VULP case, and the details of the fast-transient will be more clearly delineated in Figure 5.16 below. It is apparent that most of the discharge time is dominated by alternative effects other than pure multipactoring surface effects, and the long-timescale (compared to the VULP fast-transient timescale) oscillations experienced by the surface are at least partially the result of collisions in the volume (primarily ionization). Less apparent is that the leading edge of the oscillations depend on surface conditions, since the growth trend is seeded by surface growth.

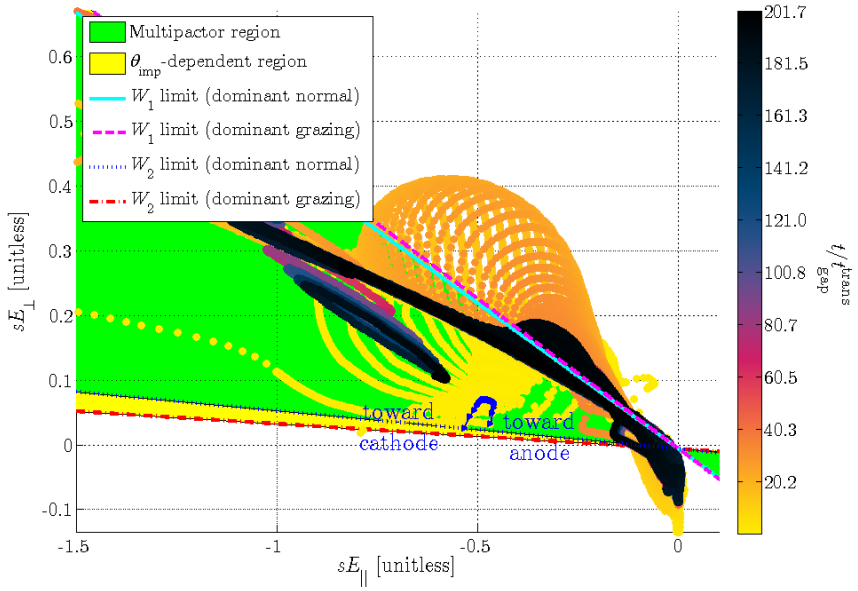


Figure 5.15: $E_\perp/E_\parallel$ plotted at the dielectric surface with $\alpha = 6.12°$ in $p_{bg} = 1$ Torr of neutral Ar. Analogous to Figure 5.11, but for a low-pressure discharge. Yellow is 0 ns and black is 50 ns. Oscillations are driven by the ion plasma frequency as was the case at lower pressures with reduced oscillatory effects, c.f. Figure 3.25, causing the field ratio to move into and out of the multiplicative region.

More detailed diagrams at key temporal intervals are shown in Figure 5.16. Figure 5.16a shows the extent of the "fast transient", which is the VULP-like growth period that happens over a very short time compared to both the standard transit time and the full discharge time shown. In this case, the fast transient occurs over $\sim 30\,\%$ (noting the

cutoff is somewhat arbitrary) of the standard transit time and $\sim 2\,\%$ of the full discharge time shown, amounting to a picosecond-scale phenomenon. The characteristics of the fast transient in 1 Torr at the center (main plot in Figure 5.16a) are very similar to the vacuum case (main plot in Figure 5.12a), with some variations towards the end of the fast-transient time shown in response to a relatively minor difference in composition and configuration of species in the volume. Note that the scaled number plot at the upper right of Figure 5.16a indicates a secondary population with a similar order of magnitude to that shown in Figure 5.12a (n.b. the additional scaling noted in the legend to allow better visualization of the number data). Clearly, there is a spike in the secondary population associated with VULP-like multipactor over the surface over a very short time frame, noted as the "fast transient", as opposed to a slower, but still multiplicative, transient later in the discharge termed the "slow transient". The variation of fields towards the end of the fast-transient time remains within about $\sim 20\,\%$ of the vacuum steady-state value from Figure 5.12c further enforcing the VULP-like behavior at the parameters for this simulation. Figure 5.16b is a snapshot after the peak electron population in a post fast-transient growth period that is assisted by ionization electrons and the movement of ions throughout the surface. This initial slow-transient growth comprises an upstream growth resulting from a "peel-away" of ions near the surface that pulls near-cathode field components up in magnitude (hovering along the saturation field-angle line) and slightly shallower in angle, while the downstream near-anode field components are reduced in magnitude by the presence of ions. An interesting point to note is that the field magnitude for points on approach to the cathode have a *larger* magnitude than fields on approach to the anode, although fields everywhere have roughly the same angle; consequently, ions closer to the cathode experience a stronger field, enforcing the peel-away effect. Ion population is largest near the anode, since any modes of multiplicative surface growth greater than unity will have the largest density near the anode, leading to greater ionization in the region. Space-charge, with larger densities of both positive ions and negative secondary and ionization electrons, reduces the local fields as a result, corroborated by the spread in field magnitude for all full-surface susceptibility snapshots, approaching the largest value near the cathode and the smallest value near the relatively particle-dense anode. Further note that Figure 5.16b happens to be the peak of ion population post fast-transient, and the time shown is around the timescale for a typical ion to traverse the full gap under the applied voltage for this simulation, and $\sim 20\times$ past the fast-transient growth period. Figure 5.16c corroborates the ion-momentum time-scale, as significant reduction of ions in the volume has occurred over the ensuing $\sim 45$ ns since the time in Figure 5.16b, with the slower ions comprising the shallow end of the decay time, as is expected. The dielectric center shows a field pull-up typical of what was seen with the multipactor front passing over a given point on the surface. Due to the larger population of electrons now assisting growth, the field pull-up extends further outside of the multipactor region than seen with the pure-multipactor front. Figure 5.16d shows the field response accompanying surface-growth saturation and the ion momentum, again noting that the time difference is on the order of the time for a typical ion to cross the full gap since the end time in Figure 5.16c. Ion are, again, peeled away from the surface, with upstream charge removed faster in an average sense from the near-surface region, and fields are pushed back down to the $W_1$ limit as the surface peel-away effectively leads to shallower angles since downstream points

see stronger negative charge upstream along the evacuated surface. Figure 5.16e shows the cumulative effect through the full discharge time, where the temporal behavior of surface multiplication followed by surface-ion peel-away produces an oscillatory pattern in both the characteristic susceptibility diagram and number plots, and an expansion-contraction pattern in the full-surface susceptibility diagram.

### 5.4.2 Low-Pressure Dark-Current Steady-State

The full-surface susceptibility diagram for the case of 22.9° is shown in Figure 5.17. As typical of low-collisionality discharges in Section 3.6.2, e.g. Figure 3.29, discharges starting outside the multiplicative region of Figure 5.17 show no early growth period as there was in, for example, Figure 5.15. Again, the early transient is dominated by surface characteristics until collisionality can become appreciable, c.f. Section 3.2.

More detailed diagrams at various temporal intervals are shown in Figure 5.18, analogous to Figure 5.12 for the 6.12° case. Figure 5.18a shows the characteristic point (again, chosen as the dielectric center) responding in a similar manner to Figure 5.13, i.e. VULP-like, albeit through about half the time shown in Figure 5.13. The fields at the final time shown in Figure 5.18a are around $\sim 10\,\%$ for each component compared to the steady-state value in Figure 5.13. Figure 5.18b shows this simulation out to the same time end time as Figure 5.13, where clearly additional effects have been added with the presence of ionization. In this case, an upstream ionization-assisted growth is occurring, pulling fields up along a near-saturated angle in response to the upstream, ionization-assisted, multipactor front in a similar manner to the field variations in Figure 5.16b. Of particular note is the absence of any fast-transient effects prior to this slower growth period, consistent with VULP-like behavior. Furthermore, Figure 5.18b is around the time for the average ion to cross the full gap at these parameters (recall $\sim 20\,\text{ns}$, so the reduction in $Ar^+$ population in the upper-right is sensible at this phase. Figure 5.18c behaves analogously to Figure 5.16c, where the ionization-assisted multipactor front has crossed the center, pulling the fields "up" as a result. Figure 5.18d is a similar peel-away of $Ar^+$ away from the surface as in Figure 5.16c, resulting in the field pull-down. Finally, Figure 5.18e shows the full discharge time, where the clear difference compared to Figure 5.16e is the much more heavily-damped oscillation, most apparent in all species shown in the number plot.

## 5.5 Chapter 5 Conclusions

A novel approach to susceptibility modeling in DC has been implemented. Susceptibility with limits drawn using the Vaughan theory is successful at showing and predicting where systems will evolve in terms of multiplicative growth using *a-priori* metrics. While certain properties of the evolved distribution should be expected to provide better agreement if used in the formulation, e.g. using the actual energy distributions in the volume from simulation to calculate ionization rates, these are necessarily *a-posteriori* metrics that do not serve the purpose of this technique. As in Chapter 3 and Chapter 4, it must be understood that the evolution of the discharges studied are limited by the physics included in the models described. The susceptibility diagram may be used to trace the

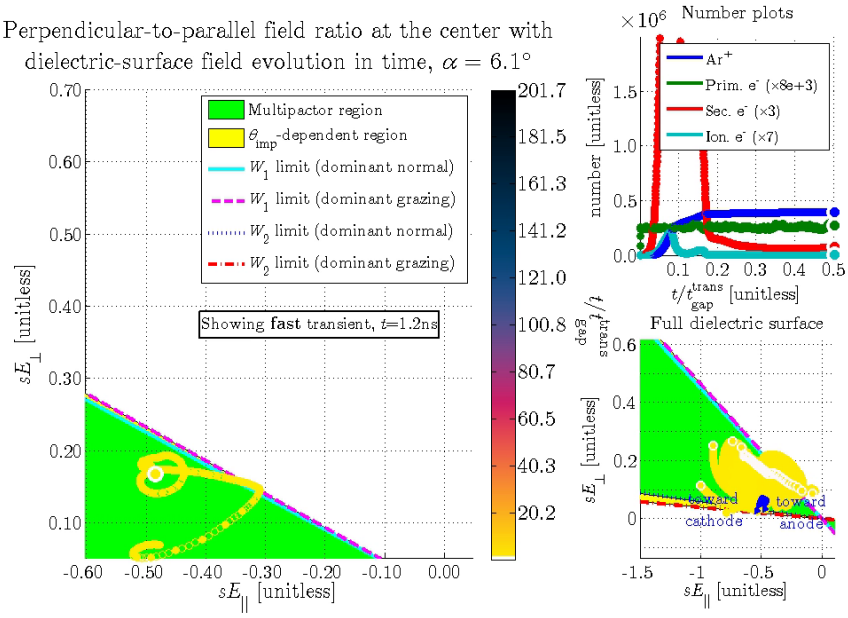


(a) End of the fast transient.

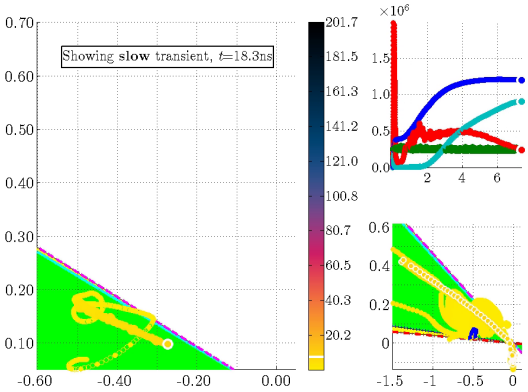


(b) Post fast-transient growth.

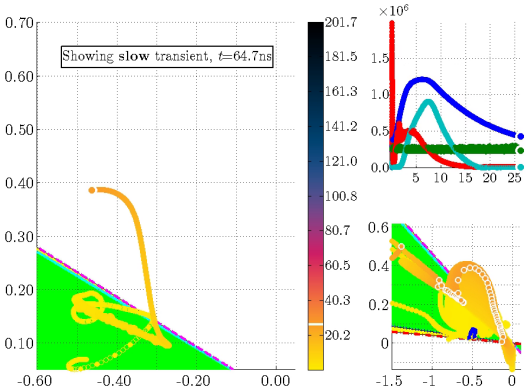


(c) Ionization-electron assisted front passing center.

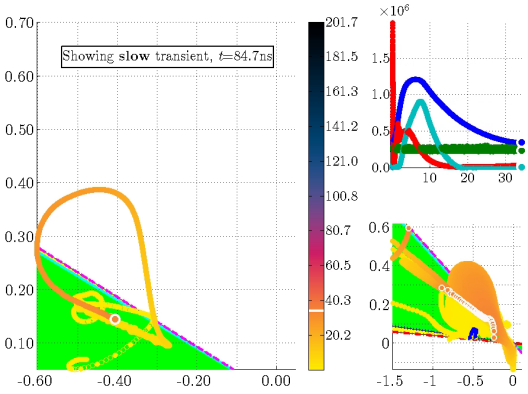


(d) Ion momentum pushing fields down.

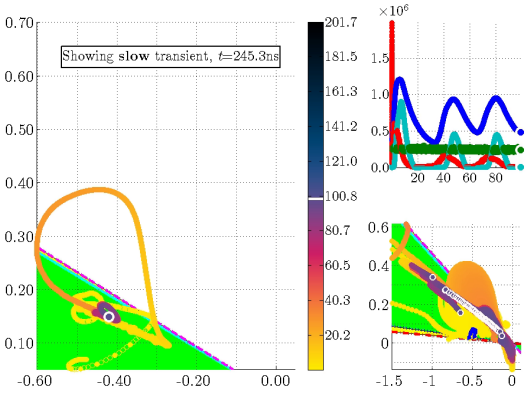


(e) Full discharge time.

Figure 5.16: Snapshots of $E_\perp/E_\parallel$ plotted at the dielectric surface with $\alpha = 6.12°$ in $p_{bg} = 1$ Torr of neutral Ar. Analogous to Figure 5.12, but for a low-pressure discharge. Yellow is 0 ns and black is 50 ns. A full video is available at as a supplement to this document.

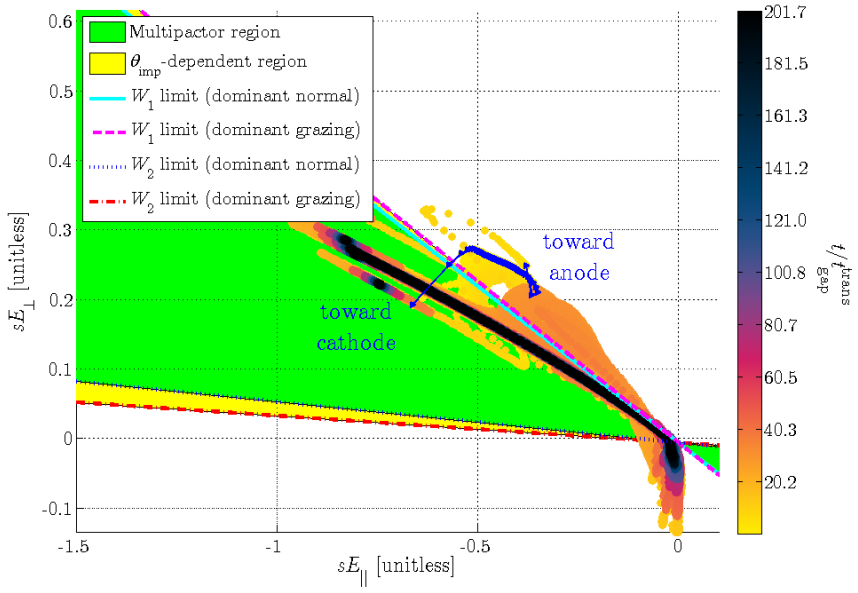


Figure 5.17: $E_\perp/E_\parallel$ plotted at the dielectric surface with $\alpha = 22.9°$ in $p_{bg} = 1\,\text{Torr}$ of neutral Ar. Analogous to Figure 5.15, but for an initially non-multiplicative discharge. Yellow is 0 ns and black is 50 ns. The time-evolution scatter includes space charge, while the $W_1$ and $W_2$ limits do not.

evolution of the discharge to further understand operating conditions and isolate the necessary direction to drive the system to desired states, e.g. to either a growing regime by maintaining field angles in the multiplicative region or to a steady-state regime by pushing fields out of the multiplicative region as fast as possible. Furthermore, susceptibility diagrams provide an engineering tool that can assess the initial characteristics of a discharge based on the initial fields and the characteristics of secondary emission for the dielectric. Engineering methods can then be devised to force the discharge characteristics into desired regions from the onset, e.g. with surface charging prior to discharge onset.

## 5.A Excursion, Lifetime, and Energy Equations

Returning to Equation (5.12) in Section 5.2.2, explicitly working out the integration to give the trajectory in $y$:

$$\begin{aligned} y &= \left[\frac{qE_\perp}{m\nu_\beta}\tau - \frac{qE_\perp}{m\nu_\beta}\frac{e^{-\nu_\beta\tau}}{-\nu_\beta} + v_{\perp 0}\frac{e^{-\nu_\beta\tau}}{-\nu_\beta}\right]_0^t \\ &= \frac{qE_\perp}{m\nu_\beta}t + \frac{qE_\perp}{m\nu_\beta^2}e^{-\nu_\beta t} - \frac{qE_\perp}{m\nu_\beta^2} - \frac{v_{\perp 0}}{\nu_\beta}e^{-\nu_\beta t} + \frac{v_{\perp 0}}{\nu_\beta} \\ &= \frac{qE_\perp}{m\nu_\beta^2}\left(\nu_\beta t + e^{-\nu_\beta t} - 1\right) - \frac{v_{\perp 0}}{\nu_\beta}\left(e^{-\nu_\beta t} - 1\right). \end{aligned} \tag{5.24}$$

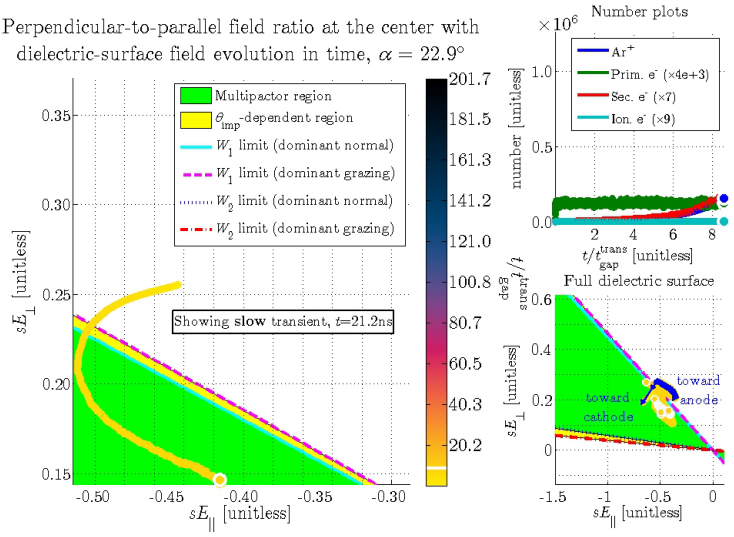


(a) Similar behavior as in Figure 5.14a, through vacuum dark-current.

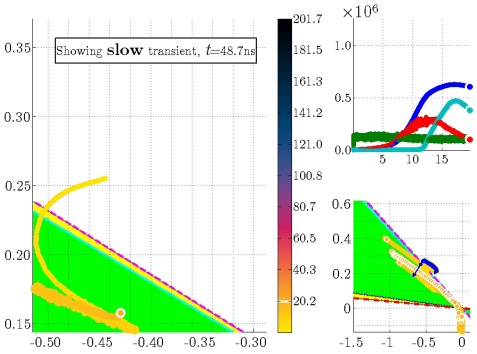


(b) Near peak volume population for all species.

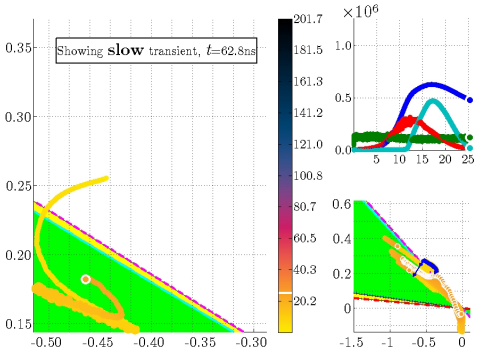


(c) Minimum Ar$^+$ population.

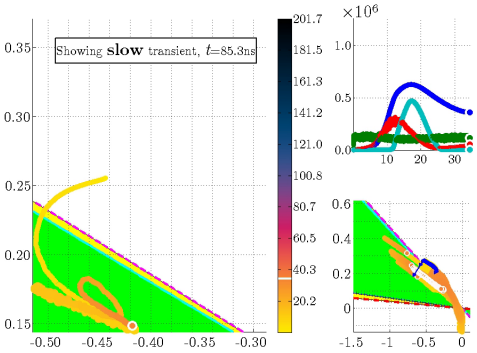


(d) Minimum secondary population.

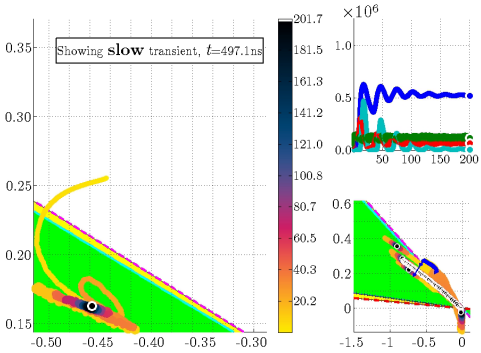


(e) Full discharge time.

Figure 5.18: Snapshots of $E_\perp/E_\parallel$ plotted at the dielectric surface with $\alpha = 22.9°$ in $p_{bg} = 1$ Torr of neutral Ar. Analogous to Figure 5.16, but for an initially non-multiplicative discharge. Yellow is 0 ns and black is 50 ns. A full video is available at as a supplement to this document.

Similarly, working out Equation (5.11):

$$\begin{aligned} x &= \left[\frac{qE_{\parallel}}{m\nu_\beta}\tau - \frac{qE_{\parallel}}{m\nu_\beta}\frac{e^{-\nu_\beta\tau}}{-\nu_\beta} + v_{\parallel 0}\frac{e^{-\nu_\beta\tau}}{-\nu_\beta}\right]_0^t \\ &= \frac{qE_{\parallel}}{m\nu_\beta}t + \frac{qE_{\parallel}}{m\nu_\beta^2}e^{-\nu_\beta t} - \frac{qE_{\parallel}}{m\nu_\beta^2} - \frac{v_{\parallel 0}}{\nu_\beta}e^{-\nu_\beta t} + \frac{v_{\parallel 0}}{\nu_\beta} \\ &= \frac{qE_{\parallel}}{m\nu_\beta^2}\left(\nu_\beta t + e^{-\nu_\beta t} - 1\right) - \frac{v_{\parallel 0}}{\nu_\beta}\left(e^{-\nu_\beta t} - 1\right). \end{aligned} \tag{5.25}$$

Setting Equation (5.24) (or Equation (5.13) in the main text) to 0 leads to Equation (5.15):

$$\begin{aligned} & y = 0 = \frac{qE_{\perp}}{m\nu_\beta^2}\left(\nu_\beta t + e^{-\nu_\beta t} - 1\right) - \frac{v_{\perp 0}}{\nu_\beta}\left(e^{-\nu_\beta t} - 1\right) \\ & \Rightarrow \frac{v_{\perp 0}}{\nu_\beta}\left(e^{-\nu_\beta t_{\text{life}}} - 1\right) = \frac{qE_{\perp}}{m\nu_\beta^2}\left(\nu_\beta t_{\text{life}} + e^{-\nu_\beta t_{\text{life}}} - 1\right), \\ & \frac{v_{\perp 0}}{\nu_\beta}e^{-\nu_\beta t_{\text{life}}} - \frac{qE_{\perp}}{m\nu_\beta^2}e^{-\nu_\beta t_{\text{life}}} - \frac{qE_{\perp}}{m\nu_\beta^2}\nu_\beta t_{\text{life}} = \frac{v_{\perp 0}}{\nu_\beta} - \frac{qE_{\perp}}{m\nu_\beta^2}, \\ & \left(\frac{m\nu_\beta v_{\perp 0} - qE_{\perp}}{m\nu_\beta^2}\right)e^{-\nu_\beta t_{\text{life}}} = \left(\frac{m\nu_\beta v_{\perp 0} - qE_{\perp}}{m\nu_\beta^2}\right) + \frac{qE_{\perp}}{m\nu_\beta^2}\nu_\beta t_{\text{life}}, \\ & \Rightarrow e^{-\nu_\beta t_{\text{life}}} = 1 - \frac{qE_{\perp}\nu_\beta}{qE_{\perp} - m\nu_\beta v_{\perp 0}}t_{\text{life}}. \end{aligned} \tag{5.26}$$

Again, Taylor expansion of the exponentiated $\nu_\beta t_{\text{life}}$ to second-order allows reduction of Equation (5.26).

$$\begin{aligned} & \left(e^{-\nu_\beta t_{\text{life}}} \approx 1 - \nu_\beta t_{\text{life}} + \frac{\left(\nu_\beta t_{\text{life}}\right)^2}{2}\right) = 1 - \frac{qE_{\perp}\nu_\beta}{qE_{\perp} - m\nu_\beta v_{\perp 0}}t_{\text{life}}, \\ & \frac{\left(\nu_\beta t_{\text{life}}\right)^2}{2} = -\frac{qE_{\perp}\nu_\beta}{qE_{\perp} - m\nu_\beta v_{\perp 0}}t_{\text{life}} + \nu_\beta t_{\text{life}}, \\ & \Rightarrow t_{\text{life}} = \frac{2}{\nu_\beta^2}\left(\nu_\beta - \frac{qE_{\perp}\nu_\beta}{qE_{\perp} - m\nu_\beta v_{\perp 0}}\right) \\ & = \frac{2}{\nu_\beta} - \frac{2qE_{\perp}}{qE_{\perp}\nu_\beta - \left(m\nu_\beta v_{\perp 0}\right)\nu_\beta} \\ & = \frac{2qE_{\perp}\nu_\beta - 2\left(m\nu_\beta v_{\perp 0}\right)\nu_\beta - 2qE_{\perp}\nu_\beta}{\nu_\beta\left(qE_{\perp}\nu_\beta - \left(m\nu_\beta v_{\perp 0}\right)\nu_\beta\right)} \\ & = \frac{-2m\nu_\beta v_{\perp 0}}{\nu_\beta\left(qE_{\perp} - m\nu_\beta v_{\perp 0}\right)} \\ & = \frac{2mv_{\perp 0}}{m\nu_\beta v_{\perp 0} - qE_{\perp}}. \end{aligned} \tag{5.27}$$

Velocities from Equation (5.11) and Equation (5.12) were simplified with a first-order

Taylor expansion:

$$\begin{aligned}
v_{\parallel}\left(t_{\text{life}}\right) &= \frac{q}{m}\frac{E_{\parallel}}{\nu_{\beta}}\left(1-e^{-\nu_{\beta}t_{\text{life}}}\right)+v_{\parallel 0}e^{-\nu_{\beta}t_{\text{life}}} \\
&= \frac{q}{m}\frac{E_{\parallel}}{\nu_{\beta}}\left(1-\left[1-\nu_{\beta}t_{\text{life}}\right]\right)+v_{\parallel 0}\left(1-\nu_{\beta}t_{\text{life}}\right) \\
&= \frac{q}{m}\frac{E_{\parallel}}{\nu_{\beta}}\nu_{\beta}t_{\text{life}}+v_{\parallel 0}-v_{\parallel 0}\nu_{\beta}t_{\text{life}} \\
&= v_{\parallel 0}+\left(\frac{qE_{\parallel}-mv_{\parallel 0}\nu_{\beta}}{m}\right)t_{\text{life}} \\
v_{\perp}\left(t_{\text{life}}\right) &= \frac{q}{m}\frac{E_{\perp}}{\nu_{\beta}}\left(1-e^{-\nu_{\beta}t_{\text{life}}}\right)+v_{\perp 0}e^{-\nu_{\beta}t_{\text{life}}} \\
&= \frac{q}{m}\frac{E_{\perp}}{\nu_{\beta}}\left(1-\left[1-\nu_{\beta}t_{\text{life}}\right]\right)+v_{\perp 0}\left(1-\nu_{\beta}t_{\text{life}}\right) \\
&= \frac{q}{m}\frac{E_{\perp}}{\nu_{\beta}}\nu_{\beta}t_{\text{life}}+v_{\perp 0}-v_{\perp 0}\nu_{\beta}t_{\text{life}} \\
&= v_{\perp 0}+\left(\frac{qE_{\perp}-mv_{\perp 0}\nu_{\beta}}{m}\right)t_{\text{life}}.
\end{aligned} \tag{5.28}$$

Plugging Equation (5.19) into the velocities in Equation (5.28) produces the simplified velocities of Equation (5.20). The impact energy is obtained by applying Equation (5.20) in the simple non-relativistic form:

$$W_{\text{imp}} = \frac{1}{2}m\left(\left[v_{\parallel}\left(t_{\text{life}}\right)\right]^{2}+\left[v_{\perp}\left(t_{\text{life}}\right)\right]^{2}\right). \tag{5.29}$$

The target metric is, again, the ratio of perpendicular to parallel fields, which is obtained

by rearranging Equation (5.22):

$$
\begin{aligned}
W_{\text{imp}} &= \frac{1}{2}m\left(\left[\frac{2v_{\perp 0}qE_{\parallel}}{m\nu_{\beta}v_{\perp 0}-qE_{\perp}}+v_{\parallel 0}\right]^{2}+v_{\perp 0}^{2}\right),\\
\frac{2W_{\text{imp}}}{m}-v_{\perp 0}^{2} &= \left(\frac{2v_{\perp 0}qE_{\parallel}}{m\nu_{\beta}v_{\perp 0}-qE_{\perp}}+v_{\parallel 0}\right)^{2},\\
\left(\sqrt{\frac{2W_{\text{imp}}}{m}-v_{\perp 0}^{2}}-v_{\parallel 0}\right) &= \frac{2v_{\perp 0}qE_{\parallel}}{m\nu_{\beta}v_{\perp 0}-qE_{\perp}},\\
\frac{1}{\left(\sqrt{\frac{2W_{\text{imp}}}{m}-v_{\perp 0}^{2}}-v_{\parallel 0}\right)} &= \frac{m\nu_{\beta}v_{\perp 0}}{2v_{\perp 0}qE_{\parallel}}-\frac{qE_{\perp}}{2v_{\perp 0}qE_{\parallel}},\\
\frac{m\nu_{\beta}v_{\perp 0}}{2v_{\perp 0}qE_{\parallel}}-\frac{1}{\left(\sqrt{\frac{2W_{\text{imp}}}{m}-v_{\perp 0}^{2}}-v_{\parallel 0}\right)} &= \frac{qE_{\perp}}{2v_{\perp 0}qE_{\parallel}},\\
\Rightarrow\frac{E_{\perp}}{E_{\parallel}} &= 2v_{\perp 0}\left[\frac{m\nu_{\beta}v_{\perp 0}}{2v_{\perp 0}qE_{\parallel}}+\frac{1}{\left(v_{\parallel 0}-\sqrt{\frac{2W_{\text{imp}}}{m}-v_{\perp 0}^{2}}\right)}\right],\\
\frac{E_{\perp}}{E_{\parallel}} &= \frac{2v_{\perp 0}}{\left(v_{\parallel 0}-\sqrt{\frac{2W_{\text{imp}}}{m}-v_{\perp 0}^{2}}\right)}+\frac{m\nu_{\beta}v_{\perp 0}}{qE_{\parallel}}.
\end{aligned}
\tag{5.30}
$$

## 5.B Surface Field Correction

### 5.B.1 Correction of Charge-Biased Surface Fields

Since the particle-weighting scheme effectively distributes charge to discrete points in space, the surface fields may experience significant error by overestimating the near-surface influence of the charge on field magnitude and angle. The error occurs when using the finite-differencing schemes for Poisson's equation in XOOPIC to calculate the fields using node values for the charge, calculating the fields via finite difference of potentials across the nodes, and finally moving back to the nodes via interpolation, causing an overall first-order error at surfaces. The error will then affect the more subtle nuances of discharge behavior dominated by near-surface fields, exposing an error of similar order to derived metrics, such as DC susceptibility.

The goal here is to weight the existing surface-field diagnostics to correctly account for the charge density at the nodes. Since charge collects at the dielectric surface, anecdotally, a large positive charge on the dielectric opposite a negative charge at the nearest node above will tend to overestimate the field magnitude and field angle (with respect to the $-x$ axis in the usual configuration for this study). Existing charge-density diagnostics are used to weight existing in-situ values for the line-integrated field to correct the field diagnostics reported by XOOPIC. A Gaussian 2-D pillbox is applied "just above" the charge density at each surface grid point, $(j,k)$, schematically shown in Figure 5.19.

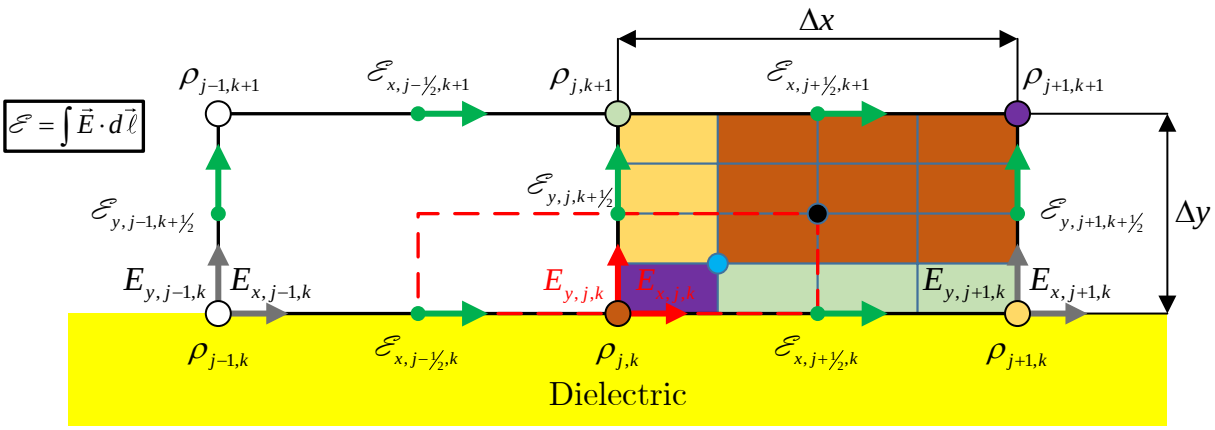


Figure 5.19: 2-D Gaussian pillbox schematic for $E_y$ correction. Charge densities, $\rho$, and potential differences (line-integrated fields), $\mathcal{E}$, are diagnostic values. Field values indexed with $k$ are conformal to the dielectric surface. The Gaussian pillbox sits with an edge on the dielectric surface, where free charge collected at the surface is included in the volume. The black dot indicates the location of the grid center, while the blue dot indicates the location of the weighting centroid, about which linear weighting is applied to each of the grid points, $(j, k)$.

Recall that this is a Yee-mesh implementation, so field values at mesh points are directed, interpolating to get field values at other locations. Gauss's law for the pillbox is:

$$\oint_S \left(\vec{E} \cdot \hat{n}\right) ds = \frac{1}{\varepsilon_0} \int_V \rho d\tau, \tag{5.31}$$

where the left-hand side integrates over surface elements, $ds$, of the Gaussian pillbox, and the right-hand side integrates over volume elements, $d\tau$. Summarizing details provided in Appendix 5.B.2, the total surface integral is:

$$\oint_S \left(\vec{E} \cdot \hat{n}\right) ds = \begin{cases} \dfrac{\Delta x}{8\Delta y}\left(\begin{array}{c} \mathcal{E}_{y,j-1,k+1/2} + 6\mathcal{E}_{y,j,k+1/2} + \mathcal{E}_{y,j+1,k+1/2} + \\ -\mathcal{E}_{y,j-1,k} - 6E_{y,j,k}\Delta y - \mathcal{E}_{y,j+1,k} \end{array}\right) + \\ \dfrac{\Delta y}{8\Delta x}\left(\mathcal{E}_{x,j+1/2,k+1} + 3\mathcal{E}_{x,j+1/2,k} - \mathcal{E}_{x,j-1/2,k+1} - 3\mathcal{E}_{x,j-1/2,k}\right) \end{cases}, \tag{5.32}$$

where the target field, $E_{y,j,k}$ is explicitly written. The volume integral of the charge density for the Gaussian pillbox is linearly weighted to the pillbox centroid, decomposing into two halves centered at $\left(\pm\frac{\delta x}{4}, \frac{\delta y}{4}\right)$, using the areal ratio in Cartesian coordinates:

$$\frac{1}{\varepsilon_0}\int_V \rho d\tau = \frac{1}{\varepsilon_0}\frac{\Delta x \Delta y}{64}\left(\begin{array}{c} 18\rho_{j,k} + 6\rho_{j,k+1} + 3\rho_{j-1,k} + \\ 3\rho_{j+1,k} + \rho_{j-1,k+1} + \rho_{j+1,k+1} \end{array}\right), \tag{5.33}$$

noting that the weighting construct in Figure 5.19 is explicitly shown for the cell to the right of $(j, k)$, but should be mirrored to the left of $(j, k)$ when writing Equation (5.33).

Returning to Gauss's law and solving for the field value $E_{y,j,k}$:

$$E_{y,j,k} = \left[ \begin{array}{c} \dfrac{\Delta y}{6(\Delta x)^2} \left( \begin{array}{c} \mathcal{E}_{x,j+1/2,k+1} + 3\mathcal{E}_{x,j+1/2,k} + \\ -\mathcal{E}_{x,j-1/2,k+1} - 3\mathcal{E}_{x,j-1/2,k} \end{array} \right) + \\ \dfrac{1}{6\Delta y} \left( \mathcal{E}_{y,j-1,k+1/2} + 6\mathcal{E}_{y,j,k+1/2} + \mathcal{E}_{y,j+1,k+1/2} \right) + \\ \dfrac{1}{6} \left( -E_{y,j-1,k} - E_{y,j+1,k} \right) + \\ -\dfrac{\Delta y}{48\varepsilon_0} \left( \begin{array}{c} 18\rho_{j,k} + 6\rho_{j,k+1} + 3\rho_{j-1,k} + \\ 3\rho_{j+1,k} + \rho_{j-1,k+1} + \rho_{j+1,k+1} \end{array} \right) \end{array} \right] \tag{5.34}$$

The field in $x$ follows a similar development, but with a shifted pillbox as in Figure 5.20.

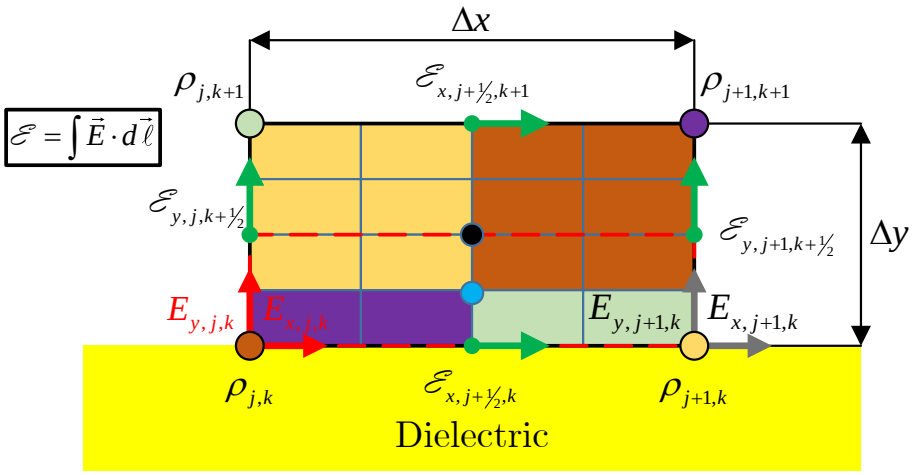


Figure 5.20: 2-D Gaussian pillbox schematic for $E_x$ correction. Characteristics are similar to Figure 5.19.

For Figure 5.20, the surface integral for the electric field, analogous to Equation (5.32) is:

$$\oint_S \left( \vec{E} \cdot \hat{n} \right) ds = \left[ \begin{array}{c} \dfrac{\Delta x}{2\Delta y} \left( \mathcal{E}_{y,j,k+1/2} + \mathcal{E}_{y,j+1,k+1/2} \right) - \dfrac{\Delta x}{2} \left( E_{y,j,k} + E_{y,j+1,k} \right) + \\ -\dfrac{\Delta y}{8} \left( E_{x,j,k+1} + 3E_{x,j,k} \right) + \dfrac{\Delta y}{8} \left( E_{x,j+1,k+1} + 3E_{x,j+1,k} \right) \end{array} \right], \tag{5.35}$$

where the values for $E_{y,*,k}$ are given by Equation (5.34), $E_{x,j+1,*}$ is taken directly from the grid, and the target quantities are the $E_{x,*,k}$ terms. The volume integral for the charge density, analogous to Equation (5.33) is:

$$\frac{1}{\varepsilon_0} \int_V \rho d\tau = \frac{1}{\varepsilon_0} \frac{\Delta x \Delta y}{16} \left[ \rho_{j,k+1} + \rho_{j+1,k+1} + 3\rho_{j+1,k} + 3\rho_{j,k} \right]. \tag{5.36}$$

Simplifying and solving for $E_{x,j,k}$ gives:

$$E_{x,j,k} = E_{x,j+1,k} - \frac{8}{3\Delta y}\left(\begin{array}{c} \dfrac{\Delta x \Delta y}{16\varepsilon_0}\left[\begin{array}{c}\rho_{j,k+1} + \rho_{j+1,k+1} + \\ 3\rho_{j+1,k} + 3\rho_{j,k}\end{array}\right] + \\ -\left[\begin{array}{c}\dfrac{\Delta x}{2\Delta y}\left(\mathcal{E}_{y,j,k+1/2} + \mathcal{E}_{y,j+1,k+1/2}\right) + \\ -\dfrac{\Delta x}{2}\left(E_{y,j,k} + E_{y,j+1,k}\right) + \\ \dfrac{\Delta y}{8}\left(E_{x,j+1,k+1} - E_{x,j,k+1}\right)\end{array}\right]\end{array}\right). \tag{5.37}$$

Note that Equations (5.34) and (5.37) are closed along the $x$ grid by the boundary conditions at the electrodes, and that this treatment is only for the surface edge cells and not applied globally since charge density accumulation is less problematic away from cell edges.

### 5.B.2 Formulation of Charge-Bias Correction

This section delineates the details of using Figures 5.19 and 5.20 to derive the field corrections to reduce field biasing by charge accumulation on the surface. Returning to Gauss's law in Equation (5.31) and the configuration of Figure 5.19, so that the field flux through the top of the Gaussian pillbox is:

$$\int_{x_{j-1/2}}^{x_{j+1/2}} E_{y,k+1/2}dx = \int_{x_{j-1/2}}^{x_j} E_{y,k+1/2}dx + \int_{x_j}^{x_{j+1/2}} E_{y,k+1/2}dx. \tag{5.38}$$

Note the fields in the electrostatic case at the midpoints of the grid can be approximated by existing diagnostics for the electric potential, i.e. the line integral of the electric field, in 2-D:

$$\mathcal{E} = -\Delta\Phi(E) = \int \vec{E}\cdot d\vec{\ell} \Rightarrow \vec{E} \approx \left(\frac{\mathcal{E}_x}{\Delta x}, \frac{\mathcal{E}_y}{\Delta y}\right), \tag{5.39}$$

which becomes exact in the limit that $\Delta$ quantities approach zero, i.e. the grid approaches continuous space. Assuming linear weighting, the right-hand side of Equation (5.38), leveraging Equation (5.39), can be written:

$$\begin{aligned}
\int_{x_{j-1/2}}^{x_j} E_{y,k+1/2}dx &= \frac{\Delta x}{2}\left(\frac{1}{4}E_{y,j-1,k+1/2} + \frac{3}{4}E_{y,j,k+1/2}\right) \\
&= \frac{\Delta x}{2}\left(\frac{1}{4}\frac{\mathcal{E}_{y,j-1,k+1/2}}{\Delta y} + \frac{3}{4}\frac{\mathcal{E}_{y,j,k+1/2}}{\Delta y}\right) \\
\int_{x_j}^{x_{j+1/2}} E_{y,k+1/2}dx &= \frac{\Delta x}{2}\left(\frac{3}{4}E_{y,j,k+1/2} + \frac{1}{4}E_{y,j+1,k+1/2}\right) \\
&= \frac{\Delta x}{2}\left(\frac{3}{4}\frac{\mathcal{E}_{y,j,k+1/2}}{\Delta y} + \frac{1}{4}\frac{\mathcal{E}_{y,j+1,k+1/2}}{\Delta y}\right),
\end{aligned} \tag{5.40}$$

which simplifies Equation (5.38) for the top of the Gaussian pillbox:

$$\int_{x_{j-1/2}}^{x_{j+1/2}} E_{y,k+1/2}dx = \frac{\Delta x}{8\Delta y}\left(\mathcal{E}_{y,j-1,k+1/2} + 6\mathcal{E}_{y,j,k+1/2} + \mathcal{E}_{y,j+1,k+1/2}\right). \tag{5.41}$$

Following similar treatment as in Equation (5.40) for the bottom, right, and left edges of the Gaussian pillbox gives:

$$\begin{aligned}
\text{Bottom}: &\int_{x_{j-1/2}}^{x_{j+1/2}} (-E_{y,k})\,dx = -\frac{\Delta x}{8}\left(E_{y,j-1,k} + 6E_{y,j,k} + E_{y,j+1,k}\right), \\
\text{Right}: &\int_{y_k}^{y_{k+1}} E_{x,j+1/2}dy = \frac{\Delta y}{8\Delta x}\left(\mathcal{E}_{x,j+1/2,k+1} + 3\mathcal{E}_{x,j+1/2,k}\right), \\
\text{Left}: &\int_{y_k}^{y_{k+1}} \left(-E_{x,j-1/2}\right)dy = -\frac{\Delta y}{8\Delta x}\left(\mathcal{E}_{x,j-1/2,k+1} + 3\mathcal{E}_{x,j-1/2,k}\right).
\end{aligned} \tag{5.42}$$

Summation of all terms gives the total surface integral for the Gaussian pillbox in Figure 5.19 as written in Equation (5.32). The charge density given in Equation (5.33) is found from the explicit weighting scheme illustrated in Figure 5.19, where:

$$\frac{1}{\varepsilon_0}\int \rho d\tau = \frac{1}{\varepsilon_0}\left[\begin{array}{l}
\overbrace{\left(\begin{array}{l}\frac{9}{16}\rho_{j,k} + \frac{3}{16}\rho_{j+1,k} + \\ \frac{3}{16}\rho_{j,k+1} + \frac{1}{16}\rho_{j+1,k+1}\end{array}\right)\frac{\Delta x}{2}\frac{\Delta y}{2}}^{\text{left of } (j,k)} + \\
\underbrace{\left(\begin{array}{l}\frac{9}{16}\rho_{j,k} + \frac{3}{16}\rho_{j-1,k} + \\ \frac{3}{16}\rho_{j,k+1} + \frac{1}{16}\rho_{j-1,k+1}\end{array}\right)\frac{\Delta x}{2}\frac{\Delta y}{2}}_{\text{right of } (j,k)}
\end{array}\right]. \tag{5.43}$$

Simplifying Equation (5.43) will produce Equation (5.33). Equating surface-integral terms for the fields with the volume integral terms for the charge density in the Gaussian pillbox will produce Equation (5.34), which is a series of coupled equations that can be solved

simultaneously:

$$\underbrace{\begin{bmatrix} E_y\left(j,k_s\right) \\ E_y\left(j+1,k_s\right) \\ E_y\left(j+2,k_s\right) \\ \vdots \\ E_y\left(n,k_s\right) \end{bmatrix}}_{\vec{E}_{y,\text{corr}}} = \left\{ \overbrace{\begin{bmatrix} 0 & -\frac{1}{6} & & & \\ -\frac{1}{6} & 0 & -\frac{1}{6} & & \\ & -\frac{1}{6} & 0 & -\frac{1}{6} & \\ & & \ddots & \ddots & \ddots \\ & & & -\frac{1}{6} & 0 \end{bmatrix}}^{\mathbf{M}_y} \overbrace{\begin{bmatrix} E_y\left(j,k_s\right) \\ E_y\left(j+1,k_s\right) \\ E_y\left(j+2,k_s\right) \\ \vdots \\ E_y\left(m,k_s\right) \end{bmatrix}}^{\vec{E}_{y,\text{corr}}} + \underbrace{\begin{bmatrix} -\frac{1}{6}E_y\left(x\left[j_c,k_c\right]\right) + A_y\left(x\left[j,k_s\right]\right) \\ A_y\left(x\left[j+1,k_s\right]\right) \\ A_y\left(x\left[j+2,k_s\right]\right) \\ \vdots \\ A_y\left(x\left[m-1,k_s\right]\right) - \frac{1}{6}E_y\left(x\left[j_a,k_a\right]\right) \end{bmatrix}}_{\vec{A}_{y,\text{grid}}} \right\}, \tag{5.44}$$

where $(j_c, k_c)$ and $(j_a, k_a)$ are indices denoting the location of the cathode and anode, respectively, closing off the equations at the specified potentials; $k_s$ is just the index for the dielectric surface, recalling that the surface is the target and typically situated at the half-space in $y$; and $\vec{A}_y(x[j,k_s])$ consists of all the grid terms, pulling directly from Equation (5.34):

$$A_y(x[j,k_s]) = \begin{bmatrix} \frac{\Delta y}{6(\Delta x)^2}\left(\begin{array}{c} \mathcal{E}_{x,j+1/2,k+1} + 3\mathcal{E}_{x,j+1/2,k} + \\ -\mathcal{E}_{x,j-1/2,k+1} - 3\mathcal{E}_{x,j-1/2,k} \end{array}\right) + \\ \frac{1}{6\Delta y}\left(\mathcal{E}_{y,j-1,k+1/2} + 6\mathcal{E}_{y,j,k+1/2} + \mathcal{E}_{y,j+1,k+1/2}\right) + \\ -\frac{\Delta y}{48\varepsilon_0}\left(\begin{array}{c} 18\rho_{j,k} + 6\rho_{j,k+1} + 3\rho_{j-1,k} + \\ 3\rho_{j+1,k} + \rho_{j-1,k+1} + \rho_{j+1,k+1} \end{array}\right) \end{bmatrix} \tag{5.45}$$

Inverting Equation (5.44) will then give the corrected fields.

$$\vec{E}_{y,\text{corr}} = \left(\mathbf{I} - \mathbf{M}_y\right)^{-1}\vec{A}_{y,\text{grid}} \tag{5.46}$$

Following a similar process for the Gaussian pillbox in Figure 5.20:

$$\int \left(\vec{E}\cdot\hat{n}\right) ds = \left\{ \begin{array}{l} \overbrace{\Delta x\left(\frac{1}{2}E_{y,j,k+1/2}+\frac{1}{2}E_{y,j+1,k+1/2}\right)}^{\text{top edge}} + \\ \overbrace{-\Delta x\left(\frac{1}{2}E_{y,j,k}+\frac{1}{2}E_{y,j+1,k}\right)}^{\text{bottom edge}} + \\ \underbrace{-\frac{\Delta y}{2}\left(\frac{1}{4}E_{x,j,k+1}+\frac{3}{4}E_{x,j,k}\right)}_{\text{left edge}} + \\ \underbrace{\frac{\Delta y}{2}\left(\frac{1}{4}E_{x,j+1,k+1}+\frac{3}{4}E_{x,j+1,k}\right)}_{\text{right edge}} \end{array} \right. . \tag{5.47}$$

Again, leveraging Equation (5.39) and simplifying will reduce Equation (5.47) to Equation (5.35), recalling that direct grid values for the fields are used for the $E_{x,j+1,*}$ values, which are calculated by weighted averaging to the grid prior to the correction. The charge density, following the weighting scheme illustrated in Figure 5.20, is:

$$\frac{1}{\varepsilon_0}\int \rho d\tau = \frac{1}{\varepsilon_0}\left[\frac{2}{16}\rho_{j,k+1}+\frac{2}{16}\rho_{j+1,k+1}+\frac{6}{16}\rho_{j+1,k}+\frac{6}{16}\rho_{j,k}\right]\Delta x\frac{\Delta y}{2}, \tag{5.48}$$

which simplifies to Equation (5.36) with minor manipulation. Again equating surface-integral terms for the fields with the volume-integral terms for the charge density in the Gaussian pillbox will produce Equation (5.37), which is simpler to solve since it is only coupled on once side once the solution for $E_y$ is found, and does not require simultaneous solution. For completion, the algebraic form to solve, following the convention in Equations (5.44) and (5.45) is:

$$E_x\left(j,k_s\right) = E_x\left(j+1,k_s\right) - \frac{8}{3\Delta y}A_x\left(x\left[j,k_s\right]\right), \tag{5.49}$$

where:

$$A_x\left(x\left[j,k_s\right]\right) = \left\{ \begin{array}{l} \frac{\Delta x\Delta y}{16\varepsilon_0}\left[\begin{array}{c}\rho_{j,k+1}+\rho_{j+1,k+1}+\\ 3\rho_{j+1,k}+3\rho_{j,k}\end{array}\right] + \\ -\left[\begin{array}{c} \frac{\Delta x}{2\Delta y}\left(\mathcal{E}_{y,j,k+1/2}+\mathcal{E}_{y,j+1,k+1/2}\right)+ \\ -\frac{\Delta x}{2}\underbrace{\left(E_{y,j,k}+E_{y,j+1,k}\right)}_{\text{from the corrected fields}}+ \\ \frac{\Delta y}{8}\underbrace{\left(E_{x,j+1,k+1}-E_{x,j,k+1}\right)}_{\text{direct from grid diagnostics}} \end{array}\right] \end{array} \right. , \tag{5.50}$$

recalling that the index $k_s$ is the grid location of the dielectric surface.

### 5.B.3 Application of Surface Field Correction

The surface field corrections delineated in Appendix 5.B.1 was applied to the standard parameter case of Table 2.7. It should be noted that, except for this section, susceptibility diagrams throughout this document do not apply the surface correction, accepting the roughly 10 % to 20 % error in the saturation condition. It will be shown that surface corrections follow similar characteristics up to peak population, but severely diverges from the cases presented, likely due to propagation of field conditions at the boundaries from coupling with necessarily error-prone fields at the boundaries.

A test case with the standard parameter set of Section 2.7, Table 2.8, is presented in Figure 5.22, where the starkly contrasting behavior into the dark-current time scales is noticeable as field behavior across the whole surface is highly ambulatory compared to the analogous diagram of Figure 5.11. The run-up to peak multiplication follows a similar behavior to that in Figure 5.11, but the field configuration into otherwise steady-state conditions are markedly different, while still maintaining non-multiplicative conditions.

The major caveats to this implementation are that the errors were minimized at the center of the dielectric, far from the electrodes. Furthermore, errors from stair-stepping the dielectric were moved to the electrodes. Since the electrodes are stair-stepped, the fields are either at $\pi/2$ or $\pi$ with respect to the surface, introducing an error on the order of the dielectric angle. It is conjectured that such an external error is being propagated though the scheme through the coupling to the boundary values or from the partial use of grid values above the surface. To clarify, it was discussed in Section 2.2 that the target error metric was the fields at the dielectric center. Discretization essentially moves errors away from the dielectric surface and onto the electrodes, and since errors propagate through every timestep, it this ambulatory field characteristic is a result of compounded errors. The accuracy of the calculations are difficult to model in this framework, which was partially addressed in Chapter 6, covering source studies and the direct calculation of fields from first principles formulation of the triple-point.

Further work remains to be done to verify the ambulatory nature of the fields in Figure 5.22, and this appendix is provided as a summary of the necessary foundations to further this study. In any case, the drive to peak current does not seem to be affected significantly, maintaining a similar drive to $\sim$ 10 % to 20 % of the expected saturation angle along the shortest chord to the $W_1$ line, so it may be conjectured that the treatment of secondary distribution draw the limit lines may be a target metric to further DC susceptibility. To further expand, the final field value in the center at the end of the peak growth towards the end of the fast transient is $\sim$ 13 % of the expected field angle along the shortest chord to the first crossover line. Over the whole discharge time, the final field value in the center is $\sim$ 70 % of the expected field angle along the shortest chord to the first crossover line. The error percentage at the peak of the fast transient growth is not especially improved from the uncorrected grid. As noted in Section 5.2, limit lines are drawn assuming secondaries in a Maxwellian distribution through the lifetime of the bulk volume. By observation of simulation, it is known that secondaries in the volume are not Maxwellian, and it was merely assumed that the space charge characteristics remain close to Maxwellian since lifetimes are relatively short. Future work can consider this shortcoming by assessing the actual distribution and determine an appropriate profile to generate limit lines; however, it should be stressed that the strength of the DC breakdown

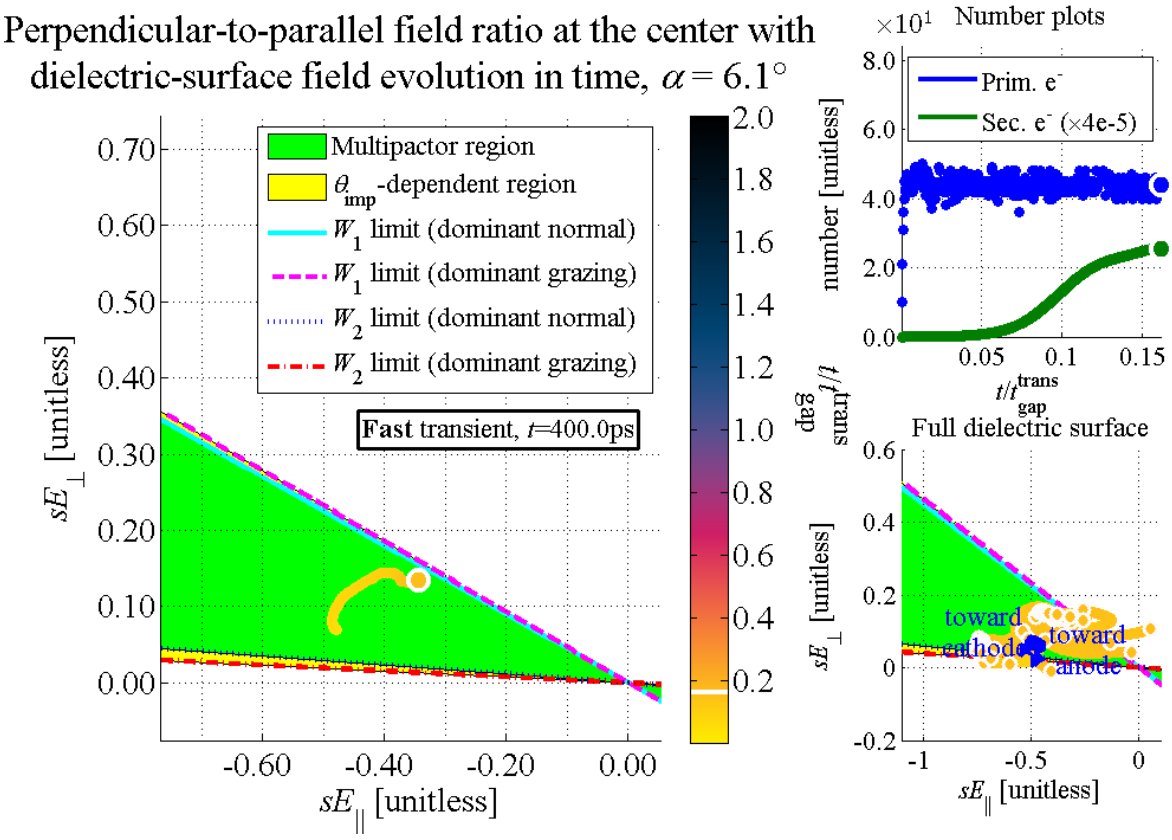


Figure 5.21: DC susceptibility diagram in breakdown with surface field correction, through 400 ps. Field correction is described in Appendix 5.B.1. Fast transient time scale shows similar behavior pushing to the first crossover line for much of the surface. The analogous susceptibility plot is shown in Figure 5.12

susceptibility framework lies in its *a-priori* treatment of discharge evolution. Since the distribution profile through a parametric simulation will vary with parameters, such a treatment would reduce the utility of the susceptibility metric. It is therefore advised that future work consider establishing a criterion for further "blurring" the $\theta_{\text{imp}}$ region.

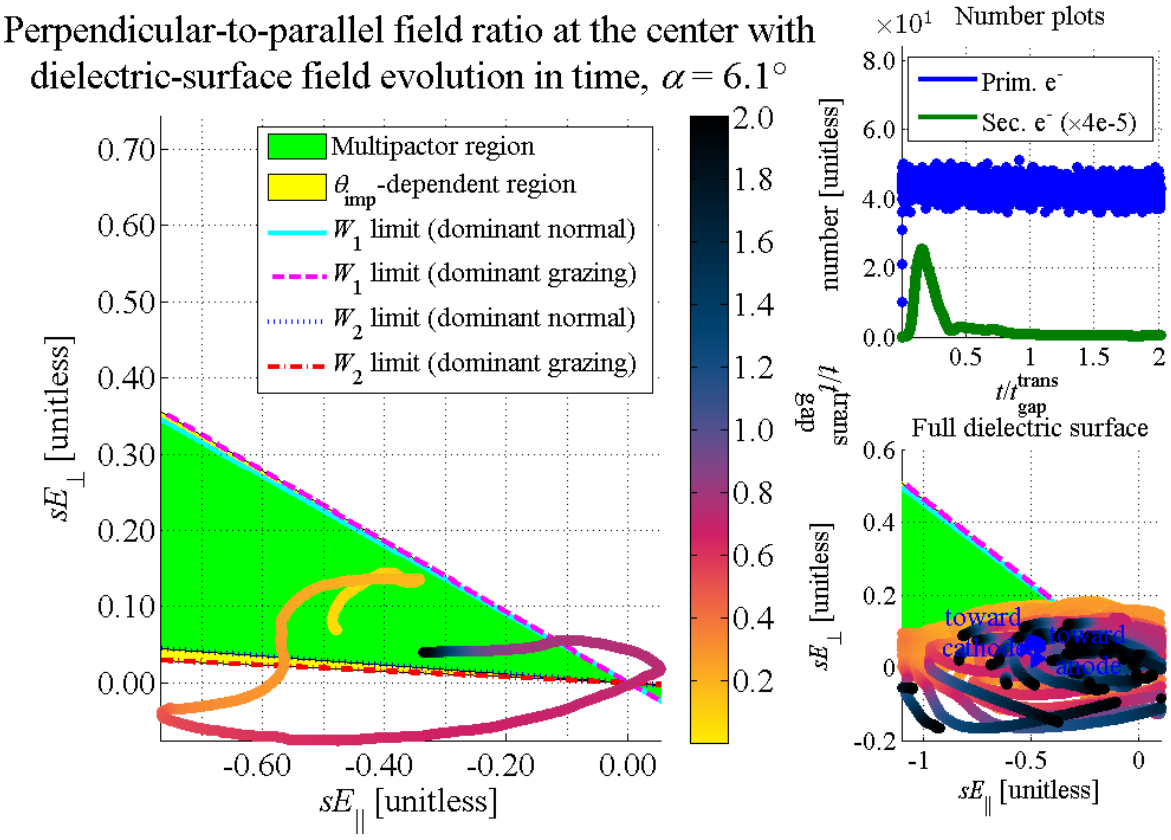


Figure 5.22: DC susceptibility diagram in breakdown with surface field correction. Field correction is described in Appendix 5.B.1.The push into steady-state shows starkly differing behavior from the analogous Figure 5.11.

# Chapter 6

# Source Studies

The objective of this chapter is to provide an assessment of the effects and modeling challenges using a broadened constant-waveform (CW) source, a Fowler-Nordheim (FN) source affected by local fields, and a source following theoretical treatment of the triple-point by Schächter to illustrate a first-principles approach on the triple-point itself; these seed models were described in Section 2.5. Sources in this chapter emit over a larger area than previously considered, normalizing to a cutoff length based on the Schächter source. Normalization to the Schächter source is most natural since, under certain parameters, the source saturates as the emitter length increases, i.e. the integration distance along the emitter gets farther from the triple point. The initial-impact region will similarly expand, distributing surface charge at impact, possibly introducing delay times and variations in multipactor growth characteristics. Fowler-Nordheim provides a self-consistent source that reacts to local variations in potentials, which can, in some cases, saturate the source with sufficient space-charge growth. The Schächter model can be considered closest to first-principles in terms of seed current magnitude for this study, using divergent field values on approach to the dielectric as the primary source of field enhancement, and providing a standard against the XOOPIC FN model, which relies on parameterized, empirical values for field enhancement characteristic of, for example, surface roughness, protrusions, impurities, etc. This treatment will focus only on multiplicative breakdown in vacuum, isolating surface-dominated discharges.

Recall Chapters 3 and 5 established that the surface-field configuration (primarily angle with respect to the surface) is the driving factor to multiplicative breakdown dominated by surface phenomena where bulk volume effects are negligible; the seed largely serves an auxiliary (although necessary) role. Furthermore, fundamental VULP multipactor has no breakdown curve, in contrast to Townsend avalanche, which is characterized by breakdown strengths parameterized in pressure and characteristic system length [20, 34]. The susceptibility theory of Chapter 5 showed that fundamental VULP multipactor breakdown is parameterized by field angle, $\chi_E$, independent of field magnitude. If $\chi_1 > \chi_E > \chi_2$, where $\chi_1$ and $\chi_2$ are the field angles associated with the crossover-limits, $W_1$ and $W_2$ (described in Section 2.3), for a characteristic particle, new secondaries will experience multiplicative growth with $\delta > 1$, c.f. Section 5.2.1. While the initial seeding is auxiliary to surface-field conditions vis-à-vis fundamental VULP breakdown, the nature of the seed can influence other discharge characteristics not heretofore emphasized in this study, such as the time to breakdown onset. The auxiliary role of the seed is partially a result of

the beam specification, which effectively saturates space-charge effects for the seed and initial impact such that discharges can adequately be modeled by a single particle with average emission characteristics. As described in Section 2.5.1, the primary seed source in the previous chapters is a specified, constant-waveform, unperturbed, Maxwellian-flux electron source at specified amperage, injected with sufficient energy to produce impact at peak secondary-emission characteristics from Section 2.3. This allows analysis across dielectric angles without concern for variations in local field magnitudes that would affect first impact, conditions for initial multiplication upon first impact, and time to initial multiplicative growth. This chapter will compare characteristic behaviors, emphasizing breakdown susceptibility evolution and driving characteristics. The behavior delineated here for multiplicative breakdown will apply for all discharges dominated by surface effects, up through pressures where collisional mean free paths are sufficiently small that any subsequent bulk volume charge does not significantly alter surface-field effects. It must be stressed that only characteristics for vacuum discharge will be explicitly delineated herein.

Considerations for developing a uniform emitter configuration for this chapter are provided in Section 6.1. A summary of the primary effects from Chapter 3 are presented in Section 6.2, for direct comparison with the succeeding three sections. Section 6.3 details an extended CW emitter over the uniform emitter length derived in Section 6.1. The application of the FN source as it relates to the effects of Section 6.2 is presented in Section 6.4. The implementation of the Schächter source and its effect on discharge behavior is presented in Section 6.5. Finally, Section 6.6 summarizes the primary discharge effects and additions from the usual case studies, with suggestions for future work.

## 6.1 Standard Emitter Configuration

Standard physical parameters are listed in Table 6.1. Reduced parameters are used here to handle the larger voltages required for the Schächter source at typical parameters used in previous chapters, which makes gains much larger than previously encountered since secondaries have access to much more energy at higher voltages for the same system length. Control of gain is maintained by reducing the system size such that the number of impacts is $\sim 10$, calculated with Equation (3.12); the associated maximum gain can be found with Equation (3.18), using $\delta_{max} = 2.95$, which remains unchanged from the previous parameter set. The particle gain (for weighted particles) is maintained below $\sim 1 \times 10^6$, with system lengths, particle weights, and currents normalized to ensure this gain limit.

It should be noted that an incidental benefit of reducing the spatial parameters by a constant factor ($1 \times 10^4$ for this case, reducing the 2 mm system down to 0.2 µm) is that the spatial resolution of particle trajectories is increased by the reduction factor for the spatial scale, holding all other computational parameters (e.g. particle weighting, temporal step-size) fixed, increasing from 35.5 µm from previous resolutions to 3.55 nm in the reduced parameter scale. The main caveat is that the results here are more applicable to pure vacuum and not as easily extensible to the low-pressure regime as the previous parameters since the system length is approaching the Townsend limit on the mean free path delineated in Section 1.3.3 at similar pressures. Assuming a typical secondary pop-

Table 6.1: List of standard physical and simulation parameters for Chapter 6 configurations. Physical parameters are reduced compared to previous chapters, and simulation parameters also modified to allow reasonable simulation times for runaway populations, noting that some physical characteristics must be monitored to ensure accuracy.

| Parameter | Value |
|---|---|
| Gap width | 0.20 µm |
| Current magnitude | 10 kA |
| Applied voltage | 3500 V |
| Maximum secondary yield | 2.95 |
| Maximum simulation electrons | $1 \times 10^3$ |
| Maximum simulation secondary electrons | $1 \times 10^6$ |

ulation at emission-energy characteristics (noting there should be consideration at higher energies for the short lifetimes), the mean free path for electrons in 100 Torr argon would be $\lambda_i \sim 10.95\,\mu\text{m}$, assuming ideal gas and $\sigma_{i,\max} \sim 2.75 \times 10^{-20}\,\text{m}$. In other words, the ratio of the mean free path to the system length at reduced parameters is $\lambda_i / D_{\text{gap}}^{\text{red}} \sim 54.8$, where the ratio is $\lambda_i / D_{\text{gap}} \sim 2.0 \times 10^{-3}$ for the previous parameters. Finally, it it important to note that ideal smooth surfaces are assumed in this treatment, and the effect of surface perturbations are not treated; it is known that system lengths in the sub-micron scale are within the characteristic lengths of engineering-scale surface perturbations, and any application of results herein should address any neglected surface effects accordingly.

From the discussions concerning the Schächter source in Section 2.5.3, the current saturates integrating over some distance, $R$, along the emitter surface from the triple-point origin. This is a highly non-linear process as a function of applied field, shown in Figure 6.1, particularly Figure 6.1a, showing the orders of magnitude in integrated current over a narrow range in applied field. The variation in $R$ is largely saturated in all cases until applied voltage is appreciable, most apparent in Figure 6.1b.

The initial intent of this study was to limit the emitter length via the saturation length for the Schächter emitter, but this approach only works well at low current for the gap widths of interest. To elaborate further on the saturation characteristics, arbitrarily choosing an applied field of $E_0 = 3000\,\text{MV/m}$ in Figure 6.2a, the integrated current starts to approach $I_{\text{top}} \sim 1\,\text{A}$ over $R \sim 800\,\mu\text{m}$. This field is about two orders of magnitude larger than typical operating characteristics from experiment for the previous parameters. In contrast, the current at the necessarily higher fields of the parameters used in this chapter (c.f. Table 6.1) looks practically linear over the same length.

The balance between emitted current, gain, and statistics on each population required re-evaluating the criterion for setting the emitter length, since the small step sizes needed to adequately resolve characteristic particle metrics (essentially the particle Courant) either leads to an excessively large number of steps to initial seed, or excessively small weights that non-physical spreading of charge would result. Ultimately, a practical approach was used such that a high primary current with high statistics (small weighting) was used, where the aforementioned reduction in spatial parameters maintains tractable

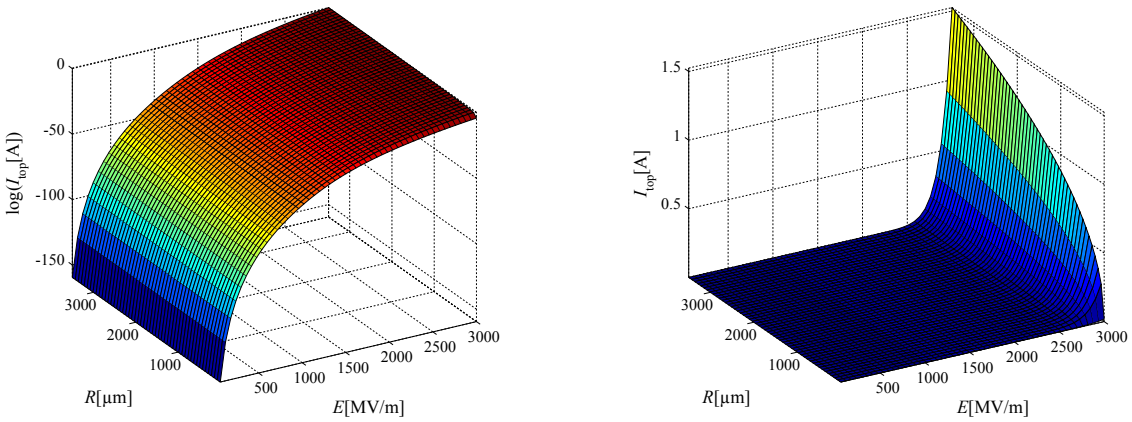


(a) Log scale.

(b) Linear scale.

Figure 6.1: Integrated current as a function of emitter length. $R$, and applied field, $E_0$. (b) shows the current on a linear scale to emphasize the nonlinearity, and (a) shows the same current on a log scale.

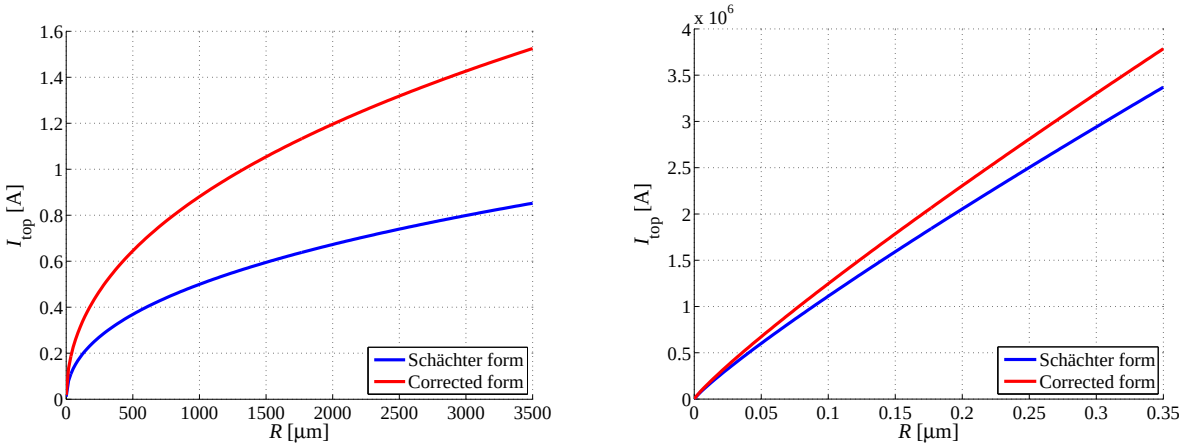


(a) Original parameter set.

(b) Reduced parameter set.

Figure 6.2: Schächter current as a function of distance, $R$, integrated from the triple point along the emitter. Integrated from the triple point along the emitter for (a) the original parameter set from the previous chapters, and for (b) for the reduced parameters from Table 6.1. The approach to saturation is illustrated (a) with specified applied voltage over increasing $R$, i.e. 6 MV over a gap of 2 mm. Table 6.1 does not saturate for the reduced parameter set.

gain by reducing the average number of bounces, and the length of the emitter was chosen so that direct primary arcs would not be induced in the geometry. Since the saturation length is very long at reduced parameters (with higher field), direct arcs would result from points along the emitting surfaces (i.e. the cathode) that are beyond $L \sim D_{\text{gap}} \tan(\alpha)$ from the triple point (slightly further than this length depending on field strength and particle average properties) for particles injecting as a Maxwellian flux with no drift. Direct arcs obviously do not contribute to the surface growth, but the fields generated by the volume charge can influence the surface characteristics, most importantly the field angle. A simple test was assembled using several CW sources over the full length of the vacuum-side cathode, each set to uniform current at 10 kA, which generally will be larger than Schächter (or limit to Schächter for sufficiently linear integrated current at very high voltages). Susceptibility diagrams with the associated species number plot for two emitter lengths are shown in Figure 6.3. There is a reduction in the peak number of secondaries by roughly a factor of three for the longest emitter, attributed to shorter lifetimes of emitted secondaries due to space charge; however, the effect of additional primary space charge is relatively limited and does not alter overall multipactoring characteristics that are best illustrated with the susceptibility diagrams. The full-surface susceptibility diagrams show no practical difference in downstream evolution between short and long emitters. There is a minor discernible difference in the main plot for the usual characteristic center evolution, where a small dip is visible during the fast transient at $t/t_{\text{trans}}^{\text{gap}} \sim 0.15$ in Figure 6.3a. Most notably, there is no significant difference in the upstream evolution, which is where space-charge would be expected to influence evolution the most, since exponential downstream growth will typically dominate the effects of primary populations towards the anode, proportionate to the multipactor gain (a difference of at least four orders of magnitude, in this case, between near-anode primary population and secondary population). The overall statistics for all populations in Figure 6.3b happen to be better due to intentional injection of more current, but the increased statistics do not contribute anything notable to the discharge evolution since the particle populations per cell were already well represented, reducing the possibility of numerically induced field fluctuations and consequent heating.

Finally, another benefit of moving to reduced spatial parameters allows reduction of the voltage. At previous parameters, the applied voltage required to generate sufficient amperage would be prohibitively large, leading to to variations in physics that would comprise a very large domain and likely require relativistic treatment in cases of long-lived electrons. Reduction of spatial parameters allows larger fields (the metric field emission depends on) at relatively moderate voltage (the order of maximum particle energy after uncollided gap excursion), keeping in line with physics heretofore discussed to concentrate discussion on differential changes resulting from broadening of the seed.

## 6.2 Summary of Constant Waveform Current Effects

To summarize the constant-waveform (CW) source effects of interest, Table 6.2 provides a list of pertinent figures from Chapters 3 and 5, with a description of notable features. To recap, the CW source is an unperturbed beam, where dielectric charge from electron impact and subsequent secondary emission is positive for most of the surface

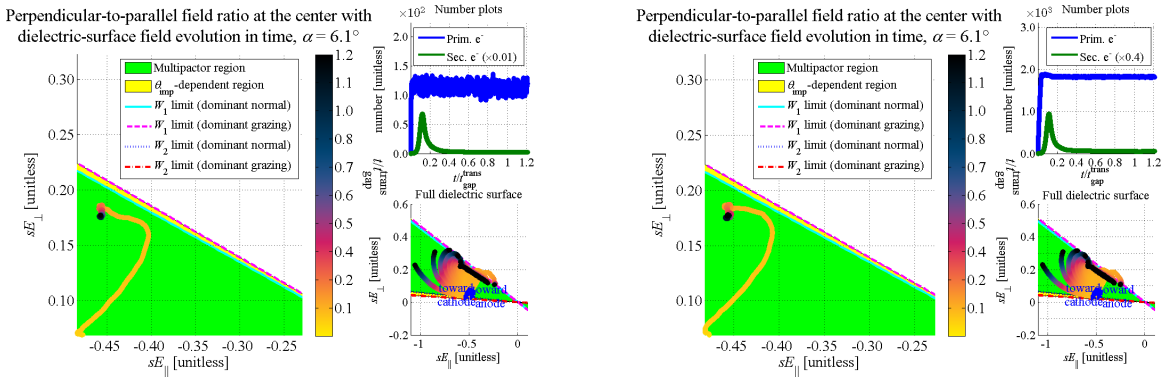


(a) Short emitter length.

(b) Long emitter length.

Figure 6.3: DC Susceptibility diagrams for CW sources over different emitter lengths. This is a cursory illustration of the minimal effect of bulk volume discharge on downstream conditions for multipactor at reduced parameters. (a) is the DC Susceptibility diagram for a CW source over $\sim 28.4\,\text{nm}$. This is the standard length chosen, which is roughly the maximum emitter length before direct arcs start to form. (b) is the DC Susceptibility diagram for a CW source over $\sim 191.7\,\text{nm}$. This is the maximum emitter length possible for this configuration, given the additional limits for geometry discussed in Section 2.2.

under multipactoring conditions at the angles used for all figures in Table 6.2. The primary electron energy distribution function (referred to as the EEDF) is highly localized, while secondaries range from energies near emission to the full potential, shown in the secondary electron energy distribution function (referred to as the SEEDF). Susceptibility characteristics are typical of all discharges dominated by multipactoring surface effects, where downstream fields evolve to support unit emission at impact near first crossover.

Table 6.2: List of pertinent figures from Chapter 3 for discussion in this chapter. Electronic document is actively linked for convenience.

| Figure | Description |
|---|---|
| Figure 3.6 on page 73 | Dielectric surface charge at 6.12° in multipactor breakdown resulting from a discharge seeded by a beam-like source, showing positive charging throughout. |
| Figure 3.7 on page 74 | Dielectric-impact energy distribution functions at 6.12° showing beam-like primary impact and distributed secondary impact. |
| Figure 5.11 on page 150 | Surface susceptibility plot at 6.12° showing the drive from multipactor surface conditions to steady-state surface conditions. |
| Figure 5.12 on page 152 | Surface susceptibility snapshots focusing on the dielectric center for a multipactoring discharge at 6.12°, emphasizing the initial multipactor conditions and illustrating the drive to steady state towards the first-crossover line. |

## 6.3 Extended Constant Waveform Emitter

Extending the constant waveform emitter over a larger emission area has the obvious consequence of distributing the initial-impact region over a *broad* region as in Figure 6.4a, rather than the *localized* initial-impact region of Figure 3.7a. The spread in energy is a result of longer excursion paths of primaries emitted further from the triple point due to the comparatively larger finite beam width than typically used. The minimum cutoff at $\sim 500\,\mathrm{eV}$ is a result of the intentional drift velocity originally used in the previous chapters to ensure maximum gain for the uniform beam profile; the drift velocity was kept in this study to merely reduce parameter variation, but it should be noted that primaries will impact with energies "to the right" of the peak for the secondary emission curve (i.e. Figure 2.9a), which is not a characteristic of the other seed sources. Primaries are therefore accessing secondary emission characteristics greater than unity towards the second crossover side. It should be clear by observation of the results herein that this particular difference does not pose significant concerns to any of the overarching ideas presented on multipactoring breakdown discussed thus far.

The dielectric charge is also broadened as in Figure 6.5, where the peak magnitude near the cathode is expectedly reduced due to charge spreading. The region associated with the "immediate downstream region" discussed in Section 3.D is still present, but shifted further downstream since the characteristic is linked to the behavior of secondaries just off the beam edge. It should be noted that the charge plots in Figure 6.5 are cumulative, with some beam spreading occurring with sufficient secondary density. Positive-charging characteristics further downstream are largely maintained, comparing Figure 6.5a and Figure 3.6. It should be noted that the comparable order of magnitude for the charges is a result of controlling gain and input current, since the input current is four orders of magnitude larger for the reduced parameter set in this chapter, while the number of bounces is reduced by $\sim 2$–$3$. Also note the different time scales between Figure 6.5 and Figure 3.6, with the reduced parameter set incurring a shorter time to anodic current, but similar front speeds of $v_{\mathrm{front}} \sim 6.67 \times 10^6\,\mathrm{m/s}$, since they are dependent on the characteristic speed of the particles, which do not change significantly.

Finally, comparing the susceptibility characteristics of the surface between Figure 5.12 and Figure 6.6, the evolution of the fields remains largely the same for the downstream region, notably past the primary impact region, which is incidentally quite well defined by a definite transition between the clearly uniform downstream field evolution and an upstream region that continues to have evolving field characteristics. The characteristic center plot shows practically identical behavior, from the slight pull in parallel field during the very early transient near around first impact due to upstream electron growth, to the pull of field angles towards the unit-emission region near first crossover during the transient multipactor phase, and finally saturating at similar normalized field values $sE_\perp/sE_\parallel \sim 0.18/(-0.45)$ at similar normalized time $t/t_{\mathrm{gap}}^{\mathrm{trans}} \sim 1.2$.

## 6.4 Fowler-Nordheim Effects

The Fowler-Nordheim source described in Section 2.5.2 provides a self-consistent seed influenced by the local potentials. Typically, to produce comparable current densities as

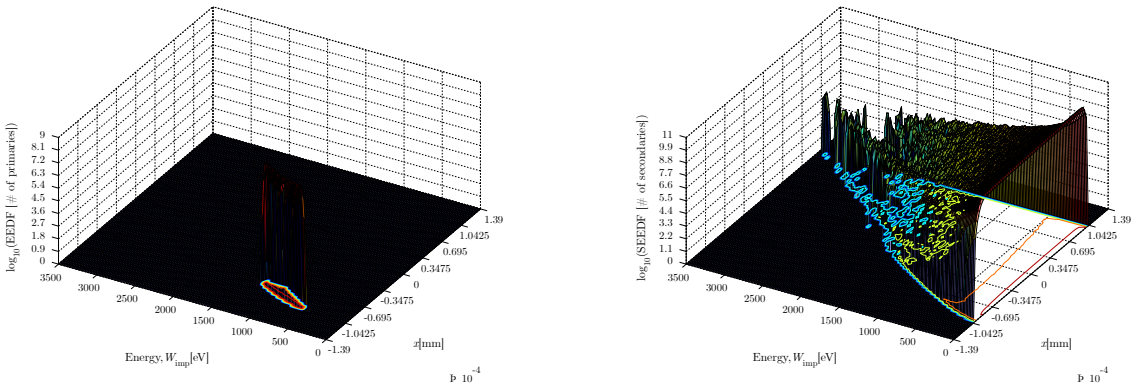


(a) Primary-electron EDF. (b) Secondary-electron EDF.

Figure 6.4: Broadened CW source electron energy distribution functions (EEDFs) on the dielectric surface for 6.12°. To be compared directly to Figure 3.7 for the narrow-beam seed source.

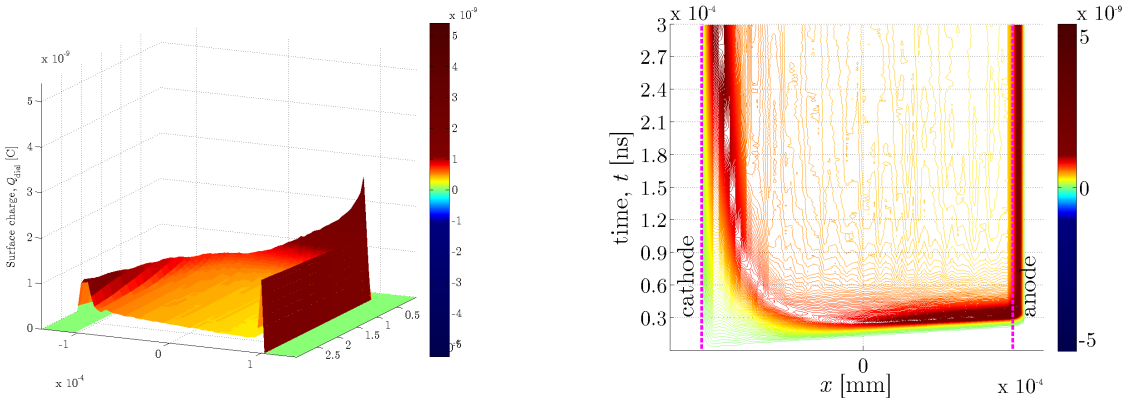


(a) Dielectric-charge full profile. (b) Dielectric charge contour in $x$ against $t$.

Figure 6.5: Broadened CW source characteristic dielectric-surface charging for a multipactoring discharge at 6.12°. To be compared directly to Figure 3.6. Similar positive charging is shown over a large region of the dielectric since surface characteristics are sufficient for multiplicative breakdown.

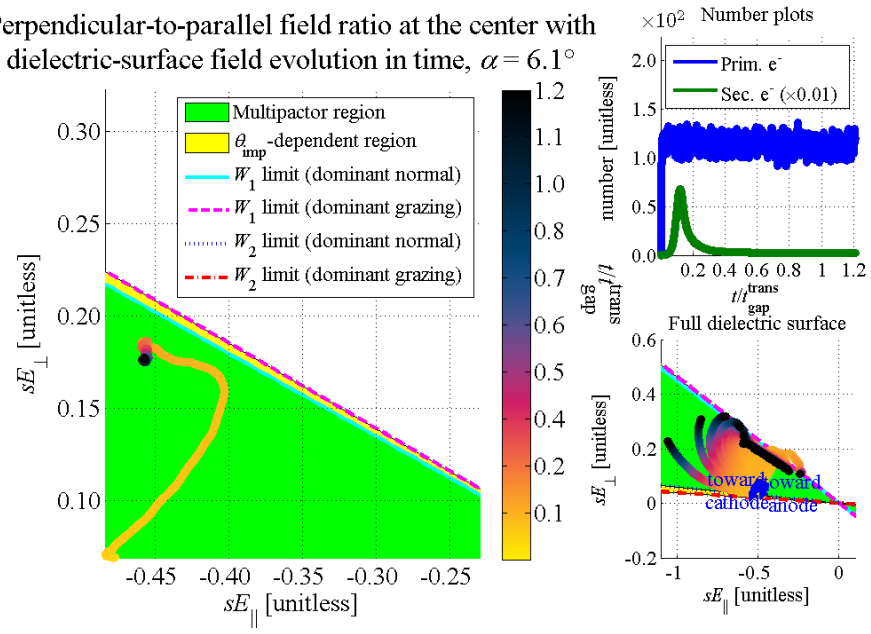


Figure 6.6: Full DC Susceptibility diagram for CW source over $\sim 28.4\,\text{nm}$.

the CW source of Section 6.3, a large enhancement factor would be required with the original parameter set ($\sim 8000$), basically modeling rough surfaces along the emitter length that concentrates fields at the tips of micro-protrusions. The reduced parameters in the configuration for this chapter produce sufficiently large fields at $\sim 17.5\,\text{GV/m}$, compared to the previous parameter set at $\sim 1.75\,\text{MV/m}$, such that the enhancement factor for reduced parameters can be modest (in this case, $\beta_{\text{FN}} \sim 0.80$) to produce comparable current at applied voltage of $3.5\,\text{kV}$ across the $0.20\,\mu\text{m}$ gap. In this case, a field enhancement less than unity would be "better" than smooth, and it would be prudent to note that this value is used for simulation purposes, and not as representative of real materials.

The primary impact characteristics show stark differences, comparing the FN EEDF in Figure 6.7a with the broad CW EEDF in Figure 6.4a. The larger spread in the FN EEDF is a result of implementation differences of the seeds, where current density calculations in the FN source are calculated in-situ with a Maxwellian distribution of emitted primaries impacting with energy proportional to the potential experienced during excursion and no drift velocity at injection; alternatively, the CW source is an unperturbed beam with uniform drift velocity to ensure impact with minimum energy near maximum emission ($\sim 500\,\text{eV}$), as discussed above). The primary EEDF for the FN source covers the entire gap width, which is a consequence of geometry and the aforementioned emission characteristics. As alluded to above, the primary EEDF also covers energies lower than the minimum cutoff enforced in the CW source, which means the primaries have access to the secondary-emission curve "to the left" of the peak. Again, while this characteristic may seem an interesting difference, it does not add significantly to the evolution of the discharge, particularly on the drive to steady state most easily communicated with the DC susceptibility diagram discussed below.

Differences in the impact profile manifest geometrically in the dielectric charge profile, most notably in the contour plot of Figure 6.8b, where there is a clear push away

from the cathode through much of the discharge time compared to the broad CW profile in Figure 6.5b, even past the fast transient ($\sim t_{\text{gap}}^{\text{trans}} = 0.2$ or $t \sim 0.3 \times 10^{-4}$ ns). This characteristic is associated with the broad distribution of the FN seed, where the impact profile leads to generally reduced positive charging compared to the CW source (recalling enforced impact near maximum emission for CW, i.e. maximum positive charging from secondary emission). Differences in the impact profile do not manifest clearly in peak magnitude of the charge (c.f. Figure 6.8a and Figure 6.5a). The uniformity between peak magnitudes suggests that both discharges are experiencing similar growth characteristics, i.e. a nontrivial population of primaries from the FN source seed a fully cascaded multipactor with similar gain characteristics as the broad CW source. Note that the maximum magnitude of the charge plots are maintained at similar values for ease of comparison.

The sensitivity of the FN source to local potentials can be seen in the number plots for primaries in Figure 6.9. The primary population is steadily growing due to changing field conditions near the cathode. Although not shown in this particular configuration, it should be noted that upstream variations near the impact region can lead to seemingly anomalous current gain compared to initial injection, occurring due to the response of the seed to changing near-cathode fields that can increase/decrease the current from initial conditions; the increased current can "ride" steady-state conditions over the remainder of the surface and appear as a steady-state current greater than initial input. This behavior is a particular consequence of seeds influenced by local potentials, but will not be explored further as they do not influence the standard characteristics of discharge evolution, but should be noted as a possible contributor to gain, particularly at steady-state.

Finally, saturation characteristics evolve into similar steady-state conditions, $sE_{\perp}/sE_{\parallel} \sim 0.18/(-0.45)$ at similar normalized time $t_{\text{gap}}^{\text{trans}} \sim 1.2$, shown in the characteristic center DC susceptibility diagram of Figure 6.9. The early transient shows some variation at the characteristic center point (and at points further downstream), where the broad CW source approaches $sE_{\parallel} \sim -0.40$ towards the end of the fast transient time $t_{\text{gap}}^{\text{trans}} \sim 0.2$ in response to the dominant, growing multipactor front (c.f. Figure 6.6. The FN source does not experience the pull to $sE_{\parallel} \sim -0.40$ since the upstream electron population is comparatively larger than the broad CW seed case by way of initial emitter configuration. Despite this, field evolution going into steady-state and in response to the overall multipactor gain remains similar to the broad CW source of Figure 6.9, as well as the initial beam-like CW source of Figure 5.12.

## 6.5 Schächter Source Effects

The Schächter source is the final configuration to be studied herein, representing a base case limit for what would be expected with a source that is driven solely by the conditions of the triple point. It should be noted that variations by the near-cathode charge state are not currently included in the model, but the capability can be extended, and similar variations to that shown in the FN model should be expected, including the possibility of steady-state current greater than initial input, possible quenching dependent on charge state, and a similar characteristic push to steady-state conditions.

Again, the reduced parameter set allows for modest voltage of $\sim 4.77$ kV, translating to initial fields of $\sim 23.9$ GV/m to produce a current of 10 kA comparable to the broad

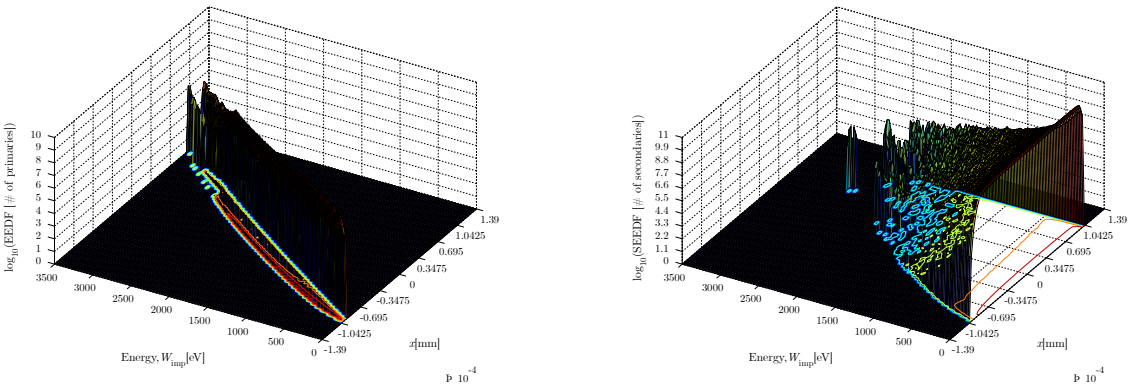


(a) Primary-electron EDF. (b) Secondary-electron EDF.

Figure 6.7: FN source electron energy distribution functions (EEDFs) on the dielectric surface for 6.12°. To be compared directly to Figure 3.7 and Figure 6.4 for the CW seed source.

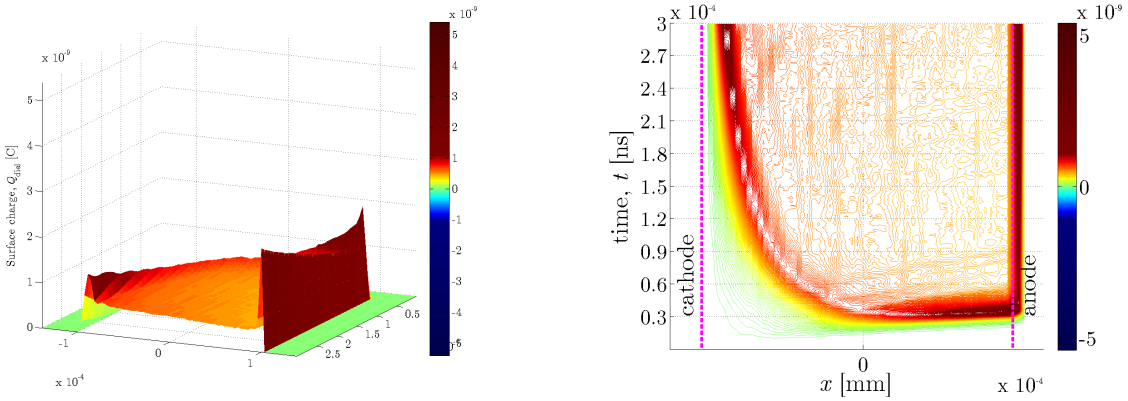


(a) Dielectric-charge full profile. (b) Dielectric charge contour in $x$ against $t$.

Figure 6.8: FN source characteristic dielectric-surface charging for a multipactoring discharge at 6.12°. To be compared directly to Figure 3.6 and Figure 6.5. Positive charging remains, and accumulates to much larger magnitude as a result of seed variations from local potentials.

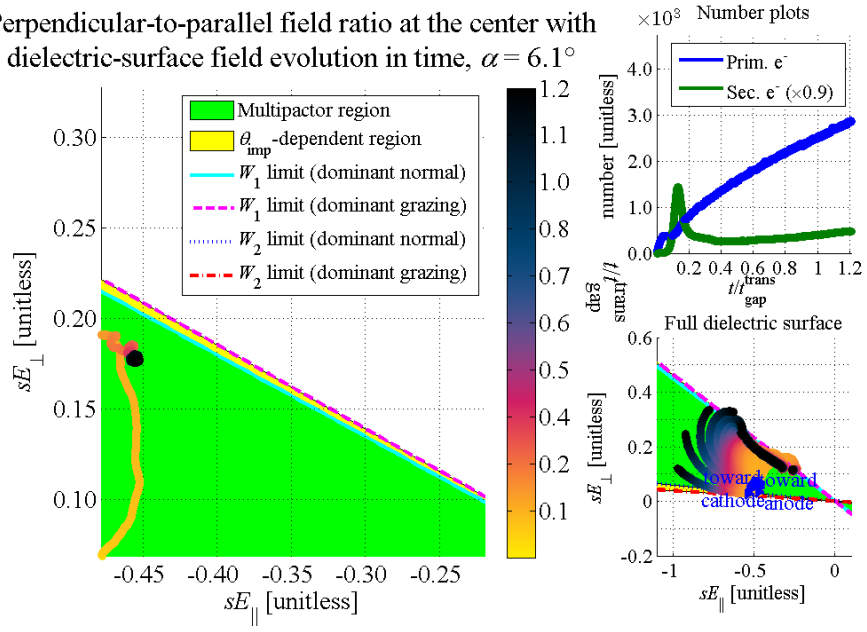


Figure 6.9: Full DC Susceptibility diagram for FN source over $\sim 28.4\,\mathrm{nm}$.

CW seed. This should be noted in contrast to the FN fields contributing to an effective field of $\beta_{\mathrm{FN}}E \sim 14\,\mathrm{GV/m}$. In principle, the larger voltage (which is a general condition, and would be much larger at the original parameters of previous chapters) means that secondaries can have access to more energy on average. Access to regions in the secondary-emission curves with $\delta > 1$, i.e. Figure 2.9, is consequently expanded for the primaries in a similar way to the FN source, compared to all CW configurations studied herein.

Similar to the FN source, the primaries are emitted as a Maxwellian distribution with no drift velocity; consequently, some primaries gain the full potential difference as they traverse the full gap length. The primary EDFs on the dielectric for the Schächter source, Figure 6.10a, show similar characteristics to the FN source, Figure 6.7a, while the secondaries for Schächter, (Figure 6.10b, show a broadened distribution consistent with increased access to energy for the secondaries. Again, the broadened secondary EDF will fill in the secondary-emission curve characteristics similar to gaseous discharges with the original CW beam, e.g. of Figure 3.8, but resulting from the broadened energy accessibility by voltage rather than through ionization in the bulk (and subsequent variability in particle lifetime).

Finally, susceptibility characteristics are very similar to the evolution of the FN discharge, although the primary number reaches a steady-state saturation since the source is not currently modeled to account for near-cathode field variations. In any case, the susceptibility diagram for the characteristic center point of the dielectric shows similar evolution to the FN source, where the pull to $sE_{\|} \sim -0.40$ does not occur as it does in the broad CW case. The steady-state evolution, again, goes to similar ratios as the other seed sources ($sE_{\perp}/sE_{\|} \sim 0.18/(-0.45)$) at similar normalized time, indicating downstream conditions are essentially the same, and illustrating the general applicability of the susceptibility construct through any particular seed variant.

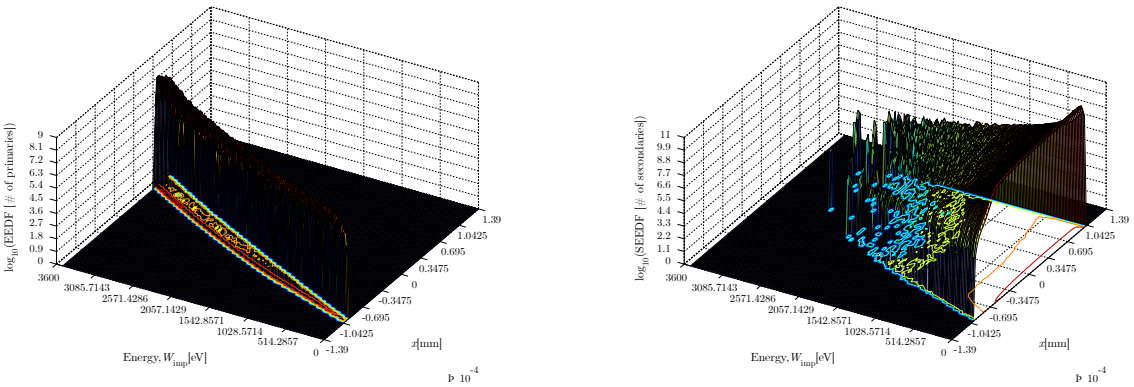


(a) Primary-electron EDF. (b) Secondary-electron EDF.

Figure 6.10: Schächter source electron energy distribution functions (EEDFs) on the dielectric surface for 6.12°. To be compared directly to Figure 3.6 and Figure 6.5.

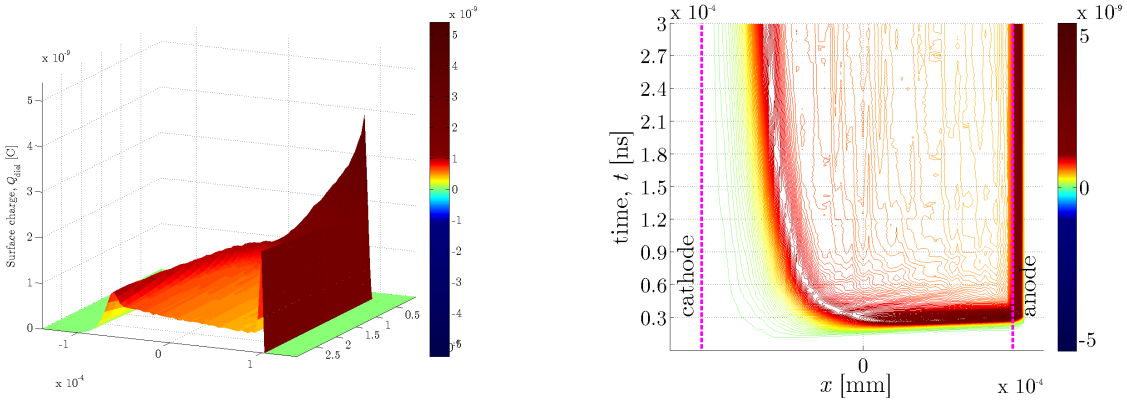


(a) Dielectric-charge full profile. (b) Dielectric charge contour in $x$ against $t$.

Figure 6.11: Schächter source characteristic dielectric-surface charging for a multipactoring discharge at 6.12°. To be compared directly to Figure 3.7 and Figure 6.4 for the CW seed source.

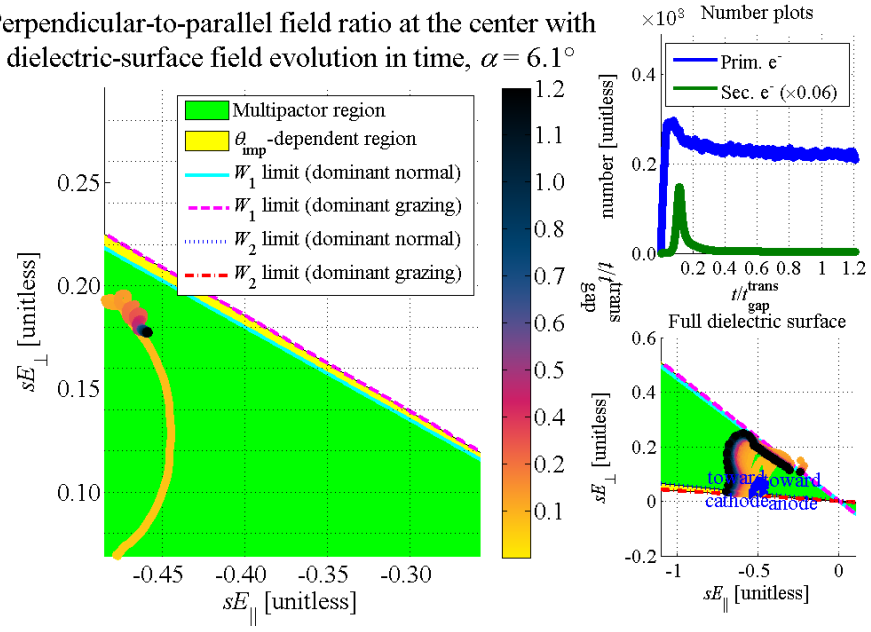


Figure 6.12: Full DC Susceptibility diagram for Schächter source over $\sim 28.4\,\text{nm}$.

## 6.6 Chapter 6 Conclusions

The configuration studied in this chapter is essentially a region in parameter space where the operating characteristics are, again, dominated by the growth characteristics dominated by surface effects, and while there may be upstream variations which present themselves in the upstream field characteristics in all diagnostics and in the susceptibility plot, the characteristics of secondary growth remain the same further downstream, even in the presence of seeds that otherwise impact the whole dielectric surface. As long as some primaries impact nearest the cathode to seed a fully cascaded multipactor avalanche, the typical multipactor discharge will occur. This fully seeded discharge is most easily described with the DC susceptibility diagrams, where the fully cascaded discharge is emphasized since the exponential gain means such a cascade will dominate. The upstream region nearest the cathode can be expected to undergo variations in behavior in some cases that leads to anodic output current greater than input at steady state, with none of the growth occurring in the field-saturated downstream region, e.g. steady-state initial growth from seeds affected by local potentials (e.g. FN and a Schächter model implemented with local charge buildup).

The most difficult aspect of modeling seed problems of the type discussed herein is the broad parameter space encompassing input current, emitter length, applied voltage, gain characteristics (secondary emission characteristics), dielectric angle, and gap width. As shown, there is minimal variation in the aggregate of the discharge for all cases studied, despite variations in primary characteristics. The delineation of breakdown evolution for this chapter should also be taken as further clarification on the validity of assuming linearity away from the surface for the configurations of the previous chapters. It was noted in previous configurations that there it is very difficult to spatially resolve the electron distribution of short-lived secondaries, and arguments were put forward in

Sections 3.3.1 and 3.3.2 to justify the relatively limited resolution. The increased resolution in this chapter provides fundamentally similar characteristics in vacuum discharges, where resolution concerns are further relieved when pressure is increased due additional space-charge shielding elongating electron lifetimes and trajectories. The stark similarity amongst all susceptibility curves for discharges dominated by surface effects justifies both the assumptions on numerical accuracy and the validity of the susceptibility framework.

Again, this document has stressed that multiplicative characteristics of a system are largely dependent on field conditions near the dielectric surface for discharges that are not otherwise dominated by Townsend-like volume effects, as demonstrated in Chapter 3. While typical diagnostics show some noteworthy variation, the evolution of the discharge is most easily understood through the DC susceptibility construct, where downstream conditions control growth characteristics, relegating upstream conditions to necessary but insufficient conditions for multipactor growth. This chapter therefore serves to further buttress the auxiliary role of the seed source in all cases.

While the parameter space for seed-configuration studies is prohibitively large, the cases presented herein are sufficient to provide a broad understanding of what to expect from a variant seed source, particularly when coupled with the developments of the previous chapters. The case of Schächter coupled with the understanding of the FN source evolution should serve as a sound foundation to expand on such similar variations.

# Chapter 7

# Conclusions and Future Work

To recapitulate, the intent of this study is to understand the evolution of DC discharges loaded with angled dielectrics subject to space charge effects that are particularly difficult to model *a-priori*. Single-surface multipactor was targeted as the most fundamental multiplicative effect. PIC is uniquely suited to modeling problems of this type since the PIC framework includes space charge and surface charge in the treatment of charge density for the field solve. Extensive work was done to model single-surface multipactor, minimizing errors in modeling the multipactoring surface, correcting existing emission models to better fit experimental data for dielectrics, correction of existing code to accurately model particle distribution, addition of various models to extend the application of the XOOPIC code, and development of a novel framework for understanding the evolution of discharges with appreciable surface effects that extends into low pressures where volume growth is comparable.

The most fundamental conclusion to draw from this study is that breakdown conditions dominated by surface effects are driven solely by the *surface field angle* (not field magnitude) from a physics perspective. This "physics perspective" must be explicitly stressed, as this result is largely in contrast to prior works characterizing fundamental breakdown [20] as a result of engineered systems having more contributions beyond fundamental order. Attributing initial surface field angle conditions to the fundamental breakdown contribution is an important result as it allows design of engineering processes that can eliminate (or enhance) growth by manipulating conditions at the onset and allow for reduction of the parameter set to monitor for further growth (i.e. previous parameters that might have been driven by surface growth need no longer be considered). Additionally, this fundamental physics perspective effectively reveals that there should be no breakdown curve from discharges dominated by surface-effects, which is, again, in contrast to previous works. This conclusion is most relevant to discharges in background pressures from vacuum through "ultra-low pressure" (VULP) of less than a few hundred mTorr, where surface effects dominate volume collisional effects. Various influences on VULP discharges were examined, including the effect of scattered and reflected primaries and the effect of electron and ion collisions with background gas. Electron collisions in VULP can lead to underdamped oscillations as space charge couples with surface charge, causing slight restoration of otherwise saturated fields into multiplicative conditions. Ion collisions add frictional effects that enhances the underdamping, hastening steady-state conditions; typical decay characteristics are enhanced by a factor of two for oscillatory

envelope functions. Despite any additional effects in VULP, the driving factor in discharge evolution is the field angle condition, eventually driving to saturation that supports unit multipactor growth on the surface.

Single-surface multipactor effects are still appreciable through low pressure ($\sim 1$ Torr), and coupling of surface charge with space charge causes oscillations in discharge metrics (e.g. particle population, surface and volume charge in time, anodic current, etc.). Volume growth is seeded by surface growth, and, again, the field-angle plays a major role even at low pressure since the onset of surface growth past early vacuum-like discharge behavior is dictated by the movement of volume charges. Wave characteristics based on ion momentum define oscillatory effects that drive periods of growth and decay in the volume, with periodicity on the order of the ion plasma frequency. Oscillation time scales are correlated to the ion plasma frequency, since the momentum of heavy ions is the driving factor in field evolution past the saturation of the electron population. Saturation of electrons prior to ion momentum is driven by near-surface field conditions evolving to support unit growth in multipactor in the same way that they evolve in VULP discharges, with variations in growth characteristics due to space charge. Oscillations may occur in discharges that are otherwise not multiplicative, e.g. with a dielectric angle at 22.9° with respect to the electrode normal, resulting from ionization over longer time scales that alters surface characteristics that are simply not accessible in vacuum-like discharges. Diffusive outgassing adds a hybrid characteristic to discharge evolution, where modest outgassing flux is insufficient to significantly alter the fast transient of vacuum-like discharges until sufficient gas species has been desorbed into the volume. Alternatively, large gas densities can be outgassed proportionate to the number of electron impacts, leading to peaked density accumulation near the anode. Modest seed conditions would cascade to the anode via multipactor, and impact-dependent outgassing causing non-uniform neutral gas densities peaked near the anode would instigate large ionization rates near the anode. Additional effects remain to be studied, but this work has laid the foundational elements for diffusive outgassing within the XOOPIC code base, and should be extended for kinetic applications with particle-particle collisions. While oxygen cross-sections have also been ported over from other PTSG codes, kinetic collisions have not been implemented, which would allow simulation of, e.g. oxygen recombination, which is known to alter discharge characteristics in certain geometries [22, 24].

Couple the perspective of initial conditions noted above with assumptions of particle characteristics grounds previous work in breakdown susceptibility [1, 10, 11] to the fundamental treatment of secondary emission, allowing *a-priori* metrics on breakdown conditions in DC. The development of DC breakdown susceptibility theory is an important step in understanding discharge evolution even up to low pressures, since breakdown onset can be explicitly tied to the near-surface fields tracked by the susceptibility theory. Breakdown susceptibility provides a practical tool to both track the evolution of a discharge and identify desirable operating regimes based purely on near-surface phenomena and secondary-emission theory using ensemble distribution characteristics at emission. It must be stressed that breakdown susceptibility successfully uses *emission* distribution characteristics to map the distribution evolution (which are generally a function of the material), as opposed to average in-volume distribution characteristics, which are not generally Maxwellian and relatively difficult to predict *a-priori* in practical settings. Under

limiting conditions of collisionality on typical particle lifetimes, DC susceptibility can be applied to cases of low pressure, where limit lines are simply shifted along $E_\perp$ in the $E_\perp/E_\parallel$ plane, i.e. "up" or "down" in the field-ratio plane.

Finally, the seed current plays a necessary but insufficient role in typical discharge evolution. The nature of the seed current does not change the characteristics of breakdown susceptibility with respect to the aforementioned dependence of discharge characteristics on *field angle*. The necessity to push out to higher applied voltage in the case of fundamental Schächter treatment serves to alter the volume characteristics of particles with sufficient lifetime to be exposed to the larger voltages. This is further evidenced by the initial push to steady-state with the self-consistent FN source, where the discharge behaves in typical fashion through the fast transient, while the saturated steady-state carries upstream perturbations to the anode. These upstream perturbations do not propagate and are the result of local charge variations near the triple point.

# Bibliography


[1] R. A. Kishek and Y. Y. Lau, "Multipactor discharge on a dielectric," *Phys. Rev. Lett.*, vol. 80, no. 1, pp. 193–196, 1998. [Online]. Available: http://link.aps.org/doi/10.1103/PhysRevLett.80.193.

[2] J. R. M. Vaughan, "A new formula for secondary emission yield," *IEEE Trans. Electron Devices*, vol. 36, no. 9, pp. 1963–1967, 1989. [Online]. Available: http://ieeexplore.ieee.org/lpdocs/epic03/wrapper.htm?arnumber=34278.

[3] R. Vaughan, "Secondary emission formulas," *IEEE Trans. Electron Devices*, vol. 40, no. 4, p. 830, 1993. [Online]. Available: http://ieeexplore.ieee.org/xpls/abs{_}all.jsp?arnumber=202798.

[4] L. Schachter, "Analytic expression for triple-point electron emission from an ideal edge," *Appl. Phys. Lett.*, vol. 72, no. 4, pp. 421–423, 1998. [Online]. Available: http://ieeexplore.ieee.org/xpls/abs{_}all.jsp?arnumber=4898552.

[5] C. K. Birdsall and A. B. Langdon, *Plasma Physics via Computer Simulation*. Adam Hilger, 1991, ISBN: 0070053715.

[6] C. Birdsall, "Particle-in-cell charged-particle simulations, plus Monte Carlo collisions with neutral atoms, PIC-MCC," *IEEE Trans. Plasma Sci.*, vol. 19, no. 2, pp. 65–85, 1991. [Online]. Available: http://ieeexplore.ieee.org/lpdocs/epic03/wrapper.htm?arnumber=106800http://ieeexplore.ieee.org/xpls/abs{_}all.jsp?arnumber=106800.

[7] J. Verboncoeur, A. Langdon, and N. Gladd, "An object-oriented electromagnetic PIC code," *Comput. Phys. Commun.*, vol. 87, no. 1-2, pp. 199–211, 1995. [Online]. Available: http://www.sciencedirect.com/science/article/pii/001046559400173Y.

[8] G. Blaise, A. J. Durand, C. le Gressus, B. G. A. Jüttner, R. Latham, A. Maitland, B. Mazurek, H. C. Miller, H. Padamsee, M. F. Rose, A. M. Shroff, and N. Xu, *High Voltage Vacuum Insulation*, R. Latham, Ed. 1995, pp. 1–597, ISBN: 0124371752.

[9] R. J. Barker and E. Schamiloglu, Eds., *High-Power Microwave Sources and Technologies*. New York: IEEE Press, 2001, pp. 1–511, ISBN: 0780360060.

[10] R. A. Kishek and Y. Y. Lau, "Multipactor discharge on a dielectric," in *Proc. 1997 Part. Accel. Conf.*, vol. 3, 1997, pp. 3198–3200, ISBN: 078034376X. [Online]. Available: http://link.aps.org/doi/10.1103/PhysRevLett.80.193.

[11] R. Kishek, Y. Lau, L. Ang, A Valfells, and R. Gilgenbach, "Multipactor discharge on metals and dielectrics: Historical review and recent theories," *Phys. Plasmas*, vol. 5, no. 5, pp. 2120–2126, 1998. [Online]. Available: http://link.aip.org/link/?php/5/2120/1.

[12] N. M. Jordan, Y. Y. Lau, D. M. French, R. M. Gilgenbach, and P. Pengvanich, "Electric field and electron orbits near a triple point," *J. Appl. Phys.*, vol. 102, no. 3, p. 033 301, 2007, ISSN: 00218979. DOI: 10.1063/1.2764211. [Online]. Available: http://link.aip.org/link/JAPIAU/v102/i3/p033301/s1{\&}Agg=doi.

[13] A. Neuber, M. Butcher, L. Hatfield, and H. Krompholz, "Electric current in dc surface flashover in vacuum," *J. Appl. Phys.*, vol. 85, no. 6, pp. 3084–3091, 1999, ISSN: 00218979. DOI: 10.1063/1.369647. [Online]. Available: http://ieeexplore.ieee.org/xpls/abs{_}all.jsp?arnumber=5022966.

[14] J Foster, S Beeson, M Thomas, J Krile, H Krompholz, and A Neuber, "Rapid formation of dielectric surface flashover due to pulsed high power microwave excitation," *IEEE Trans. Dielectr. Electr. Insul.*, vol. 18, no. 4, pp. 964–970, 2011, ISSN: 1070-9878. DOI: 10.1109/TDEI.2011.5976082.

[15] S. R. Beeson, P. J. Ford, J. Foster, H. G. Krompholz, and A. a. Neuber, "Imaging of Pressure-Dependent High-Power Microwave Surface Flashover," *IEEE Trans. Plasma Sci.*, vol. 39, no. 11, pp. 2600–2601, 2011, ISSN: 0093-3813. DOI: 10.1109/TPS.2011.2149546.

[16] J. T. Krile, A. A. Neuber, H. G. Krompholz, and T. L. Gibson, "Monte Carlo simulation of high power microwave window breakdown at atmospheric conditions," *Appl. Phys. Lett.*, vol. 89, no. 20, p. 201 501, 2006, ISSN: 00036951. DOI: 10.1063/1.2388877. [Online]. Available: http://link.aip.org/link/?APL/89/201501/1http://link.aip.org/link/APPLAB/v89/i20/p201501/s1{\&}Agg=doi.

[17] P. P. J. Ford, S. S. R. Beeson, H. G. H. Krompholz, and A. A. Neuber, "A finite-difference time-domain simulation of high power microwave generated plasma at atmospheric pressures," *Phys. Plasmas*, vol. 19, no. 7, p. 73 503, 2012. DOI: 10.1063/1.4736863. [Online]. Available: http://link.aip.org/link/?PHP/19/073503/1http://link.aip.org/link/?PHPAEN/19/073503/1.

[18] F. W. Strong, J. L. Skinner, A. A. Talin, P. M. Dentinger, and N. C. Tien, "Electrical Breakdown Response for Multiple-Gap MEMS Structures," in *2006 IEEE Int. Reliab. Phys. Symp. Proc.*, 2006, pp. 421–426, ISBN: 0780394984.

[19] F. W. Strong, J. L. Skinner, P. M. Dentinger, and N. C. Tien, "Electrical Breakdown across Micron Scale Gaps in MEMS Structures," *Proc. SPIE*, vol. 6111, D. M. Tanner and R. Ramesham, Eds., 2006. DOI: 10.1117/12.646508. [Online]. Available: http://proceedings.spiedigitallibrary.org/proceeding.aspx?articleid=1320981.

[20] K. Bergeron, "Theory of the secondary electron avalanche at electrically stressed insulator-vacuum interfaces," *J. Appl. Phys.*, vol. 48, no. 7, pp. 3073–3080, 1977. [Online]. Available: http://ieeexplore.ieee.org/xpls/abs{_}all.jsp?arnumber=5103902.

[21] S. Taverniers and J. P. Verboncoeur, "2D particle-in-cell modeling of dielectric insulator breakdown," Tech. Rep., 2009, p. 29.

[22] J Krile, A Neuber, J Dickens, and H Krompholz, "Imaging of dielectric surface flashover in atmospheric conditions," *Plasma Sci. IEEE ...*, vol. 33, no. 2, pp. 270–271, 2005. [Online]. Available: http://ieeexplore.ieee.org/xpls/abs{_}all.jsp?arnumber=1420431.

[23] M. T. P. Aldan and J. P. Verboncoeur, "Simulations of Multipactor Breakdown in Low-pressure Background Gas for Angled Dielectrics in DC," *IEEE Trans. Dielectr. Electr. Insul.*, vol. 20, no. 4, pp. 1209–1217, 2013.

[24] A. A. Neuber, M Butcher, H Krompholz, L. L. Hatfield, and M Kristiansen, "The Role of Outgassing in Surface Flashover Under Vacuum," *IEEE Trans. Plasma Sci.*, vol. 28, no. 5, pp. 1593–1598, 2000. [Online]. Available: http://ieeexplore.ieee.org/xpls/abs{_}all.jsp?arnumber=901239.

[25] Y. Lau, Y Liu, and R. Parker, "Electron emission: From the Fowler-Nordheim relation to the Child-Langmuir law," *Phys. Plasmas*, vol. 1, no. 6, pp. 2082–2085, 1994. [Online]. Available: http://ieeexplore.ieee.org/lpdocs/epic03/wrapper.htm?arnumber=588693http://link.aip.org/link/?PHPAEN/1/2082/1.

[26] A Neuber, J. Dickens, D. Hemmert, H. Krompholz, L. Hatfield, and M. Kristiansen, "Window breakdown caused by high-power microwaves," *IEEE Trans. Plasma Sci.*, vol. 26, no. 3, pp. 296–303, 1998. [Online]. Available: http://ieeexplore.ieee.org/xpls/abs{_}all.jsp?arnumber=700757.

[27] J. G. Leopold, U Dai, Y Finkelstein, E Weissman, and S Humprhies, "Optimizing the performance of flat-surface, high-gradient vacuum insulators," *IEEE Trans. Dielectr. Electr. Insul.*, vol. 12, no. 3, pp. 530–536, 2005. [Online]. Available: http://ieeexplore.ieee.org/xpls/abs{_}all.jsp?arnumber=1453458.

[28] J. G. Leopold, R. Gad, E. Hillel, C. Leibovitz, M. Markovits, and I. Navon, "Applying a different approach to pulsed high-voltage insulation," in *2010 IEEE Int. Power Modul. High Volt. Conf.*, Dept. of Applied Physics, Rafael Laboratories, POBox 2250, Haifa 31021, Israel, Ieee, 2010, pp. 449–452.

[29] J. Z. Gleizer, Y. E. Krasik, U. Dai, and J. Leopold, "Vacuum Surface Flashover: Experiments and Simulations," *IEEE Trans. Dielectr. Electr. Insul.*, vol. 21, 2014.

[30] J. Verboncoeur, M. Alves, V. Vahedi, and C. Birdsall, "Simulataneous Potential and Circuit Solution for 1D Bounded Plasma Particle Simulation Codes," *J. Comput. Phys.*, vol. 104, pp. 321–328, 1993. [Online]. Available: http://ptsg.berkeley.edu/publications/Verboncoeur1993JCP.pdf.

[31] H. Kim, J. Verboncoeur, and Y. Lau, "Invited Paper-Modeling RF Window Breakdown: from Vacuum Multipactor to RF Plasma," *IEEE Trans. Dielectr. Electr. Insul.*, vol. 14, no. 4, pp. 766–773, 2007. [Online]. Available: http://ieeexplore.ieee.org/xpls/abs{_}all.jsp?arnumber=4286505.

[32] R. E. Peterkin and J. W. Luginsland, "A Virtual Prototyping Environment for Directed-Energy Concepts," *Comput. Sci. Eng.*, pp. 42–49, 2002.

[33] G. F. Knoll, *Radiation Detection and Measurement*, 3rd. New York, NY: John Wiley & Sons, Inc., 2000, p. 802, ISBN: 0-471-07338-5.

[34] M. A. Lieberman and A. J. Lichtenberg, *Principles of Plasma Discharges and Materials Processing*. Hoboken, NJ: John Wiley & Sons, Inc., 2005, p. 757, ISBN: 9786468600.

[35] G Ni, B Gao, and J Lu, "Research on high power microwave weapons," in *Asia-Pacific Microw. Conf. Proceedings, APMC 2005*, vol. 2, 2005, p. 4, ISBN: 078039433X. [Online]. Available: http://ieeexplore.ieee.org/xpls/abs{_}all.jsp?arnumber=1606492.

[36] S. Nam and J. Verboncoeur, "Theory of Filamentary Plasma Array Formation in Microwave Breakdown at Near-Atmospheric Pressure," *Phys. Rev. Lett.*, vol. 103, no. 5, p. 055 004, 2009, ISSN: 0031-9007. DOI: 10.1103/PhysRevLett.103.055004. [Online]. Available: http://link.aps.org/doi/10.1103/PhysRevLett.103.055004.

[37] Y. Hidaka, E. M. Choi, I. Mastovsky, M. a. Shapiro, J. R. Sirigiri, and R. J. Temkin, "Observation of large arrays of plasma filaments in air breakdown by 1.5-MW 110-GHz gyrotron pulses," *Phys. Rev. Lett.*, vol. 100, no. January, pp. 3–6, 2008, ISSN: 00319007. DOI: 10.1103/PhysRevLett.100.035003.

[38] J. Benford, J. A. Swegle, and E. Schamiloglu, *High Power Microwaves*, 2nd. New York: Taylor & Francis, 2007, pp. 1–534, ISBN: 9780750307062.

[39] G. A. Loew and J. W. Wang, "Field emission and rf breakdown in copper linac structures," in *XIV Int. Conf. High Energy Accel.*, 1989, p. 6. [Online]. Available: http://www.osti.gov/energycitations/product.biblio.jsp?osti{_}id=5861003.

[40] J. W. Wang and G. A. Loew, "Field Emission and RF Breakdown in High-Gradient Room-Temperature Linac Structures," *Slac-Pub*, vol. 7684, no. October, 1997. [Online]. Available: c:$\backslash$DocumentsandSettings$\backslash$Daniel$\backslash$MyDocuments$\backslash$Bibliographie$\backslash$1997$\backslash$SLACPUB7684.pdf.

[41] M. M. J. Kushner, "Modeling of Surface Flashover on Spacecraft," Tech. Rep. December, 1991, p. 47. [Online]. Available: http://scholar.google.com/scholar?hl=en{\&}btnG=Search{\&}q=intitle:Modeling+of+surface+flashover+on+spacecraft{\#}2.

[42] J. P. Brainard and L. A. Andrews, "Dielectric Stimulated Arcs in Lightning-Arrestor Connectors," *Components, Hybrids, Manuf. Technol. IEEE Trans.*, vol. CHMT-2, no. 3, pp. 309–316, 1979, ISSN: 0148-6411. DOI: 10.1109/TCHMT.1979.1135464.

[43] M. Caldwell and L. E. Martinez, "The Sandia Lightning Simulator," Tech. Rep., 1996, pp. 3–6. [Online]. Available: http://www.sandia.gov/electromagnetics/New{_}Reports/reports/CaldwellEMC05.pdf.

[44] T. J. Dolan, *Fusion Research: Principles, Experiments, and Technology*. Pergamon Press, 2000, ISBN: 0-06-025565-5.

[45] J. P. Verboncoeur, "Particle simulation of plasmas: review and advances," *Plasma Phys. Control. Fusion*, vol. 47, no. 5A, A231–A260, 2005, ISSN: 0741-3335. DOI: 10.1088/0741-3335/47/5A/017. [Online]. Available: http://stacks.iop.org/0741-3335/47/i=5A/a=017?key=crossref.c855d4d27c6daaf363c1c23c98f94d28.

[46] V. Vahedi and M. Surendra, "A Monte Carlo collision model for the particle-in-cell method: applications to argon and oxygen discharges," *Comput. Phys. Commun.*, vol. 87, no. 1-2, pp. 179–198, 1995, ISSN: 00104655. DOI: 10.1016/0010-4655(94)00171-W.

[47] R. Leveque, *Finite Difference Methods for Ordinary and Partial Differential Equations: Steady-State and Time-Dependent Problems*. Philadelphia: SIAM, 2007, pp. 181–183.

[48] S. Doss, "Dynamic ADI Methods for Elliptic Equations with Gradient Dependent Coefficients," PhD thesis, 1977, pp. 1–128.

[49] S. Doss and K. Miller, "Dynamic ADI Methods for Elliptic Equations," *SIAM J. Numer. Anal.*, vol. 16, no. 5, pp. 837–856, 1979.

[50] H Kim, Y Feng, and J Verboncoeur, "Algorithms for accurate collection, ejection, and loading in particle simulations," *J. Comput. Phys.*, vol. 223, no. 2, pp. 629–642, 2007, ISSN: 00219991. DOI: 10.1016/j.jcp.2006.09.026. [Online]. Available: http://linkinghub.elsevier.com/retrieve/pii/S0021999106004657.

[51] V. Vahedi and J. Verboncoeur, "XGrafix: An X-Windows Environment for Real-Time Interactive Simulation," in *Proc. 14th Int. Conf. Numer. Simul. Plasmas*, Annapolis, MD, 1991.

[52] F. F. Chen, *Introduction to Plasma Physics and Controlled Fusion*, 2nd. Springer, 2006, vol. 1, p. 421, ISBN: 0-306-41332-9.

[53] P. M. Bellan, *Fundamentals of Plasma Physics*. Cambridge: Cambridge University Press, 2006, pp. 1–536, ISBN: 9780511807183. DOI: 10.1017/CBO9780511807183. [Online]. Available: http://ebooks.cambridge.org/ref/id/CBO9780511807183.

[54] M. T. P. Aldan, "Evaluation of Numerical Errors in Energy and Transport due to Numerically-Induced Divergence of Static Magnetic Fields," University of California, Berkeley, Tech. Rep., 2009, p. 11.

[55] H. Ueda, Y. Omura, H. Matsumoto, and T. Okuzawa, "A study of the numerical heating in electrostatic particle simulations," *Comput. Phys. Commun.*, vol. 79, pp. 249–259, 1994, ISSN: 00104655. DOI: 10.1016/0010-4655(94)90071-X.

[56] R. F. Willis and D. K. Skinner, "Secondary Eleectron Emission Yield Behavior of Polymers," *Solid State Commun.*, vol. 13, pp. 685–688, 1973. [Online]. Available: http://www.sciencedirect.com/science/article/pii/0038109873904596.

[57] M. C. Baker, "Secondary Electron Emission from Dielectrics," PhD thesis, Texas Tech University, 1985, pp. 1–61.

[58] M. A. Furman and M. T. F. Pivi, "Probabilistic model for the simulation of secondary electron emission," *Phys. Rev. Spec. Top. - Accel. Beams*, vol. 5, no. 12, pp. 1–18, 2002, ISSN: 1098-4402. DOI: 10.1103/PhysRevSTAB.5.124404. [Online]. Available: http://link.aps.org/doi/10.1103/PhysRevSTAB.5.124404.

[59] S. A. Rice and J. P. Verboncoeur, "A Comparison of Multipactor Predictions Using Two Popular Secondary Electron Models," *IEEE Trans. Plasma Sci.*, vol. 42, no. 6, pp. 1484–1487, 2014.

[60] R. J. Elsey, "Outgassing of vacuum materials-II," *Vacuum*, vol. 25, no. 8, pp. 347–361, 1975. [Online]. Available: http://linkinghub.elsevier.com/retrieve/pii/0042207X7591653Xhttp://www.sciencedirect.com/science/article/pii/0042207X7591653X.

[61] R. A. Anderson, P Brainard, and I Introduction, "Mechanism of pulsed surface flashover involving electron-stimulated desorption," *J. Appl. Phys.*, vol. 51, no. 3, pp. 1414–1421, 1980.

[62] C. Chang, G. Liu, C. Tang, C. Chen, S. Qiu, J. Fang, and Q. Hou, "The influence of desorption gas to high power microwave window multipactor," *Phys. Plasmas*, vol. 15, no. 9, pp. 093 508–1 093508–6–, 2008, ISSN: 1070664X. DOI: 10.1063/1.2977988. [Online]. Available: http://link.aip.org/link/PHPAEN/v15/i9/p093508/s1{\&}Agg=doihttp://scitation.aip.org/content/aip/journal/pop/15/9/10.1063/1.2977988.

[63] Y. A. Cengel, *Heat and Mass Transfer*, 3rd. Boston: McGraw-Hill, 2007, ISBN: 978-0-07-312930-3.

[64] R. B. Bird, W. E. Stewart, and E. N. Lightfoot, *Transport Phenomena*. John Wiley & Sons, Ltd, 1960, p. 780.

[65] B. Y. P. V. Danckwerts, "Absorption by simultaneous diffusion and chemical reaction," *Trans. Faraday Soc.*, vol. 46, pp. 300–304, 1949.

[66] J. Dendy, "Alternating Direction Methods for Nonlinear Time-Dependent Problems," *SIAM J. Numer. Anal.*, vol. 14, no. 2, pp. 313–326, 1977.

[67] K. Cartwright, J. Verboncoeur, and C. Birdsall, "Loading and injection of Maxwellian distributions in particle simulations," *J. Comput. Phys.*, vol. 162, no. 2, pp. 483–513, 2000, ISSN: 00219991. DOI: 10.1006/jcph.2000.6549. [Online]. Available: http://linkinghub.elsevier.com/retrieve/pii/S0021999100965495http://www.sciencedirect.com/science/article/pii/S0021999100965495.

[68] R. H. Fowler and L. Nordheim, "Electron Emission in Intense Electric Fields," *Proc. R. Soc. London A*, vol. 119, no. 781, pp. 173–181, 1928, ISSN: 1364-5021. DOI: 10.1098/rspa.1928.0091. [Online]. Available: http://rspa.royalsocietypublishing.org/cgi/doi/10.1098/rspa.1928.0091.

[69] T. Takuma and B. Techaumnat, *Electric Fields in Composite Dielectrics and their Applications*. New York: Springer, 2010, ISBN: 978-90-481-9392-9.

[70] L.-K. Ang, Y. Y. Lau, R. A. Kishek, and R. M. Gilgenbach, "Power deposited on a dielectric by multipactor," *IEEE Trans. Plasma Sci.*, vol. 26, no. 3, pp. 290–295, 1998.

[71] R. L. Burden and J. D. Faires, *Numerical Analysis*, 8th, X. Belmont: Thomson Brooks/Cole, 2005, ISBN: 0-534-39200-8.

[72] D. Rapp and P. Englander-Golden, "Total Cross Sections for Ionization and Attachment in Gases by Electron Impact. I. Positive Ionization," *J. Chem. Phys.*, vol. 43, no. 5, p. 1464, 1965, ISSN: 00219606. DOI: 10.1063/1.1696957. [Online]. Available: http://scitation.aip.org/content/aip/journal/jcp/43/5/10.1063/1.1696957.

[73] E. Schamiloglu, "High power microwave sources and applications," *Microw. Symp. Dig. 2004 IEEE MTT-S Int.*, vol. 2, pp. 1001–1004, 2004. DOI: 10.1109/MWSYM.2004.1339150. [Online]. Available: http://ieeexplore.ieee.org/xpls/abs{_}all.jsp?arnumber=1339150http://ieeexplore.ieee.org/lpdocs/epic03/wrapper.htm?arnumber=1339150.

[74] H. C. Kim and J. P. Verboncoeur, "Time-dependent physics of a single-surface multipactor discharge," *Phys. Plasmas*, vol. 12, no. 12, p. 123 504, 2005, ISSN: 1070664X. DOI: 10.1063/1.2148963. [Online]. Available: http://search.ebscohost.com/login.aspx?direct=true{\&}db=a9h{\&}AN=19406254{\&}site=ehost-live.

[75] T Takuma and T Kawamoto, "Field enhancement at a triple junction in arrangements consisting of three media," *IEEE Trans. Dielectr. Electr. Insul.*, vol. 14, no. 3, pp. 566–571, 2007.